

**Spin Labile Conducting Metallopolymers:  
A new architecture for hybrid multifunctional materials**

Brandon Djukic, B.Sc.

Department of Chemistry

Submitted in partial fulfillment  
of the requirements for the degree of

**DOCTOR OF PHILOSOPHY**

Faculty of Science, Brock University  
St. Catharines, Ontario

© 2010

## Abstract

The synthesis of 3-ethynylthienyl- (**2.07**), 3-ethynylterthienyl- (**2.19**) substituted qsal [qsalH = *N*-(8-quinolyl)salicylaldimine] and 3,3'-diethynyl-2,2'-bithienyl bridging *bis*-qsal (**5.06**) ligands are described along with the preparation and characterization of eight cationic iron(III) complexes containing these ligands with a selection of counteranions [(**2.07**) with: SCN<sup>-</sup> (**2.08**), PF<sub>6</sub><sup>-</sup> (**2.09**), and ClO<sub>4</sub><sup>-</sup> (**2.10**); (**2.19**) with PF<sub>6</sub><sup>-</sup> (**2.20**); (**5.06**) with: Cl<sup>-</sup> (**5.07**), SCN<sup>-</sup> (**5.08**), PF<sub>6</sub><sup>-</sup> (**5.09**), and ClO<sub>4</sub><sup>-</sup> (**5.10**)]. Spin-crossover is observed in the solid state for (**2.08**) – (**2.10**) and (**5.07**) – (**5.10**), including a very rare *S* = 5/2 to 3/2 spin-crossover in complex (**2.09**). The unusual reduction of complex (**2.10**) produces a high-spin iron(II) complex (**2.12**).

Six iron(II) complexes that are derived from thienyl analogues of bispicen [bispicen = *bis*(2-pyridylmethyl)-diamine] [2,5-thienyl substituents = H- (**3.11**), Phenyl- (**3.12**), 2-thienyl (**3.13**) or *N*-phenyl-2-pyridinalimine ligands [2,5-phenyl substituents = diphenyl (**3.23**), di(2-thienyl) (**3.24**), 4-phenyl substituent = 3-thienyl (**3.25**)] are reported. Complexes (**3.11**), (**3.23**) and (**3.25**) display thermal spin-crossover in the solid state and (**3.12**) remains high-spin at all temperatures. Complex (**3.13**) rearranges to form an iron(II) complex (**3.14**) with temperature dependent magnetic properties best described as a one-dimensional ferromagnetic chain, with interchain antiferromagnetic interactions and/or ZFS dominant at low temperatures. Magnetic susceptibility and Mössbauer data for complex (**3.24**) display a temperature dependent mixture of spin isomers.

The preparation and characterization of two cobalt(II) complexes containing 3-ethynylthienyl- (**4.04**) and 3-ethynylterhienyl- (**4.06**) substituted bipyridine ligands [(**4.05**):  $[\text{Co}(\text{dbsq})_2(\text{4.04})]$ ; (**4.07**):  $[\text{Co}(\text{dbsq})_2(\text{4.06})]$ ] [ $\text{dbsq} = 3,5\text{-dbsq} = 3,5\text{-di-}i\text{-tert-butyl-1,2-semiquinonate}$ ] are reported. Complexes (**4.05**) and (**4.07**) exhibit thermal valence tautomerism in the solid state and in solution.

Self assembly of complex (**2.10**) into polymeric spheres (**6.11**) afforded the first spin-crossover, polydisperse, micro- to nanoscale material of its kind. Complexes (**2.20**), (**3.24**) and (**4.07**) also form polymers through electrochemical synthesis to produce hybrid metallopolymer films (**6.12**), (**6.15**) and (**6.16**), respectively. The films have been characterized by EDX, FT-IR and UV-Vis spectroscopy. Variable-temperature magnetic susceptibility measurements demonstrate that spin lability is operative in the polymers and conductivity measurements confirm the electron transport properties. Polymer (**6.15**) has a persistent oxidized state that shows a significant decrease in electrical resistance.

## Acknowledgement

I would like to express my sincere gratitude to the people who have contributed to the work described in this dissertation.

Prof. Martin Lemaire and the Lemaire research group

|                   |                                 |
|-------------------|---------------------------------|
| Thomas O'Sullivan | (VT synthesis)                  |
| Haojin Cheng      | (bispicen derivative synthesis) |

Prof. Fereidoon S. Razavi and the Razavi research group

|                            |                               |
|----------------------------|-------------------------------|
| Patrick Reuvekamp          | (resistivity measurements)    |
| Jim Britten                | (X-ray crystallography, PXRD) |
| Paul Dube                  | (magnetic susceptibility)     |
| Serge Gorelsky             | (computational analysis)      |
| Glenda Hooper              | (SEM)                         |
| Hilary Jenkins             | (X-ray crystallography)       |
| Tim Jones                  | (Mass spectrometry)           |
| Steve Korpich              | (EDX)                         |
| Prashanth Poddutoori Kumar | (ESR)                         |
| Alan Lough                 | (X-ray crystallography)       |
| Prof. Muralee Murugesu     | (magnetic susceptibility)     |
| Prof. Georgii I. Nikonov   | (Puresolve solvents)          |
| Prof. Takele Seda          | (Mössbauer spectroscopy)      |
| Prof. Marsha Singh         | (SAXS)                        |

## Table of Contents

### Preface

|  |       |
|--|-------|
| Title page.....                        | i     |
| Abstract.....                          | ii    |
| Acknowledgement.....                   | iv    |
| Table of contents.....                 | v     |
| List of tables.....                    | xvii  |
| List of figures.....                   | xviii |
| List of schemes.....                   | xxix  |
| List of symbols and abbreviations..... | xxxi  |

|   |          |
|---|----------|
| <b>Chapter 1: Spin-crossover and valence tautomerism in molecules</b> | <b>1</b> |
| <b>1.01 Introduction to magnetic materials with labile spin</b>       | <b>1</b> |
| <b>1.02 The spin-crossover phenomenon</b>                             | <b>1</b> |
| i) Geometry and spin state  | 1        |
| ii) Ligand field theory   | 3        |
| iii) Spin labile complexes  | 3        |
| iv) Thermodynamics of spin-crossover                                  | 4        |
| <b>1.03 Characterization of magnetically labile materials</b>         | <b>5</b> |
| i) Variable temperature magnetic susceptibility                       | 5        |
| ii) Mössbauer spectroscopy  | 6        |
| iii) Electron spin resonance  | 9        |

|             |   |           |
|-------------|---|-----------|
| iv)         | Heat capacity measurements                                      | 10        |
| v)          | Electronic absorption spectroscopy                              | 11        |
| vi)         | X-ray diffraction   | 12        |
| <b>1.04</b> | <b>External control of magnetic switching</b>                   | <b>13</b> |
| i)          | Thermal magnetic switching                                      | 13        |
|             | a) Thermal spin-crossover                                       | 13        |
|             | b) Thermal valence tautomerism                                  | 14        |
| ii)         | The The light induced excited spin state trapping effect effect | 16        |
| iii)        | Pressure effects on spin-crossover                              | 20        |
|             | a) Variable pressure effects on compounds that exhibit SCO      | 20        |
|             | b) Pressure induced spin-crossover                              | 21        |
| <b>1.05</b> | <b>Profiles of thermally induced spin-crossover</b>             | <b>22</b> |
| i)          | Abrupt spin-crossover   | 23        |
| ii)         | Gradual spin-crossover  | 24        |
| iii)        | Incomplete spin-crossover                                       | 26        |
| iv)         | Multistep spin-crossover  | 27        |
|             | a) Bimetallic spin-crossover complexes                          | 27        |
|             | b) Polymetallic spin-crossover complexes                        | 29        |
| v)          | Hysteresis in spin-crossover                                    | 31        |
|             | a) Magnetic bistability and path dependent memory               | 32        |
|             | b) Thermal hysteresis in iron(II) spin-crossover complexes      | 33        |
|             | c) Thermal hysteresis in iron(III) spin-crossover complexes     | 34        |
|             | d) Multistate thermal hysteresis                                | 35        |

|   |               |
|---|---------------|
| e) Thermal hysteresis near room temperature                           | 36            |
| <b>1.06 Multifunctionality in spin-crossover materials</b>            | <b>37</b>     |
| <b>1.07 Spin-crossover and electrical conductivity</b>                | <b>38</b>     |
| i) An overview of spin-crossover conductors                           | 38            |
| ii) The coexistence of magnetic switching and electrical conductivity | 39            |
| iii) Interactions between magnetic switching and conductivity         | 41            |
| iv) The chemical pressure effect                                      | 43            |
| v) Developing other kinds of of SCO conductors                        | 44            |
| <br><b>Chapter 2: Iron(III) spin-crossover complexes</b>              | <br><b>48</b> |
| <b>2.01 Goals and objectives</b>                                      | <b>48</b>     |
| <b>2.02 The spin-crossover component</b>                              | <b>48</b>     |
| <b>2.03 Iron(III) qsal complexes</b>                                  | <b>49</b>     |
| i) A preliminary investigation of iron(III) qsal complexes            | 49            |
| ii) Synthesis and characterization                                    | 49            |
| iii) Structural properties  | 50            |
| <b>2.04 Thienyl-substituted qsal complexes</b>                        | <b>51</b>     |
| i) Synthetic methodology  | 51            |
| ii) Ligand synthesis  | 52            |
| iii) Coordination chemistry   | 54            |
| iv) Structural properties   | 56            |
| v) Magnetic characterization  | 63            |
| vi) Electronic absorption spectroscopy                                | 71            |

|                   |   |            |
|-------------------|---|------------|
| vii)              | Electrochemistry  | 72         |
| viii)             | Summary   | 76         |
| <b>2.05</b>       | <b>Terthienyl-substituted qsal complexes</b>                        | <b>77</b>  |
| i)                | Extending the conjugation   | 77         |
| ii)               | Ligand synthesis  | 78         |
| iii)              | Coordination chemistry  | 80         |
| iv)               | Magnetic characterization   | 82         |
| v)                | Electrochemistry  | 83         |
| vi)               | Summary   | 85         |
| <br>              |   |            |
| <b>Chapter 3:</b> | <b>Iron(II) spin-crossover complexes</b>                            | <b>86</b>  |
| <b>3.01</b>       | <b>Iron(II) bispicen derivatives bearing thiophene substituents</b> | <b>86</b>  |
| i)                | Goals and objectives  | 86         |
| ii)               | Ligand synthesis  | 87         |
| iii)              | Coordination chemistry  | 91         |
| iv)               | Magnetic characterization   | 95         |
| v)                | Electronic absorption spectroscopy                                  | 99         |
| vi)               | Electrochemistry  | 100        |
| <b>3.02</b>       | <b>Substituted iron(II) ppi derivatives</b>                         | <b>102</b> |
| i)                | Ligand synthesis  | 102        |
| ii)               | Coordination chemistry  | 107        |
| iii)              | Structural properties   | 108        |
| iv)               | Magnetic characterization   | 112        |



|   |   |            |
|---|---|------------|
| v)  | Electronic absorption spectroscopy                                      | 116        |
| vi)   | Electrochemistry  | 117        |
| vi)   | Summary   | 121        |
| <b>Chapter 4: Cobalt(II) Valence Tautomers</b>                  |   | <b>122</b> |
| <b>4.01</b>   | A valence tautomer bearing a thiophene substituent                      | 122        |
| i)  | Goals and objectives  | 122        |
| ii)   | Ligand synthesis  | 123        |
| iii)  | Coordination chemistry  | 124        |
| iv)   | Magnetic characterization   | 125        |
| v)  | Electronic absorption spectroscopy                                      | 126        |
| vi)   | Electrochemistry  | 127        |
| <b>4.02</b>   | A valence tautomer bearing a terthiophene substituent                   | 128        |
| i)  | Extending the conjugation   | 128        |
| ii)   | Ligand synthesis  | 129        |
| iii)  | Coordination chemistry  | 131        |
| iv)   | Magnetic characterization   | 132        |
| v)  | Electronic absorption spectroscopy                                      | 133        |
| vi)   | Electrochemistry  | 134        |
| vii)  | Summary   | 135        |
| <b>Chapter 5: Bimetallic iron(III) spin-crossover complexes</b> |   | <b>136</b> |
| <b>5.01</b>   | Spin-crossover complexes containing a bridging <i>bis</i> -qsalH ligand | 136        |
| i)  | Goals and objectives  | 136        |
| ii)   | Ligand synthesis  | 137        |

|                   |   |            |
|-------------------|---|------------|
| iii)              | Coordination chemistry  | 140        |
| iv)               | Magnetic characterization   | 141        |
| v)                | Electrochemistry  | 147        |
| vi)               | Summary   | 150        |
| <b>Chapter 6:</b> | <b>Polymeric Materials</b>  | <b>152</b> |
| <b>6.01</b>       | <b>Conjugated polymers</b>  | <b>152</b> |
| i)                | Electrical conductivity in conjugated polymers                    | 152        |
| ii)               | P-doped conducting polymers                                       | 154        |
| iii)              | N-doped conducting polymers                                       | 155        |
| iv)               | Spectroscopic properties  | 155        |
| <b>6.02</b>       | <b>Polymetallic materials</b>                                     | <b>156</b> |
| i)                | Coordination polymers   | 156        |
| ii)               | Conjugated metallopolymers  | 157        |
| iii)              | Type I conjugated metallopolymers                                 | 158        |
| iv)               | Type II conjugated metallopolymers                                | 158        |
| v)                | Type III conjugated metallopolymers                               | 158        |
| <b>6.03</b>       | <b>Synthesis of conjugated polymers</b>                           | <b>159</b> |
| i)                | Chemical synthesis  | 159        |
| ii)               | Electrochemical synthesis   | 159        |
| <b>6.04</b>       | <b>Characterization techniques for conjugated metallopolymers</b> | <b>162</b> |
| i)                | Scanning electron microscopy                                      | 162        |
| ii)               | Energy dispersive X-ray spectroscopy                              | 162        |
| iii)              | Small angle X-ray scattering                                      | 163        |

|                   |   |            |
|-------------------|---|------------|
| <b>6.05</b>       | <b>Goals and objectives</b>                     | <b>164</b> |
| <b>6.06</b>       | <b>Chemical polymerization of (2.10)</b>        | <b>165</b> |
| i)                | Synthesis and characterization                  | 165        |
| ii)               | Structural properties                           | 167        |
| iii)              | Electronic absorption spectroscopy              | 169        |
| iv)               | Magnetic characterization                       | 170        |
| <b>6.07</b>       | <b>Electrochemical polymerization of (2.21)</b> | <b>171</b> |
| i)                | Synthesis and characterization                  | 171        |
| ii)               | Magnetic properties                             | 174        |
| iii)              | Variable temperature conductivity               | 176        |
| <b>6.08</b>       | <b>Electrochemical polymerization of (3.24)</b> | <b>178</b> |
| i)                | Synthesis and characterization                  | 178        |
| ii)               | Magnetic properties                             | 181        |
| iii)              | Electronic absorption spectroscopy              | 182        |
| iv)               | Variable temperature conductivity               | 183        |
| <b>6.09</b>       | <b>Electrochemical polymerization of (4.07)</b> | <b>185</b> |
| i)                | Synthesis and characterization                  | 185        |
| ii)               | Magnetic properties                             | 188        |
| iii)              | Electronic absorption spectroscopy              | 189        |
| iv)               | Variable temperature conductivity               | 191        |
| <br>              |   |            |
| <b>Chapter 7:</b> | <b>General conclusions</b>                      | <b>193</b> |

|   |            |
|---|------------|
| <b>Chapter 8: Experimental</b>  | <b>201</b> |
| <b>8.01</b> General procedures  | 201        |
| <b>8.02</b> Instrumentation   | 201        |
| <b>8.03</b> Variable temperature magnetic susceptibility measurements | 204        |
| <b>8.04</b> Electrochemical experiments                               | 205        |
| <b>8.05</b> Electrical conductivity                                   | 206        |
| <b>8.06</b> X-ray structure determination and powder diffraction      | 206        |
| <b>8.07</b> Computation   | 207        |
| <b>8.08</b> Experimental for Chapter 2                                | 208        |
| 1. Iron(III) qsal complexes   | 208        |
| i) Ligand synthesis   | 208        |
| (2.01)H: qsalH  | 208        |
| ii) Complex syntheses   | 209        |
| (2.02): [Fe(2.01) <sub>2</sub> ]Cl                                    | 209        |
| (2.03): [Fe(2.01) <sub>2</sub> ]I·H <sub>2</sub> O                    | 209        |
| 2. Thienyl-substituted complexes                                      | 211        |
| i) Ligand synthesis   | 211        |
| (2.04): 5-(Ethynyltrimethylsilyl)salicylaldehyde                      | 211        |
| (2.05): 5-Ethynylsalicylaldehyde                                      | 212        |
| (2.06): 5-(3'-Ethynylthienyl)salicylaldehyde                          | 213        |
| (2.07)H: theqsalH   | 214        |
| ii) Complex syntheses   | 215        |
| (2.08): [Fe(2.07) <sub>2</sub> ]PF <sub>6</sub>                       | 215        |
| (2.09): [Fe(2.07) <sub>2</sub> ]SCN·2.5H <sub>2</sub> O               | 216        |
| (2.10): [Fe(2.07) <sub>2</sub> ]ClO <sub>4</sub>                      | 217        |

|  |     |
|--|-----|
| (2.11): [Mn(2.07) <sub>2</sub> ]   | 218 |
| (2.12): [Fe(2.07) <sub>2</sub> ]·C <sub>3</sub> H <sub>6</sub> O·1.5H <sub>2</sub> O | 219 |
| 3. Terthienyl-substituted qsal complexes   | 219 |
| i) Ligand synthesis  | 219 |
| (2.13): 2,3,5-tribromothiophene  | 219 |
| (2.14): 3'-bromo-2,2':5',2''-terthiophene  | 220 |
| (2.15): 3'-(3-hydroxy-3-methylbut-1-ynyl)-2,2':5',2''-terthiophene                   | 221 |
| (2.16): 3'-(ethynyl)-2,2':5',2''-terthiophene  | 222 |
| (2.17): 5-iodosalicylaldehyde  | 223 |
| (2.18): 3'-(5-ethynylsalicylaldehyde)-2,2':5',2''-terthiophene                       | 223 |
| (2.19): H: tertheqsalH   | 225 |
| ii) Complex syntheses  | 226 |
| (2.20): [Fe(2.19) <sub>2</sub> ]PF <sub>6</sub>                                      | 226 |
| (2.21): [Mn(2.19) <sub>2</sub> ]   | 227 |
| 8.09 Experimental for Chapter 3  | 228 |
| 1. Bispicen derivatives  | 228 |
| i) Thiophene derivative  | 228 |
| (3.02): 2,5-dibromo-3,4-dinitrothiophene   | 228 |
| (3.03): 3,4-diaminothiophene·2HCl  | 229 |
| (3.04): <i>N,N'</i> -bis(2-pyridylmethyl)-3,4-diaminothiophene                       | 229 |
| ii) Diphenylthiophene derivative   | 230 |
| (3.05): 3,4-dinitro-2,5-diphenylthiophene  | 230 |
| (3.06): 3,4-diamino-2,5-diphenylthiophene·2HCl                                       | 231 |
| (3.07): <i>N,N'</i> -bis(2-pyridylmethyl)-3,4-diamino-2,5-diphenylthiophene          | 232 |
| iii) Terthiophene derivative   | 233 |

|      |   |     |
|------|---|-----|
|      | (3.08): 3',4'-dinitro-2,2':5',2''-terthiophene  | 233 |
|      | (3.09): 3',4'-diamino-2,2':5',2''-terthiophene·2HCl   | 234 |
|      | (3.10): <i>N,N'</i> -bis(2-pyridylmethyl)-3,4-diamino-2,2':5',2''-terthiophene                  | 234 |
| iv)  | Complex syntheses   | 236 |
|      | (3.11): [Fe(3.04)(NCS) <sub>2</sub> ]   | 236 |
|      | (3.12): [Fe(3.07)(NCS) <sub>2</sub> ]   | 237 |
|      | (3.13): [Fe(3.10)(NCS) <sub>2</sub> ]   | 238 |
|      | (3.14): [Fe(C <sub>56</sub> H <sub>40</sub> N <sub>8</sub> S <sub>2</sub> )(NCS) <sub>2</sub> ] | 239 |
|      | (3.15): [Fe(C <sub>48</sub> H <sub>32</sub> N <sub>8</sub> S <sub>6</sub> )(NCS) <sub>2</sub> ] | 239 |
| 2.   | Substituted “ppi” complexes   | 240 |
| i)   | [Fe(ppi) <sub>2</sub> (NCS) <sub>2</sub> ] synthesis  | 240 |
|      | (3.16): [Fe(ppi) <sub>2</sub> (NCS) <sub>2</sub> ]  | 240 |
| ii)  | Diphenyl-substitued ppi ligand synthesis  | 241 |
|      | (3.17): 2,5-diphenylaniline   | 241 |
|      | (3.18): <i>N'</i> -(2,2':5',2''-terphenyl)-2-pyridinalimine                                     | 242 |
| iii) | Dithienyl-substitued ppi ligand synthesis   | 243 |
|      | (3.19): 2,5-dithienylaniline  | 243 |
|      | (3.20): <i>N</i> -(2,5-di(2-thienyl)phenyl)-2-pyridinalimine                                    | 244 |
| iv)  | Thienyl-substitued ppi ligand synthesis   | 245 |
|      | (3.21): 4-thienylaniline  | 245 |
|      | (3.22): <i>N</i> -(4-(3-thienyl)phenyl)-2-pyridinalimine  | 246 |
| v)   | Complex synthesis   | 247 |
|      | (3.23): [Fe(3.18) <sub>2</sub> (NCS) <sub>2</sub> ]   | 247 |
|      | (3.24): [Fe(3.20) <sub>2</sub> (NCS) <sub>2</sub> ]   | 248 |
|      | (3.25): [Fe(3.22) <sub>2</sub> (NCS) <sub>2</sub> ]   | 249 |

|             |   |            |
|-------------|---|------------|
| <b>8.10</b> | <b>Experimental for Chapter 4</b>                           | <b>250</b> |
| 1.          | A thienyl-substituted valence tautomer                      | 250        |
| i)          | Ligand synthesis  | 250        |
|             | (4.01): 5-bromobipyridine                                   | 250        |
|             | (4.02): 5-(trimethylsilylethynyl)bipyridine                 | 251        |
|             | (4.03): 5-ethynylbipyridine                                 | 252        |
|             | (4.04): 5-(3'-ethynylthienyl)bipyridine                     | 252        |
| ii)         | Complex synthesis   | 253        |
|             | (4.05): [Co(dbsq) <sub>2</sub> (4.04)]                      | 253        |
| 2.          | A terthienyl-substituted valence tautomer                   | 254        |
| i)          | Ligand synthesis  | 254        |
|             | (4.06): 3'-(5-ethynylbipyridine)-2,2':5',2''-terthiophene   | 254        |
| ii)         | Complex synthesis   | 256        |
|             | (4.07): [Co(dbsq) <sub>2</sub> (4.06)]                      | 256        |
| <b>8.11</b> | <b>Experimental for Chapter 5</b>                           | <b>257</b> |
| 1.          | Bimetallic qsal complexes                                   | 257        |
| i)          | Ligand synthesis  | 257        |
|             | (5.01): 3,3',5,5'-tetrabromo-2,2'-bithiophene               | 257        |
|             | (5.02): 3,3'-dibromothiophene                               | 258        |
|             | (5.03): 3,3'-bis(trimethylsilylethynyl)-2,2'-bithiophene    | 258        |
|             | (5.04): 3,3'-dithienyl-2,2'-bithiophene                     | 259        |
|             | (5.05): 3,3'-bis(5-ethynylsalicylaldehyde)-2,2'-bithiophene | 260        |
|             | (5.06): bis-qsalH   | 261        |
| ii)         | Complex syntheses   | 263        |
|             | (5.07): [(Fe(2.01)) <sub>2</sub> (5.06)]Cl <sub>2</sub>     | 263        |

|  |     |
|--|-----|
| <b>(5.08):</b> $[(\text{Fe}(\mathbf{2.01}))_2(\mathbf{5.06})](\text{SCN})_2 \cdot 2\text{KCl}$ | 264 |
| <b>(5.09):</b> $[(\text{Fe}(\mathbf{2.01}))_2(\mathbf{5.06})](\text{PF}_6)_2$                  | 265 |
| <b>(5.10):</b> $[(\text{Fe}(\mathbf{2.01}))_2(\mathbf{5.06})](\text{ClO}_4)_2$                 | 266 |
| <b>8.12 Experimental for Chapter 6</b>   | 267 |
| 1. Chemical polymerization   | 267 |
| i) Iron(III) microspheres  | 267 |
| <b>(6.11):</b> poly( <b>2.10</b> )   | 267 |
| 2. Electrochemical polymerization  | 268 |
| i) Iron(III) spin-crossover related polymers   | 268 |
| <b>(6.12):</b> poly( <b>2.21</b> )   | 268 |
| <b>(6.13):</b> poly( <b>2.20</b> )   | 270 |
| <b>(6.14):</b> poly( <b>2.22</b> )   | 271 |
| ii) Iron(II) spin-crossover polymer  | 272 |
| <b>(6.15):</b> poly( <b>3.24</b> )   | 272 |
| iii) Cobalt(II) valence tautomer related polymers  | 274 |
| <b>(6.16):</b> poly( <b>4.07</b> )   | 274 |
| <b>(6.17):</b> poly( <b>4.06</b> )   | 276 |
| <b>References</b>  | 278 |
| <b>Appendix A: Crystallographic parameters</b>   | 290 |
| <b>Appendix B: Polymer images</b>  | 298 |



## List of tables

|  |     |
|--|-----|
| <b>Table 2.01:</b> Selected bond distances and angles for <b>(2.02)</b>                                    | 51  |
| <b>Table 2.02:</b> Selected bond distances and angles for <b>(2.12)</b>                                    | 57  |
| <b>Table 2.03:</b> Selected bond distances and angles for <b>(2.12)</b>                                    | 60  |
| <b>Table 2.04:</b> Mössbauer data for <b>(2.08)</b> and <b>(2.09)</b>                                      | 67  |
| <b>Table 2.05:</b> Electrochemical data for <b>(2.01)H</b> and <b>(2.07)H</b> in DCM                       | 72  |
| <b>Table 2.06:</b> Electrochemical data for <b>(2.02)</b> , <b>(2.08)</b> – <b>(2.11)</b> in ACN           | 74  |
| <b>Table 2.07:</b> Electrochemical data for <b>(2.19)H</b> in DCM and <b>(2.20)</b> - <b>(2.21)</b> in ACN | 83  |
| <b>Table 3.01:</b> Selected bond distances and angles for <b>(3.14)</b>                                    | 94  |
| <b>Table 3.02:</b> Electrochemical data for <b>(3.13)</b> in ACN   | 100 |
| <b>Table 3.03:</b> Selected bond distances and angles for <b>(3.18)</b>                                    | 106 |
| <b>Table 3.04:</b> Selected bond distances and angles for <b>(3.23)</b>                                    | 109 |
| <b>Table 3.05:</b> Selected bond distances and angles for <b>(3.24)</b>                                    | 111 |
| <b>Table 3.06:</b> Mössbauer data for <b>(3.24)</b> and <b>(3.25)</b>                                      | 113 |
| <b>Table 3.07:</b> Electrochemical data for derivatives of <b>(3.16)</b> in DCM                            | 119 |
| <b>Table 4.01:</b> Electrochemical data for <b>(4.04)</b> in DCM and <b>(4.05)</b> in DMF                  | 127 |
| <b>Table 4.02:</b> Electrochemical data for <b>(4.06)</b> and <b>(4.07)</b> in DCM                         | 134 |
| <b>Table 5.01:</b> Selected bond distances and angles for <b>(5.05)</b>                                    | 138 |
| <b>Table 5.02:</b> Mössbauer data for <b>(5.07)</b> - <b>(5.10)</b>  | 144 |
| <b>Table 5.03:</b> Electrochemical data for <b>(5.06)H<sub>2</sub></b> – <b>(5.10)</b> in ACN              | 149 |
| <b>Table 8.01:</b> EDX analysis for <b>(6.12)</b>  | 269 |
| <b>Table 8.02:</b> EDX analysis for <b>(6.15)</b>  | 273 |
| <b>Table 8.03:</b> EDX analysis for <b>(6.16)</b>  | 275 |

## List of figures

|  |    |
|--|----|
| <b>Figure 1.01:</b> The energy level diagram of transition metals with octahedral coordination geometry <sup>[3]</sup>   | 1  |
| <b>Figure 1.02:</b> A low-spin d <sup>5</sup> transition metal with octahedral geometry <sup>[3]</sup>   | 2  |
| <b>Figure 1.03:</b> A high-spin d <sup>5</sup> transition metal with octahedral geometry <sup>[3]</sup>  | 2  |
| <b>Figure 1.04:</b> The spectrochemical series (field strength increases to the right) [bpy = 2,2'-bipyridine] <sup>[3]</sup>  | 3  |
| <b>Figure 1.05:</b> Mössbauer spectra of (1.01) <sup>[14]</sup>  | 8  |
| <b>Figure 1.06:</b> A diagram of complex (1.02)  | 9  |
| <b>Figure 1.07:</b> Variable temperature ESR spectra of (1.02) <sup>[17]</sup>   | 10 |
| <b>Figure 1.08:</b> Variable temperature specific heat capacity of (1.03) <sup>[20]</sup>  | 11 |
| <b>Figure 1.09:</b> Variable temperature electronic absorption spectra of (1.04) <sup>[21]</sup>   | 11 |
| <b>Figure 1.10:</b> A diagram of the cation [Fe(qnal) <sub>2</sub> ] <sup>+</sup> (1.05)   | 12 |
| <b>Figure 1.11:</b> Variable temperature magnetic susceptibility of (1.06) <sup>[28]</sup>   | 13 |
| <b>Figure 1.12:</b> The valence tautomerism of (1.08) <sup>[1]</sup>   | 14 |
| <b>Figure 1.13:</b> The magnetic profile of (1.08) <sup>[1]</sup>  | 15 |
| <b>Figure 1.14:</b> A diagram of complex (1.04)  | 16 |
| <b>Figure 1.15:</b> The LIESST effect of complex (1.04) with arrows indicating the excited state region <sup>[67]</sup>  | 16 |
| <b>Figure 1.16:</b> Diagrams of (1.09) (left) and (1.10) (right) <sup>[72]</sup>   | 17 |
| <b>Figure 1.17:</b> The LIESST effect for (a) (1.09) and (b) (1.10) with arrows indicating the excited state region <sup>[72]</sup>  | 17 |
| <b>Figure 1.18:</b> The Mössbauer spectra of (1.10) (a) room temperature (b) 5 K (c) 5 K after illumination at 532 nm <sup>[72]</sup>  | 19 |
| <b>Figure 1.19:</b> Pressure effects on spin-crossover in compound (1.03) (a) 10 <sup>5</sup> Pa before and after applying pressure (b) 0.17 GPa (c) 0.34 GPa (d) 0.57 GPa <sup>[75]</sup> | 20 |

|   |    |
|---|----|
| <b>Figure 1.20:</b> A diagram of complex <b>(1.11)</b>  | 21 |
| <b>Figure 1.21:</b> Pressure induced spin-crossover of <b>(1.11)</b> at (a) 105 Pa (b) 0.44 GPa (c) 0.56 GPa (d) 0.86 GPa (e) 1.05 GPa <sup>[75]</sup>      | 21 |
| <b>Figure 1.22:</b> Typical profiles of thermally induced spin-crossover (i) abrupt (ii) gradual (iii) gradual and incomplete (iv) multistep (v) hysteretic | 22 |
| <b>Figure 1.23:</b> The abrupt spin-crossover exhibited by <b>(1.03)</b> <sup>[2]</sup>   | 23 |
| <b>Figure 1.24:</b> The packing diagram of complex <b>(1.03)</b> <sup>[2]</sup>   | 23 |
| <b>Figure 1.25:</b> The gradual spin-crossover exhibited by <b>(1.12)</b> <sup>[2]</sup>  | 24 |
| <b>Figure 1.26:</b> The packing diagram of complex <b>(1.12)</b> <sup>[2]</sup>   | 25 |
| <b>Figure 1.27:</b> The 1-isopropyltetrazole (iptz) ligand of $[\text{Fe}(\text{iptz})_6](\text{SCN})_2$ <b>(1.13)</b>                                      | 26 |
| <b>Figure 1.28:</b> The gradual and incomplete spin-crossover exhibited by <b>(1.13)</b> <sup>[82]</sup>  | 26 |
| <b>Figure 1.29:</b> Examples of ligands used in bimetallic spin-crossover complexes <sup>[83-87]</sup>  | 27 |
| <b>Figure 1.30:</b> The molecular structure of complex <b>(1.19)</b> <sup>[88]</sup>  | 28 |
| <b>Figure 1.31:</b> The two step spin-crossover of <b>(1.19)</b> <sup>[88]</sup>  | 28 |
| <b>Figure 1.32:</b> The molecular structure (left) and a diagram displaying the Fe(II)-ligand coordination of <b>(1.21)</b> (right) <sup>[90]</sup>         | 29 |
| <b>Figure 1.33:</b> The variable temperature magnetic profile of <b>(1.21)</b> <sup>[90]</sup>  | 30 |
| <b>Figure 1.34:</b> The Mössbauer spectra for complex <b>(1.21)</b> <sup>[90]</sup>   | 30 |
| <b>Figure 1.35:</b> The variable temperature magnetic profile of <b>(1.22)</b> <sup>[2]</sup>   | 31 |
| <b>Figure 1.36:</b> A diagram of complex <b>(1.22)</b>  | 31 |
| <b>Figure 1.37:</b> A general diagram for the memory effect of SCO materials <sup>[94]</sup>  | 32 |
| <b>Figure 1.38:</b> A diagram of $[\text{Fe}(\text{pmpea})_2(\text{NCS})_2]$ <b>(1.23)</b>  | 33 |
| <b>Figure 1.39:</b> The variable temperature magnetic profile of <b>(1.23)</b> <sup>[95]</sup>  | 33 |
| <b>Figure 1.40:</b> The variable temperature magnetic profile of <b>(1.25)</b> <sup>[97]</sup>  | 35 |
| <b>Figure 1.41:</b> A diagram of $[\text{Fe}(\text{sal}_2\text{-trien})]^+[\text{Ni}(\text{dmit})_2]^-$ <b>(1.28)</b>                                       | 39 |

|  |    |
|--|----|
| <b>Figure 1.42:</b> A packing diagram of <b>(1.28)</b> in the high-spin state <sup>[107]</sup>   | 39 |
| <b>Figure 1.43:</b> The variable temperature magnetic profile of <b>(1.28)</b> <sup>[107]</sup>  | 40 |
| <b>Figure 1.44:</b> A diagram of [Fe(qsal) <sub>2</sub> ][Ni(dmit) <sub>2</sub> ] <sub>3</sub> <b>(1.29)</b>   | 41 |
| <b>Figure 1.45:</b> A packing diagram of <b>(1.29)</b> in the high-spin state <sup>[108]</sup>   | 41 |
| <b>Figure 1.46:</b> The (a) magnetic and (b) the resistivity profiles of <b>(1.29)</b> <sup>[108]</sup>  | 42 |
| <b>Figure 1.47:</b> The interaction between conductivity and spin-crossover in <b>(1.29)</b> <sup>[108]</sup>  | 42 |
| <b>Figure 1.48:</b> The interaction between conductivity and spin-crossover in <b>(1.30)</b> <sup>[25]</sup>   | 43 |
| <b>Figure 1.49:</b> A diagram of complex <b>(1.31)</b>   | 44 |
| <b>Figure 1.50:</b> The variable temperature magnetic profile of <b>(1.31)</b> <sup>[109]</sup>  | 45 |
| <b>Figure 1.51:</b> A packing diagram of complex <b>(1.31)</b> <sup>[109]</sup>  | 45 |
| <b>Figure 1.52:</b> The interaction between conductivity and spin-crossover in <b>(1.32)</b> <sup>[110]</sup>  | 47 |
| <b>Figure 2.01:</b> The molecular structure of <b>(2.03)</b> with ellipsoids drawn at the 50 % probability level   | 50 |
| <b>Figure 2.02:</b> <sup>1</sup> H-NMR spectrum of <b>(2.07)</b> H in CDCl <sub>3</sub>  | 53 |
| <b>Figure 2.03:</b> The molecular structure of <b>(2.12)</b> with ellipsoids drawn at the 50 % probability level   | 57 |
| <b>Figure 2.04:</b> The packing diagram of <b>(2.12)</b>   | 58 |
| <b>Figure 2.05:</b> The molecular structure of <b>(2.11)</b> with ellipsoids drawn at the 50 % probability level   | 59 |
| <b>Figure 2.06:</b> The X-ray powder diffraction pattern of <b>(2.09)</b> <sup>[111]</sup>   | 61 |
| <b>Figure 2.07:</b> The calculated powder diffraction pattern of <b>(2.11)</b> <sup>[111]</sup>  | 61 |
| <b>Figure 2.08:</b> A low angle comparison between <b>(2.09)</b> and <b>(2.11)</b> <sup>[111]</sup>  | 61 |
| <b>Figure 2.09:</b> The X-ray powder diffraction pattern of <b>(2.10)</b> <sup>[111]</sup>   | 62 |
| <b>Figure 2.10:</b> Variable temperature magnetic susceptibility measurements for complexes <b>(2.08)</b> - <b>(2.10)</b> in a 5000 Oe magnetic field <sup>[111]</sup> | 63 |

|  |    |
|--|----|
| <b>Figure 2.11:</b> The Mössbauer spectra for complex <b>(2.08)</b> with experimental data (dots) fitted to theoretical lines <sup>[111]</sup>               | 64 |
| <b>Figure 2.12:</b> Reduced magnetization versus field data for <b>(2.09)</b> (large black dots) recorded at 5 K between theoretical curves <sup>[111]</sup> | 65 |
| <b>Figure 2.13:</b> Mössbauer spectra for complex <b>(2.09)</b> with experimental data (dots) fitted to theoretical lines <sup>[111]</sup>                   | 67 |
| <b>Figure 2.14:</b> A powder ESR spectra of <b>(2.09)</b> at 298 and 120 K <sup>[111]</sup>  | 69 |
| <b>Figure 2.15:</b> A powder ESR spectra of <b>(2.10)</b> at 120 K <sup>[111]</sup>  | 69 |
| <b>Figure 2.16:</b> The variable temperature absorbance profile of <b>(2.09)</b> <sup>[111]</sup>  | 71 |
| <b>Figure 2.17:</b> Cyclic voltammograms of (a) <b>(2.01)</b> H and (b) <b>(2.07)</b> H  | 72 |
| <b>Figure 2.18:</b> Cyclic (left) and differential pulse (right) voltammograms of <b>(2.02)</b>  | 73 |
| <b>Figure 2.19:</b> Cyclic (left) and differential pulse (right) voltammograms of <b>(2.08)</b>  | 73 |
| <b>Figure 2.20:</b> Cyclic (left) and differential pulse (right) voltammograms of <b>(2.09)</b>  | 73 |
| <b>Figure 2.21:</b> Cyclic (left) and differential pulse (right) voltammograms of <b>(2.10)</b>  | 74 |
| <b>Figure 2.22:</b> Cyclic voltammogram of complex <b>(2.11)</b>   | 75 |
| <b>Figure 2.23:</b> <sup>1</sup> H-NMR spectrum of <b>(2.19)</b> H in CDCl <sub>3</sub>  | 79 |
| <b>Figure 2.24:</b> The magnetic profile of <b>(2.20)</b> in a 5000 Oe magnetic field <sup>[118]</sup>   | 82 |
| <b>Figure 2.25:</b> Cyclic voltammogram of the ligand <b>(2.19)</b>  | 83 |
| <b>Figure 2.26:</b> Cyclic voltammogram of complex <b>(2.20)</b>   | 84 |
| <b>Figure 2.27:</b> Cyclic voltammogram of complex <b>(2.21)</b>   | 84 |
| <b>Figure 3.01:</b> The bispicen ligand <b>(3.01)</b>  | 86 |
| <b>Figure 3.02:</b> <sup>1</sup> H-NMR spectrum of <b>(3.04)</b> in CDCl <sub>3</sub>  | 87 |
| <b>Figure 3.03:</b> <sup>1</sup> H-NMR spectrum of <b>(3.07)</b> in CDCl <sub>3</sub>  | 89 |
| <b>Figure 3.04:</b> <sup>1</sup> H-NMR spectrum of <b>(3.10)</b> in CDCl <sub>3</sub>  | 90 |

|  |     |
|--|-----|
| <b>Figure 3.05:</b> The molecular structure of complex (3.14) with ellipsoids drawn at the 50 % probability level  | 93  |
| <b>Figure 3.06:</b> The packing diagram of (3.14)  | 93  |
| <b>Figure 3.07:</b> Variable temperature magnetic properties of (3.11) and (3.13) in a 5000 Oe magnetic field <sup>[121]</sup>   | 95  |
| <b>Figure 3.08:</b> Variable temperature magnetic properties of (3.14) in a 5000 Oe magnetic field <sup>[121]</sup>  | 96  |
| <b>Figure 3.09:</b> Reduced magnetization versus field data for (3.14) recorded at 5 K <sup>[121]</sup>  | 97  |
| <b>Figure 3.10:</b> Calculated spin density distribution in (3.14) with natural population analysis derived atomic spin density shown for the most important contributors <sup>[121]</sup> | 98  |
| <b>Figure 3.11:</b> Variable temperature absorbance profile of (3.11) in ethanol <sup>[121]</sup>  | 99  |
| <b>Figure 3.12:</b> Solutions of (3.11) in ethanol at variable temperatures  | 99  |
| <b>Figure 3.13:</b> Cyclic (left) and differential pulse (right) voltammograms of (3.13)   | 100 |
| <b>Figure 3.14:</b> A diagram of Fe(ppi) <sub>2</sub> (NCS) <sub>2</sub> (3.16)  | 102 |
| <b>Figure 3.15:</b> <sup>1</sup> H-NMR spectrum of (3.18) in CDCl <sub>3</sub>   | 103 |
| <b>Figure 3.16:</b> <sup>1</sup> H-NMR spectrum of (3.20) in CDCl <sub>3</sub>   | 103 |
| <b>Figure 3.17:</b> <sup>1</sup> H-NMR spectrum of (3.22) in CDCl <sub>3</sub>   | 104 |
| <b>Figure 3.18:</b> The molecular structure of (3.20) with thermal ellipsoids drawn at the 50 % probability level  | 106 |
| <b>Figure 3.19:</b> The molecular structure of (3.23) with thermal ellipsoids drawn at the 50 % probability level  | 108 |
| <b>Figure 3.20:</b> The molecular structure of (3.24) with thermal ellipsoids drawn at the 50 % probability level  | 110 |
| <b>Figure 3.21:</b> A space filling diagram showing the imine (N4)-thiophene (S3) contact of (3.24)  | 110 |
| <b>Figure 3.22:</b> Variable temperature magnetic susceptibility measurements for complexes (3.23) - (3.25) in a 5000 Oe magnetic field  | 112 |
| <b>Figure 3.23:</b> The Mössbauer spectra for complex (3.24) (left) and (3.25) (right) with experimental data (dots) fitted to theoretical lines   | 114 |

|  |     |
|--|-----|
| <b>Figure 3.24:</b> Solvatochromism exhibited by (3.23)  | 116 |
| <b>Figure 3.25:</b> Cyclic (left) and differential pulse (right) voltammograms of (3.23)   | 117 |
| <b>Figure 3.26:</b> Cyclic (left) and differential pulse (right) voltammograms of (3.18)   | 117 |
| <b>Figure 3.27:</b> Cyclic (left) and differential pulse (right) voltammograms of (3.24)   | 117 |
| <b>Figure 3.28:</b> Cyclic (left) and differential pulse (right) voltammograms of (3.20)   | 118 |
| <b>Figure 3.29:</b> Cyclic (left) and differential pulse (right) voltammograms of (3.25)   | 118 |
| <b>Figure 3.30:</b> Cyclic (left) and differential pulse (right) voltammograms of (3.16)   | 118 |
| <b>Figure 4.01:</b> Variable temperature magnetic susceptibility plot for complex (4.05) in a 5000 Oe magnetic field <sup>[137]</sup>                        | 125 |
| <b>Figure 4.02:</b> Variable temperature absorbance profile of (4.05) <sup>[137]</sup>   | 126 |
| <b>Figure 4.03:</b> Cyclic voltammograms of (a) (4.04) and (b) (4.05)  | 127 |
| <b>Figure 4.04:</b> <sup>1</sup> H-NMR spectrum of (4.06)  | 130 |
| <b>Figure 4.05:</b> Variable temperature magnetic data of (4.07) in a 5000 Oe magnetic field <sup>[139]</sup>  | 132 |
| <b>Figure 4.06:</b> Variable temperature absorbance profile of (4.07) in ethanol <sup>[139]</sup>  | 133 |
| <b>Figure 4.07:</b> Cyclic voltammograms of (a) (4.06) and (b) (4.07)  | 134 |
| <b>Figure 5.01:</b> The molecular structure of (5.05) with ellipsoids drawn at the 50 % probability level  | 138 |
| <b>Figure 5.02:</b> <sup>1</sup> H-NMR spectrum of (5.06)H <sub>2</sub> in CDCl <sub>3</sub>   | 139 |
| <b>Figure 5.03:</b> Variable temperature magnetic susceptibility of (5.07) - (5.10) in a 5000 Oe magnetic field <sup>[141]</sup>                             | 141 |
| <b>Figure 5.04:</b> Variable temperature Mössbauer data for complexes (5.07) - (5.10), experimental data (dots) fitted to theoretical lines <sup>[141]</sup> | 143 |
| <b>Figure 5.05:</b> Powder ESR spectra of (a) (5.09) and (b) (5.10) <sup>[141]</sup>   | 146 |
| <b>Figure 5.06:</b> Cyclic (left) and differential pulse (right) voltammograms of (5.07)   | 147 |
| <b>Figure 5.07:</b> Cyclic (left) and differential pulse (right) voltammograms of (5.08)   | 148 |
| <b>Figure 5.08:</b> Cyclic (left) and differential pulse (right) voltammogram of (5.09)  | 148 |

|   |     |
|---|-----|
| <b>Figure 5.09:</b> Cyclic (left) and differential pulse (right) voltammogram of <b>(5.10)</b>  | 148 |
| <b>Figure 5.10:</b> The cyclic voltammogram of <b>(5.06)</b> H <sub>2</sub>   | 149 |
| <b>Figure 6.01:</b> Conjugated polymers (i) polyacetylene <b>(6.01)</b> , (ii) polythiophene <b>(6.02)</b> , (iii) polythiazole <b>(6.03)</b> , (iv) poly(3-methylthiophene) <b>(6.04)</b> , (v) polyphenylene <b>(6.05)</b> , (vi) poly(thiophene-phenylene-thiophene) | 152 |
| <b>Figure 6.02.</b> Energy band diagram for increasing lengths of <b>(6.01)</b> <sup>[150]</sup>  | 153 |
| <b>Figure 6.03:</b> The spectroelectrochemistry of <b>(6.04)</b> <sup>[158]</sup>   | 155 |
| <b>Figure 6.04:</b> A general coordination polymer diagram  | 156 |
| <b>Figure 6.05:</b> Type I - III conjugated metallopolymers <sup>[146]</sup>  | 157 |
| <b>Figure 6.06:</b> Conjugated polymers with higher (left) and lower (right) regioregularity  | 159 |
| <b>Figure 6.07:</b> A diagram of Ni(saloth) <b>(6.09)</b>   | 160 |
| <b>Figure 6.08:</b> The cyclic voltammograms of <b>(6.08)</b> and <b>(6.09)</b> <sup>[166]</sup>  | 161 |
| <b>Figure 6.09:</b> Purple microspheres of <b>(6.11)</b> <sup>[171]</sup>   | 165 |
| <b>Figure 6.10:</b> The X-ray powder diffraction pattern of <b>(6.11)</b> <sup>[171]</sup>  | 167 |
| <b>Figure 6.11:</b> X-ray scattering (left) and Guinier (right) plots of <b>(6.11)</b> <sup>[171]</sup>   | 168 |
| <b>Figure 6.12:</b> The reflectance spectrum of <b>(2.10)</b> <sup>[171]</sup>  | 169 |
| <b>Figure 6.13:</b> Variable temperature magnetic susceptibility data for <b>(6.11)</b> in a 5000 Oe magnetic field <sup>[171]</sup>  | 170 |
| <b>Figure 6.14:</b> The electrochemical polymerization of <b>(2.21)</b> on an ITO substrate (left) and the cyclic voltammogram of <b>(6.12)</b> on a platinum button (right)  | 171 |
| <b>Figure 6.15:</b> Current versus scan rate experiments for <b>(6.12)</b>  | 172 |
| <b>Figure 6.16:</b> Electrochemical polymerization of <b>(2.21)</b> (left) and <b>(2.07)</b> H (right) on an ITO substrate  | 174 |
| <b>Figure 6.17:</b> Variable temperature magnetic susceptibility data for <b>(6.12)</b> in a 15000 Oe magnetic field <sup>[118]</sup>   | 174 |
| <b>Figure 6.18:</b> Variable temperature conductivity of electrodeposited films of <b>(6.12)</b> - <b>(6.14)</b> <sup>[118]</sup>   | 176 |



|  |     |
|--|-----|
| <b>Figure 6.19:</b> The electrochemical polymerization of (3.24) (left) and the cyclic voltammogram of (6.15) on a platinum button (right) | 178 |
| <b>Figure 6.20:</b> Current versus scan rate experiments for (6.12)  | 178 |
| <b>Figure 6.21:</b> Differential pulse voltammograms of (6.15) (left) and the iron(II) oxidation of (6.15) (right)                         | 179 |
| <b>Figure 6.22:</b> Differential pulse voltammograms polymer precursors (3.20) (left) and (3.24) (right)                                   | 180 |
| <b>Figure 6.23:</b> Variable temperature magnetic properties of (6.15) in a 15000 Oe field   | 181 |
| <b>Figure 6.24:</b> The spectroelectrochemical properties of (6.15)  | 182 |
| <b>Figure 6.25:</b> Variable temperature conductivity of polymer (6.15) measured by sweeping (left) and settling (right)                   | 183 |
| <b>Figure 6.26:</b> Variable temperature resistance of (6.15) measured before (solid line) and after (dotted line) oxidation               | 184 |
| <b>Figure 6.27:</b> The electrochemical polymerization of (4.07) (left) and the cyclic voltammogram of (6.16) on a platinum button (right) | 185 |
| <b>Figure 6.28:</b> Current versus scan rate experiments for (6.16)  | 186 |
| <b>Figure 6.29:</b> The electrochemical polymerization of (6.17)   | 187 |
| <b>Figure 6.30:</b> Variable temperature magnetic properties of (6.16) and (6.17) in a 15000 Oe field <sup>[139]</sup>                     | 188 |
| <b>Figure 6.31:</b> Variable temperature absorption profile of (6.16) (left) and (6.17) (right) <sup>[139]</sup>                           | 189 |
| <b>Figure 6.32:</b> Variable temperature conductivity profile of (6.16)  | 191 |
| <b>Figure 8.01:</b> (2.01)H  | 208 |
| <b>Figure 8.02:</b> (2.02)   | 209 |
| <b>Figure 8.03:</b> (2.03)   | 209 |
| <b>Figure 8.04:</b> (2.04)   | 211 |
| <b>Figure 8.05:</b> (2.05)   | 212 |
| <b>Figure 8.06:</b> (2.06)   | 213 |

|                             |     |
|-----------------------------|-----|
| <b>Figure 8.07: (2.07)H</b> | 214 |
| <b>Figure 8.08: (2.08)</b>  | 215 |
| <b>Figure 8.09: (2.09)</b>  | 216 |
| <b>Figure 8.10: (2.10)</b>  | 217 |
| <b>Figure 8.11: (2.11)</b>  | 218 |
| <b>Figure 8.12: (2.12)</b>  | 219 |
| <b>Figure 8.13: (2.13)</b>  | 219 |
| <b>Figure 8.14: (2.14)</b>  | 220 |
| <b>Figure 8.15: (2.15)</b>  | 221 |
| <b>Figure 8.16: (2.16)</b>  | 222 |
| <b>Figure 8.17: (2.17)</b>  | 223 |
| <b>Figure 8.18: (2.18)</b>  | 223 |
| <b>Figure 8.19: (2.19)H</b> | 225 |
| <b>Figure 8.20: (2.20)</b>  | 226 |
| <b>Figure 8.21: (2.21)</b>  | 227 |
| <b>Figure 8.22: (3.02)</b>  | 228 |
| <b>Figure 8.23: (3.03)</b>  | 229 |
| <b>Figure 8.24: (3.04)</b>  | 229 |
| <b>Figure 8.25: (3.05)</b>  | 230 |
| <b>Figure 8.26: (3.06)</b>  | 231 |
| <b>Figure 8.27: (3.07)</b>  | 232 |
| <b>Figure 8.28: (3.08)</b>  | 233 |
| <b>Figure 8.29: (3.29)</b>  | 234 |

|                            |     |
|----------------------------|-----|
| <b>Figure 8.30: (3.10)</b> | 234 |
| <b>Figure 8.31: (3.11)</b> | 236 |
| <b>Figure 8.32: (3.12)</b> | 237 |
| <b>Figure 8.33: (3.13)</b> | 238 |
| <b>Figure 8.34: (3.14)</b> | 239 |
| <b>Figure 8.35: (3.15)</b> | 239 |
| <b>Figure 8.36: (3.16)</b> | 240 |
| <b>Figure 8.37: (3.17)</b> | 241 |
| <b>Figure 8.38: (3.18)</b> | 242 |
| <b>Figure 8.39: (3.19)</b> | 243 |
| <b>Figure 8.40: (3.20)</b> | 244 |
| <b>Figure 8.41: (3.21)</b> | 245 |
| <b>Figure 8.42: (3.22)</b> | 246 |
| <b>Figure 8.43: (3.23)</b> | 247 |
| <b>Figure 8.44: (3.24)</b> | 248 |
| <b>Figure 8.45: (3.25)</b> | 249 |
| <b>Figure 8.46: (4.01)</b> | 250 |
| <b>Figure 8.47: (4.02)</b> | 251 |
| <b>Figure 8.48: (4.03)</b> | 252 |
| <b>Figure 8.49: (4.04)</b> | 252 |
| <b>Figure 8.50: (4.05)</b> | 253 |
| <b>Figure 8.51: (4.06)</b> | 254 |
| <b>Figure 8.52: (4.07)</b> | 256 |

|   |     |
|---|-----|
| <b>Figure 8.53: (5.01)</b>  | 257 |
| <b>Figure 8.54: (5.02)</b>  | 258 |
| <b>Figure 8.55: (5.03)</b>  | 258 |
| <b>Figure 8.56: (5.04)</b>  | 259 |
| <b>Figure 8.57: (5.05)</b>  | 260 |
| <b>Figure 8.58: (5.06)H<sub>2</sub></b>   | 261 |
| <b>Figure 8.59: (5.07)</b>  | 263 |
| <b>Figure 8.60: (5.08)</b>  | 264 |
| <b>Figure 8.61: (5.09)</b>  | 265 |
| <b>Figure 8.62: (5.10)</b>  | 266 |
| <b>Figure 8.63: (6.11)</b>  | 267 |
| <b>Figure 8.64: (6.12)</b>  | 268 |
| <b>Figure 8.65: (6.13)</b>  | 270 |
| <b>Figure 8.66: (6.14)</b>  | 271 |
| <b>Figure 8.67: (6.15)</b>  | 272 |
| <b>Figure 8.68: (6.16)</b>  | 274 |
| <b>Figure 8.69: (6.17)</b>  | 276 |
| <b>Figure A-1: SEM images of (5.07) [with NaB(Ph)<sub>4</sub>] precipitates at (a) 50X (b) 150X (c) 200X (d) 200X (e) 250X (f) 400X magnification</b> | 298 |
| <b>Figure A-2: SEM images of (5.10) precipitates at (a) 90X (b) 300X (c) 500X (d) 1500X magnification</b>   | 299 |
| <b>Figure A-3: SEM images of (6.12) at (a) 50X (b) 250X (c) 1250X magnification</b>   | 300 |
| <b>Figure A-4: SEM images of (6.15) at (a) 406X (b) 1010X (c) 5000X magnification</b>   | 301 |
| <b>Figure A-5: Electropolymerization of (4.06) (left) and (6.15) connected to the variable temperature resistivity apparatus (right)</b>              | 301 |

## List of schemes

|  |     |
|--|-----|
| <b>Scheme 2.01:</b> The synthesis of complexes (2.02) and (2.03) | 49  |
| <b>Scheme 2.02:</b> The synthesis of (2.07)H                     | 52  |
| <b>Scheme 2.03:</b> The synthesis of complexes (2.08) - (2.10)   | 54  |
| <b>Scheme 2.04:</b> The synthesis of complex (2.11)              | 55  |
| <b>Scheme 2.05:</b> The reduction of (2.10)                      | 56  |
| <b>Scheme 2.06:</b> The synthesis of (2.19)H                     | 78  |
| <b>Scheme 2.07:</b> The synthesis of (2.20)                      | 80  |
| <b>Scheme 2.08:</b> The synthesis of (2.21)                      | 81  |
| <b>Scheme 3.01:</b> The synthesis of ligand (3.04)               | 87  |
| <b>Scheme 3.02:</b> The synthesis of ligand (3.07)               | 88  |
| <b>Scheme 3.03:</b> The synthesis of ligand (3.10)               | 89  |
| <b>Scheme 3.04:</b> The synthesis of complexes (3.11) – (3.13)   | 91  |
| <b>Scheme 3.05:</b> The synthesis of (3.12) – (3.13)             | 92  |
| <b>Scheme 3.06:</b> The synthesis of ligands (3.18) and (3.20)   | 102 |
| <b>Scheme 3.07:</b> The synthesis of ligand (3.22)               | 104 |
| <b>Scheme 3.08:</b> The synthesis of complexes (3.23) – (3.24)   | 107 |
| <b>Scheme 3.09:</b> The synthesis of complex (3.25)              | 107 |
| <b>Scheme 4.01:</b> The synthesis of ligand (4.04)               | 123 |
| <b>Scheme 4.02:</b> The synthesis of complex (4.05)              | 124 |
| <b>Scheme 4.03:</b> The synthesis of ligand (4.06)               | 129 |
| <b>Scheme 4.04:</b> The synthesis of (4.07)                      | 131 |
| <b>Scheme 5.01:</b> The synthesis of (5.06)H <sub>2</sub>        | 137 |

|  |     |
|--|-----|
| <b>Scheme 5.02:</b> The synthesis of <i>bis</i> -qsal complexes (5.07) – (5.10)      | 140 |
| <b>Scheme 6.01:</b> A mechanism for thiophene electropolymerization <sup>[165]</sup> | 159 |
| <b>Scheme 6.02:</b> The synthesis of (6.11)  | 166 |
| <b>Scheme 6.03:</b> The synthesis of (6.12)  | 171 |
| <b>Scheme 6.04:</b> The synthesis of (6.13)  | 173 |
| <b>Scheme 6.05:</b> The synthesis of (6.14)  | 173 |
| <b>Scheme 6.06:</b> The synthesis of (6.15)  | 178 |
| <b>Scheme 6.07:</b> The synthesis of (6.16)  | 185 |
| <b>Scheme 6.08:</b> The synthesis of (6.17)  | 187 |

## List of symbols and abbreviations

|                   |  |
|-------------------|--|
| 2-pic             | 2-picolylamine   |
| 2-Th              | 2-thiopheneboronic acid  |
| a                 | glide plane direction, unit cell length                                    |
| A                 | ampere   |
| abpt              | 4-amino-3,5- <i>bis</i> (pyridin-2-yl)-1,2,4-triazole                      |
| Ac                | acetate  |
| b                 | unit cell length   |
| B3LYP             | Becke, three-parameter, Lee-Yang- Parr                                     |
| bispicen          | <i>bis</i> (2-pyridylmethyl)-diamine                                       |
| <i>bis</i> -QsalH | <b>(5.06)</b>  |
| bpen              | 1,6- <i>bis</i> (2-pyridyl)-2,5-diazaheptane                               |
| bpy               | 2,2'-bipyridine  |
| br                | broad  |
| btz               | 2,2'-bithiazoline  |
| btzpen            | <i>N</i> -benzyl- <i>N,N',N'</i> -tris(2-pyridylmethyl)-ethane-1,2-diamine |
| Bu                | butyl  |
| c                 | glide plane direction, unit cell length                                    |
| C                 | C-centred Bravais lattice  |
| cm                | centimeter   |
| cm <sup>-1</sup>  | wavenumber   |
| conc.             | concentrated   |
| CV                | cyclic voltammogram  |
| C=N               | imine  |

|                |   |
|----------------|---|
| d              | atomic orbital, days, doublet                           |
| D              | dimension   |
| dbsq           | 3,5-dbsq=3,5-di- <i>tert</i> -butyl-1,2-semiquinonate   |
| dbcat          | 3,5-di- <i>tert</i> -butyl-1,2-catecholate              |
| DCM            | dichloromethane   |
| dd             | doublet of doublets                                     |
| ddpp           | 2,5-di(2',2''-dipyridylamino)pyridine                   |
| DFT            | density functional theory                               |
| DIPA           | diisopropyl amine                                       |
| DME            | dimethoxyethane   |
| DMF            | dimethylformamide                                       |
| dmit           | 4,5-dimercapto-1,3-dithiole-2-thione                    |
| DMSO           | dimethylsulfoxide                                       |
| dppz           | dipyrido[3,2- <i>a</i> :2'3'- <i>c</i> ]phenazine       |
| DPV            | differential pulse voltammogram                         |
| DZVP           | double zeta valence with polarization                   |
| EDTA           | ethylenediaminetetraacetic acid                         |
| EDX            | energy dispersive X-ray spectroscopy                    |
| e <sub>g</sub> | atomic orbitals of higher energy in an octahedral field |
| EI             | electron impact   |
| ESI            | electrospray ionization                                 |
| ESR            | electron spin resonance                                 |
| Et             | ethyl   |
| EtOAc          | ethylacetate  |
| EtOH           | ethanol   |



|                          |   |
|--------------------------|---|
| $E^{\circ}_{\text{ox}}$  | electrochemical oxidation potential         |
| $E^{\circ}_{\text{red}}$ | electrochemical reduction potential         |
| $F$                      | structure factor                            |
| FAB                      | fast atom bombardment                       |
| fc                       | ferrocene                                   |
| FT-IR                    | Fourier transform – infrared (spectroscopy) |
| g                        | gram  |
| $G$                      | Gibb's energy                               |
| GHz                      | gigahertz                                   |
| GPa                      | gigapascal                                  |
| h                        | hours, Miller index                         |
| $H$                      | enthalpy                                    |
| HOMO                     | highest occupied molecular orbital          |
| HRMS                     | high resolution mass spectrometry           |
| HS                       | high-spin                                   |
| Htrz                     | 1,2,4-1 <i>H</i> -triazole                  |
| Hz                       | hertz                                       |
| $I$                      | current                                     |
| ILCT                     | intraligand charge transfer                 |
| iptz                     | 1-isopropyltetrazole                        |
| IS                       | isomer shift                                |
| ITO                      | indium tin oxide                            |
| $J$                      | coupling constant                           |
| k                        | Miller index                                |
| K                        | Kelvin                                      |

|            |   |
|------------|---|
| kV         | kilivolt  |
| K $\alpha$ | alpha decay energy  |
| l          | Miller index  |
| LIESST     | light induced excited spin state trapping                 |
| LMCT       | ligand to metal charge transfer                           |
| LS         | low-spin  |
| LUMO       | lowest unoccupied molecular orbital                       |
| m          | medium, metre, multiplet                                  |
| M          | molar (molarity), transition metal                        |
| mA         | milliampere   |
| MALDI      | matrix-assisted laser desorption/ionization               |
| MeOH       | methanol  |
| mg         | milligram   |
| Mg         | megagram  |
| MHz        | megahertz   |
| mL         | mililitre   |
| MLCT       | metal to ligand charge transfer                           |
| mm         | millimetre  |
| mmol       | milimole  |
| mol        | mole  |
| mol %      | concentration percentage based on the moles of a reactant |
| Mp         | melting point   |
| $m_s$      | spin quantum number                                       |
| MS         | mass spectroscopy   |
| $M_{sat}$  | saturation magnitization                                  |

|                     |  |
|---------------------|--|
| mT                  | militesla  |
| mV                  | milivolt   |
| m/z                 | mass to charge ratio   |
| n                   | fractional oxidation state, glide plane direction  |
| n-doped             | negatively doped   |
| NH <sub>2</sub> trz | 4-amino-1,2,4-triazole   |
| NIR                 | near infrared  |
| nm                  | nanometre  |
| NMR                 | nuclear magnetic resonance   |
| Nμ <sub>B</sub>     | reduced magnetization  |
| Oe                  | Oersted  |
| ORTEP               | Oak Ridge thermal ellipsoid plot   |
| <i>p</i>            | pressure   |
| P                   | primitive centred Bravais lattice  |
| Pa                  | pascal   |
| papH                | 2-hydroxyphenyl-(2-pyridyl)-methaneimine   |
| ph                  | phenyl   |
| pH                  | the negative logarithm (base 10) of the molar concentration of dissolved hydrogen ions     |
| phen                | 1,10-phenanthroline  |
| pmpea               | <i>cis-bis</i> (thiocyanato)bis[ <i>N</i> -(2'-pyridylmethylene)-4-(phenylethynyl)-anilino |
| ppi                 | <i>N</i> -phenyl-2-pyridinaldimine   |
| ppm                 | parts per million  |
| ptz                 | 1-propyltetrazole  |
| PXRD                | powder X-ray diffraction   |
| p-doped             | positively doped   |

|                         |  |
|-------------------------|--|
| q                       | represents the angle in small angle x-ray scattering experiments |
| qnalH                   | <i>N</i> -(8-quinolyl)-2-hydroxy-1-naphthalaldimine              |
| QS                      | quadrupole splitting   |
| qsalH                   | <i>N</i> -(8-quinolyl)salicylaldimine                            |
| R                       | residual factor (R1)   |
| redox                   | reduction oxidation  |
| RT                      | room temperature   |
| s                       | second, sharp (IR), singlet ( <sup>1</sup> H-NMR)                |
| S                       | siemen   |
| <i>S</i>                | entropy, magnetic spin   |
| sal <sub>2</sub> -trien | bissalicylideneaminotriethylenetetramine                         |
| salothH <sub>2</sub>    | <i>N,N'</i> -bis(salicylidene)-3,4-thiophenediamine              |
| SAXS                    | small angle x-ray scattering                                     |
| SCO                     | spin-crossover   |
| SEM                     | scanning electron microscopy                                     |
| SQUID                   | superconducting quantum interference device                      |
| t                       | triplet  |
| T                       | tesla  |
| <i>T</i>                | temperature  |
| <i>T</i> <sub>1/2</sub> | midway temperature between the equilibrium of two states         |
| <i>T</i> <sub>c</sub>   | critical temperature   |
| td                      | triplet of doublets  |
| TEA                     | triethylamine  |
| tertheqsal              | <b>(2.20)</b>  |
| thebipy                 | <b>(4.04)</b>  |

|          |                                     |
|----------|-------------------------------------|
| theqsalH | (2.07)                              |
| THF      | tetrahydrofuran                     |
| TLC      | thin layer chromatography           |
| TMS      | trimethylsilyl-                     |
| TOF      | time of flight                      |
| $U$      | potential, potential energy         |
| UV       | ultraviolet                         |
| V        | volt                                |
| $V$      | volume                              |
| Vis      | visible                             |
| VT       | valence tautomer                    |
| w        | weak                                |
| wR2      | weighted residual factor            |
| X        | optical magnification power         |
| Z        | number of molecules                 |
| ZFS      | zero-field splitting                |
| Å        | angstrom                            |
| °        | degree                              |
| °C       | degrees Celcius                     |
| -        | inversion centre                    |
| %        | percent                             |
| $\alpha$ | thiophene carbon 2, unit cell angle |
| $\beta$  | thiophene carbon 3, unit cell angle |
| $\gamma$ | unit cell angle                     |
| $\delta$ | chemical shift                      |

|                  |  |
|------------------|--|
| $\Delta E_Q$     | quadrupole splitting   |
| $\Delta_o$       | energy difference between $e_g$ and $t_{2g}$ orbitals in an octahedral field |
| $\varepsilon$    | molar absorptivity   |
| $\theta$         | angle  |
| $\lambda$        | wavelength   |
| $\lambda_{\max}$ | maximum absorbance value   |
| $\mu A$          | microampere  |
| $\mu_B$          | Bohr magneton  |
| $\mu_{eff}$      | magnetic moment  |
| $\mu\text{mol}$  | micromole  |
| $\mu\text{m}$    | micrometre   |
| $\mu_{so}$       | spin only magnetic moment  |
| $\sigma$         | electrical conductance   |
| $\chi_M$         | magnetic susceptibility  |
| $\chi_M T$       | product of magnetic susceptibility and temperature                           |
| $\omega$         | angle  |

## Chapter 1: Spin-crossover and valence tautomerism in molecules

### 1.01 Introduction to spin labile magnetic materials

For the development of fundamental science, in addition to practical applications, examining the magnetic properties of new materials is an area of great interest. Ambitions within this field include attempting to enhance the versatility of materials by including labile magnetic properties that switch as a result of external perturbations. In this regard, many molecular compounds, including spin-crossover (SCO) complexes and valence-tautomers (VT), have already been studied. The spin active centres in SCO and VT compounds display labile electronic configurations and are typically switchable between high- and low-spin states leading to distinctive changes in magnetism. These changes can be caused by external perturbations like the variation of temperature, pressure or by light irradiation.<sup>[1-2]</sup>

### 1.02 The spin-crossover phenomenon

#### i) Geometry and spin state

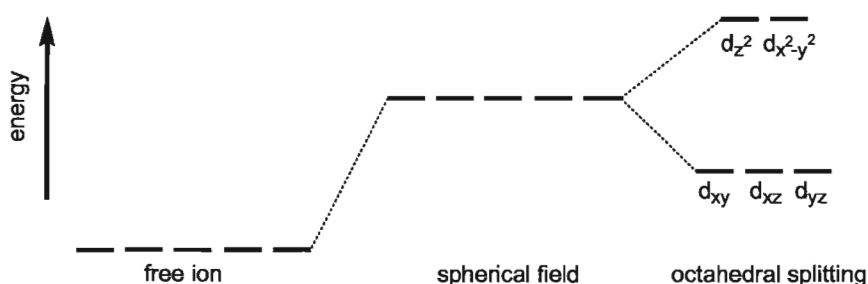


**Figure 1.01:** The energy level diagram of transition metal ions with octahedral coordination geometry<sup>[3]</sup>

The crystal field effect occurs when the  $d$ -orbitals are split as a result of ligand coordination. The  $d$ -orbitals become lower or higher in energy with respect to a spherical field, the barycenter, in which all five orbitals are degenerate. For transition metals with octahedral coordination geometry, orbitals that fall directly on the axis of the octahedron are higher in energy than the orbitals that are diagonal with respect to the axis and partially filled shells ( $d^4$  to  $d^7$ ) have several possible spin states because of these non-degenerate  $d$ -orbitals (**Figure 1.01**).<sup>[3-5]</sup>

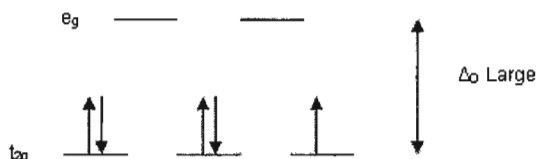


**Figure 1.02:** A low-spin  $d^5$  transition metal with octahedral geometry<sup>[3]</sup>

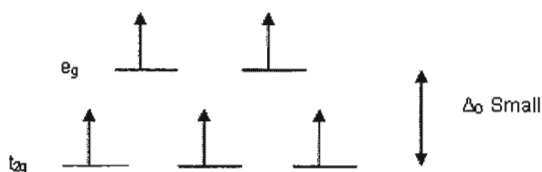


**Figure 1.03:** A high-spin  $d^5$  transition metal with octahedral geometry<sup>[3]</sup>

One electronic configuration resulting from the non-degenerate energy levels occurs when the energy difference between the orbitals ( $\Delta_o$ ) is larger than the energy used in pairing the electrons. The electrons are paired according to the Aufbau principle causing a cancellation of the electron spin, giving rise to the term *low-spin* (LS). The example in **Figure 1.02** depicts a low-spin  $d^5$  transition metal with octahedral geometry. A second configuration, called *high-spin* (HS), occurs when the energy difference between the



orbitals is smaller than the energy required to pair the electrons and the electrons spread out in accordance to Hund's rule of maximum multiplicity. The example in **Figure 1.03** depicts a high-spin  $d^5$  transition metal with octahedral geometry.<sup>[3-5]</sup>

ii) Ligand field theory



**Figure 1.04:** The spectrochemical series (field strength increases to the right)  
[bpy = 2,2'-bipyridine]<sup>[3]</sup>

Ligands affect the magnitude of the  $d$ -orbitals splitting ( $\Delta_o$ ) according to their field strength as described by the spectrochemical series (**Figure 1.04**). Strong-field ligands ( $\pi$ -acceptors) like 2,2'-bipyridine and  $\text{CN}^-$  are more likely to form low-spin complexes because they create a larger  $\Delta_o$  splitting. Weak-field ligands ( $\pi$ -donors) like  $\text{I}^-$  and  $\text{SCN}^-$  cause a smaller  $\Delta_o$  splitting and are more likely to produce high-spin complexes. When first transition series metals are coordinated to ligands of intermediate field strength, or by combining strong and weak field ligands, a moderate  $\Delta_o$  splitting is created. The potential for spin lability is then furthered because neither spin state is significantly beneficial in achieving the lowest possible energy state.<sup>[3]</sup>

iii) Spin labile complexes

Most transition metal complexes feature only one spin state (across a range of temperatures), either high- or low-spin, but in 1931 Cambi and Szego first reported

complexes, [*tris*(*N,N*-diorganodithiocarbamato)iron(III)], which exhibited solid and solution magnetic moments that were between the two values normally observed for iron(III) complexes (high-spin,  $\mu_{eff} \approx 5.9 \mu_B$ ; low-spin,  $\mu_{eff} \approx 2.0 \mu_B$ ). The anomalous behaviour was accounted for by suggesting an equilibrium between the two “magnetically isomeric” high- and low-spin forms and resulted in introducing the concept of spin lability.<sup>[6]</sup>

#### iv) Thermodynamics of spin-crossover

Spin lability can be described by considering the energy available for the system in question. The  $\Delta_o$  splitting is related to the internal potential energy ( $U$ ) of the transition metal, with energy costs associated with either pairing electrons or populating the higher energy levels of the  $\Delta_o$  splitting, and in combination with the pressure ( $p$ ) and volume ( $V$ ) can be used to determine the enthalpy ( $H$ ) in (Eq. 1)<sup>[7]</sup>:

$$H = U + pV \quad (\text{Eq. 1})$$

Using the enthalpy and entropy ( $S$ ), spin-crossover can be rationalized by the Gibbs ( $G$ ) energy equation in (Eq. 2)<sup>[7]</sup>:

$$G = H - TS \quad (\text{Eq. 2})$$

In standard examples of thermal SCO, the transition from high- to low-spin occurs as the sample is cooled. The enthalpy term of the low-spin state is slightly lower in energy than that of the high-spin state. At low temperature, the entropy term becomes smaller increasing the significance of the enthalpy term and since the enthalpy of the low-spin state is lower in energy it is the preferred configuration at low temperature. At high temperature, the entropy term becomes significant, as an increase in entropy can now drive the Gibbs energy of the system to a value lower than the low-spin state. The greatest amount of entropy and therefore lowest possible energy configuration is then achieved when the electrons are unpaired.<sup>[8]</sup>

### 1.03 Characterization of magnetically labile materials

#### i) Variable temperature magnetic susceptibility

The magnetic moment ( $\mu_{eff}$ ), a measure of the strength and direction of magnetism, is a highly prevalent way to quantify the magnetic spin in transition metals and can be observed by measuring the magnetic field surrounding the metal with a SQUID (superconducting quantum interference device) magnetometer. The contribution of the system's internal magnetism to the external magnetic field of the SQUID is the sum of the intrinsic and orbital magnetic moments of the unpaired electrons in the material. Greater numbers of unpaired electrons can, therefore, create larger magnetic moments. The magnetic moment is expressed in Bohr magnetons ( $\mu_B$ ) and is derived from the

magnetic susceptibility ( $\chi_M$ ) ( $\text{cm}^3\text{mol}^{-1}\text{K}^{-1}$ ) measurements (Eq. 3) and is also closely related to the spin only formula ( $\mu_{so}$ ) (Eq. 4)<sup>[9]</sup>:

$$\mu_{eff} = 2.83\sqrt{\chi_M T} \quad (\text{Eq. 3})$$

$$\mu_{so} = 2\sqrt{S(S+1)} \quad (\text{Eq. 4})$$

As an example, a typical high-spin iron(II) complex ( $S = 2$ ) has values of  $\chi_M T = 3.2 \text{ cm}^3 \text{ mol}^{-1}\text{K}^{-1}$  corresponding to  $\mu_{eff} = 5.1 \mu_B$ . Whereas, iron(II) in the low-spin state ( $S = 0$ ) has typical values around  $\mu_{eff} = 0.0 \mu_B$ .<sup>[10-11]</sup>

## ii) Mössbauer spectroscopy

Mössbauer spectroscopy is a technique based on the resonant emission and absorption of gamma-rays in solids. Mössbauer is similar to nuclear magnetic resonance (NMR) spectroscopy because it probes nuclear transitions and is sensitive to similar electron-nucleus interactions that cause chemical shifts. The advantage of Mössbauer spectroscopy is that it has an extremely fine energy resolution and can detect even subtle changes in the nuclear environment of the relevant atoms including changes in spin state. A sample is exposed to a beam of gamma radiation and a detector measures the intensity of the beam transmitted through the sample. The atoms in the source, emitting the gamma-rays, must be of the same isotope as the atoms in the sample absorbing them, which limits the application of Mössbauer spectroscopy. Fortunately,  $^{57}\text{Fe}$  is a naturally occurring isotope that can provide gamma-rays suitable for Mössbauer experiments on

samples containing iron and is therefore an invaluable tool in verifying the occurrence of spin-crossover.<sup>[12-13]</sup>

In Mössbauer experiments, three types of nuclear interactions can be observed:

1) The isomer shift (IS) reflects the chemical bonding of the atoms and is related to the electron density at the nucleus. The isomer shift is observed as a shift of all peaks in the spectra corresponding to a particular atomic environment. Thermal vibration of the nuclei will cause a small shift the gamma ray energy as a result of a second order doppler effect.<sup>[12]</sup>

2) The quadrupole splitting (QS) results from an interaction between the electric quadrupole of the nuclei and the surrounding electric field gradient, creating non-degenerate states that split the nuclear transitions into two peaks. The QS is measured as the separation between the two peaks and reflects the character of the electric field at the nucleus.<sup>[12]</sup>

3) The third interaction is called hyperfine or Zeeman splitting and is a result of the interaction between the nucleus and any surrounding magnetic field.<sup>[12]</sup>

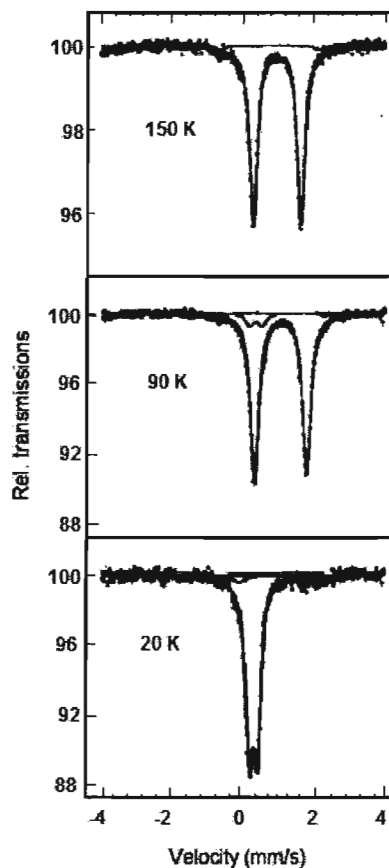


**Figure 1.05:** Mössbauer spectra of (1.01)<sup>[14]</sup>

In the resulting spectra, gamma-ray absorbance intensity is plotted as a function of the source velocity where the intensities of the peaks reflect the relative concentrations of compounds in the sample and can be used for semi-quantitative analysis. For example, the Mössbauer spectra of an iron(II) complex  $[\text{Fe}(\text{bpen})(\text{NCS})_2]$  [ $\text{bpen} = 1,6\text{-bis}(2\text{-pyridyl})\text{-}2,5\text{-diazahexane}$ ] (1.01) displays temperature dependent absorptions (**Figure 1.05**). A symmetrical doublet is observed at 150 K with an IS of  $\delta = 0.963 \text{ mm/s}$  and a QS of  $\Delta E_Q = 1.355 \text{ mm/s}$ , representing the high-spin state of the iron(II) complex. At 90 K the symmetry of the doublet is broken, as one of the two peaks becomes slightly more intense, due to an additional doublet appearing with parameters that represent the low-

spin state. As the temperature is decreased, the intensity of the first doublet diminishes as the second doublet increases in intensity. At 20 K the spectrum is dominated by the doublet produced by low-spin iron(II) with an IS of  $\delta = 0.400$  mm/s and a QS of  $\Delta E_Q = 0.230$  mm/s.<sup>[14]</sup>

### iii) Electron spin resonance

Electron spin resonance (ESR) is a technique for studying chemical species that have one or more unpaired electrons, such as complexes possessing a transition metal ion or free radicals. The basic physical concepts of ESR involve exciting the electron spins in the presence of an external magnetic field. Electrons have a magnetic moment associated with the spin ( $S = 1/2$ ) and a spin quantum number with magnetic components  $m_s = +1/2$  and  $m_s = -1/2$ . In the magnetic field, the electron's magnetic moment aligns itself either parallel ( $m_s = -1/2$ ) or antiparallel ( $m_s = +1/2$ ) to the field. The electrons are exposed to microwaves at a fixed frequency. As the external magnetic field is increased, the gap between the  $m_s = +1/2$  and  $m_s = -1/2$  energy states is widened until it matches the energy of the microwaves so that the unpaired electrons can move between the two spin states.<sup>[15-16]</sup>

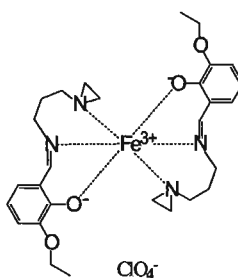


**Figure 1.06:** A diagram of complex (1.02)

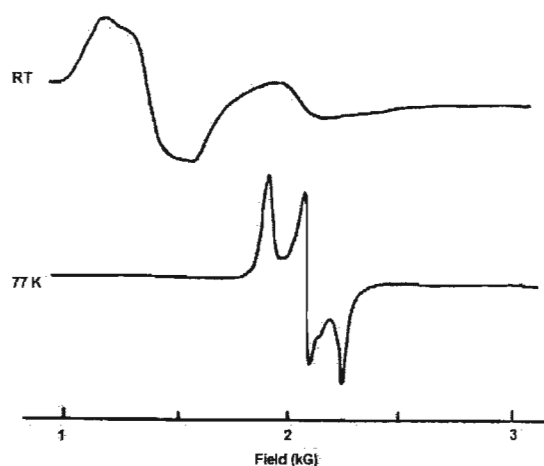


**Figure 1.07:** Variable temperature ESR spectra of (1.02)<sup>[17]</sup>

Since a paramagnetic analyte is the principal requirement for observing an ESR transition, it is a technique particularly useful in studying the states of iron(III) SCO materials. For example, the spectra of (1.02) (Figure 1.06), an iron(III) spin-crossover compound with an  $N_4O_2$  donor set, shows three Kramer's doublets with a broad ESR signal of the high-spin state at room temperature and a sharp ESR signal of the low-spin state at 77 K (Figure 1.07).<sup>[17-19]</sup>

#### iv) Heat capacity measurements

Molar specific heat capacity can be defined as the amount of the heat energy required to increase the temperature of a mole of a substance by one Kelvin. The heat capacity is a physical quantity containing contributions from various molecular degrees of freedom including the potential energy in vibrational modes. Consequently, calorimetry is a suitable experimental tool to help explore the mechanism involved in SCO phenomena as



is illustrated in **Figure 1.08** by the complex  $[\text{Fe}(\text{phen})_2(\text{NCS})_2]$  [phen = 1,10-phenanthroline] (**1.03**). The transition entropy due to SCO involves a dominant contribution from the non-electronic vibrations, in addition to a contribution from a change in the spin multiplicity, and results in a discontinuity of the lattice heat capacity at the transition temperature.<sup>[20]</sup>

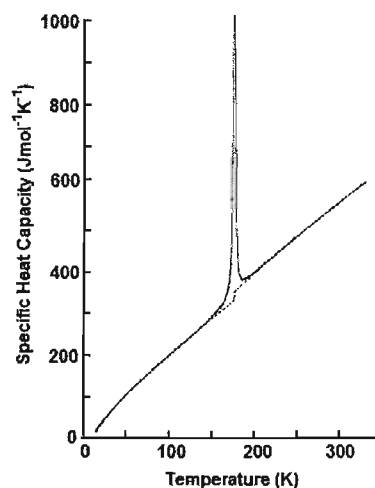


**Figure 1.08:** Variable temperature specific heat capacity of (**1.03**)<sup>[20]</sup>

v) Electronic absorption spectroscopy

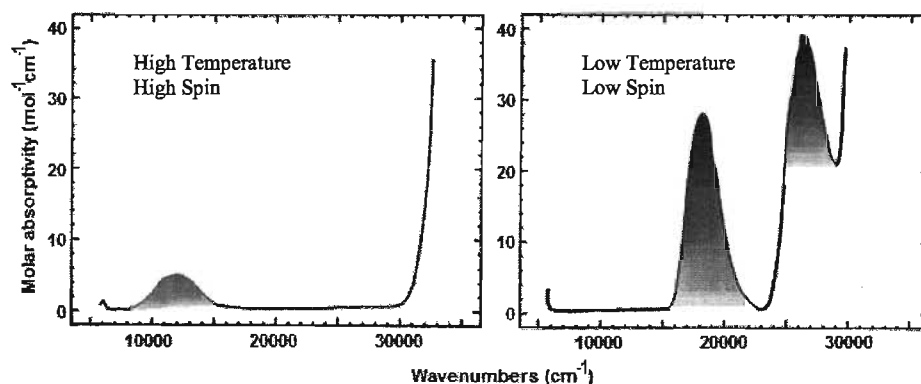


**Figure 1.09:** Variable temperature electronic absorption spectra of (**1.04**)<sup>[21]</sup>

The absorption bands resulting from ligand field transitions in the high- and low-spin states of SCO complexes have different energies that can be observed by electronic absorption spectroscopy. As the SCO occurs, the intensity of each band changes to reflect the population of each state. A thermally induced SCO will usually result in thermochromism and a variable temperature UV-Vis experiment can provide a preliminary detection method for the transition. The electronic spectrum of the iron(II) complex  $[\text{Fe}(\text{ptz})_6(\text{BF}_4)_2]$  [ptz = 1-propyltetrazole] (**1.04**), in the high-spin state, shows one ligand field band in the near-infrared region (**Figure 1.09**). In contrast, the low-spin ion has two ligand field bands, one in the visible region and another in the ultra-violet region. The absorptions resulting from charge transfer bands can often obscure the ligand field transitions in the visible region. In this case, however, the charge transfer transitions do not occur in the visible region and the ligand field transitions are the only factor determining the colours observed, resulting in a vibrant change from violet to colourless.<sup>[21-24]</sup>

vi) X-ray diffraction

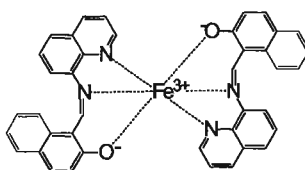


Figure 1.10: A diagram of the cation  $[\text{Fe}(\text{qnal})_2]^+$  (**1.05**)

X-ray diffraction is a widely used tool for the characterization of SCO complexes, in part because it offers structural evidence regarding the synthesis of a compound but also because the crystallographic metal-ligand bond lengths can be used to characterize the spin state of a complex. In ideal cases, the structure can be solved both above and below the spin transition and the observed change in coordinate bond lengths can be used as evidence to support magnetic switching. In typical examples like  $[\text{Fe}(\text{qnal})_2]^+$  [ $\text{qnalH} = N\text{-(8-quinolyl)-2-hydroxy-1-naphthaldimine}$ ] (**1.05**), the high-spin coordinate bond lengths are longer than the low-spin bond lengths because populating the high-spin state results in partially filling orbitals that have antibonding character. In (**1.05**), the change in bond lengths between Fe-N are more pronounced in comparison to Fe-O,  $\Delta_{\text{Fe-N}} 0.15\text{-}0.18 \text{ \AA}$  and  $\Delta_{\text{Fe-O}} 0.03\text{-}0.04 \text{ \AA}$ .<sup>[1,25-27]</sup>

#### 1.04 External control of magnetic switching

##### i) Thermal magnetic switching

###### a) Thermal spin-crossover

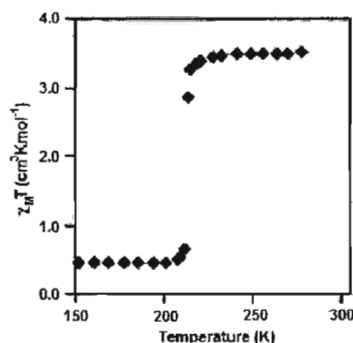


**Figure 1.11:** Variable temperature magnetic susceptibility of (**1.06**)<sup>[28]</sup>

In the 1960s the anomalous magnetic properties of  $[\text{Fe}(\text{bpy})_2(\text{NCS})_2]$  (**1.06**) were observed by Baker and Bobonich<sup>[28]</sup> and afterwards by König and Madeja<sup>[29]</sup>. A profile showing the thermal variation of  $\chi_M T$  was used to examine the magnetic properties (**Figure 1.11**). The compound (**1.06**) undergoes a change from high-spin to low-spin as a result of decreasing temperature, which is centred at  $T_{1/2} = 213 \text{ K}$ , where  $T_{1/2}$  denotes the midway point between the equilibrium of the two states. For temperatures greater than  $T_{1/2}$ ,  $\chi_M T$  remains constant (close to  $3.53 \text{ cm}^3\text{Kmol}^{-1}$ ) upon cooling, with values corresponding to what is expected for iron(II) ions in the high-spin state. When the temperature decreases below  $T_{1/2}$ ,  $\chi_M T$  drops to  $0.4 \text{ cm}^3\text{Kmol}^{-1}$ , indicating a change to low-spin state. Thermal SCO is the name given to this type of transition because the complex can crossover from one spin state to another as a result of the temperature change.<sup>[28-30]</sup> Since the observations of Baker and Bobonich, there have been many interesting reports of complexes that exhibit thermal spin-crossover. For the most part, the complexes contain either iron(II)<sup>[31-41]</sup> or iron(III)<sup>[42-52]</sup> atoms as the spin labile component, but in a few rare cases, cobalt(II)<sup>[53-56]</sup>, chromium(II)<sup>[57-58]</sup> and manganese(III)<sup>[59-64]</sup> complexes also undergo thermal spin-crossover.

#### b) Thermal valence tautomerism

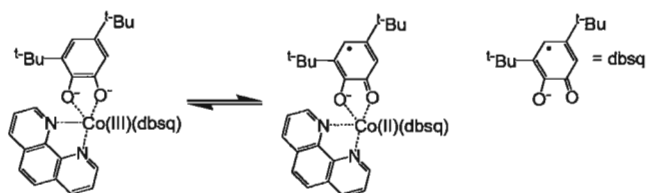


**Figure 1.12:** The valence tautomerism of (**1.08**)<sup>[1]</sup>

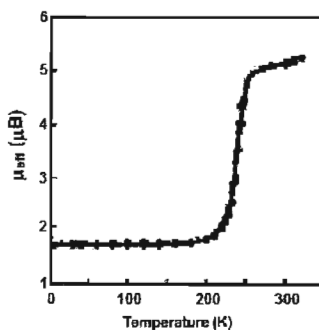


**Figure 1.13:** The magnetic profile of **(1.08)**<sup>[1]</sup>

Buchanan and Pierpont reported the cobalt complex  $[\text{Co}(\text{II})(3,5\text{-dbsq})_2(\text{bpy})]$  [ $\text{dbsq} = 3,5\text{-dbsq} = 3,5\text{-di-}i\text{-tert-butyl-1,2-semiquinonate}$ ] **(1.07)**, which undergoes a thermally induced electron transfer between the cobalt(II) centre and the semiquinone ligand in solution. The valence tautomerism of **(1.07)** can be expressed as  $[\text{Co}(\text{II}^{\text{HS}})(3,5\text{-dbsq})_2(\text{bpy})] \rightleftharpoons [\text{Co}(\text{III}^{\text{LS}})(3,5\text{-dbsq})(3,5\text{-dbcat})(\text{bpy})]$  [HS = high-spin; LS = low-spin; dbcat = 3,5-di-*tert*-butyl-1,2-catecholate], thus accompanying the electron transfer is a SCO process from high- to low-spin. After the initial discovery, valence tautomerism was also reported in the solid state for  $[\text{Co}(\text{II})(3,5\text{-dbsq})_2(\text{phen})] \cdot \text{CH}_3\text{C}_6\text{H}_5$  **(1.08)**, with abrupt transitions between the high and low temperature magnetic states (**Figure 1.12**). The plot resulting from the  $\chi_{\text{M}}T$  product versus temperature displays magnetic properties and a transition curve similar to other SCO compounds (**Figure 1.13**).<sup>[1,65-66]</sup>

ii) The light induced excited spin state trapping effect

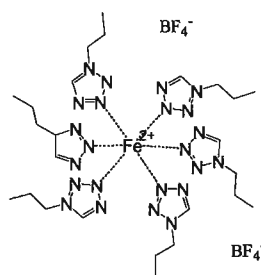


Figure 1.14: A diagram of complex (1.04)

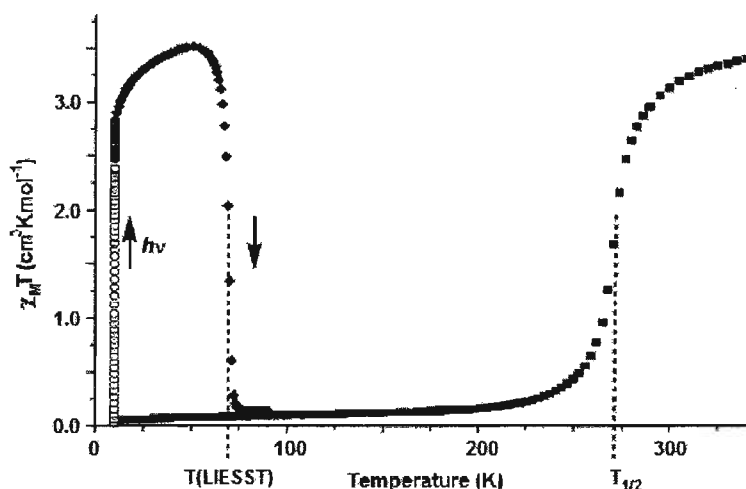
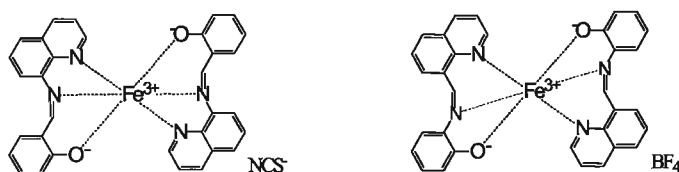


Figure 1.15: The LIESST effect of complex (1.04) with arrows indicating the excited state region<sup>[67]</sup>

The discovery of light induced SCO was a significant advancement in the development of SCO materials because it represented the first step towards the practical control of magnetic switching.<sup>[68-69]</sup> Decurtins *et al.* observed light induced excited spin state trapping (LIESST) in the solid state with the mononuclear iron(II) SCO complex  $[\text{Fe}(\text{ptz})_6](\text{BF}_4)_2$  [ptz = 1-propyltetrazole] (1.04) (Figures 1.14-1.15). Complex (1.04) undergoes an abrupt thermal spin transition upon cooling at  $T_{1/2} = 271$  K, favouring the low-spin state at low temperature. However, by irradiating (1.04) with green light ( $\lambda =$

540 nm) at 10 K the low-spin complex can then be converted back to high-spin. The compound remains in the high-spin state until it reaches the critical temperature  $T_c = 70$  K, at which point the thermal energy becomes sufficient to overcome the activation barrier to thermal relaxation of the material.<sup>[70]</sup> The UV-Vis spectrum of the low-spin complex shows a MLCT band at 548 nm that corresponds to the green light used in exciting the complex. The metastable high-spin state has an absorbance band at 850 nm and when (1.04) is irradiated with red light corresponding this band, it converts back to the low-spin state. Consequently, the complex exhibits photo induced bistability below 70 K because it can adopt either the low-spin (ground) state or a metastable high-spin (excited) state depending on its history.<sup>[71]</sup>



**Figure 1.16:** Diagrams of (1.09) (left) and (1.10) (right)<sup>[72]</sup>

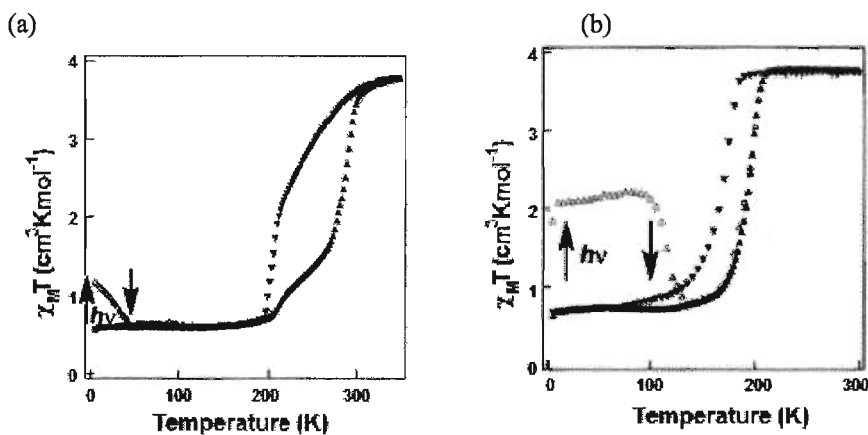


**Figure 1.17:** The LIESST effect for (a) (1.09) and (b) (1.10) with arrows indicating the excited state region<sup>[72]</sup>

Some iron(III) complexes also undergo a spin conversion upon irradiation, although fewer examples are known in comparison to iron(II) complexes. The known examples, containing iron(III), are fully characterized and have the general formula  $[\text{Fe(III)}(\text{L})_2]^+$  with  $\text{N}_4\text{O}_2$  donor ligands. The structurally related complexes  $[\text{Fe}(\text{qsal})_2]\text{NCS}$  [ $\text{qsalH} = N$ -(8-quinolyl)salicylalimine] (**1.09**) and  $[\text{Fe}(\text{pap})_2]\text{BF}_4$  [ $\text{papH} = 2$ -hydroxyphenyl-(2-pyridyl)-methaneimine] (**1.10**) (Figure 1.16), for example, both display an increase in magnetization associated with the LIESST effect when irradiated (800-1000 nm and 500-600 nm respectively) at 5 K in a SQUID magnetometer (Figure 1.17). In (**1.09**), the increase in magnetization by illumination was observed, but relaxation from the high-spin state to low-spin was induced even at 5 K. In contrast, a sample of (**1.10**) that was illuminated at 532 nm for 1 h at 5 K had more sustainable results. Upon illumination, the magnetic response of (**1.10**) increased, reaching a limiting value of  $\chi_m T = 2.0 \text{ cm}^3 \text{Kmol}^{-1}$ , which suggested 50 % of the low-spin isomer was converted to high-spin. The  $\chi_m T$  value remained constant when the temperature was sufficiently low but decreased as the temperature increased.<sup>[72-74]</sup>



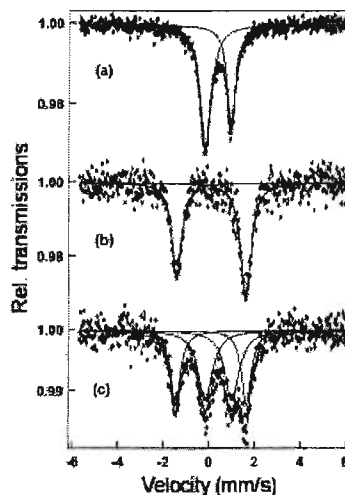


**Figure 1.18:** The Mössbauer spectra of **(1.10)** (a) room temperature (b) 5 K (c) 5 K after illumination at 532 nm<sup>[72]</sup>

The room temperature Mössbauer spectrum of **(1.10)** shows a doublet with a narrow quadrupole-splitting ( $IS = 0.38$  mm/s;  $QS = 1.14$  mm/s) representing the HS state (**Figure 1.18**). On cooling to 5 K the Mössbauer spectrum shows a new absorption doublet with wide quadrupole splitting ( $IS = 0.09$  mm/s;  $QS = 3.09$  mm/s) representing the low-spin state. After collecting the spectrum, the sample was illuminated at 532 nm for one hour and measured once again. In the spectrum measured after illumination, a doublet with a narrow quadrupole-splitting appeared ( $IS = 0.43$  mm/s;  $QS = 1.17$  mm/s), representing the HS state, and confirmed that half the low-spin iron ions were converted to high-spin. The metastable state was sustainable provided that the sample was kept below 80 K. When the sample temperature was increased to 150 K and then lowered to 5 K, only the low-spin state was observed.<sup>[72]</sup>

iii) Pressure effects on spin-crossover

a) Variable pressure effects on compounds that exhibit SCO

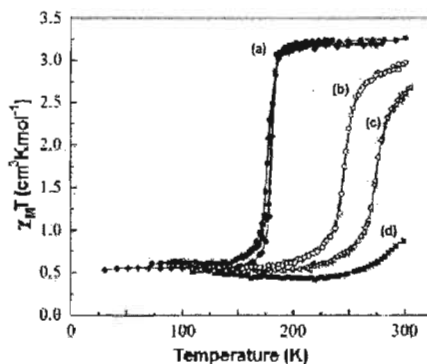


**Figure 1.19:** Pressure effects on spin-crossover in compound **(1.03)** (a)  $10^5$  Pa before and after applying pressure (b) 0.17 GPa (c) 0.34 GPa (d) 0.57 GPa<sup>[75]</sup>

The investigations into the thermal spin transition of  $[\text{Fe}(\text{phen})_2(\text{NCS})_2]$  (**1.03**) include studies of the SCO exhibited at varied pressures (**Figure 1.19**). At ambient pressure, the transition curve in (**1.03**) is extremely steep with  $T_{1/2} = 177$  K. As the pressure is increased to 0.17 GPa, the shape of the spin transition curve is essentially unchanged, but is parallel to the original curve and shifted to higher temperature. As the pressure is increased, the transition curve becomes more gradual. At pressures around 0.6 GPa the sample is mostly in the low-spin state even at room temperature. The LS state has a smaller molecular volume than the high-spin state and becomes favoured as pressure increases in the molecule. With increased pressure, there is a relatively larger enthalpy term in the Gibb's energy of the high-spin state, which reduces its population until it disappears entirely.<sup>[75]</sup>

b) Pressure induced spin-crossover

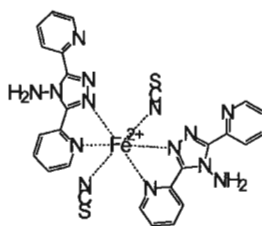


**Figure 1.20:** A diagram of complex (1.11)

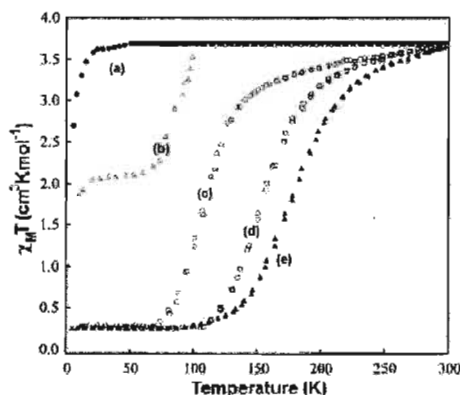


**Figure 1.21:** Pressure induced spin-crossover of (1.11) at (a) 105 Pa (b) 0.44 GPa (c) 0.56 GPa (d) 0.86 GPa (e) 1.05 GPa<sup>[75]</sup>

The variable temperature  $\chi_M T$  product of  $[\text{Fe}(\text{abpt})_2(\text{NCS})_2]$  [abpt = 4-amino-3,5-bis(pyridin-2-yl)-1,2,4-triazole] (1.11) (Figure 1.20), at different pressures, is displayed in Figure 1.21. At atmospheric pressure, the complex is high-spin at room temperature and as the temperature is lowered,  $\chi_M T$  remains constant until temperatures below 25 K are reached. The sharp decrease in  $\chi_M T$  beyond 25 K was accounted for as the zero-field splitting of the high-spin iron(II) ions. As the pressure is increased to 0.44 GPa, the compound initially exhibits the same high-spin character at high temperature, but an incomplete thermal SCO appears around  $T_{1/2} = 65$  K. Relatively sharp spin transitions begin to occur at  $T_{1/2} = 106$ , 152 and 179 K, as the pressure increases to 0.56, 0.86 and 1.05 GPa, respectively. The application of hydrostatic pressure to the high-spin

compound  $[\text{Fe}(\text{abpt})_2(\text{NCS})_2]$  demonstrates the principle of inducing thermal spin-crossover, in a controlled manner, by shifting the enthalpy parameter to larger, more positive values.<sup>[75,78-79]</sup>

### 1.05 Profiles of thermally induced spin-crossover

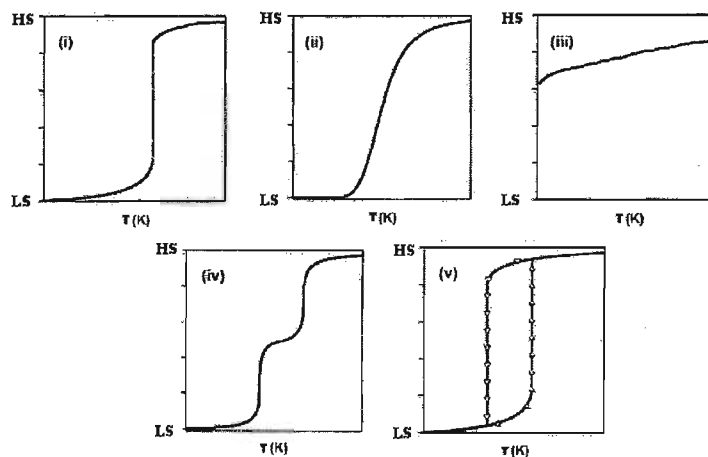


**Figure 1.22:** Typical profiles of thermally induced spin-crossover (i) abrupt (ii) gradual (iii) gradual and incomplete (iv) multistep (v) hysteretic

The origin of the SCO phenomenon is purely intramolecular but in the solid state interactions between molecules, including subtle structural and electronic modifications, can dramatically influence the change in spin state and are referred to as cooperative effects. In molecular compounds, the cooperativity parameter depends greatly on the intermolecular interactions between molecules, which include hydrogen bonding and  $\pi$ - $\pi$  orbital overlap, or through polymeric coordination bonds. Typical profiles of thermally induced spin-crossover are represented in **Figure 1.22** as plots of high- and low-spin state fractions versus the temperature.<sup>[2]</sup>

i) Abrupt spin-crossover

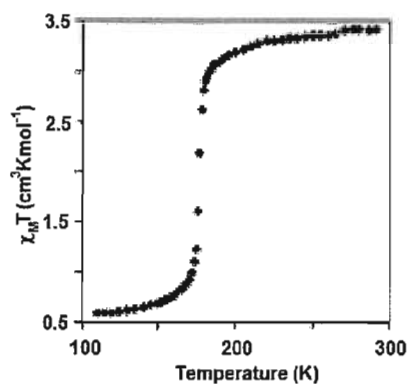


**Figure 1.23:** The abrupt spin-crossover exhibited by (1.03)<sup>[2]</sup>

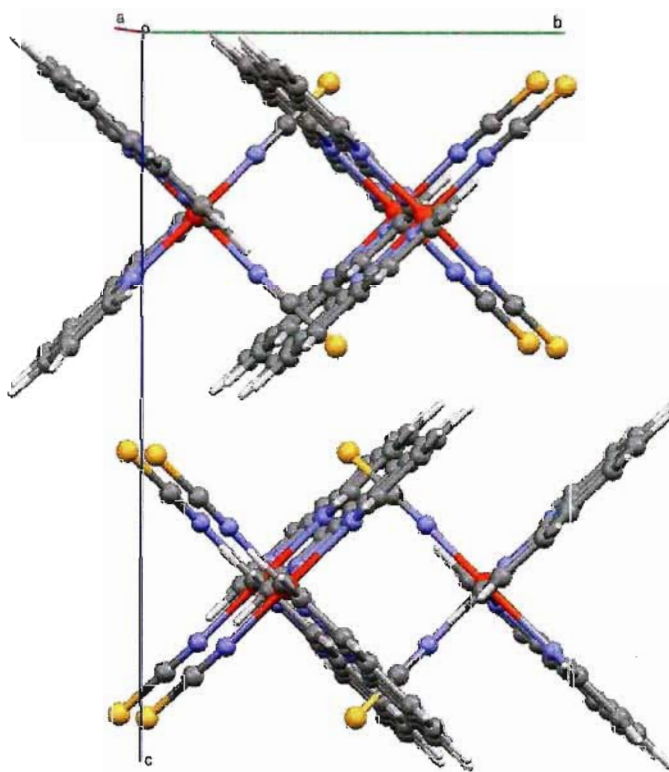


**Figure 1.24:** The packing diagram of complex (1.03)<sup>[2]</sup>

**Figure 1.22 (i)** depicts an abrupt transition between the high- and low-spin states, which usually occurs if communication between neighboring metal centres is strong, as in the

example  $[\text{Fe}(\text{phen})_2(\text{NCS})_2]$  (**1.03**). For (**1.03**), at 292 K the magnetic data indicates that the complex is in the high-spin state  $\chi_m T = 3.41 \text{ cm}^3 \text{mol}^{-1} \text{K}^{-1}$ , and gradually decreases to  $\chi_m T = 2.83 \text{ cm}^3 \text{mol}^{-1} \text{K}^{-1}$  at 178 K (**Figure 1.23**). Suddenly, at  $T_{1/2} = 176.5 \text{ K}$  the  $\chi_m T$  product decreases to  $1.04 \text{ cm}^3 \text{mol}^{-1} \text{K}^{-1}$  and is indicative of an abrupt change in spin state. X-ray analysis of a single crystal revealed that the molecular packing consisted of continuous sheets of molecules, where neighboring 1,10-phenanthroline (aromatic) ligands have considerable  $\pi$ - $\pi$  interactions to facilitate cooperativity (**Figure 1.24**).<sup>[2,80]</sup>

ii) Gradual spin-crossover

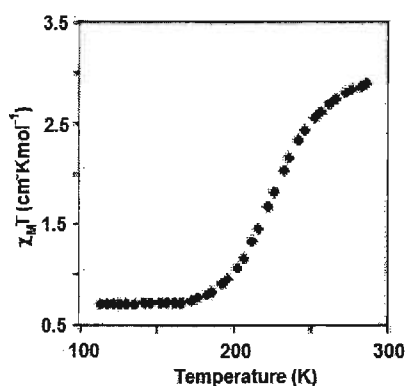


**Figure 1.25:** The gradual spin-crossover exhibited by (**1.12**)<sup>[2]</sup>

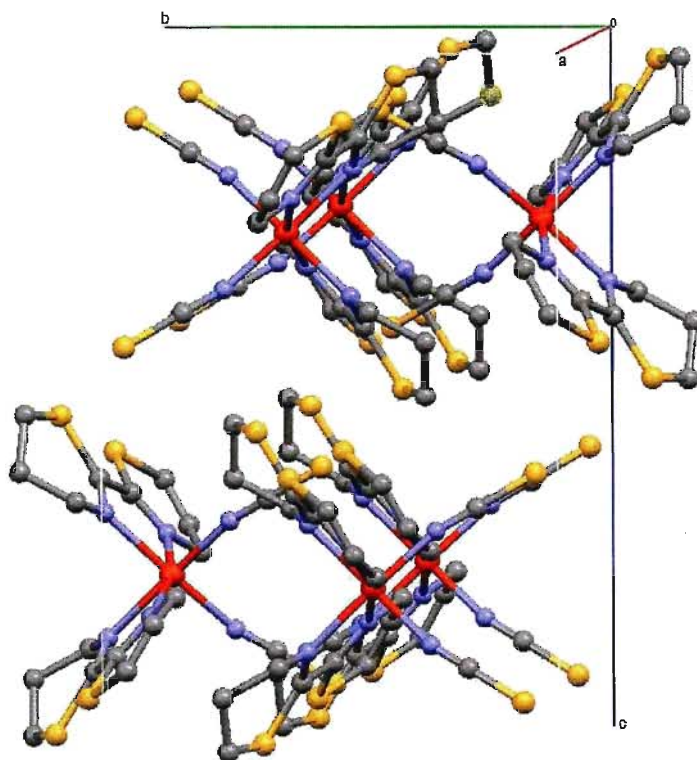


**Figure 1.26:** The packing diagram of complex **(1.12)**<sup>[2]</sup>

Gradual SCO is illustrated in **Figure 1.22** (ii) and is usually the result of molecules that do not interact strongly with each other in the solid state. In gradual SCO, the change in magnetism occurs very slowly over a wide temperature range. For instance,  $[\text{Fe}(\text{btz})_2(\text{NCS})_2]$  [btz = 2,2'-bithiazoline] **(1.12)** is known to undergo gradual thermal SCO (**Figure 1.25**) and helps to further justify the significance of enhanced cooperativity through molecular interactions like  $\pi$ - $\pi$  orbital overlap. Single crystal X-ray analysis of **(1.12)** was used to examine the structural attributes and it was found that the molecular packing was similar in comparison to the packing of **(1.03)**, with continuous sheets of molecules along the ab plane. Neighboring ligands of **(1.12)** were found to position themselves in a nearly identical way to **(1.03)** and yet the significant change in

magnetism occurred over a much wider temperature range (**Figure 1.26**). A key difference between these two compounds, **(1.03)** and **(1.12)**, is that the bithiazoline ligand of **(1.12)** is made of non-aromatic heterocycles and the  $\pi$ - $\pi$  interactions are significantly reduced, which also reduces the amount of cooperativity in the sample.<sup>[2,81]</sup>

### iii) Incomplete spin-crossover

Incomplete SCO results when a change in spin state is observed but the spin equilibrium is not driven fully from one extreme to the other at any temperature. The manifestation usually results in a magnetic moment that is significantly different than the anticipated high- or low-spin value. Despite the abrupt change in the magnetic properties of **(1.03)**, it is also an example of an incomplete spin-crossover. At 110 K,  $\chi_m T$  is  $0.58 \text{ cm}^3 \text{ mol}^{-1} \text{ K}^{-1}$  corresponding to a magnetic moment of  $2.16 \mu_B$ , which is higher than expected for a low-spin iron(II) complex. The anomalously large magnetic moment can be rationalized as 17 % of the high-spin isomer remaining even at low temperature.<sup>[75]</sup>



**Figure 1.27:** The 1-isopropyltetrazole (iptz) ligand of  $[\text{Fe}(\text{iptz})_6](\text{SCN})_2$  (**1.13**)

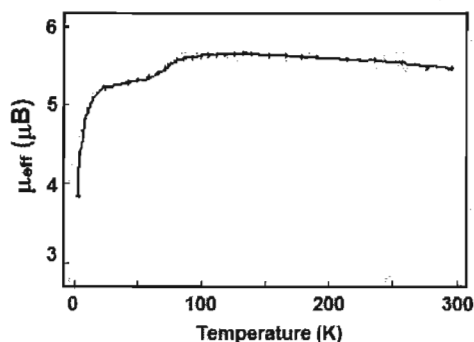


**Figure 1.28:** The gradual and incomplete spin-crossover exhibited by **(1.13)**<sup>[82]</sup>



**Figure 1.22** (iii) shows the profile of a spin-crossover that is both gradual and incomplete. This form of SCO is particularly difficult to identify by SQUID magnetometry, often requiring Mössbauer spectroscopy for a more accurate description of the magnetic states. An example,  $[\text{Fe}(\text{iptz})_6](\text{SCN})_2$  [iptz = 1-isopropyltetrazole (**Figure 1.27**)] (**1.13**), features an incomplete and gradual SCO represented in **Figure 1.28** that, when compared to the more standard profile of (**1.03**), appears as a less obvious form of magnetic lability.<sup>[82]</sup>

#### iv) Multistep spin-crossover

##### a) Bimetallic spin-crossover complexes

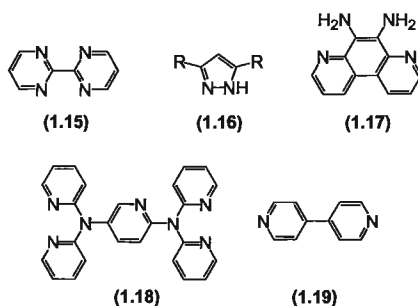


**Figure 1.29:** Examples of ligands used in bimetallic spin-crossover complexes<sup>[83-87]</sup>

The majority of reported SCO complexes contain a single metal ion; however, the preparation of bi- or polymetallic spin-crossover complexes have also afforded materials that display cooperative magnetic switching. Typically, *N*-heterocyclic bridging ligands are used in the assembly of bimetallic iron(II) SCO complexes and include ligands such as 2,2'-bipyrimidine (**1.14**)<sup>[83]</sup>, pyrazoles (**1.15**)<sup>[84]</sup>, 4,7-phenanthroline-5,6-diamine

(1.16)<sup>[85]</sup>, pyridine derivatives like ddpp [ddpp = 2,5-di(2',2''-dipyridylamino)pyridine] (1.17)<sup>[86]</sup>, and 4,4'-bipyridine (1.18)<sup>[87]</sup> (Figure 1.29).

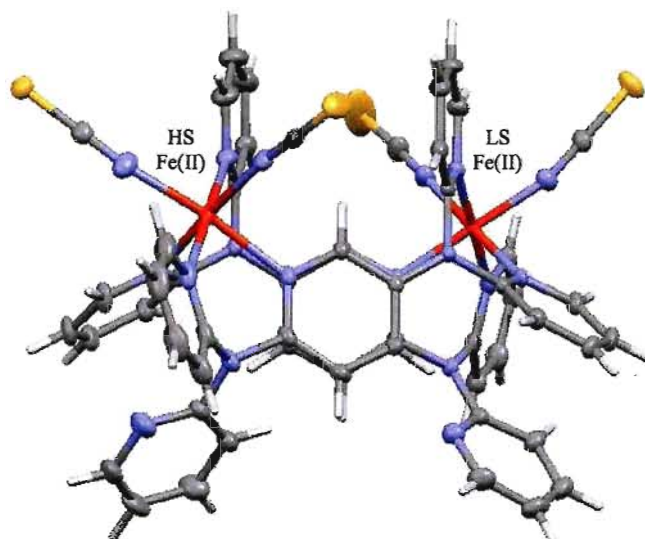


Figure 1.30: The molecular structure of complex (1.19)<sup>[88]</sup>

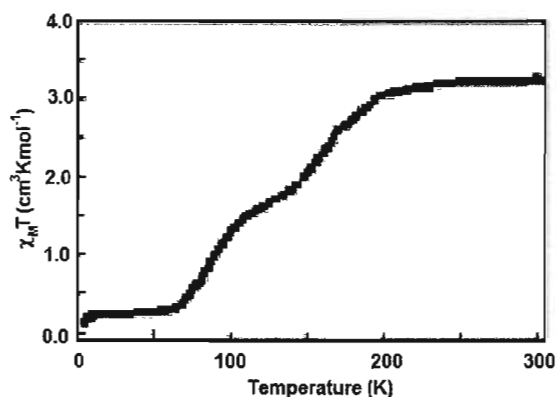
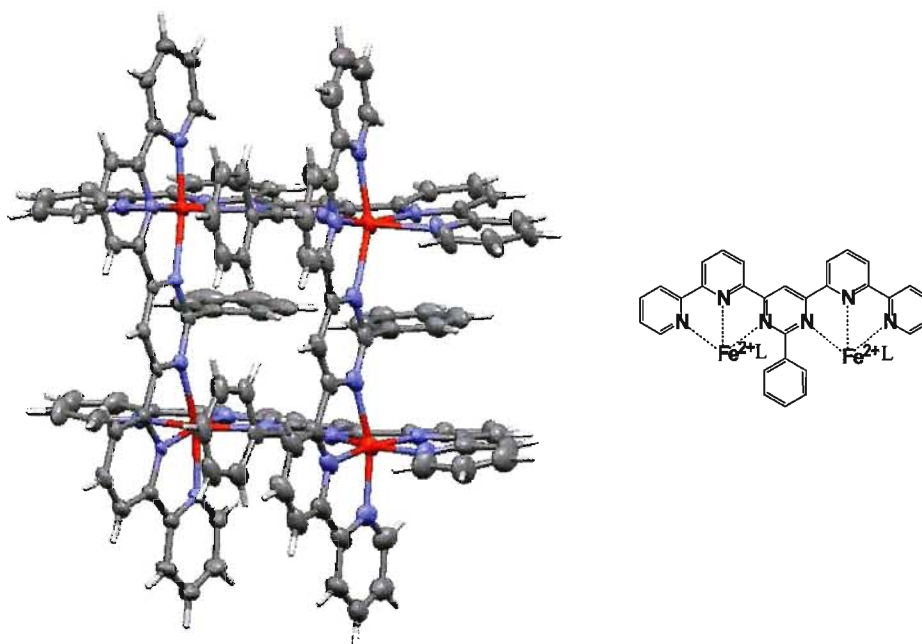


Figure 1.31: The two step spin-crossover of (1.19)<sup>[88]</sup>

The compound  $[\text{Fe}_2(\text{ddpp})_2(\text{NCS})_4] \cdot 4\text{DCM}$  (1.19), has the dinuclear structure shown in Figure 1.30 and has extensive intra- and interdimeric  $\pi$ - $\pi$  interactions, in addition to interactions involving the thiocyanate sulfur atoms. A two-step spin transition from HS- HS  $\rightarrow$  HS-LS  $\rightarrow$  LS-LS was observed by SQUID magnetometry, with transitions at

$T_{1/2(1)} = 180$  K and  $T_{1/2(2)} = 80$  K (**Figure 1.31**). The crystal structure in the plateau region, between the steps, showed that each dinuclear molecule was trapped in an ordered HS-LS form with appropriate Fe-N distances and octahedral distortions. For comparison, the HS-LS structure contrasts with the averaged (disordered) structure found at the plateau temperature in the compound  $[(\text{bztpe})\text{Fe}(\mu\text{-N}(\text{CN})_2)\text{Fe}(\text{bztpe})](\text{PF}_6)_3$  [ $\text{bztpe} = N\text{-benzyl-}N,N',N'\text{-tris(2-pyridylmethyl)-ethane-1,2-diamine}$ ] (**1.20**).<sup>[87-89]</sup>

b) Polymetallic spin-crossover complexes



**Figure 1.32:** The molecular structure (left) and a diagram displaying the Fe(II)-ligand coordination of (**1.21**) (right)<sup>[90]</sup>

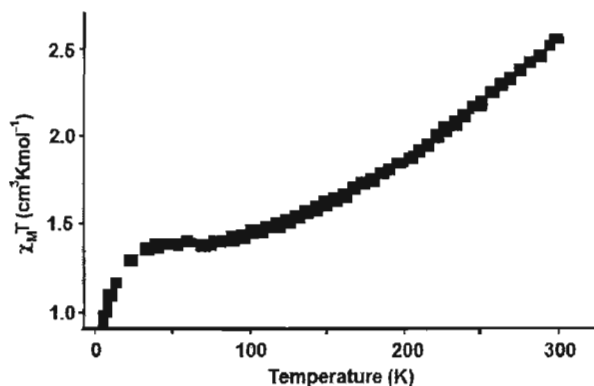


**Figure 1.33:** The variable temperature magnetic profile of (1.21)<sup>[90]</sup>

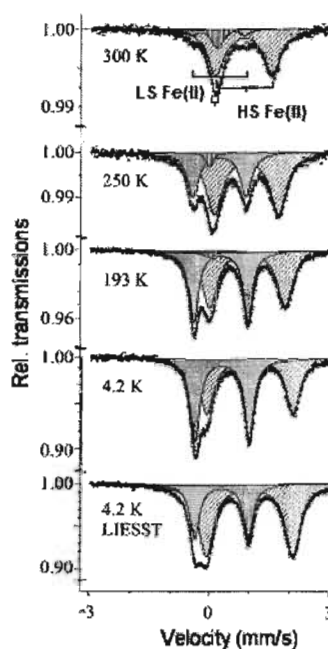


**Figure 1.34:** The Mössbauer spectra for complex (1.21)<sup>[90]</sup>

Polynuclear molecular systems of the are accessible via self assembly and can be used to precisely arrange spin active metal centres. In one such system,  $[\text{Fe}_4(\text{L}_4)(\text{ClO}_4)_8]$  [ $\text{L} = 4,6\text{-bis}(2',2''\text{-bipyrid-6'-yl-2phenyl-pyrimidine})$  (1.21), displayed in **Figure 1.32**, a plot of  $\chi_m T$  versus temperature affords a profile that suggests a noncooperative one step gradual spin-crossover (**Figure 1.33**). However, further examination with Mössbauer

spectroscopy (**Figure 1.34**) and X-ray crystallography revealed that the population shifted as a result of SCO from approximately 3LS:1HS  $\rightarrow$  2LS:2HS  $\rightarrow$  1LS:3HS upon increasing temperature. In addition, the magnetic properties of **(1.21)** can also be affected by light and pressure, representing a unique prototype for a multilevel magnetic device.<sup>[90-91]</sup>

v) Hysteresis in spin-crossover

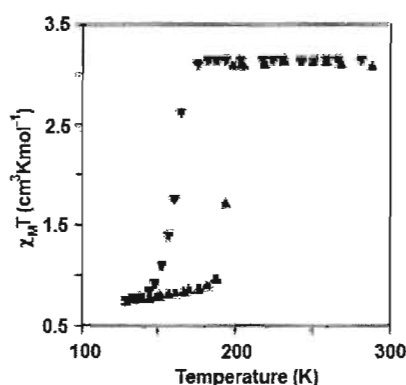


**Figure 1.35:** The variable temperature magnetic profile of **(1.22)**<sup>[2]</sup>

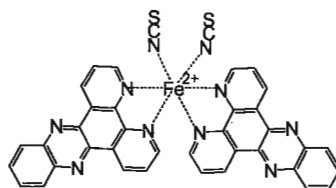


**Figure 1.36:** A diagram of complex **(1.22)**

**Figure 1.22** (v) displays a type of spin-crossover that has a hysteretic profile, where non-identical  $T_{1/2}$  temperatures between warming and cooling runs occur and produce two transitions between the high- and low-spin states. The magnetic profile of  $[\text{Fe}(\text{dppz})_2(\text{NCS})_2]$  [dppz = dipyrro[3,2-*a*:2'-3'-*c*]phenazine] **(1.22)** features abrupt and hysteretic transitions between warming and cooling (**Figures 1.35 - 1.36**). The ligand of

complex (1.22) has an extended aromatic system, capable of significant  $\pi$ - $\pi$  interactions between neighbouring molecules due to the ligand overlap. The aromatic overlap is identified as a significant factor in the observation of hysteresis and demonstrates the benefit to cooperativity through  $\pi$ - $\pi$  extension.<sup>[2,92]</sup>

a) Magnetic bistability and path dependent memory

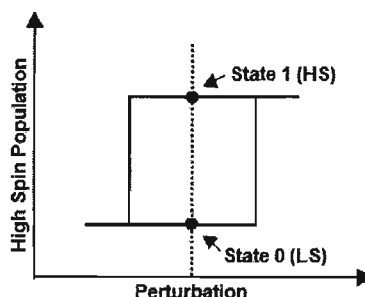


**Figure 1.37:** A general diagram for the memory effect of SCO materials<sup>[94]</sup>

A fundamental concept of SCO materials is *molecular bistability*, which may refer to either a single molecule or to an assembly of molecules, and can be defined as the ability of the system to be observed in two different electronic states at the same temperature.<sup>[93]</sup> One of the most notable examples of molecular bistability is the magnetic hysteresis that results from thermal perturbations of SCO materials because two distinct electronic states are accessible at the same temperature, conferring a path dependent memory effect (**Figure 1.37**).<sup>[94]</sup> As a result, the presence of hysteresis and an abrupt change in the magnetization curve are considered highly important requirements for SCO materials in order to realize useful magnetic switching. Thus, examining the methods used in controlling SCO is an important subject to consider when attempting to develop large hysteresis loops that are also centred around room temperature.<sup>[28]</sup>

b) Thermal hysteresis in iron(II) spin-crossover complexes

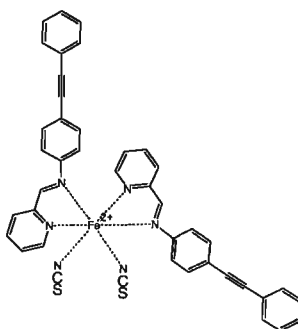


**Figure 1.38:** A diagram of  $[\text{Fe}(\text{pmpea})_2(\text{NCS})_2]$  (**1.23**)

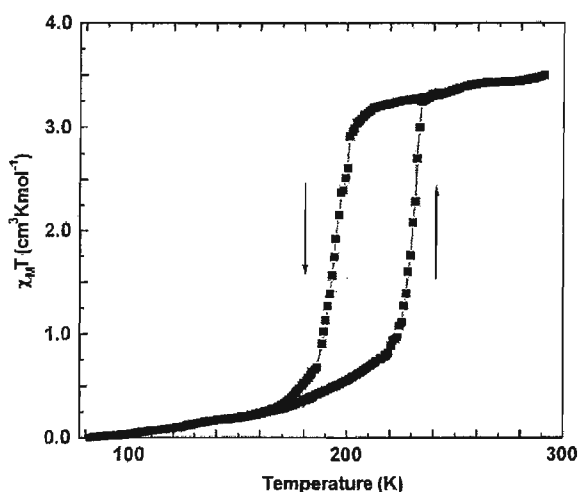


**Figure 1.39:** The variable temperature magnetic profile of (**1.23**)<sup>[95]</sup>

$[\text{Fe}(\text{pmpea})_2(\text{NCS})_2]$  [pmpea = *cis-bis*(thiocyanato)*bis*[*N*-(2'-pyridylmethylene)-4-(phenylethynyl)-anilino] (**1.23**) is an example of an iron(II) compound that shows a large hysteresis loop as a result of cooperative  $\pi$ - $\pi$  interactions (**Figure 1.38**). In the magnetic profile, the spin transition temperatures were identified as  $T_{1/2}(\text{cooling}) = 194$  K and  $T_{1/2}(\text{warming}) = 231$  K, corresponding to a hysteresis width of 37 K (**Figure 1.39**). The crystal structures of both the high- and low-spin states were obtained, revealing the characteristic changes in Fe-N bond lengths as a result of the transition. Another key aspect was the short contacts (3.45 Å) between the phenyl rings of adjacent (**1.23**)

molecules because their proximity was assigned as the pathway for the cooperativity that resulted in the large hysteresis loop.<sup>[95]</sup>

### c) Thermal hysteresis in iron(III) spin-crossover complexes

Thermal hysteresis has also been observed in some iron(III) SCO complexes including [Fe(qsal)<sub>2</sub>]NCSe·DMSO (**1.24**), which was found to exhibit a very wide thermal hysteresis. In the first cycle, the compound exhibits an apparent hysteresis loop of 115 K ( $T_{1/2}$ (warming) = 324 K and  $T_{1/2}$  (cooling) = 209 K). However, solvent molecules of the compound are removed at around 324 K and cause the magnetic profile to change during the second warming sweep. The spin transition in the warming mode now occurs at  $T_{1/2}$  = 285 K and the hysteresis width is estimated at 76 K. Again, it is thought that the main pathway for the observed cooperativity arises from the intermolecular  $\pi$ - $\pi$  interactions between the quinoline and phenyl rings.<sup>[96]</sup>



d) Multistate thermal hysteresis

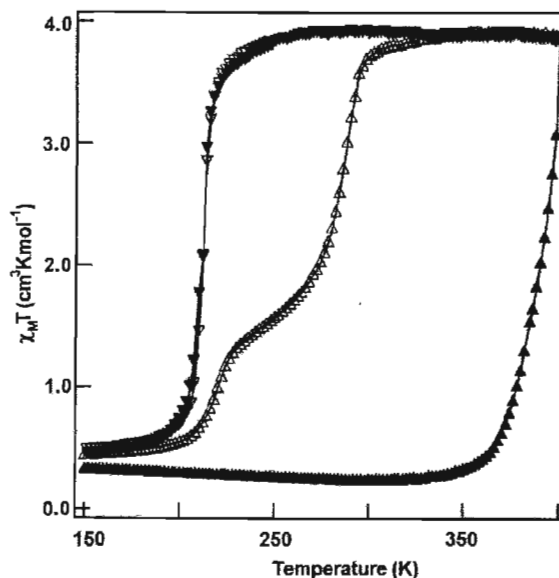


**Figure 1.40:** The variable temperature magnetic profile of **(1.25)**<sup>[97]</sup>

In a closely related compound,  $[\text{Fe}(\text{qsal})_2]\text{NCSe} \cdot \text{DCM}$  (**1.25**), a similar apparent spin transition is observed in the initial sweep ( $T_{1/2}(\text{warming}) = 392 \text{ K}$  and  $T_{1/2}(\text{cooling}) = 212 \text{ K}$ ) (**Figure 1.40**). After the first loop, it shows an interesting two-step spin-crossover in warming mode. The transitions of “step 1” and “step 2” are centred around  $T_{1/2}(\text{Step 1}) = 215 \text{ K}$  and  $T_{1/2}(\text{Step 2}) = 282 \text{ K}$ , respectively. The hysteresis widths are estimated at 3 K (step 1) and 70 K (step 2), the second being another example of an extremely wide span in comparison to other spin-crossover complexes.<sup>[97]</sup>

The two step hysteresis resulting from the desolvation of **(1.25)** is a curious phenomenon, especially when contrasting the observed magnetic properties with those of **(1.24)** and considering that in their nonsolvated forms, **(1.24)** and **(1.25)** have an identical molecular formula (i.e.  $[\text{Fe}(\text{qsal})_2]\text{NCSe}$ ). In this case, single crystal X-ray analysis provided vital

information to help understand the differences between **(1.24)** and **(1.25)**. The structures are closely related, each of the iron(III) atoms has pseudo-octahedral geometry, coordinated by the four nitrogen atoms and two oxygen atoms of the two ligands, an N<sub>4</sub>O<sub>2</sub> donor set in each case. However, when examining the space groups of the crystal structures, notable differences between **(1.24)** and **(1.25)** were identified. The crystal structure of **(1.24)** has the P1 space group and contains a continuous chain of quinoline groups that have considerable  $\pi$ - $\pi$  overlap with neighbouring phenyl rings. In the case of **(1.25)**, X-ray analysis revealed the P-1 space group, with an inversion centre. The main interactions were, again, attributed to the  $\pi$ - $\pi$  overlap of quinoline and neighbouring phenyl rings. However, the dihedral angles of the two ligands on each iron atom of **(1.24)** and **(1.25)** were considerably different and they were identified as distinct ligands in **(1.25)**, "A" and "B". Within the crystal, ligand A interacts with a neighbouring ligand A and ligand B interacts with a neighbouring ligand B resulting in the creation of two distinct  $\pi$ - $\pi$  interactions, one through the A ligands and one through the B ligands. Under the assumption that the symmetry remained upon desolvation, the compound was fitted to a model of the form (B:Fe:A)(A:Fe:B) and was described as undergoing a (LS)(LS) $\leftrightarrow$ (HS)(LS) $\leftrightarrow$ (HS)(HS) spin-crossover.<sup>[96-98]</sup>

#### e) Thermal hysteresis near room temperature

For most practical applications the hysteresis in SCO materials must occur around room temperature and there is a focus on the rational design of new SCO systems to achieve this goal. In some instances, the temperature range of the thermal hysteresis loop can be

tuned by varying the ligands coordinated to the iron. When perfectly dry, the compound  $[\text{Fe}(\text{Htrz})_3(\text{ClO}_4)_2]$  [ $\text{Htrz} = 1,2,4\text{-}H\text{-triazole}$ ] (**1.26**) shows a rather smooth spin transition around 265 K with a 5 K thermal hysteresis. However, when one drop of water is added to 50 mg of the complex, the transitions in both the warming and cooling mode become very abrupt ( $T_{1/2}(\text{warming}) = 313 \text{ K}$  and  $T_{1/2}(\text{cooling}) = 296 \text{ K}$ ) as a result of increased communication through hydrogen bonding. Further tailoring resulted from the addition of  $\text{NH}_2\text{trz}$  [ $\text{NH}_2\text{trz} = 4\text{-amino-}1,2,4\text{-triazole}$ ] to the reaction flask, preparing compounds with the general formula  $[\text{Fe}(\text{Htrz})_{3-3x}(\text{4-NH}_2\text{trz})_{3x}](\text{ClO}_4)_2 \cdot n\text{H}_2\text{O}$ . It has been shown that the critical temperatures of the spin transitions decrease with increasing  $\text{NH}_2\text{trz}$ . When  $x = 0.05$  the iron centres undergo a thermal hysteresis that spans room temperature ( $T_{1/2}(\text{warming}) = 304 \text{ K}$  and  $T_{1/2}(\text{cooling}) = 288 \text{ K}$ ).<sup>[99]</sup>

The iron(II) compound,  $[\text{Fe}(\text{2-pic})_3]\text{Cl}_2 \cdot \text{H}_2\text{O}$  [ $\text{2-pic} = 2\text{-picolylamine}$ ] (**1.27**), exhibits thermal bistability spanning 91 K ( $T_{1/2}(\text{warming}) = 295 \text{ K}$  and  $T_{1/2}(\text{cooling}) = 204 \text{ K}$ ) and the difference in magnetic states can be observed even at room temperature. However, the duration of this transition is not solely a result of SCO and has been accounted for by a low temperature phase transition in addition to the SCO process.<sup>[100-101]</sup>

## 1.06 Multifunctionality in spin-crossover materials

Having arrived at a reasonable understanding of how to control spin-crossover through cooperative interactions, current research is focused on developing practical applications for spin-crossover materials. One facet of these efforts includes micro- and

nanopatterning of spin-crossover compounds into logical structures.<sup>[102-103]</sup> Other efforts have been devoted to the design of new spin-crossover compounds in which SCO may be combined with other physical or chemical properties in a synergistic manner. Efforts towards this multifunctionality include combinations of SCO with magnetic exchange, liquid crystalline properties, host–guest or ligand isomerisation effects and electrical conductivity.<sup>[104]</sup>

### 1.07 Spin-crossover and electrical conductivity

#### i) An overview of spin-crossover conductors

Spin-crossover compounds are an attractive component in hybrid materials that combine electrical conductivity and magnetism. Within these materials, it is implied that the physical properties coexist, but combining them could also cause the properties to influence one another, directly, or through a mutual secondary effect. In this regard, SCO is an interesting magnetic property to incorporate into these hybrid materials because of the ability to switch between high-spin and low-spin states by variation of temperature, pressure or light irradiation. The interest is further enhanced in some examples when bistability is observed. The switching leads to distinctive changes in magnetism, but also changes in the coordinate bond lengths of the metal, which can alter the structure of the material. The change in structure and morphology can, in turn, have significant influences on the conductivity.<sup>[104]</sup> Although SCO is commonly observed in both neutral and positively charged complexes, the SCO conductors previously reported use

combinations of cationic SCO complexes with known anionic/radical molecular conductors in their design. Furthermore, the redox stability and cationic nature of most iron(III) SCO compounds, in comparison to iron(II), makes them more suitable for this approach. As a result, the known SCO conductors all fall within the general formula of an iron(III) SCO cation and an anionic conductor.<sup>[104-106]</sup>

ii) The coexistence of magnetic switching and electrical conductivity

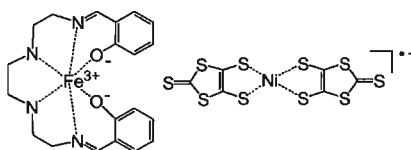


**Figure 1.41:** A diagram of  $[\text{Fe}(\text{sal}_2\text{-trien})]^+[\text{Ni}(\text{dmit})_2]^{n-}$  (1.28)

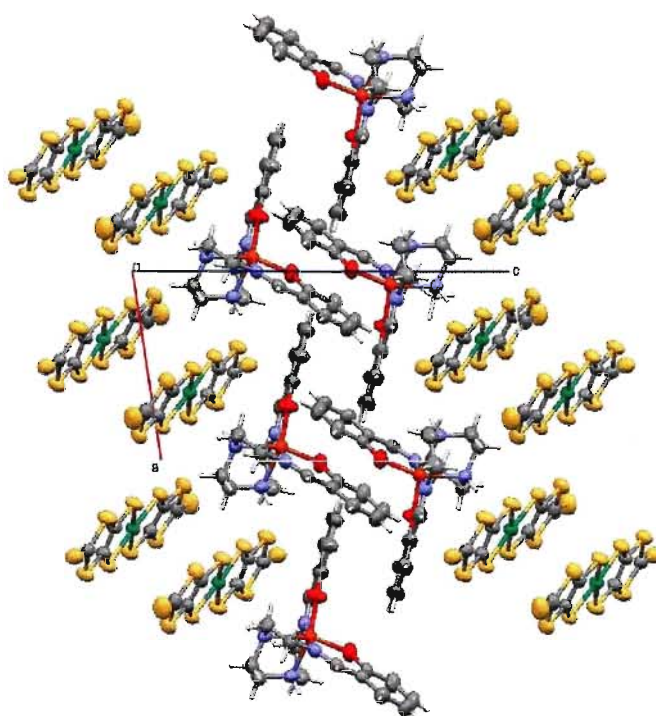


**Figure 1.42:** A packing diagram of (1.28) in the high-spin state<sup>[107]</sup>

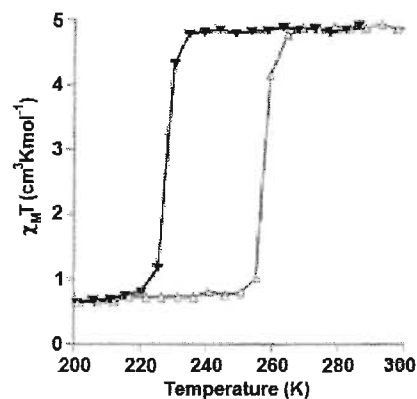


**Figure 1.43:** The variable temperature magnetic profile of (1.28)<sup>[107]</sup>

The iron(III) complex  $[\text{Fe}(\text{sal}_2\text{-trien})]^+[\text{Ni}(\text{dmit})_2]^{n-}$  [ $\text{sal}_2\text{-trien}$  = bis(salicylidene)aminotriethylenetetramine,  $\text{dmit}$  = 4,5-dimercapto-1,3-dithiole-2-thione] (1.28) (Figure 1.41) is a typical example of an iron(III) SCO conductor. Within this material, the layers of  $[\text{Ni}(\text{dmit})_2]^{n-}$  are described as being in a fractional oxidation state that give rise to the electron transport properties, a room temperature electrical conductivity of  $0.20 \text{ Scm}^{-1}$ . The  $[\text{Ni}(\text{dmit})_2]^{n-}$  layers form segregated stacks separated by layers of  $[\text{Fe}(\text{sal}_2\text{-trien})]^+$  cations (Figure 1.42). The  $[\text{Fe}(\text{sal}_2\text{-trien})]^+$  units undergo cooperative SCO behaviour including a hysteresis loop of 30 K centred at 240 K (Figure 1.43). In this example (of a hybrid SCO conductor), the two physical properties, electrical conductivity and magnetic switching, coexist in the same material, although they are not reported to have a significant influence on each other.<sup>[107]</sup>

iii) Interactions between magnetic switching and conductivity

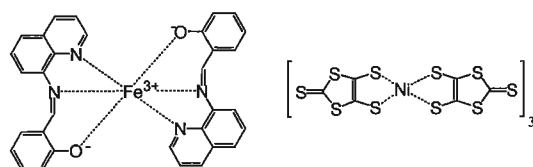


**Figure 1.44:** A diagram of  $[\text{Fe}(\text{qsal})_2][\text{Ni}(\text{dmit})_2]_3$  (**1.29**)

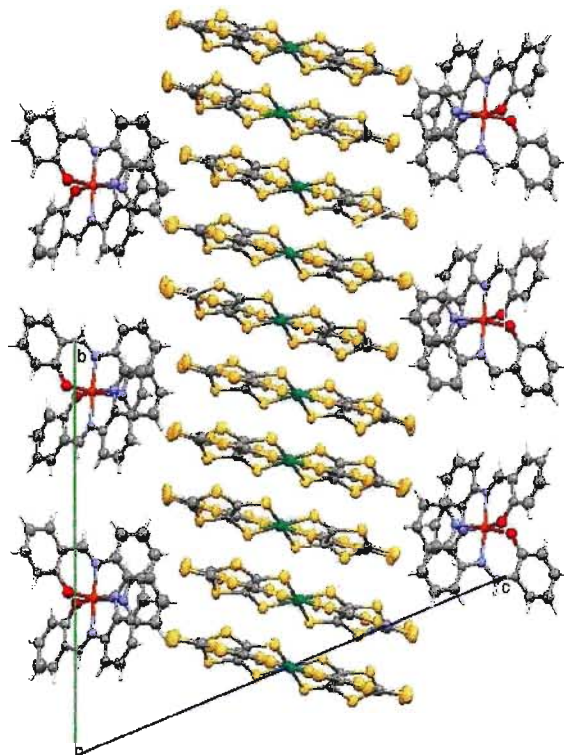


**Figure 1.45:** A packing diagram of (**1.29**) in the high-spin state<sup>[108]</sup>

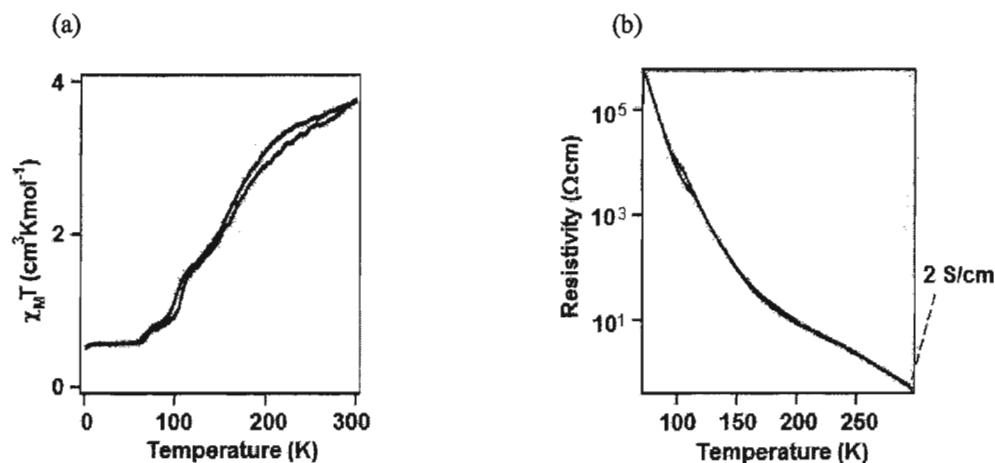


**Figure 1.46:** The (a) magnetic and (b) the resistivity profiles of (1.29)<sup>[108]</sup>

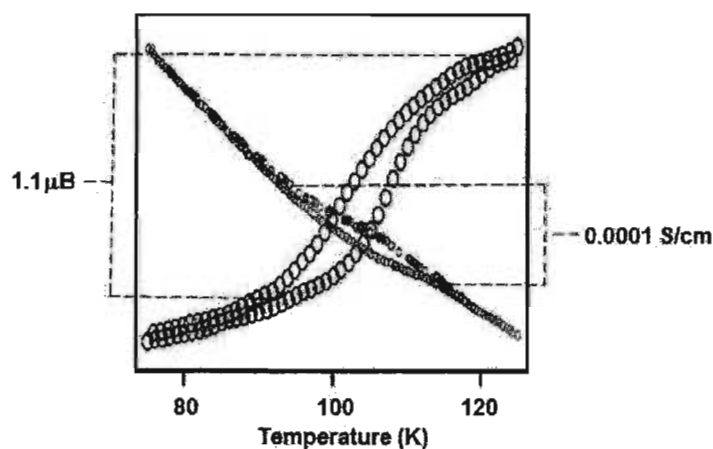


**Figure 1.47:** The interaction between conductivity and spin-crossover in (1.29)<sup>[108]</sup>

A similar iron(III) complex,  $[\text{Fe}(\text{qsal})_2][\text{Ni}(\text{dmit})_2]_3$  (1.29) (Figures 1.44 - 1.45), is noteworthy because it is one of the few SCO conductors reported that exhibits an interaction between electrical conductivity and a change in spin state. A narrow hysteresis is observed between 90 - 120 K in both the magnetic and resistivity profiles (Figures 1.46 - 1.47). At room temperature, this material is a semiconductor and becomes more resistant upon decreasing temperature, which is typical for molecular



conductors. However, the hysteresis in the resistivity profile is atypical because measurements taken during the heating sweep were more conductive than in the cooling sweep, indicating that the spin-crossover was influencing the electrical conductivity. Unfortunately, the crystal structure of the low temperature phase was not determined and the mechanism of the conducting states bistability remains unclear.<sup>[108]</sup>

#### iv) The chemical pressure effect

A mechanism explaining how the spin transition can affect conductivity was achieved from further studies on another related iron(III) SCO system,  $[\text{Fe}(\text{qnal})_2][\text{Pd}(\text{dmit})_2]_5 \cdot \text{acetone}$  (**1.30**). In this example, an abrupt and almost complete spin transition between the low-spin and high-spin states was observed at around 220 K and the crystal structures, both above and below the spin transition, were obtained. Structural changes in the coordination bond lengths ( $\Delta_{\text{Fe-O}}$ : 0.03–0.04 Å,  $\Delta_{\text{Fe-N}}$ : 0.15–0.18 Å) and angles around the Fe(III) atoms resulted from the spin-crossover and were indicated as the cause of a uniaxial crystal lattice deformation (shrinking of one axis by 0.2 Å upon cooling).

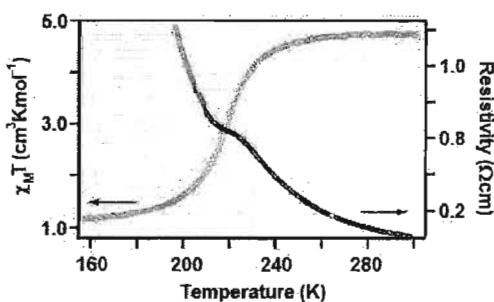


**Figure 1.48:** The interaction between conductivity and spin-crossover in (**1.30**)<sup>[25]</sup>

The material **(1.30)** is a semiconductor, with a conductivity of  $1.6 \times 10^{-2} \text{ Scm}^{-1}$  at room temperature, that depends strongly upon its crystal structure and packing to achieve electron transport. The packing of the  $[\text{Pd}(\text{dmit})_2]^{n-}$  layers is affected by the crystal lattice deformation and results in an anomaly in the resistivity profile observed around 220 K, at the temperature range of the spin transition (**Figure 1.48**). This result displayed that the expansion and contraction of an iron(III) SCO complex can induce a chemical pressure effect similar to those caused by modifying a molecular structure by substitution of smaller or larger substituents.<sup>[25]</sup>

v) Developing other kinds of of SCO conductors

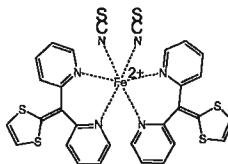


**Figure 1.49:** A diagram of complex **(1.31)**

Many of the successful efforts in designing spin-crossover conductors involve using compounds that are closely related (described previously). However, there have been efforts to develop a more diverse selection of spin-crossover components for use in new materials. One important effort is aimed at developing iron(II) SCO conductors because they have well documented cooperative effects (through  $\pi$ - $\pi$  interactions, hydrogen and coordination bonding, in addition to intriguing LIESST effect properties) and it is thought that these properties can be used to strongly modulate or influence the electrical conductivity. One design, complex **(1.31)**, uses chalcogen atoms attached to the SCO complex through conjugated bonds to achieve strong intermolecular interactions (**Figure**

1.49). Since chalcogens are often used in molecular-based conductors their close proximity also functions as a potential path for electron transport.<sup>[109]</sup>

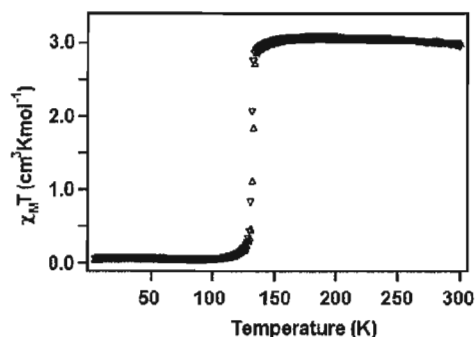


**Figure 1.50:** The variable temperature magnetic profile of **(1.31)**<sup>[109]</sup>

At room temperature **(1.31)** favours the HS state ( $\chi_M T = 3.1 \text{ cm}^3 \text{ K mol}^{-1}$ ) and upon decreasing the temperature to 130.5 K ( $T_{1/2}$  cooling) an abrupt change in the magnetic profile was observed **(1.31)** (**Figure 1.50**). After the transition the  $\chi_M T$  value is almost 0, indicating the equilibrium begins to favour the LS state. Upon heating the sample (after cooling) the reverse transition to HS occurred at 132.5 K ( $T_{1/2}$  warming).<sup>[109]</sup>

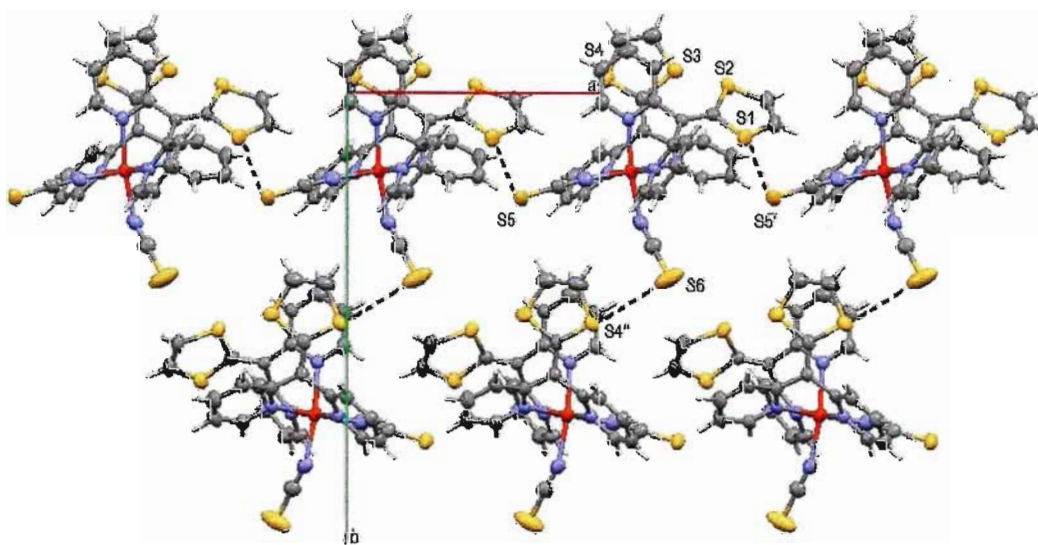


**Figure 1.51:** A packing diagram of complex **(1.31)**<sup>[109]</sup>

The crystal structures of **(1.31)**, in both the LS state at 103 K and the HS state at 160 K, were determined and changes in the coordinate bond lengths clearly indicated that the spin transition was occurring. Intermolecular S...S distances in the sample were also observed to change as a result of the spin transition (**Figure 1.51**). At 160 K there are two short S...S contacts. One contact is 3.542 Å between S(1) and S(5') in the ligand and thiocyanate anion respectively. The other contact, 3.689 Å, is found between ligand molecules containing S(2) and S(3), forming a one-dimensional S...S chain-like structure. At 103 K, the contacts are still in the same relative positions, as observed in the high temperature phase, but the S(2) and S(3) contact is now much shorter at 3.573(2) Å. A third S...S contact with a distance of 3.689(3) Å also forms between S(4') and S(6), converting the solid into a two-dimensional S...S network.<sup>[109]</sup>

The abrupt spin transition and narrow hysteresis loop of **(1.31)** suggest that strong cooperative interactions derived mainly from short S...S contacts are present within this molecule. Unfortunately, the cooperative effects were not observed to influence the conductivity because measurements verified that the complex was an insulator. It was then suggested that in order to introduce conducting properties into an iron(II) spin-crossover system, further extension of the ligand's  $\pi$ -system was required.<sup>[109]</sup>

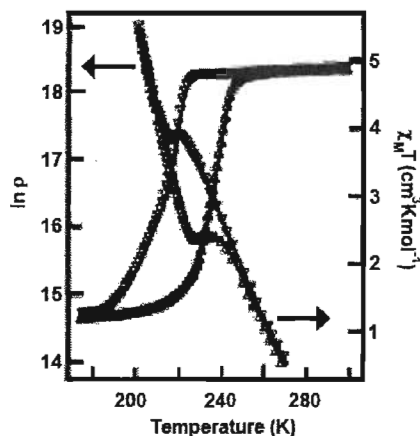


**Figure 1.52:** The interaction between conductivity and spin-crossover in **(1.32)**<sup>[110]</sup>

FeCo Prussian blue analogues are another example of multifunctional materials that combine temperature dependent resistivity and magnetism. In  $[\text{Na}_{0.38}\text{Co(II)}_{1.31}[\text{Fe(III)(CN)}_6] \cdot 5.4\text{H}_2\text{O}]$  **(1.32)** for example, the  $\chi_M T$  values varied significantly depending on temperature due to switching between the  $\text{Fe(III}^{\text{LS}}\text{)-Co(II}^{\text{HS}}\text{)}$  and  $\text{Fe(II}^{\text{LS}}\text{)-Co(III}^{\text{LS}}\text{)}$  states, which also causes a reversible phase transition in the material. The resistivity versus temperature plot shows an abrupt change in conductivity at the temperature where the phase transition occurs, in addition to a hysteresis loop in both the resistivity and magnetism plots (**Figure 1.52**).<sup>[110]</sup>

## Chapter 2: Iron(III) spin-crossover complexes

### 2.01 Goals and objectives

Our goal is the generation of polymeric materials from molecular SCO precursors that are attached, through covalent bonds, to thiophene heterocycles. The thiophene groups of the complexes will then be linked together through oxidative coupling to form conjugated polymers. These will be the first examples of electrically conductive metallopolymer that contain spin-labile substituents. Also, since each SCO unit will be joined through a covalent linkage, a new structural paradigm for spin-crossover materials will result from this synthesis.

### 2.02 The spin-crossover component

With respect to the choice of the spin-crossover component, several preliminary considerations were addressed. Since conjugated polymers can be prepared through oxidative coupling, a SCO component featuring a metal in a higher oxidation state, like iron(III), could impart added stability towards our synthetic goals. A number of iron(III) complexes are known to exhibit spin-crossover, including those made from the qsal ligand (**2.01**) [qsalH = *N*-(8-quinolyl)salicylaldehyde]. Spin-crossover complexes based on qsal, with SCN<sup>-</sup> or SeCN<sup>-</sup> counteranions, are notable examples because they feature very abrupt spin-transitions.<sup>[72,96-98]</sup> These complexes also display wide thermal

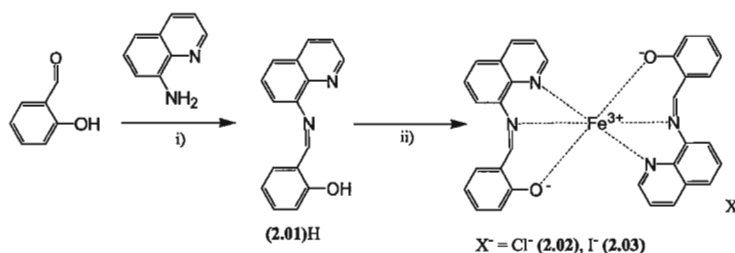
hysteresis loops that result from increased co-operativity through strong intermolecular interactions generated by close  $\pi$ - $\pi$  contacts in the solid state.<sup>[25]</sup>

### 2.03 Iron(III) qsal complexes

#### i) A preliminary study on iron(III) qsal complexes

Iron(III) qsal complexes were identified as an ideal starting point for the aims of this research. However, familiarity with the synthesis and characterization of these complexes, in addition to their structural properties were preliminary goals set before attempting to append the ligand with a thiophene group. These compounds would be used as reference points to assess the appended complexes we would prepare afterwards.

#### ii) Synthesis and characterization



Reagents and conditions: (i) MeOH. (ii) 0.5 eq  $\text{FeCl}_3 \cdot 6\text{H}_2\text{O}$ , MeOH (and KI,  $\text{H}_2\text{O}$  for **(2.03)**).

**Scheme 2.01:** The synthesis of complexes **(2.02)** and **(2.03)**

Complex **(2.02)** was generated by reaction of two equivalents of the ligand precursor **(2.01)H** with hydrated iron(III) chloride to produce  $[\text{Fe}(\text{2.01})_2]\text{Cl}$ . A metathesis reaction followed with an aqueous solution containing an excess of KI to afford the precipitate

**(2.03)** (**Scheme 2.01**). The complexes **(2.02)** and **(2.03)** are analytically pure and produce clean ESI mass spectra, with the largest peak corresponding to the  $[\text{Fe}(\mathbf{2.01})_2]^+$  cation. Also, the FT-IR spectra for both complexes show a highly characteristic absorption, the imine (C=N) stretch at  $1601\text{ cm}^{-1}$ , attributed to the coordinated ligand **(2.01)**.

iii) Structural properties

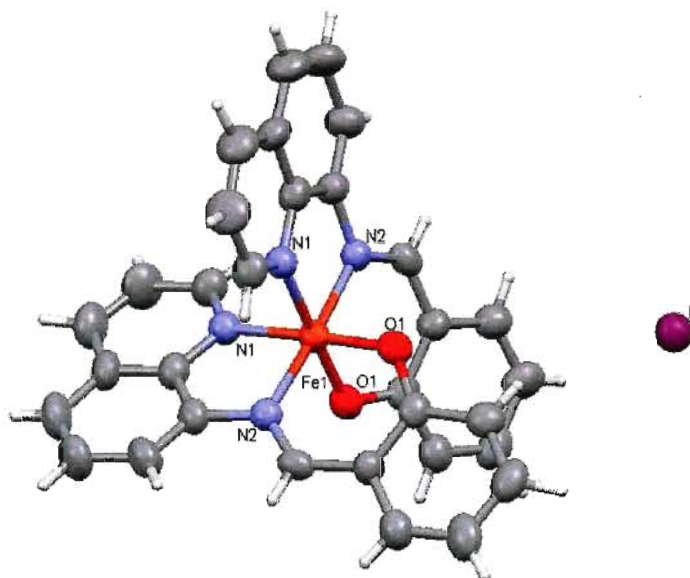


**Figure 2.01:** The molecular structure of **(2.03)** with ellipsoids drawn at the 50 % probability level



---

**Table 2.01:** Selected bond distances and angles for **(2.02)**

| Atoms      | Distance (Å) | Atoms           | Angle (°) |
|------------|--------------|-----------------|-----------|
| Fe(1)-N(1) | 1.986(4)     | N(1)-Fe(1)-N(1) | 88.4(2)   |
| Fe(1)-N(2) | 1.940(4)     | N(1)-Fe(1)-N(2) | 82.3(2)   |
| Fe(1)-O(1) | 1.871(3)     | N(1)-Fe(1)-N(2) | 94.7(2)   |
|            |              | N(1)-Fe(1)-O(1) | 90.4(1)   |
|            |              | N(2)-Fe(1)-O(1) | 89.0(1)   |
|            |              | N(2)-Fe(1)-O(1) | 93.9(1)   |
|            |              | O(1)-Fe(1)-O(1) | 91.1(1)   |
|            |              | N(1)-Fe(1)-N(2) | 175.9(2)  |
|            |              | N(2)-Fe(1)-O(1) | 175.9(2)  |

---

(standard deviations in the last digit are quoted in parenthesis)

---

Single crystals of **(2.03)**, suitable for X-ray diffraction, were grown from slow evaporation of a saturated methanol solution. The expected pseudo-octahedral coordination geometry of **(2.03)** reveals bond lengths and angles that are all consistent with those of similar iron(III) compounds (**Figure 2.01**).<sup>[97]</sup> The Fe–O distances are shorter than the Fe–N distances and induce a slight distortion in the nearly perpendicular FeN<sub>4</sub>O<sub>2</sub> octahedron of **(2.03)** (**Table 2.01**).

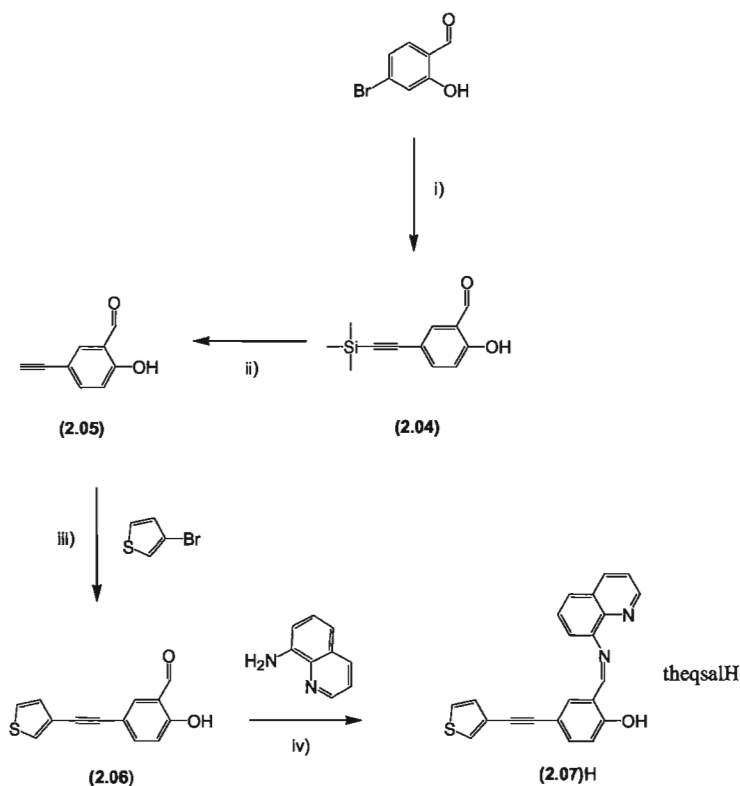
## **2.04** Thienyl-substituted qsal complexes\*

### i) Synthetic methodology

After our preliminary investigation of iron(III) qsal complexes, we shifted towards our main synthetic objective, namely appending the qsal ligand **(2.01)** with a thiophene heterocycle. The framework of **(2.01)** is amenable to structural modification, which is

advantageous for tethering to the thiophene component. We also chose to incorporate an ethynyl spacer between the qsal ligand and the thiophene group to help prevent steric congestion of the compounds while still maintaining the conjugation. The structurally modified (**2.01**) ligand was then used in the synthesis of model complexes containing iron(III), to investigate the effect of thiophene ring substitution on the electronic or magnetic properties of the  $[\text{Fe}(\mathbf{2.01})_2]^+$  moiety.

## ii) Ligand synthesis



Reagents and conditions: (i) TMS-acetylene,  $(i\text{-Pr})_2\text{NH}$ , 2 mol %  $\text{PPh}_3$ , 2 mol %  $\text{PdCl}_2(\text{PPh}_3)_2$ , 3 mol %  $\text{CuI}$ , 84 °C, 4 h. (ii) MeOH, THF, KOH. (iii) 3-bromothiophene, THF,  $(i\text{-pr})_2\text{NH}$ , 2 mol %  $\text{PPh}_3$ , 2 mol %  $\text{PdCl}_2(\text{PPh}_3)_2$ , 3 mol %  $\text{CuI}$ , 65 °C, 20 h. (iv) 8-aminoquinoline, EtOH.

**Scheme 2.02:** The synthesis of (**2.07**)H

A 3-ethynylthienyl substituted qsalH ligand was prepared in four steps from the commercially available reagents 5-bromosalicylaldehyde and 3-bromothiophene (Scheme 2.02). Sonogashira cross-coupling between 5-bromosalicylaldehyde and ethynyltrimethylsilane afforded the protected acetylene precursor (2.04), which was deprotected by stirring overnight in base to afford (2.05). Another Sonogashira reaction between (2.05) and 3-bromothiophene provided the aldehyde precursor (2.06) as a yellow powder, which was condensed with 8-aminoquinoline to yield the modified ligand (2.07)H as a crimson oil, which is somewhat unstable in solution but has been fully characterized.

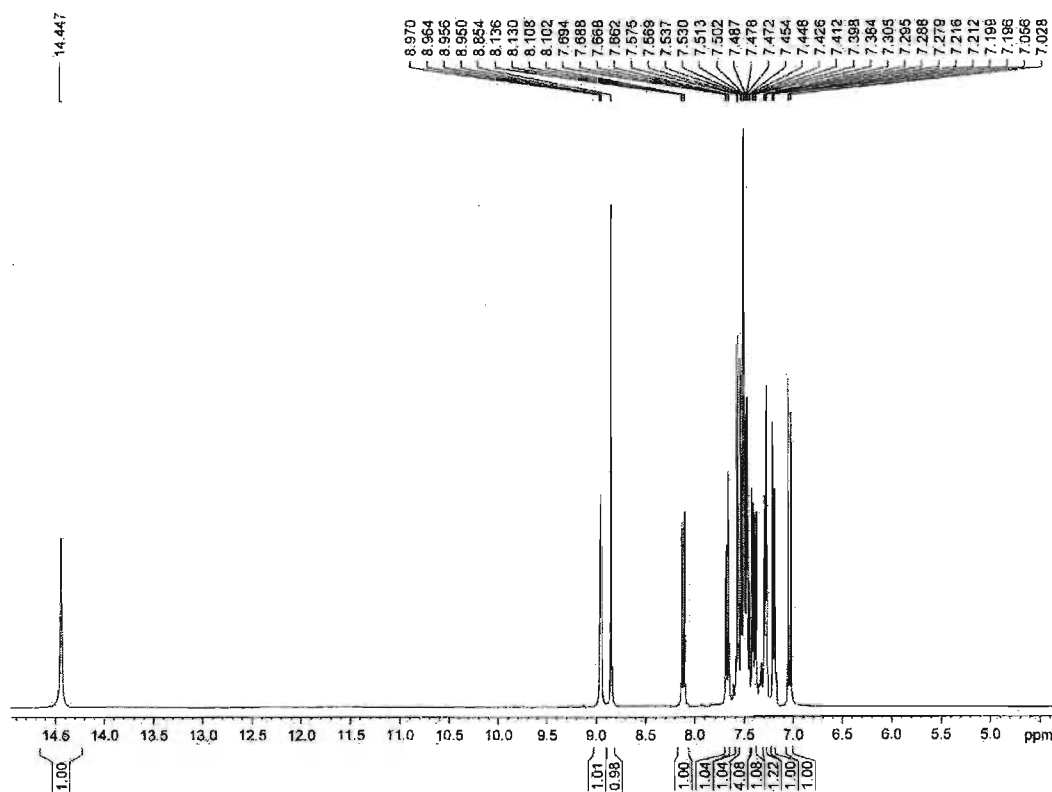
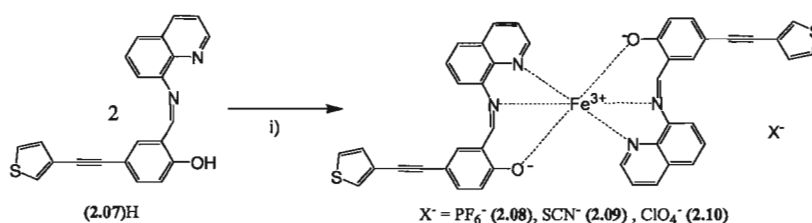


Figure 2.02:  $^1\text{H}$ -NMR spectrum of (2.07)H in  $\text{CDCl}_3$

In the  $^1\text{H}$ -NMR spectrum of **(2.07)**H (**Figure 2.02**), the peak attributed to the hydroxyl proton at 14.45 ppm is shifted downfield relative to hydroxyl proton resonance at 11.13 ppm in the aldehyde precursor **(2.06)**. The singlet observed at 8.93 ppm is characteristic of the imine proton when compared to the imine singlet at 8.95 ppm observed for **(2.01)**H. Twelve additional peaks are found in the aromatic region of the spectrum and are consistent with the expected resonances of the three thienyl, three salicyl and six quinoline protons. The imine C=N stretch is also observed in the FT-IR spectrum.

### iii) Coordination chemistry

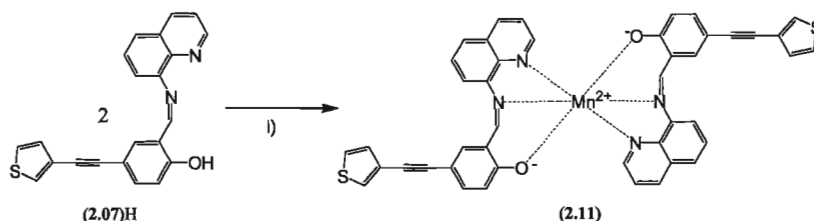


Reagents and conditions: (i) **(2.08)**  $\text{FeCl}_3 \cdot 6\text{H}_2\text{O}$ ,  $\text{NaPF}_6$ ,  $\text{MeOH}$ ,  $\text{H}_2\text{O}$ ; **(2.09)**  $\text{FeCl}_3 \cdot 6\text{H}_2\text{O}$ ,  $\text{KSCN}$ ,  $\text{MeOH}$ ,  $\text{H}_2\text{O}$ ; **(2.10)**  $\text{Fe}(\text{ClO}_4)_3 \cdot 6\text{H}_2\text{O}$ ,  $\text{KSCN}$ ,  $\text{MeOH}$ ,  $\text{H}_2\text{O}$ .

**Scheme 2.03:** The synthesis of complexes **(2.08)** - **(2.10)**

Homoleptic coordination complexes were generated by reaction of two equivalents of **(2.07)**H with hydrated iron(III) chloride in the presence of triethylamine, followed by metathesis with aqueous solutions containing an excess of  $\text{NaPF}_6$  or  $\text{KSCN}$  to afford dark green precipitates of the  $\text{PF}_6^-$  **(2.08)** or  $\text{SCN}^-$  **(2.09)** salts containing the  $[\text{Fe}(\text{2.07})_2]^+$  cation (**Scheme 2.03**). Complex **(2.10)**, containing a perchlorate anion, was prepared by direct reaction of  $\text{Fe}(\text{ClO}_4)_3 \cdot 6\text{H}_2\text{O}$  with two equivalents of **(2.07)**H in a dichloromethane (DCM)–acetonitrile solution. All complexes are analytically pure and produce ESI mass spectra with a dominant peak corresponding to the  $[\text{Fe}(\text{2.07})_2]^+$  cation. The FT-IR

spectra for complexes **(2.08)** - **(2.10)** are very similar, the only significant changes being due to the characteristic absorptions of the different anionic component. A slight shift ( $\sim 15\text{ cm}^{-1}$ ) in the C=N stretching frequency to lower energy, relative to uncoordinated **(2.07)H**, also indicates coordination.

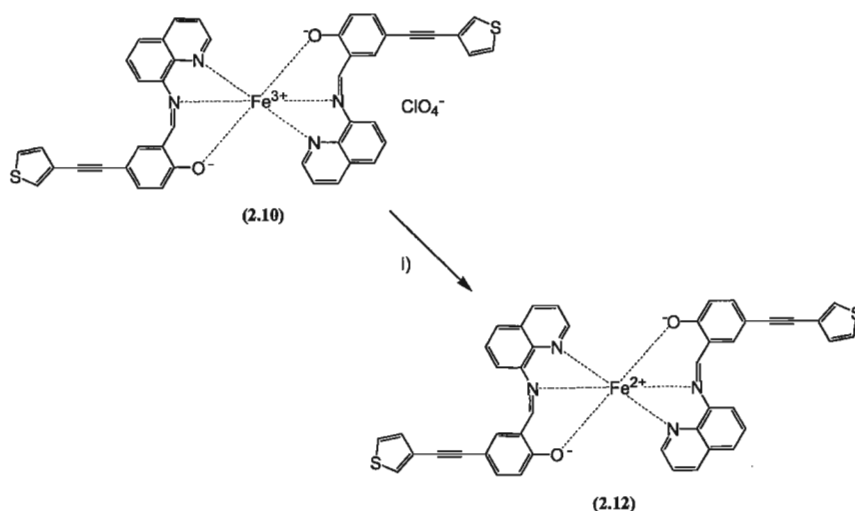


Reagents and conditions: (i)  $\text{Mn}(\text{C}_2\text{H}_3\text{O}_2)_2 \cdot 4\text{H}_2\text{O}$ , DCM, MeOH.

**Scheme 2.04:** The synthesis of complex **(2.11)**

In addition to our targeted iron(III) containing SCO compounds we also prepared a closely related complex that was not spin labile so that we could further probe the magnetic and electronic properties of our models. A homoleptic manganese complex **(2.11)** was generated in an analogous procedure to the iron containing species. Two equivalents of **(2.07)H** were combined with hydrated manganese(II) acetate to afford the neutral  $[\text{Mn}(\text{2.07})_2]$  complex as a red precipitate (**Scheme 2.04**). The complex was analytically pure and produced an ESI mass spectrum with a dominant peak corresponding to the  $[\text{Mn}(\text{2.07})_2]^+$  cation. The FT-IR spectrum for complex **(2.11)** is similar to **(2.08)** - **(2.10)**, with a nearly identical C=N stretching frequency ( $\sim 4\text{ cm}^{-1}$  lower).

iv) Structural properties



Reagents and conditions: (i)  $[\text{Fe}(\mathbf{2.07})_2]\text{SCN} \cdot 2.5 \cdot \text{H}_2\text{O}$ , acetone.

**Scheme 2.05:** The reduction of (2.10)

Using a variety of different techniques and solvent combinations, efforts to grow single crystals of complexes (2.08) - (2.10) suitable for X-ray diffraction studies were unsuccessful. On the basis of the characterization data collected, however, we are confident in the proposed formulations for complexes (2.08) - (2.10). Curiously, the attempted recrystallization of (2.10) in an aerobic acetone solution generated black plate crystals of the reduced iron(II) complex (2.12) as an acetone and water solvate. Redox stability certainly accounts for some of the difficulties encountered during the attempted crystal growth of (2.08) - (2.10), but we have only observed this reduction for complex (2.10) in acetone solution (Scheme 2.05).

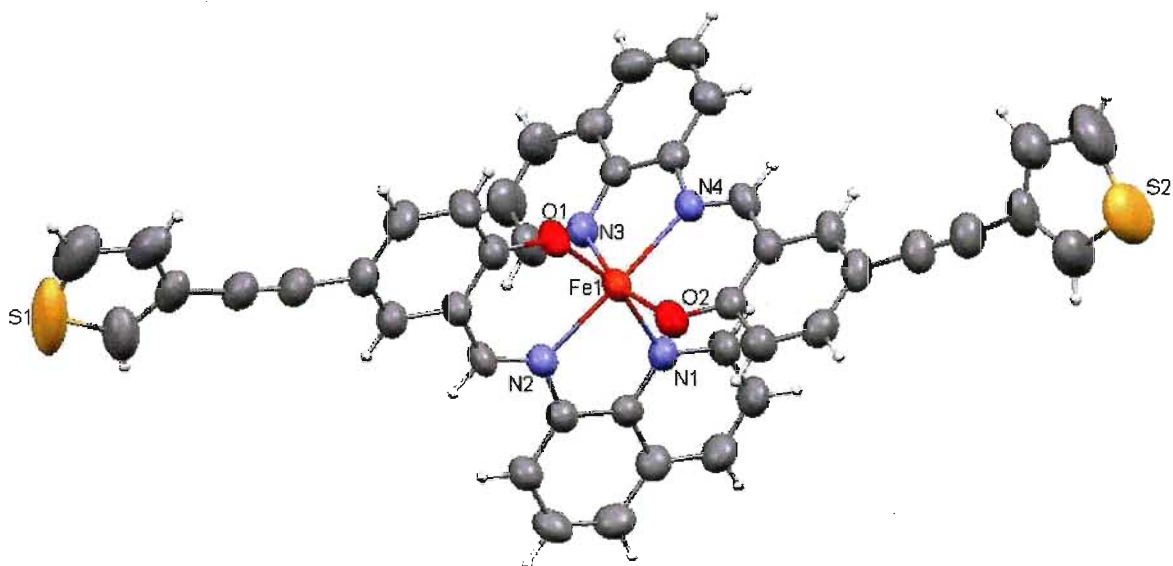


**Figure 2.03:** The molecular structure of (2.12) with ellipsoids drawn at the 50 % probability level

**Table 2.02:** Selected bond distances and angles for (2.12)

| Atoms      | Distance (Å) | Atoms           | Angle (°) |
|------------|--------------|-----------------|-----------|
| Fe(1)-N(1) | 2.143(2)     | N(1)-Fe(1)-N(2) | 76.8(1)   |
| Fe(1)-N(2) | 2.130(2)     | N(1)-Fe(1)-N(3) | 87.5(1)   |
| Fe(1)-N(3) | 2.157(3)     | N(1)-Fe(1)-N(4) | 97.7(1)   |
| Fe(1)-N(4) | 2.142(3)     | N(2)-Fe(1)-N(3) | 92.9(1)   |
| Fe(1)-O(1) | 1.913(2)     | N(3)-Fe(1)-N(4) | 76.4(1)   |
| Fe(1)-O(2) | 1.915(2)     | N(1)-Fe(1)-O(2) | 90.5(1)   |
|            |              | N(2)-Fe(1)-O(1) | 87.50(9)  |
|            |              | N(2)-Fe(1)-O(2) | 102.99(9) |
|            |              | N(3)-Fe(1)-O(1) | 90.3(1)   |
|            |              | N(4)-Fe(1)-O(1) | 97.16(9)  |
|            |              | N(4)-Fe(1)-O(2) | 87.16(9)  |
|            |              | O(1)-Fe(1)-O(2) | 96.1(1)   |
|            |              | N(2)-Fe(1)-N(4) | 168.37(9) |
|            |              | N(1)-Fe(1)-O(1) | 164.09(1) |
|            |              | N(3)-Fe(1)-O(2) | 163.0(1)  |

(standard deviations in the last digit are quoted in parenthesis)

The expected iron pseudo-octahedral coordination geometry is shown in an ORTEP diagram of the molecular structure of **(2.12)** (**Figure 2.03**). Two anionic molecules of **(2.07)** are coordinated at three meridional positions through their donor phenolate oxygen, as well as the quinolyl and imine nitrogen atoms. Coordinate bond lengths indicate the +2 oxidation state for the metal, with Fe-N lengths greater than 2.13 Å in all cases and each Fe-O bond length is greater than 1.9 Å (**Table 2.02**). In comparison to other similar, structurally characterized, iron(III) complexes coordinated to **(2.01)**, Fe-N coordinate bond lengths are all less than 2 Å and Fe-O bond lengths are less than 1.9 Å. The absence of a perchlorate counteranion in **(2.12)** also supports the +2 iron oxidation state.<sup>[97]</sup>

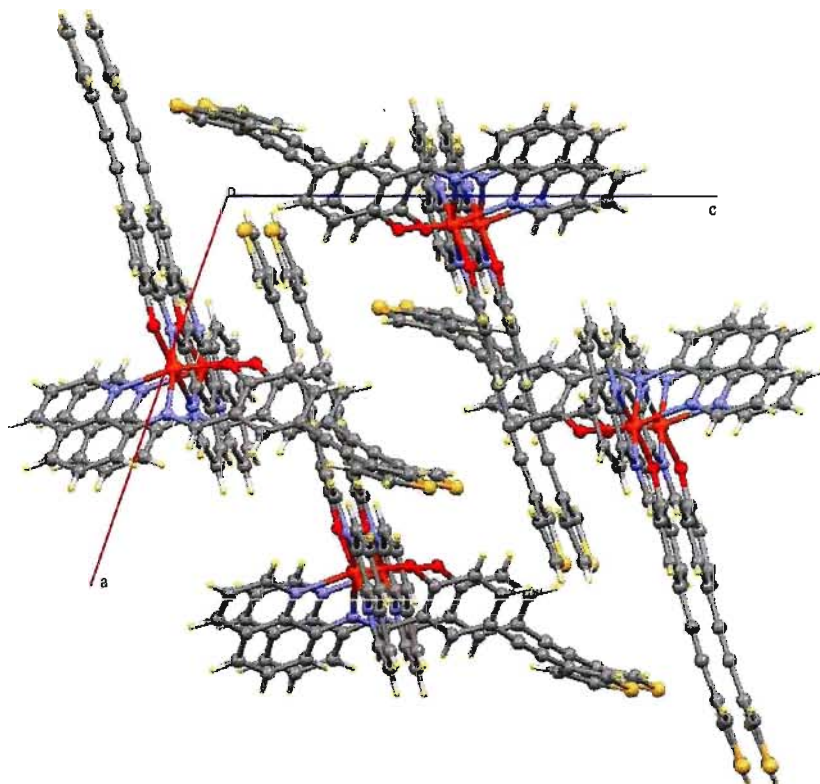


**Figure 2.04:** The packing diagram of **(2.12)**



A packing diagram of (2.12) (Figure 2.04) highlights a  $\pi$ - $\pi$  interaction between a quinolyl ring fragment from one molecule and the ethynyl substituent of an adjacent molecule. The distance between the ethynyl triple bond and the centroids of the quinolyl ring is 3.499 Å.

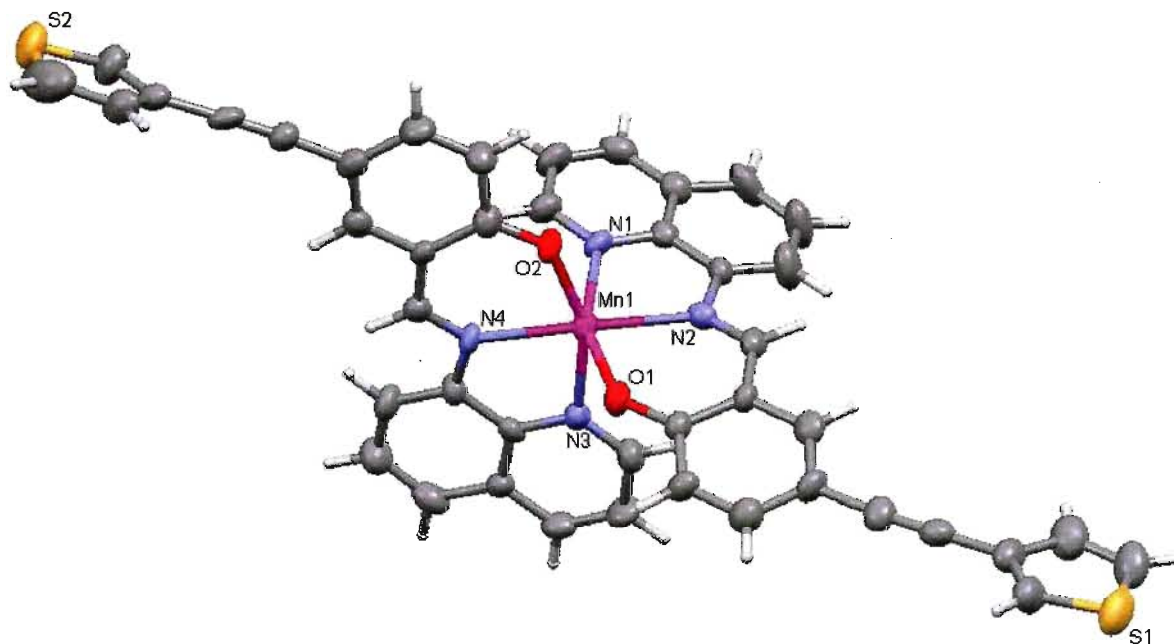


**Figure 2.05:** The molecular structure of (2.11) with ellipsoids drawn at the 50 % probability level

---

**Table 2.03:** Selected bond distances and angles for **(2.11)**

| Atoms      | Distance (Å) | Atoms           | Angle (°) |
|------------|--------------|-----------------|-----------|
| Mn(1)-N(1) | 2.283(5)     | N(1)-Mn(1)-N(2) | 72.3(2)   |
| Mn(1)-N(2) | 2.270(6)     | N(1)-Mn(1)-N(3) | 94.0(2)   |
| Mn(1)-N(3) | 2.276(5)     | N(1)-Mn(1)-N(4) | 91.1(2)   |
| Mn(1)-N(4) | 2.254(6)     | N(2)-Mn(1)-N(3) | 90.0(2)   |
| Mn(1)-O(1) | 2.087(4)     | N(3)-Mn(1)-N(4) | 73.0(2)   |
| Mn(1)-O(2) | 2.091(4)     | N(1)-Mn(1)-O(2) | 86.9(2)   |
|            |              | N(2)-Mn(1)-O(1) | 84.6(2)   |
|            |              | N(2)-Mn(1)-O(2) | 111.8(2)  |
|            |              | N(3)-Mn(1)-O(1) | 87.4(2)   |
|            |              | N(4)-Mn(1)-O(1) | 111.4(2)  |
|            |              | N(4)-Mn(1)-O(2) | 84.2(2)   |
|            |              | O(1)-Mn(1)-O(2) | 100.5(2)  |
|            |              | N(2)-Mn(1)-N(4) | 155.6(2)  |
|            |              | N(1)-Mn(1)-O(1) | 156.8(2)  |
|            |              | N(3)-Mn(1)-O(2) | 157.3(2)  |

---

(standard deviations in the last digit are quoted in parenthesis)

---

The recrystallization of **(2.11)** in a mixture of methanol and DCM generated orange crystals of the manganese(II) complex. An ORTEP diagram of the molecular structure features the same pseudo-octahedral coordination geometry for **(2.11)** (**Figure 2.05**) as found for the iron complex **(2.12)**. In **(2.11)**, two molecules of **(2.07)** are coordinated at the three meridional positions through the oxygen and two nitrogen atoms. The Mn-N coordinate bond lengths are within the range of 2.25-2.28 Å and the Mn-O bond lengths are both around 2.09 Å. The O-Mn-O bond angle of 100.5° in **(2.11)** is comparable to the 95.9° O-Fe-O angle of **(2.12)** and demonstrates the structural similarity between the iron and manganese qsal complexes (**Table 2.03**).

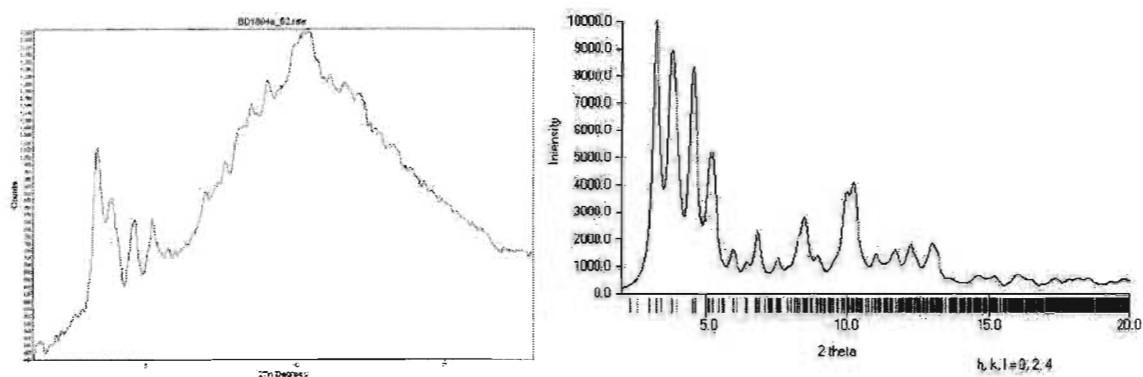


**Figure 2.06:** The X-ray powder diffraction pattern of (2.09)<sup>[111]</sup>

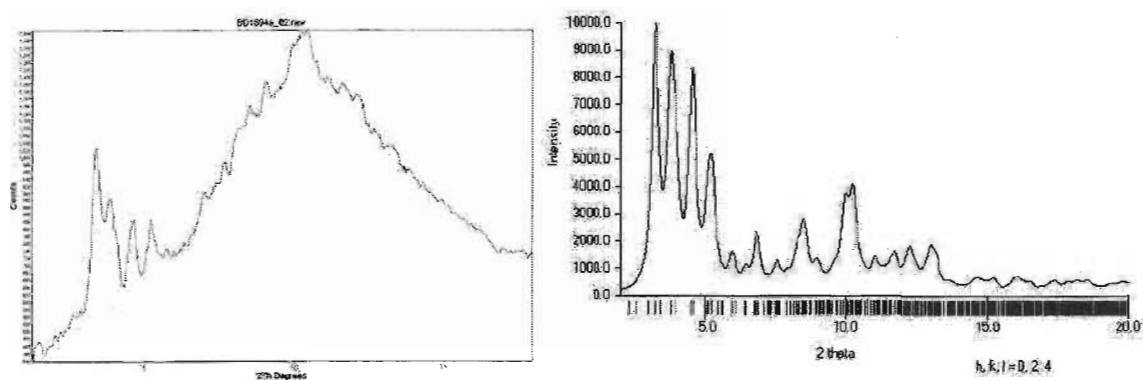


**Figure 2.07:** The calculated powder diffraction pattern of (2.11)<sup>[111]</sup>

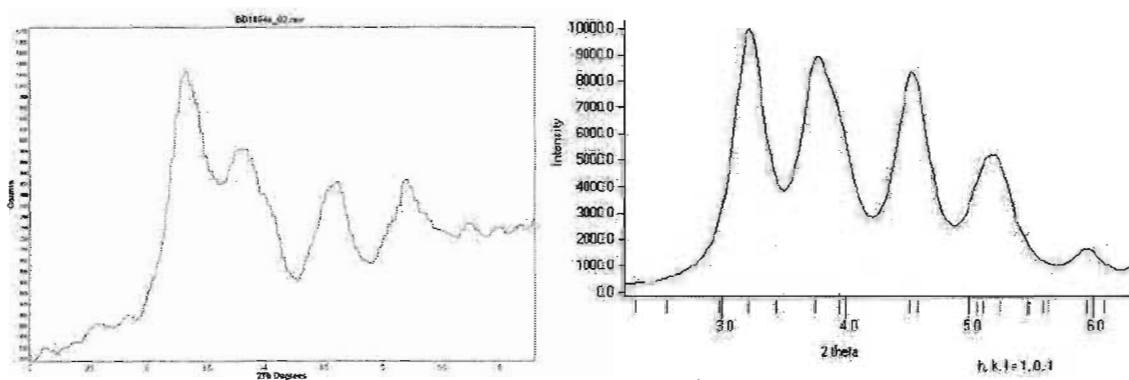


**Figure 2.08:** A low angle comparison between (2.09) and (2.11)<sup>[111]</sup>

We attempted to obtain X-ray powder diffraction patterns to further examine the structural properties of complexes (2.08) - (2.10). Complex (2.08) was not sufficiently crystalline to provide us with a diffraction profile. However, data was acquired for a poorly crystalline sample of (2.09) (Figure 2.06). The low angle powder data for (2.09) matches well with the calculated powder profile for (2.11) and suggests that these complexes may share similar structural properties (Figures 2.07 - 2.08).

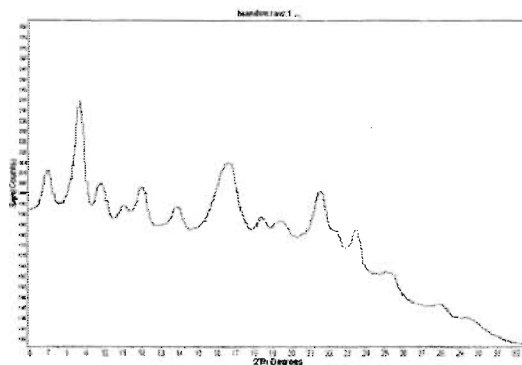


**Figure 2.09:** The X-ray powder diffraction pattern of (2.10)<sup>[111]</sup>

The profile obtained from polycrystalline (2.10) (Figure 2.09) is substantially different from both the calculated pattern of (2.11) and the observed pattern of (2.09) and does not allow us to draw any relationships regarding the structural properties of this material.

v) Magnetic characterization

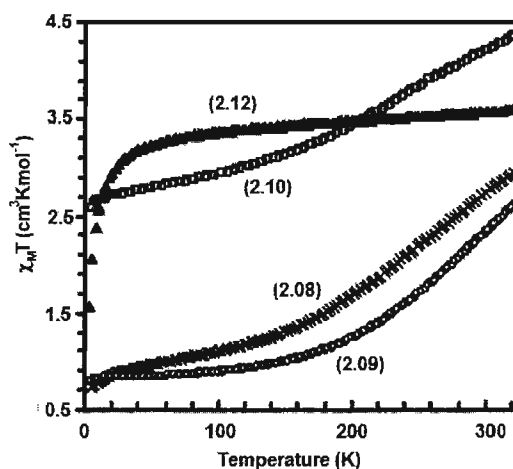


**Figure 2.10:** Variable temperature magnetic susceptibility measurements for complexes **(2.08)** - **(2.10)** in a 5000 Oe magnetic field<sup>[111]</sup>

Magnetic susceptibility measurements were carried out with a SQUID magnetometer over the temperature range 2.5 K - 325 K for complexes **(2.08)** - **(2.09)** and 5.0 K - 325 K for complex **(2.10)** and are displayed as plots of  $\chi_M T$  versus  $T$  (**Figure 2.10**). For complexes **(2.08)** and **(2.10)**, spin-crossover from an  $S = 5/2$  to an  $S = 1/2$  state is indicated by the decrease in  $\chi_M T$  with decreasing temperature. The observed values of  $\chi_M T$  for complexes **(2.08)** and **(2.10)** at 325 K (respectively 2.89 and 2.66 cm<sup>3</sup>molK<sup>-1</sup>) are less than the expected spin-only values for pseudo-octahedrally coordinated high-spin iron(III) (4.34 cm<sup>3</sup>molK<sup>-1</sup>), which is possibly due to some proportion of the low-spin component present at this temperature. As the temperature is decreased, a concomitant decrease in  $\chi_M T$  is observed. The temperature is then raised from the lowest point of measurement and the  $\chi_M T$  values observed are virtually identical to those recorded during the initial cooling. The profile of these data indicate that the spin-crossover in complexes **(2.08)** and **(2.10)** are best described as a gradual transition without thermal hysteresis,

which is typical for iron(III) complexes. At the lowest temperature of measurement 2.5 K (or 5 K for **(2.10)**)  $\chi_M T$  values of 0.74 and 0.79 cm<sup>3</sup>molK<sup>-1</sup>, for complexes **(2.08)** and **(2.10)** respectively, are a little higher than the anticipated value for low-spin iron(III) (0.375 cm<sup>3</sup>molK<sup>-1</sup>) but are comparable to related iron(III) complexes.

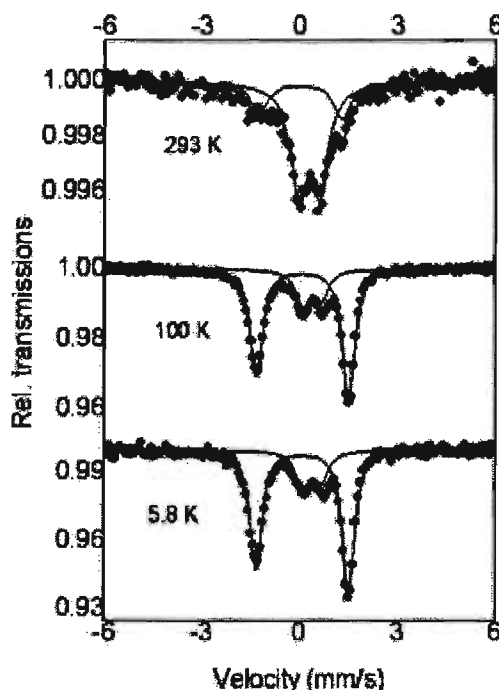


**Figure 2.11:** The Mössbauer spectra for complex **(2.08)** with experimental data (dots) fitted to theoretical lines<sup>[111]</sup>

Mössbauer spectra (**Figure 2.11**) for complex **(2.08)**, recorded at 293, 100, and 5.8 K, mirrors the variable temperature magnetic susceptibility data. At 293 K two sets of doublets with distinct quadrupole splittings (QS) are observed, which are typical for iron(III) complexes that exhibit gradual spin-crossover. The inner doublet with QS of 0.66 mm/s and an IS of 0.41 mm/s is assigned the high-spin isomer. The outer doublet with a QS of 2.56 mm/s and IS of 0.14 mm/s, is assigned to the low-spin isomer. The intensity of the inner doublet decreases with decreasing temperature, while a concomitant

increase in the intensity of the outer doublet occurs. At 100 K the outer doublet becomes the dominant absorption and the intensity ratio of the inner and outer doublets changes very little with further decreases in temperature. The QS for the outer doublet, at 5 K, is 2.849 mm/s and is consistent with low-spin iron(III).

Complex **(2.09)** has different variable temperature magnetic properties when compared to **(2.08)** or **(2.10)**. Although the profile of the data for **(2.09)** is typical for iron(III) spin-crossover complexes and is similar to the profiles of **(2.08)** and **(2.10)**, the  $\chi_M T$  values are anomalously higher (**Figure 2.10**). During the data acquisition, the experiments to obtain values for **(2.09)** were run very slowly to ensure thermal equilibrium at each point of measurement (data was collected in triplicate and from two independently prepared batches of the complex). The data obtained in all cases were very similar, the  $\chi_M T$  values decreased gradually between 325 and 5 K. At 325 K, the  $\chi_M T$  value ( $4.37 \text{ cm}^3 \text{ mol K}^{-1}$ ) for **(2.09)** is consistent with high-spin iron(III) and is higher than the values observed for **(2.08)** or **(2.10)**.

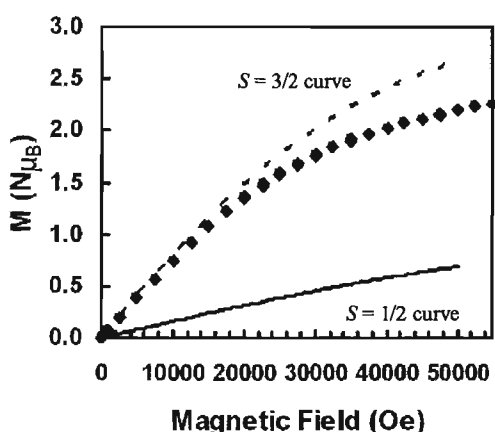


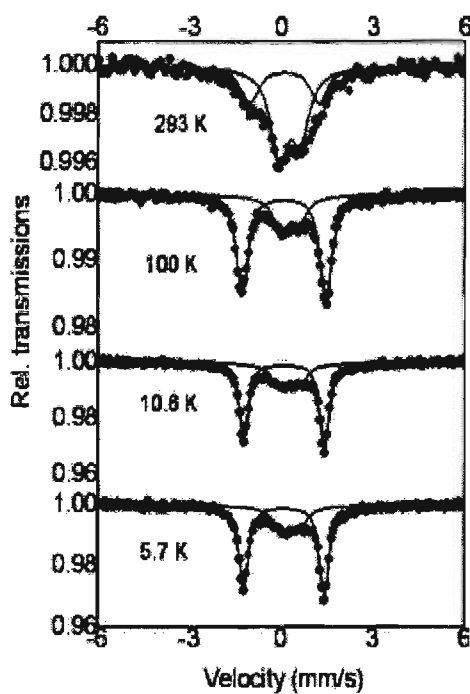
**Figure 2.12:** Reduced magnetization versus field data for **(2.09)** (large black dots) recorded at 5 K between theoretical curves<sup>[11]</sup>

There is a very slight increase in  $\chi_M T$  between 13 and 10 K, and magnetization versus field experiments at 5 K indicated no magnetic ordering for (2.09), ruling out the possibility of a magnetic phase transition. The magnetization versus field data for (2.09) is shown in **Figure 2.12** and plotted between dotted and solid lines that represent theoretical  $S = 3/2$  and  $S = 1/2$  respectively. The value of  $M_{sat}$  at 5.5 T (5 K) approaches  $2.3 \text{ N}\mu_B$ , which is significantly higher than the expected value for low-spin iron(III) ( $0.69 \text{ N}\mu_B$ ) and is closer to the expected value for an  $S = 3/2$  *intermediate* state ( $2.67 \text{ N}\mu_B$ ). Below 10 K,  $\chi_M T$  continues to slowly decrease to a final value of  $2.58 \text{ cm}^3 \text{ molK}^{-1}$  at 5 K, which is higher than the  $\chi_M T$  values observed for (2.08) and (2.10) at similar temperatures and is, again, much closer to the anticipated value for an  $S = 3/2$  state ( $1.87 \text{ cm}^3 \text{ molK}^{-1}$ ) than an  $S = 1/2$  state. Thus, the variable temperature magnetic susceptibility data obtained from (2.09) suggests a thermally induced spin-crossover to an intermediate  $S = 3/2$  state. An  $S = 3/2$  state can occur if the energy levels of the orbitals are non-degenerate and the occupancy of four orbitals requires less energy than the pairing energy while the fifth has a  $\Delta_o$  splitting large enough to cause the pairing of one electron.



**Table 2.04:** Mössbauer data for **(2.08)** and **(2.09)**

| Compound      | Temperature (°C) | IS (mm/s) | QS (mm/s) | Site (%) | Fe(III) Spin State |
|---------------|------------------|-----------|-----------|----------|--------------------|
| <b>(2.08)</b> | 293              | 0.41(1)   | 0.66(2)   | 73.6     | 5/2                |
|               |                  | 0.14(2)   | 2.56(4)   | 26.4     | 1/2                |
|               | 100              | 0.50(1)   | 0.61(2)   | 24.7     | 5/2                |
|               |                  | 0.200(1)  | 2.837(3)  | 75.3     | 1/2                |
|               | 5.8              | 0.51(1)   | 0.58(2)   | 23.0     | 5/2                |
|               |                  | 0.201(2)  | 2.849(7)  | 77.0     | 1/2                |
| <b>(2.09)</b> | 293              | 0.38(1)   | 0.69(2)   | 66.5     | 5/2                |
|               |                  | 0.19(2)   | 2.28(4)   | 33.5     | 3/2                |
|               | 100              | 0.40(1)   | 0.61(2)   | 27.0     | 5/2                |
|               |                  | 0.203(2)  | 2.76(1)   | 73.0     | 3/2                |
|               | 10.6             | 0.37(1)   | 0.66(2)   | 30.5     | 5/2                |
|               |                  | 0.205(2)  | 2.649(3)  | 69.5     | 3/2                |
|               | 5.7              | 0.41(2)   | 0.60(2)   | 29.3     | 5/2                |
|               |                  | 0.210(2)  | 2.649(4)  | 70.7     | 3/2                |

**Figure 2.13:** Mössbauer spectra for complex **(2.09)** with experimental data (dots) fitted to theoretical lines<sup>[111]</sup>

In an attempt to help us understand this unusual magnetic behaviour and to confirm the unusual  $S = 5/2$  to  $S = 3/2$  crossover in **(2.09)** Mössbauer spectra were recorded on a freshly prepared sample at a variety of temperatures (**Table 2.04**, **Figure 2.13**). The Mössbauer data collected for complex **(2.09)** at 293 K indicate that there is a mixture of spin isomers, as in the data collected for complex **(2.08)**. The high-spin isomer of **(2.09)** is dominant at 293 K, displaying QS and IS values that are consistent with  $S = 5/2$  iron(III) (**Table 2.04**). As the temperature is lowered from 293 to 100 K, the intensity of the inner doublet decreases and the intensity of the outer doublet increases, which is similar to the observations made with **(2.08)** and suggests that a thermally induced spin-crossover is operative in **(2.09)**. At the lowest temperature of measurement (5.7 K), the QS value measured for the outer doublet (2.649 mm/s) of **(2.09)** is much smaller than the QS observed for **(2.08)** at the same temperature, which was ascribed to low-spin ( $S = 1/2$ ) iron(III) in **(2.08)** in conjunction with variable temperature magnetic susceptibility results.

Although the iron(III)  $S = 3/2$  spin state is quite rare, a similar observation was made by Neva *et al.* during Mössbauer studies on an azide-substituted iron(III) porphyrin complex. The QS of 2.649 mm/s observed for **(2.08)** is consistent with the  $S = 3/2$  state observed in Neva's azide complex.<sup>[112-113]</sup> Other iron(III) porphyrin complexes that reportedly exhibit an intermediate spin state typically exhibit QS values that are greater than 3 mm/s.<sup>[114]</sup> However, from a structural and electronic perspective, complex **(2.09)** is significantly different from iron(III) porphyrin complexes, and we have no reason to assume that the Mössbauer properties of **(2.09)** will be similar. Also of note, the feature

described in the  $\chi_M T$  profile of (2.09) at approximately 10 K is mirrored in the Mössbauer spectrum at 10.6 K. Relative to the spectrum taken at 100 K, the intensity of the outer doublet decreases slightly between 10.6 and 5.7 K, with a small increase in the intensity of the inner doublet. We cannot rule out the possibility of a structural phase transition in the very low temperature regime, which results in a slight increase of the high-spin isomer population. However, this feature does not detract from the clear observation of a thermally induced spin-crossover operative in (2.09).

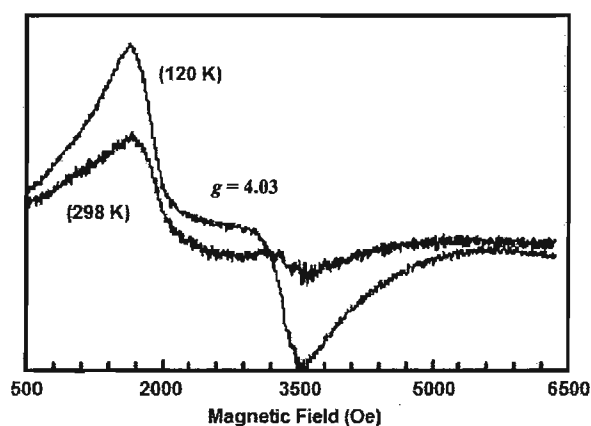


Figure 2.14: A powder ESR spectra of (2.09) at 298 and 120 K<sup>[111]</sup>

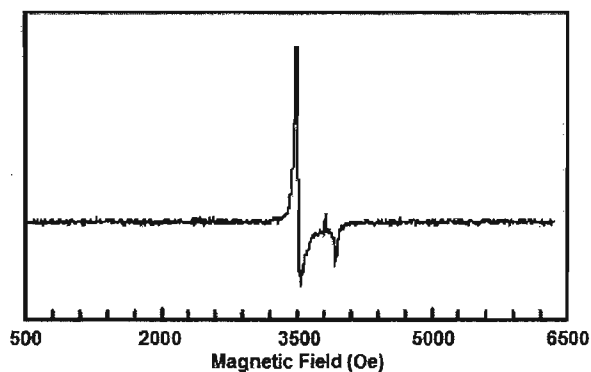


Figure 2.15: A powder ESR spectra of (2.10) at 120 K<sup>[111]</sup>

The transition between  $S = 3/2$  and  $5/2$  states in iron(III) porphyrin complexes has been observed by Ohgo through low temperature ESR studies.<sup>[115]</sup> Currently, there are no other reported examples of non-porphyrin iron(III) complexes that display a thermal equilibrium between  $S = 5/2$  and  $S = 3/2$  states. However, as with the iron(III) porphyrin complexes, ESR spectroscopy provided clear and unambiguous confirmation of the  $S = 3/2$  state on powdered samples of **(2.09)** at 298 K and 120 K (**Figure 2.14**). A resonance at  $g = 4.03$  is observed at 298 K, which is characteristic for  $S = 3/2$  systems. As the temperature is decreased, the intensity of the  $g = 4.03$  resonance increases, suggesting, in accordance with the data from variable temperature magnetic susceptibility experiments, that the proposed  $S = 5/2$  to  $S = 3/2$  crossover is a thermal equilibrium, with a distinct  $S = 3/2$  state dominant at low temperature. For comparison purposes, we ran an ESR experiment with complex **(2.10)** at 298 K but could not obtain a spectrum (**Figure 2.15**). At 120 K, however, a spectrum is observed from **(2.10)**, which is typical for  $S = 1/2$  systems, with no indication of a  $g \sim 4$  resonance, indicating that the iron(III) ion is in the low-spin state. Taken together, the data from variable temperature magnetic, Mössbauer and ESR measurements, provide strong evidence that a very unusual  $S = 5/2$  to  $S = 3/2$  crossover is operative in **(2.09)**.

Complex **(2.12)** features iron(II) in the high-spin state,  $\chi_M T = 3.60 \text{ cm}^3 \text{ mol K}^{-1}$  at 325 K, and no significant temperature dependence or solid-state spin-crossover is evident from the magnetic data for temperatures above 50 K (**Figure 2.10**).  $\chi_M T$  begins to drop sharply below 50 K, however, likely resulting from a combination of zero-field splitting

(ZFS) of the high-spin state and weak intermolecular antiferromagnetic interactions through close intermolecular  $\pi$ - $\pi$  contacts observed in the crystal packing of **(2.12)**.

vi) Electronic absorption spectroscopy

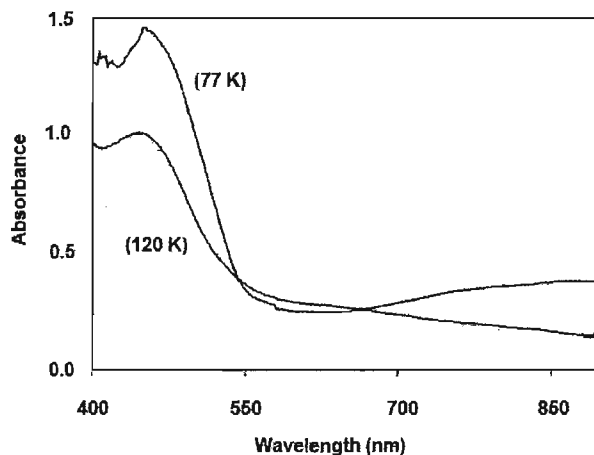


**Figure 2.16:** The variable temperature absorbance profile of **(2.09)**<sup>[111]</sup>

In the visible region of the spectrum at 298 K, solutions of ligand **(2.07)**H in DCM exhibit an absorbance maximum at 500 nm, ( $\epsilon$ ) = 285 M<sup>-1</sup>cm<sup>-1</sup>, resulting from an intraligand charge transfer absorption (ILCT). At room temperature, darkly coloured ethanol solutions of complexes **(2.08)** - **(2.10)** each exhibit LMCT bands at approximately 450 nm, ( $\epsilon$ ) = 4100 M<sup>-1</sup>cm<sup>-1</sup> for **(2.10)**. Cooling ethanol solutions of **(2.08)** - **(2.10)** in liquid nitrogen results in changes to the physical appearance of the solutions. The absorption measurements (400 - 900 nm) at 77 K for complexes **(2.08)** - **(2.10)** were examined as ethanol glasses. As a typical example, the spectra obtained for **(2.09)** at 298 and 77 K are shown in **Figure 2.16**. For each complex, a dramatic increase in absorbance of the LMCT band is observed at lower temperatures, along with the appearance of a new broad absorption centred at approximately 850 nm.

vii) Electrochemistry

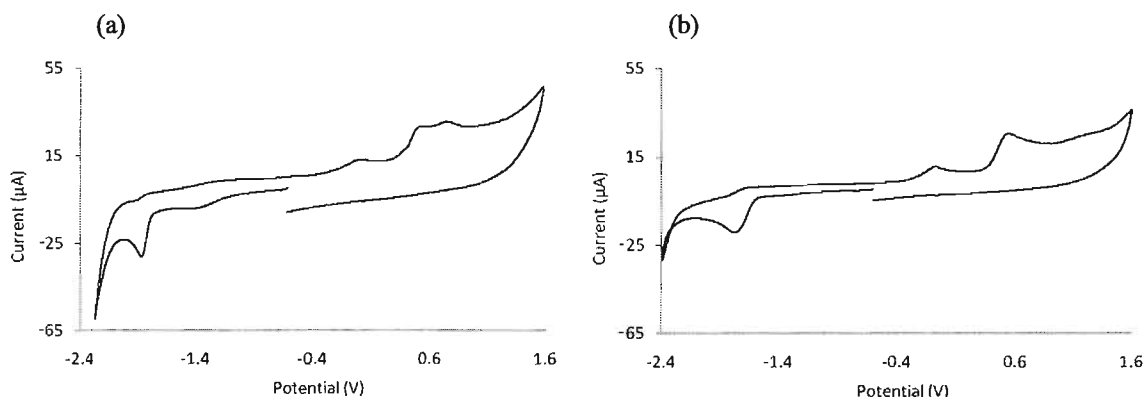


**Figure 2.17:** Cyclic voltammograms of (a) (2.01)H and (b) (2.07)H

**Table 2.05:** Electrochemical data for (2.01)H and (2.07)H in DCM

| Compound | $E^{\circ}_{\text{ox}}$ (V) vs. fc | $E^{\circ}_{\text{ref}}$ (V) vs. fc |
|----------|------------------------------------|-------------------------------------|
| (2.01)H  | 0, +0.6, +0.8                      | -1.8                                |
| (2.07)H  | 0, +0.6                            | -1.8                                |

(Refer to section 8.04 for experimental details)

Cyclic voltammograms of the ligand (2.07)H were obtained primarily to assess the thiophene oxidation potential (**Figure 2.17**). In a cathodic scan of (2.07)H, no reduction processes are evident until approximately -1.8 V versus ferrocene (fc). At -1.8 V an irreversible wave, likely corresponding to the reduction of the imine, is observed at a slightly more negative potential in comparison to the voltammogram of unsubstituted (2.01)H (**Figure 2.17**). An irreversible anodic process is noted at 0.0 V, which is also present in the voltammogram of (2.01)H and likely represents oxidation of the hydroxyl group. Above +0.4 V, irreversible oxidations are observed in (2.07)H, which are also

present in the profile of unsubstituted **(2.01)H**. These oxidations obscure the oxidation of the thiophene ring in **(2.07)H**, but it is observed as an irreversible feature at +1.2 V. Refer to **Table 2.05** for a complete list of redox events for **(2.01)H** and **(2.07)H**.

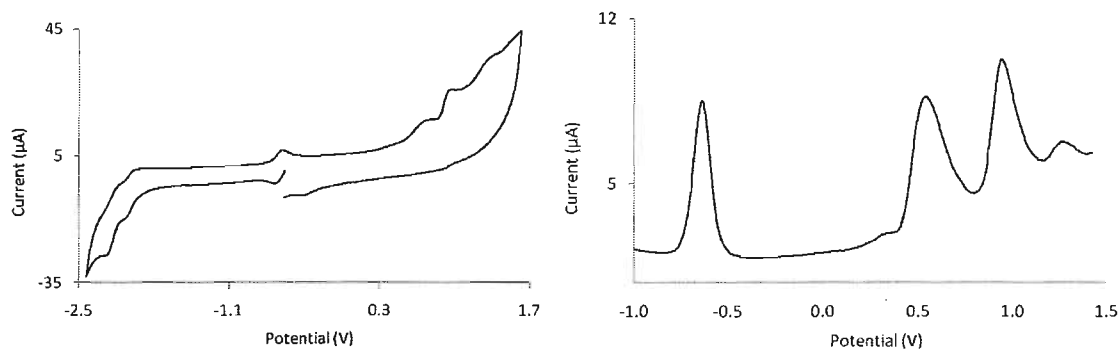


**Figure 2.18:** Cyclic (left) and differential pulse (right) voltammograms of **(2.02)**

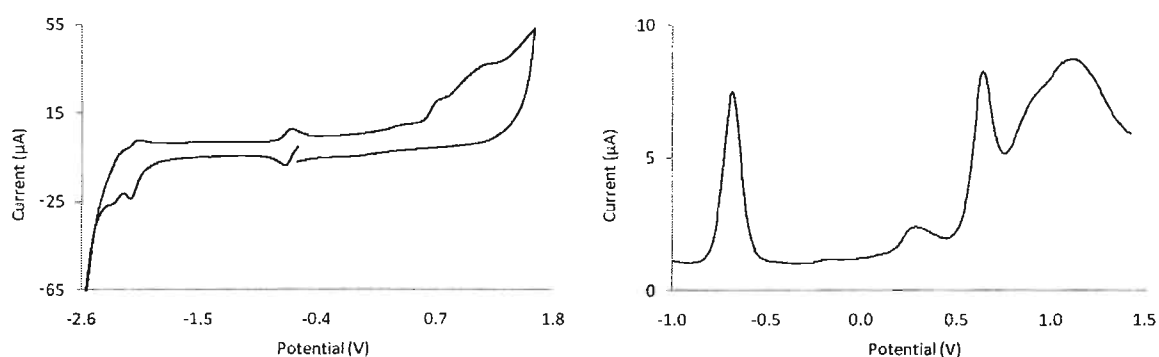


**Figure 2.19:** Cyclic (left) and differential pulse (right) voltammograms of **(2.08)**

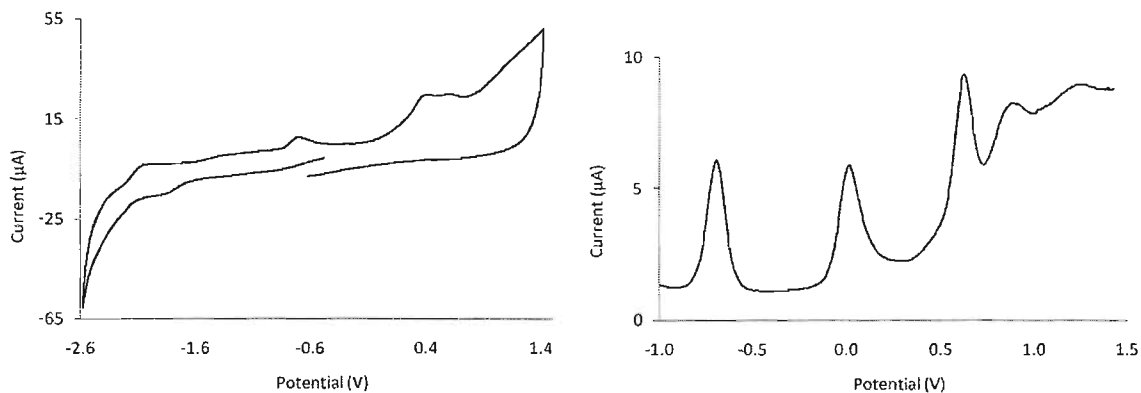


**Figure 2.20:** Cyclic (left) and differential pulse (right) voltammograms of **(2.09)**

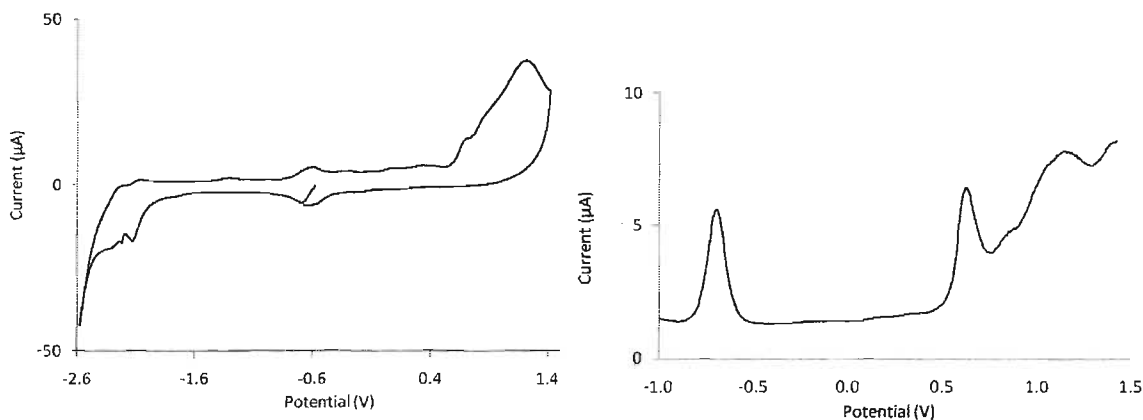


**Figure 2.21:** Cyclic (left) and differential pulse (right) voltammograms of **(2.10)**

---

**Table 2.06:** Electrochemical data for **(2.02)**, **(2.08)** – **(2.11)** in ACN

| Compound      | $E^{\circ}_{\text{ox}}$ (V) vs. fc | $E^{\circ}_{\text{red}}$ (V) vs. fc |
|---------------|------------------------------------|-------------------------------------|
| <b>(2.02)</b> | +0.7, +0.9, +1.3                   | -0.6, -2.0, -2.2                    |
| <b>(2.08)</b> | +0.7, +0.9, +1.2                   | -0.7, -2.1, -2.3                    |
| <b>(2.09)</b> | +0.3, +0.7, +0.9, +1.2             | -0.7, -1.9, -2.1                    |
| <b>(2.10)</b> | +0.7, +0.9, +1.2                   | -0.7, -2.1, -2.3                    |
| <b>(2.11)</b> | +0.3, +0.7, +0.9                   | -1.8, 2.1                           |

---

(Refer to section 8.04 for experimental details)

---

The cyclic voltammograms of the iron(III) complexes **(2.08)** - **(2.10)** are all very similar. The cathodic scan reveals a reversible  $\text{Fe}^{3+/2+}$  couple at -0.7 V (versus fc), followed by two quasi-reversible reduction processes at -2.1 and -2.3 V, (-1.9, -2.1 V for **(2.09)**) that occur as a result of reducing the imine double bonds of each coordinated ligand **(2.07)**. Over anodic potentials, irreversible features are observed at +0.7, +0.9 V, and +1.2 V that are also observed in the profile of **(2.02)** and represent oxidation of the qsal ligand components. An extra irreversible feature, centred at +0.3 V, is noted in the CV of **(2.09)**, but not in the voltammogram of **(2.02)**, **(2.08)**, or **(2.10)**, and is ascribed to a thiocyanate-



based oxidation process. For comparison, the cyclic voltammogram of KSCN in acetonitrile shows an irreversible feature at about +0.2 V. An effort to resolve the anodic waves was attempted by using differential pulse voltammetry over a potential of -1.0 V to +1.5 V. In this region, the differential pulse voltammogram (DPV) of **(2.02)** exhibits four broad waves, corresponding to the reduction and oxidation events present in the CV (**Figure 2.18**). In the DPVs of complexes **(2.08)** - **(2.10)** four waves are also noted over this same region, plus one additional wave for the  $\text{SCN}^-$  component of **(2.09)** (**Figures 2.19 - 2.21**). The key difference between **(2.08)** - **(2.10)** and **(2.02)** is found in the anodic wave centred at +1.2 V. The peak at +1.2 V is much broader for **(2.08)** - **(2.10)** because the thiophene ring oxidation falls within this regime, overlapping with the qsal oxidations. Repeated cycling between 0 and 1.5 V for solutions of **(2.08)** - **(2.10)** did not result in electropolymerization as indicated by the absence of an electroactive film deposited on the working electrode following the experiment.

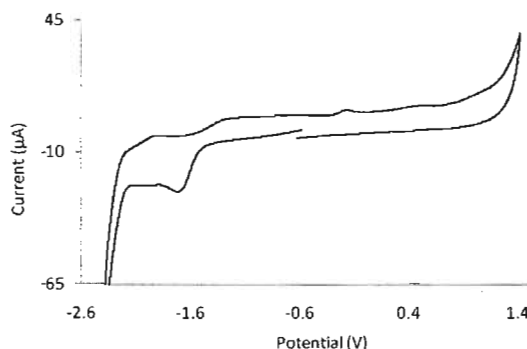


**Figure 2.22:** Cyclic voltammogram of complex **(2.11)**

The cyclic voltammogram of the manganese(II) complex **(2.11)** is similar to the iron(III) complexes (**Figure 2.22**). The cathodic scan reveals a two quasi-reversible reduction processes beyond -1.6 V that occur as a result of reducing the imine double bonds of each

coordinated ligand **(2.07)**. Over anodic potentials, the complex reveals a quasi-reversible oxidation event at 0.33 V, characteristic of the  $\text{Mn}^{2+/3+}$  redox couple.<sup>[116]</sup> The ligand based oxidations were broad and observed at potentials above +0.5 V. Refer to **Table 2.06** for a complete list of redox events for **(2.02)**, **(2.08)** – **(2.11)**.

#### vii) Summary

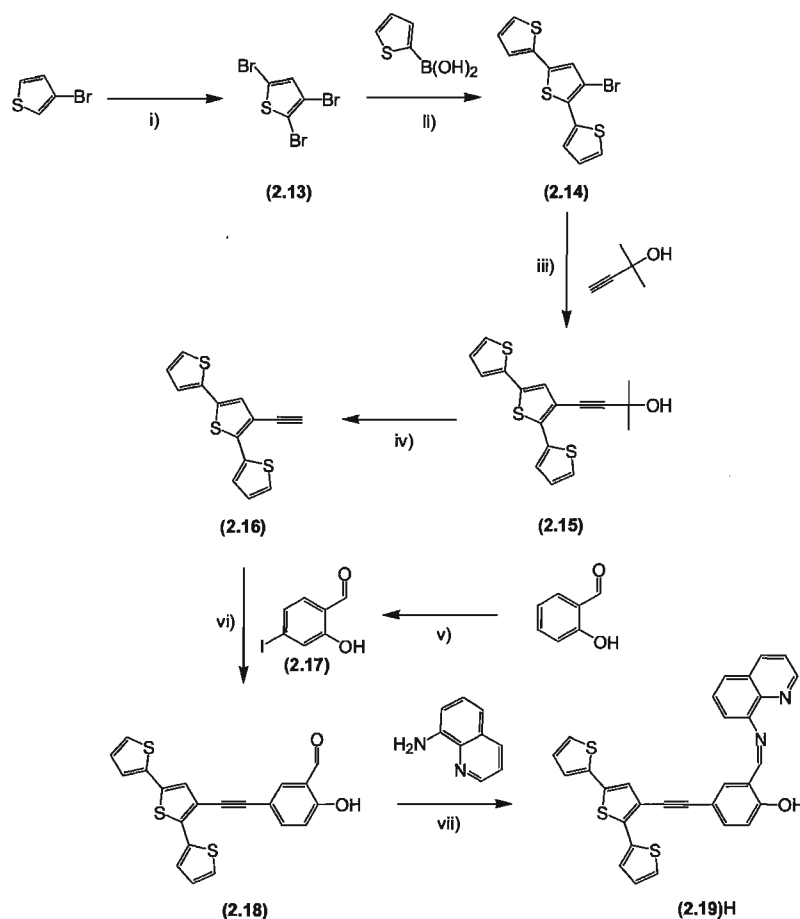
The results have demonstrated that 3-ethynylthienyl substitution of ligand **(2.01)** is compatible with the iron complexes because their spin-crossover properties are maintained. However, complexes **(2.08)** – **(2.10)** did not undergo electropolymerization, likely because of the high, irreversible thiophene oxidation potential and steric bulk of the  $[\text{Fe}(\text{qsal})_2]^+$  substituent. Further efforts to lower the oxidation potential of the polymerizable component (while also reducing steric congestion) are required to make qsal-type ligands containing substituents more amenable to electropolymerization reactions.

## 2.05 Terthienyl-substituted qsal complexes<sup>†</sup>

### i) Extending the conjugation

An important prerequisite for electropolymerization of many metal-containing monomers is a relatively low oxidation potential, which may be achieved by incorporating longer polymerizable groups with extended conjugation or by using electron-donating substituents. Lower oxidation potentials allow for polymerization without significant decomposition or competing side-reactions that can occur at higher potentials. Longer polymerizable groups also reduce steric interactions between bulky metal centres, which may prevent efficient coupling of monomers. In this regard our next synthetic target included a terthiophene substituted variation of complex **(2.08)** to assist in our efforts towards polymerization.<sup>[117]</sup>

## ii) Ligand synthesis



Reagents and conditions: (i)  $\text{Br}_2$ , 48 %  $\text{HBr}_{(\text{aq})}$   $\text{Et}_2\text{O}$  35 °C, 3 h. (ii) 2-thiopheneboronic acid, DME,  $\text{H}_2\text{O}$ , 10 mol %  $\text{PdCl}_2(\text{PPh}_3)_2$ ,  $\text{K}_2\text{CO}_3$ , 100 °C, 3 d. (iii) 2-methyl-but-3-yn-2-ol, (i-Pr) $_2\text{NH}$ , 3 mol %  $\text{PdCl}_2(\text{PPh}_3)_2$ , 3 mol %  $\text{CuI}$ , 84 °C, 24 h. (iv) MeOH, Toluene, KOH, 6 d. (v)  $\text{ICl}$ , THF. (vi) 5-iodosalicylaldehyde, THF, TEA, 3 mol %  $\text{PPh}_3$ , 3 mol %  $\text{PdCl}_2(\text{PPh}_3)_2$ , 5 mol %  $\text{CuI}$ , 65 °C, 5 d. (vii) 8-aminoquinoline,  $\text{CHCl}_3$ .

**Scheme 2.06:** The synthesis of (**2.19**)H

The terthienyl-substituted qsalH ligand was prepared in a seven step convergent synthesis from the commercially available reagents 3-bromothiophene and salicylic acid (**Scheme 2.06**). 3-bromothiophene was reacted with bromine in the 2 and 5 positions, affording the precursor (**2.13**), which was used in a Suzuki cross-coupling reaction with 2-thiophene boronic acid producing (**2.14**). A Sonogashira coupling between the

terthiophene derivative and 3-methyl-3-buten-2-ol provided **(2.15)**, a terthiophene compound with a protected ethynyl group, which was then deprotected by refluxing in the presence of base giving **(2.16)**. At the same time, 5-iodosalicylaldehyde **(2.17)** was prepared by reacting iodine monochloride with salicylaldehyde and then used immediately in another Sonogashira reaction with the deprotected ethynyl group of **(2.16)**. The resulting aldehyde precursor **(2.18)** was then condensed with 8-aminoquinoline to yield the modified qsalH ligand **(2.19)H** as a crimson oil, which was hydrolytically unstable in solution.

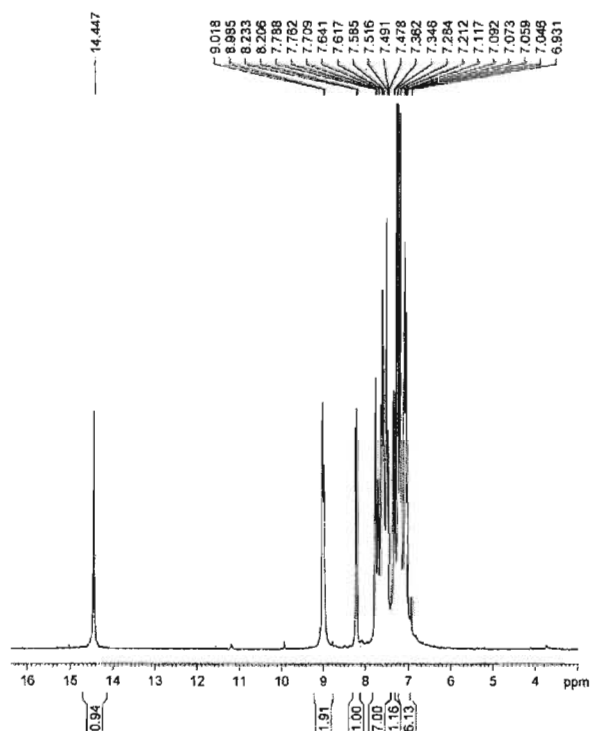
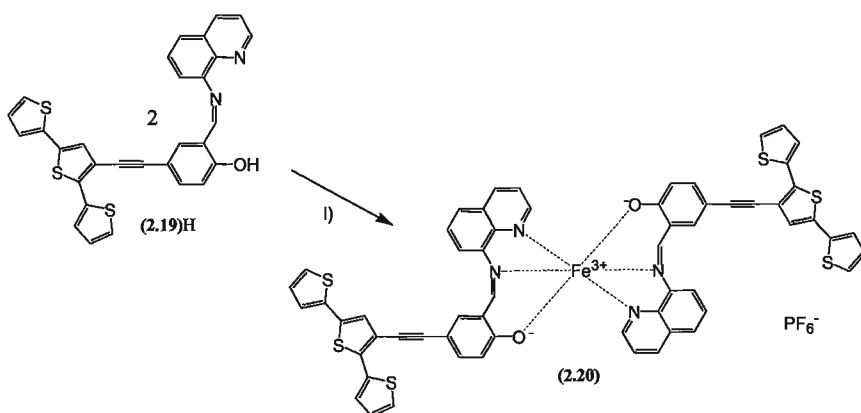


**Figure 2.23:**  $^1\text{H}$ -NMR spectrum of **(2.19)H** in  $\text{CDCl}_3$

Ligand **(2.19)H** has been fully characterized and has notably similar spectroscopic properties in comparison to **(2.07)H**. In the  $^1\text{H}$ -NMR spectrum of **(2.19)H** (Figure 2.23), the peak attributed to the hydroxyl proton at 14.45 ppm is shifted downfield relative to

the hydroxyl proton resonance at 11.19 ppm in the aldehyde precursor **(2.18)**. A peak found at 9.00 ppm is characteristic of the imine proton when compared to the imine singlet at 8.95 ppm observed for **(2.01)H**. Sixteen additional peaks are found in the aromatic region of the spectrum and are consistent with the expected resonances of the seven terthienyl, three salicyl and six quinoline protons. The imine C=N stretch is also observed in the FT-IR spectrum at  $1618\text{ cm}^{-1}$ .

### iii) Coordination chemistry

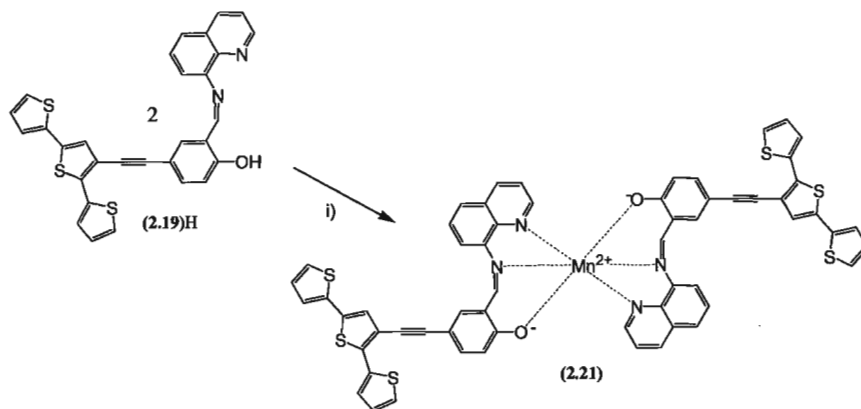


Reagents and conditions: (i)  $\text{FeCl}_3 \cdot 6\text{H}_2\text{O}$ ,  $\text{NaPF}_6$ ,  $\text{MeOH}$ ,  $\text{H}_2\text{O}$ .

**Scheme 2.07:** The synthesis of **(2.20)**

A homoleptic coordination complex was generated by reacting 2 equivalents of **(2.19)H** with hydrated iron(III) chloride, followed by metathesis with an aqueous solution containing an excess of  $\text{NaPF}_6$  to afford a green precipitate of the  $\text{PF}_6^-$  salt **(2.20)** containing the  $[\text{Fe}(\text{2.19})_2]^+$  cation (**Scheme 2.07**). The complex was analytically pure, producing an ESI mass spectrum with a dominant peak corresponding to the  $[\text{Fe}(\text{2.19})_2]^+$  cation. The FT-IR spectrum for complex **(2.20)** displays characteristic absorptions

including vibrations of the anionic  $\text{PF}_6^-$  component and a slight shift in the C=N stretching frequency to  $1603\text{ cm}^{-1}$  indicating the coordination of **(2.19)** to the iron(III) cation.



Reagents and conditions: (i)  $\text{Mn}(\text{C}_2\text{H}_3\text{O}_2)_2 \cdot 4\text{H}_2\text{O}$ , MeOH.

**Scheme 2.08:** The synthesis of **(2.21)**

A closely related homoleptic manganese(II) complex **(2.21)** was generated in an analogous procedure to the iron containing species so that we could further probe the magnetic and electronic properties of our models. Two equivalents of **(2.19)H** were combined with hydrated manganese(II) acetate to afford the neutral  $[\text{Mn}(\text{2.19})_2]$  complex as an orange solid (**Scheme 2.08**). The complex produced an ESI mass spectrum, with a peak corresponding to the  $[\text{Mn}(\text{2.19})_2]^+$  cation. The FT-IR spectrum of complex **(2.21)** is also very similar to **(2.20)**, with a nearly identical C=N stretching frequency ( $\sim 4\text{ cm}^{-1}$  higher). Previous studies on complex **(2.11)** confirmed that manganese(II) was non-spin-crossover when coordinated to the  $\text{N}_4\text{O}_2$  donor set of the qsal ligands, and would therefore be useful in preparing non-spin-crossover analogues of polymers generated from **(2.20)**.

iv) Magnetic characterization

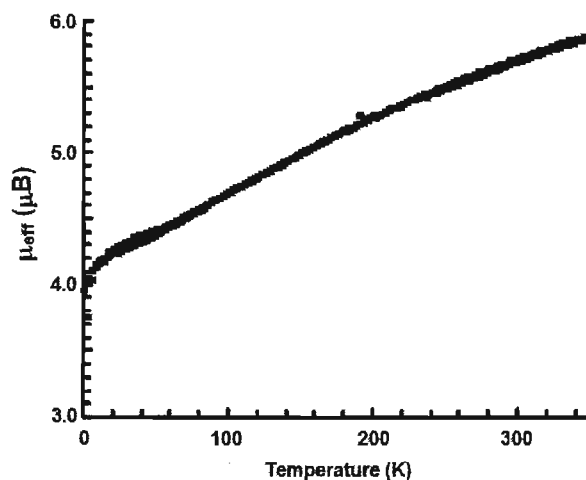


**Figure 2.24:** The magnetic profile of (2.20) in a 5000 Oe magnetic field<sup>[118]</sup>

Magnetic susceptibility measurements were carried out with a SQUID magnetometer over the temperature range 2 - 350 K for complex (2.20) and are displayed as a plot of magnetic moment ( $\mu_{\text{eff}}$ ) versus temperature (Figure 2.24). The observed value of  $\mu_{\text{eff}}$  for complex (2.20) at 350 K is 5.9  $\mu_B$  and is in good agreement with the expected value for one pseudo-octahedrally coordinated high-spin iron(III) ion. Spin-crossover from an  $S = 5/2$  to an  $S = 1/2$  state is indicated by the decrease in moment with decreasing temperature. As the temperature is raised from the lowest temperature measurement, the  $\mu_{\text{eff}}$  values observed are identical to those recorded during the initial cooling. The profile of these data indicates a typical iron(III) spin-crossover in complex (2.20) with a gradual transition without thermal hysteresis. At the lowest temperature of measurement, 2.0 K, a  $\mu_{\text{eff}}$  of 3.7  $\mu_B$  is observed, which is higher than the anticipated value (1.73  $\mu_B$ ) for low spin iron(III) and suggests some proportion of high-spin component is still present at this temperature.

v) Electrochemistry



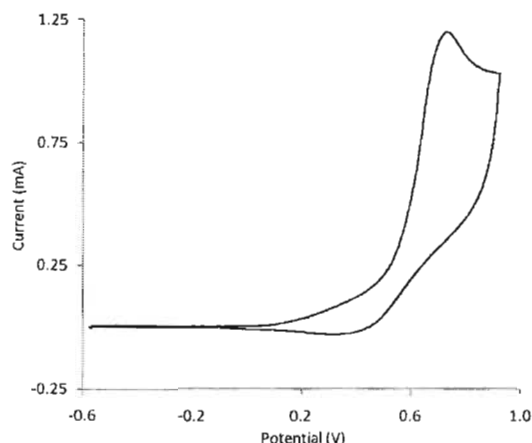


**Figure 2.25:** Cyclic voltammogram of the ligand **(2.19)**

---

**Table 2.07:** Electrochemical data for **(2.19)H** in DCM and **(2.20)** - **(2.21)** in ACN

| Compound       | $E^{\circ}_{\text{ox}}$ (V) vs. fc | $E^{\circ}_{\text{red}}$ (V) vs. fc |
|----------------|------------------------------------|-------------------------------------|
| <b>(2.19)H</b> | +0.7                               | -                                   |
| <b>(2.20)</b>  | +0.4, +0.5, +0.8, +1.1, +1.2       | -0.7, -2.1 -2.3                     |
| <b>(2.21)</b>  | +0.3, +0.6, +1.2                   | -1.3, -2.0                          |

---

(Refer to section 8.04 for experimental details)

---

Cyclic voltammograms of the ligand **(2.19)H** and complexes **(2.20)** – **(2.21)** were obtained to assess their suitability for electrochemical polymerization. The cyclic voltammogram of **(2.19)H** reveals a quasi-reversible peak centred around +0.7 V (versus fc) assigned to oxidation of the terthienyl substituent (**Figure 2.25**). Ligand **(2.07)H**, our first thiophene bearing qsal ligand, had an irreversible oxidation at higher potential indicating that this ligand and complexes made from it may be more suitable for electropolymerization.

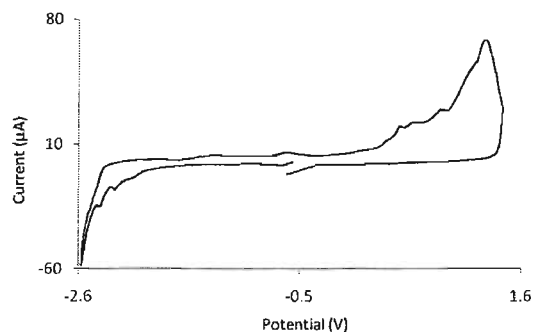


**Figure 2.26:** Cyclic voltammogram of complex (2.20)

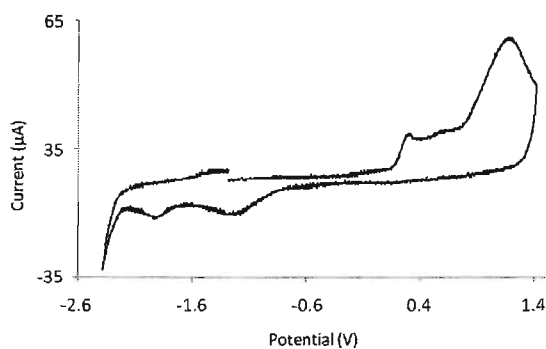


**Figure 2.27:** Cyclic voltammogram of complex (2.21)

The cyclic voltammogram of the iron(III) complex (2.20) reveals a reversible  $\text{Fe}^{3+/2+}$  couple at -0.6 V in the cathodic scan followed by two quasi-reversible reduction processes after -2.0 V that occur as a result of reducing the imine double bonds of each coordinated ligand (2.19) (Figure 2.26). Over anodic potentials, broad and quasi-reversible features above +0.4 V are assigned to oxidation of the terthienyl substituent. Beyond +0.7 broad irreversible oxidations occur, representing the oxidation of the qsal ligand components. The cathodic scan of the manganese complex (2.21) shows two quasi-reversible reduction events are present that are similar to the monothienyl manganese complex (2.21) (Figure 2.27). The anodic scan of the manganese(II) complex (2.21) reveals a quasi-reversible oxidation at +0.3 V, characteristic of the

Mn<sup>2+/3+</sup> redox couple. As in complex (2.20), complex (2.21) displays the same ligand based quasi-reversible and irreversible oxidations at +0.6 V and after +0.7 V. Refer to **Table 2.07** for a list of redox events for compounds (2.19)H - (2.21).

vi) Summary

Complex (2.20), with the occurrence of a gradual and incomplete spin-crossover, has very similar magnetic properties to the monothienyl iron(III) complexes formed from (2.07). The electrochemical properties of (2.20) are also enhanced in comparison to complexes derived from (2.07) because the terthienyl oxidation occurs at a significantly lower potential. The lower oxidation potential of terthiophene, combined with its improved steric properties, have made complex (2.20) better suited for further electrochemical polymerization experiments.

**Notes:**

*A version of this chapter has been published:*

\* Djukic, B.; Dube, P. A.; Razavi, F.; Seda, T.; Jenkins, H. A.; Britten, J. F.; Lemaire, M. T. *Inorg. Chem.* **2009**, 48, 699-707.

† Djukic, B.; Lemaire, M. T. *Inorg. Chem.* **2009**, 48, 10489–10491.

## Chapter 3: Iron(II) spin-crossover complexes

### 3.01 Iron(II) bispicen derivatives bearing thiophene substituents<sup>†</sup>

#### i) Goals and objectives

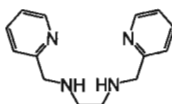
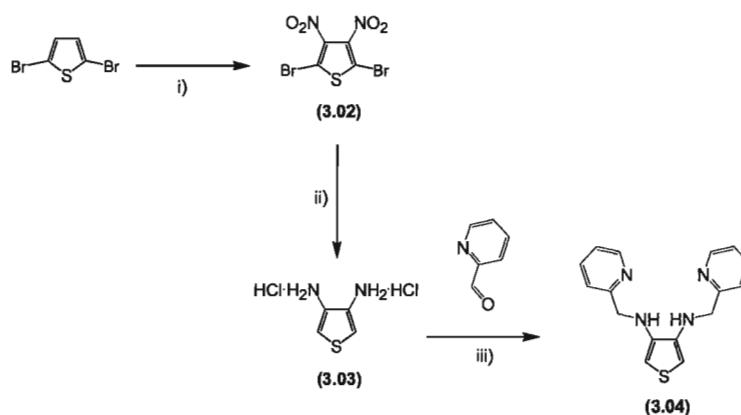


**Figure 3.01:** The bispicen ligand (3.01)

We are interested in developing multifunctional spin-crossover conducting materials and our approach is focused on combining these properties by preparing hybrid metallopolymers. To date, however, all reported SCO conductors have contained iron(III) but, since iron(II) complexes tend to have sharper spin transitions in comparison to iron(III), we decided to produce iron(II) containing SCO analogues as well. We also wanted the ligand to coordinate to the metal ion so it could be closer to the anticipated polymer backbone, in an effort to facilitate stronger interactions between the coordinated SCO unit and the conducting polymer. Inspection of the SCO literature led us to bispicen [bispicen = *bis*(2-pyridylmethyl)-diamine] (3.01) reported by Toftlund and co-workers in the 1980s (Figure 3.01).<sup>[119]</sup> These tetradentate ligands feature an ethyl or propyl spacer between the 2-pyridylmethylamine substituents, which could easily be replaced with a thiophene heterocycle substituted at the 3,4-ring positions. As an initial foray into this research, we have designed new ligands with structural features that could enable electropolymerization of the precursor iron(II) coordination complexes.

ii) Ligand synthesis



Reagents and conditions: (i) conc.  $\text{H}_2\text{SO}_4$  < 20 °C, conc.  $\text{HNO}_3$ , < 30 °C, 3h. (ii) Sn, conc. HCl, < 30 °C. (iii) NaOH, MeOH, 2-pyridinecarboxaldehyde,  $\text{NaBH}_4$  75 °C, 15.5 h.

**Scheme 3.01:** The synthesis of ligand (3.04)

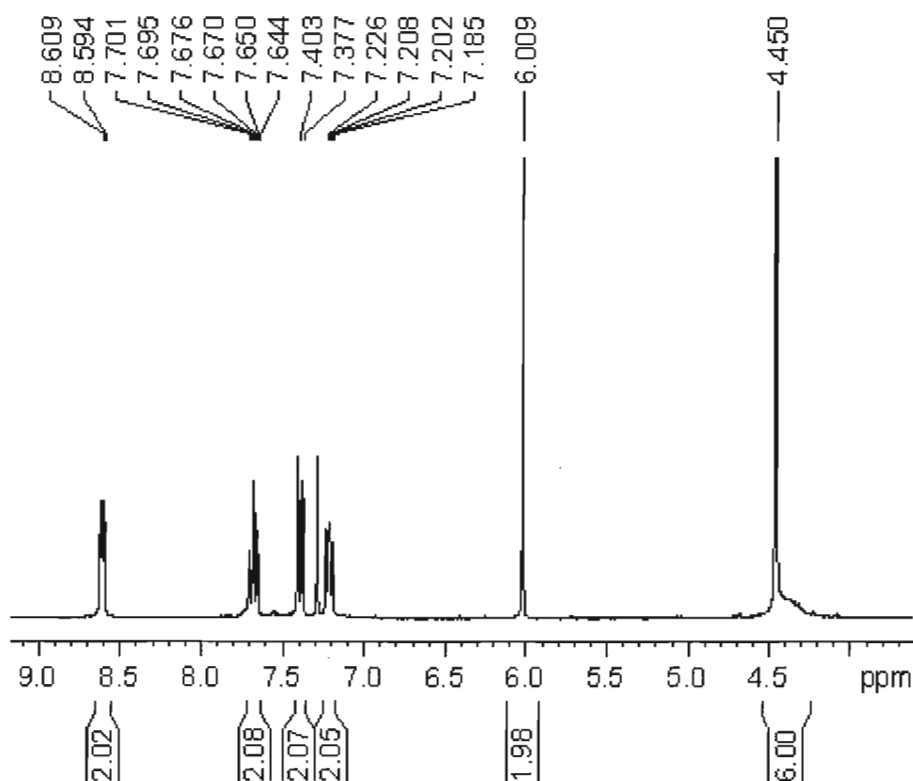
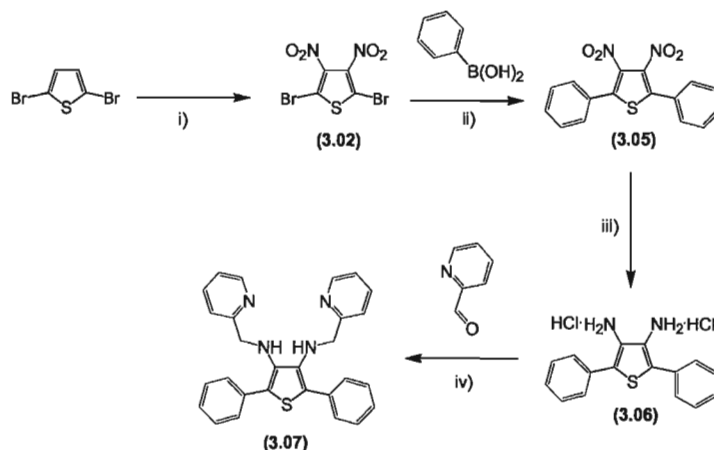


**Figure 3.02:**  $^1\text{H}$ -NMR spectrum of (3.04) in  $\text{CDCl}_3$

The thiophene substituted bispicen ligands were prepared in several steps from the commercially available reagent 2,5-dibromothiophene (**Scheme 3.01**). In a modified literature procedure, where we used non-fuming concentrated acids, 2,5-dibromo-3,4-dinitrothiophene (**3.02**) was made by nitration of the 2,5-dibromothiophene and collected in a reasonably good yield.<sup>[120]</sup> Compound (**3.02**) was reduced with an excess of mossy tin precipitating the dihydrochloride salt of 3,4-diaminothiophene (**3.03**). Neutralization of (**3.03**) with KOH, followed by condensation reactions in methanol with 2-pyridinecarboxaldehyde, generated an imine intermediate that was reduced with NaBH<sub>4</sub> to afford the tetradentate ligand (**3.04**). The <sup>1</sup>H-NMR spectrum of ligand (**3.04**) indicates the correct peak integration for the purported structure (**Figure 3.02**). Ten peaks are observed around the aromatic region of the spectrum and are consistent with the eight pyridyl and two thienyl protons. A multiplet observed at 4.45 ppm representing six resonances has the correct integration for the expected NH and aliphatic protons.



Reagents and conditions: (i) conc. H<sub>2</sub>SO<sub>4</sub> < 20 °C, conc. HNO<sub>3</sub>, < 30 °C, 3h. (ii) 2-phenylboronic acid, DME, H<sub>2</sub>O, 6 mol % Pd(PPh<sub>3</sub>)<sub>4</sub>, K<sub>2</sub>CO<sub>3</sub>, 65 °C, 13 h. (iii) Sn, EtOH, conc. HCl, 15 h. (iv) KOH, MeOH, 2-pyridinecarboxaldehyde, NaBH<sub>4</sub> 75 °C, 2 h.

**Scheme 3.02:** The synthesis of ligand (**3.07**)

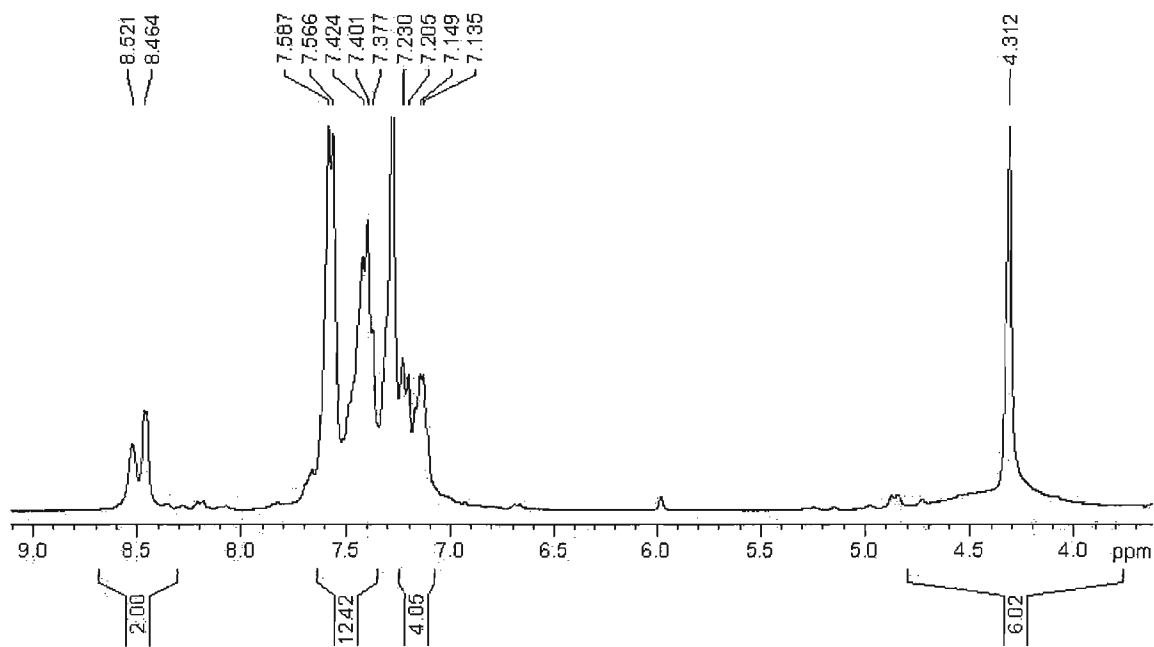
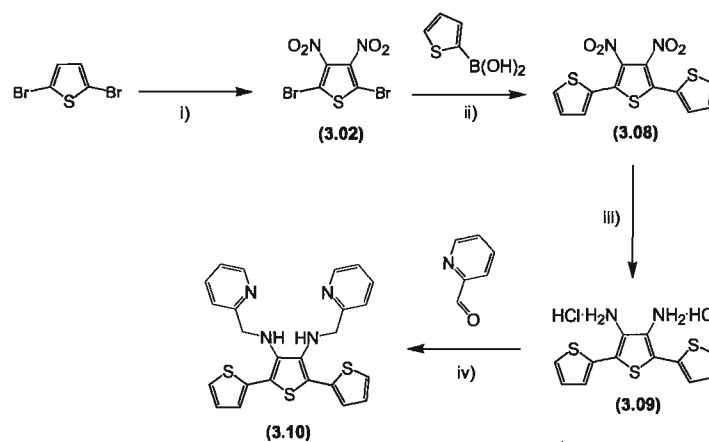


**Figure 3.03:**  $^1\text{H}$ -NMR spectrum of (3.07) in  $\text{CDCl}_3$



Reagents and conditions: (i) conc.  $\text{H}_2\text{SO}_4$  < 20 °C, conc.  $\text{HNO}_3$ , < 30 °C, 3 h. (ii) 2-thiopheneboronic acid, DME,  $\text{H}_2\text{O}$ , 6 mol %  $\text{Pd}(\text{PPh}_3)_4$ ,  $\text{K}_2\text{CO}_3$ , 100 °C, 8 h. (iii)  $\text{Sn}$ ,  $\text{EtOH}$ , conc.  $\text{HCl}$ , 15 h. (iv)  $\text{KOH}$ ,  $\text{MeOH}$ , 2-pyridinecarboxaldehyde,  $\text{NaBH}_4$  75 °C, 2 h.

**Scheme 3.03:** The synthesis of ligand (3.10)

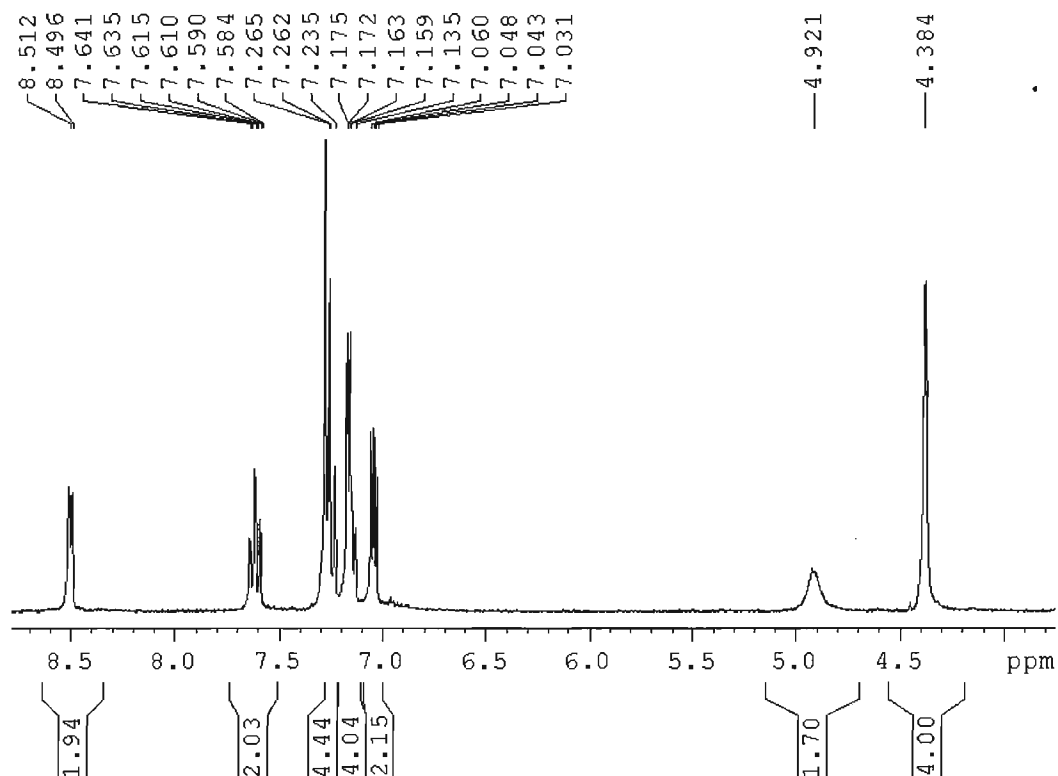


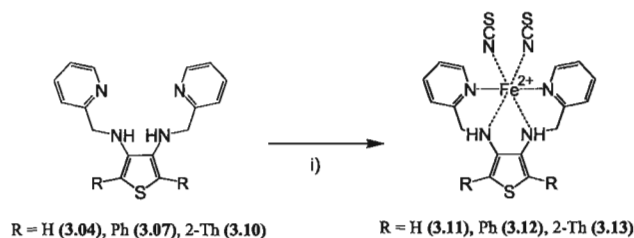
**Figure 3.04:**  $^1\text{H}$ -NMR spectrum of (3.10) in  $\text{CDCl}_3$

Compound (3.02) was also used in a Suzuki-Miyaura cross-coupling reaction with phenylboronic acid to generate a 2,5-diphenyl substituted compound (3.05), which was also reduced with excess tin (3.06) and reacted with 2-pyridinecarboxaldehyde to give the ligand (3.07) (Scheme 3.02). A second Suzuki coupling between (3.02) and 2-thiopheneboronic acid generated the 2,5-dithienyl substituted compound (3.08), again reduced with excess tin (3.09) and reacted with 2-pyridinecarboxaldehyde affording the ligand (3.10) (Scheme 3.03). The ligands (3.04), (3.07) and (3.10) are very unstable oils that had to be purified quickly and used directly in subsequent coordination reactions. These instability issues are not observed with similar reported ligands that do not feature thiophene substitution, and likely arise from nucleophilic reaction of the nitrogen atoms



at the 3,4-thiophene ring positions. Despite this instability, we were still able to acquire high-resolution mass spectra and  $^1\text{H}$ -NMR spectra for each ligand showing the correct integration and confirming the molecular formulae in each case (**Figures 3.03 - 3.04**). In the spectrum for ligand (**3.07**), 18 peaks are observed in the aromatic region, which are consistent with the expected 10 phenyl and 8 pyridyl protons of the ligand. The multiplet observed at 4.31 ppm represents six resonances that have the correct integration for the expected NH and aliphatic protons. In the spectrum for ligand (**3.10**), 14 peaks are observed in the aromatic region, which are consistent with the expected 6 thienyl and 8 pyridyl protons of the ligand. The singlet observed at 4.38 ppm represents four resonances that have the correct integration for the expected aliphatic protons and the broad peak at 4.92 ppm likely represents the NH protons.

### iii) Coordination chemistry

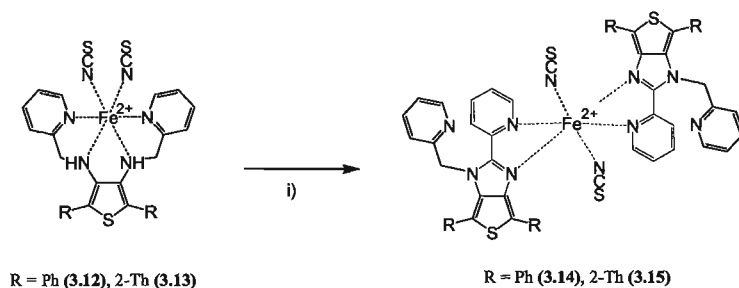


Reagents and conditions: (i)  $\text{FeBF}_4$ , KSCN, MeOH.

**Scheme 3.04:** The synthesis of complexes (**3.11**) – (**3.13**)

Iron(II) complexes were prepared by coordination of (**3.04**), (**3.07**) and (**3.10**) with iron(II) tetrafluoroborate in deareated methanol solutions, followed by the addition of excess aqueous KSCN, to generate green precipitates of complexes (**3.11**) – (**3.13**) (**Scheme 3.04**). Complexes (**3.11**) and (**3.13**) are analytically pure powders, stable to air

in the solid-state but very unstable in solution, even when deaerated, which hindered single crystal growth and the collection of X-ray diffraction data. Despite this, we could use FT-IR spectroscopy ( $\nu_{\text{C}\equiv\text{N}}$ ) to identify the stereochemistry about the metal centre. Complexes **(3.11)** and **(3.13)** feature a strong “doublet” between 2060-2080  $\text{cm}^{-1}$ , indicating *cis*-stereochemistry, which has been observed in other similar reported complexes. The energy of this band has been previously correlated to the electronic ground-state of the complex and the energies observed for complexes **(3.11)** or **(3.13)** suggest a significant population of the high-spin  $^5T_2$  state at room temperature. Complex **(3.12)**, which was prepared under identical conditions to **(3.11)** or **(3.13)**, is unstable in the solid state and in solution, making characterization difficult, but based on our spectroscopic data, we are confident in the purported structure. As opposed to **(3.11)** or **(3.13)**, complex **(3.12)** features a sharp and strong single band at 2070  $\text{cm}^{-1}$ , which suggests an unusual *trans* disposition of the thiocyanate ligands and a HS ground state.



Reagents and conditions: (i) MeOH/DCM

**Scheme 3.05:** The synthesis of **(3.12)** – **(3.13)**

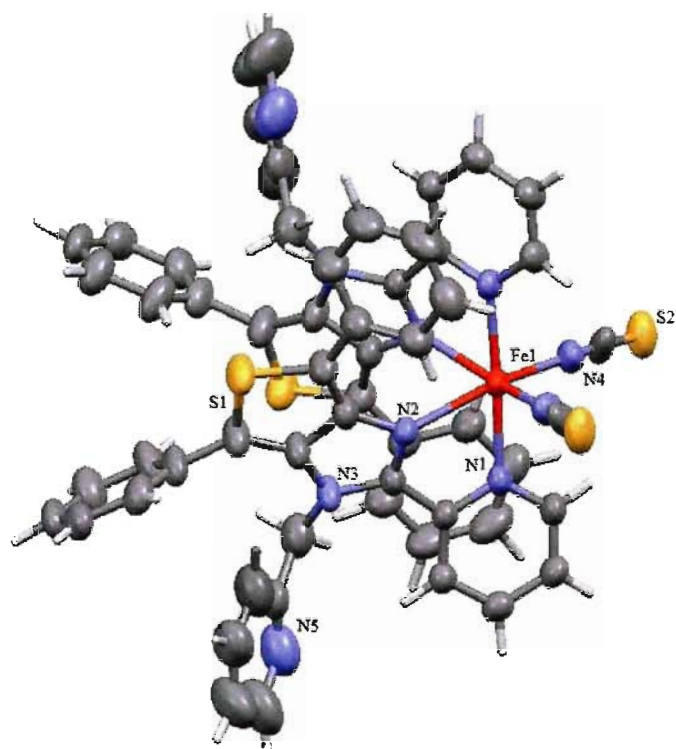
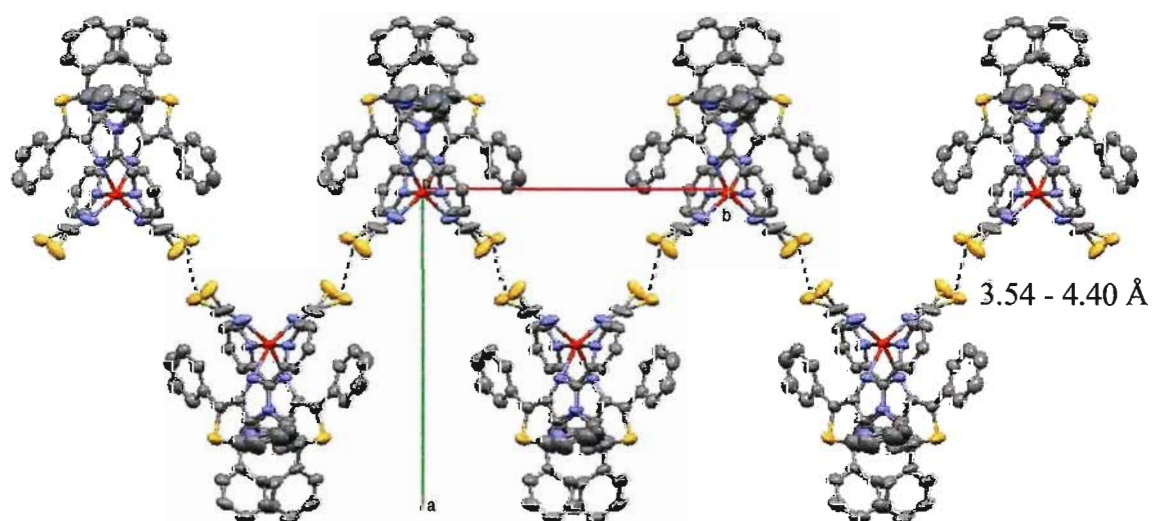


**Figure 3.05:** The molecular structure of complex (3.14) with ellipsoids drawn at the 50 % probability level



(dashed lines indicate an intermolecular S...S contact)

**Figure 3.06:** The packing diagram of (3.14)

---

**Table 3.01:** Selected bond distances and angles for **(3.14)**

| Atoms        | Distance (Å) | Atoms           | Angle (°) |
|--------------|--------------|-----------------|-----------|
| Fe(1)-N(1)   | 2.291(3)     | N(1)-Fe(1)-N(2) | 73.5(1)   |
| Fe(1)-N(2)   | 2.087(4)     | N(1)-Fe(1)-N(2) | 104.3(1)  |
| Fe(1)-N(4)   | 2.202(4)     | N(1)-Fe(1)-N(4) | 89.9(1)   |
| Fe(1)-Fe(1)' | 12.914(2)    | N(1)-Fe(1)-N(4) | 91.7(1)   |
|              |              | N(2)-Fe(1)-N(2) | 77.5(1)   |
|              |              | N(2)-Fe(1)-N(4) | 93.1(1)   |
|              |              | N(4)-Fe(1)-N(4) | 102.1(2)  |
|              |              | N(1)-Fe(1)-N(1) | 177.3(1)  |
|              |              | N(2)-Fe(1)-N(4) | 157.9(1)  |

---

(standard deviations in the last digit are quoted in parenthesis)

---

Attempts to recrystallize deaerated solutions of **(3.11)** - **(3.13)** consistently resulted in solution colour changes, from green to red over a period of days, which we attributed to iron(II) oxidation at first. Red solutions of **(3.12)** deposited X-ray quality crystals and, surprisingly, revealed a structurally rearranged material **(3.14)** (**Scheme 3.05**). Complex **(3.14)** contains two coordinated molecules of rearranged **(3.07)** and is shown in an ORTEP diagram of the molecular structure (**Figure 3.05**). The iron(II) metal centre falls on a two-fold axis, rendering each coordinated ligand symmetrically equivalent with coordinate bond lengths consistent with an oxidation state assignment of +2 for the iron ion (**Table 3.01**). Coordination of the ambidentate thiocyanate ligand occurs exclusively through the nitrogen atoms, which are a harder donor in comparison to the sulfur and are more suitable for coordination with the iron(II) ion. Each molecule of rearranged **(3.07)** coordinates through N1 and N2 of a bidentate pyridine-imidazole-type fragment of the molecule. In the other imidazole-type ring, atom N3 features a covalently bound and uncoordinated 2-pyridylmethylene substituent. Crystallographically equivalent

thiocyanate ligands are coordinated *cis* to the iron centre and are disordered over two positions. Molecules of **(3.14)** pack in a one-dimensional chain structure along the *c*-axis, with intermolecular S $\cdots$ S contacts (3.54–4.40 Å due to disorder) between coordinated thiocyanate ligands among adjacent molecules along the chain (**Figure 3.06**). Over time, red solutions of **(3.13)** also deposit a dark red powder **(3.15)** from which FT-IR and mass spectrometric data indicate that a similar structural rearrangement occurs, but we could not obtain X-ray quality crystals from these solutions. Similar structural rearrangements have not been reported for other iron(II) *bis*(thiocyanate) complexes containing tetradentate *bis*(2-pyridylmethyl)-type ligands, suggesting that the thienyl substituent or the electronic effect of this substituent is involved in the mechanism for this rearrangement.

iv) Magnetic characterization

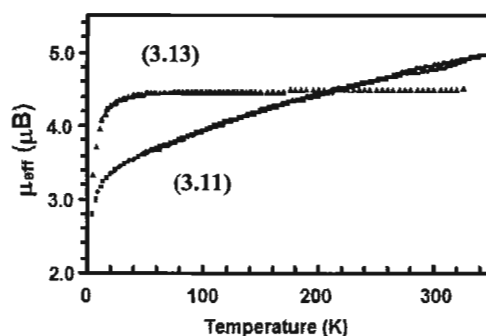


**Figure 3.07:** Variable temperature magnetic properties of **(3.11)** and **(3.13)** in a 5000 Oe magnetic field<sup>[121]</sup>

The variable temperature magnetic properties of **(3.11)**, **(3.13)** and **(3.14)** were analyzed with SQUID magnetometry and the data is presented as plots of the effective magnetic

moment ( $\mu_{\text{eff}}$ ) versus temperature. In powder samples of **(3.11)**, the variable temperature magnetic susceptibility data indicates the possibility of a gradual and incomplete spin-crossover without thermal hysteresis (**Figure 3.07**). At 350 K, the magnetic moment of **(3.11)** is 4.95  $\mu\text{B}$  and gradually decreases while decreasing the temperature to 2 K. At 2 K, the observed magnetic moment of 2.4  $\mu\text{B}$  is higher than anticipated for a complete crossover to the low-spin state (theoretical value is 0  $\mu\text{B}$ ). However, the moment at low temperature is very similar to that observed by Toftlund for structurally similar iron(II) complexes and points toward an incomplete spin-crossover in these materials. The magnetic properties of **(3.13)** between 5 - 325 K feature little temperature dependence with magnetic moment values that suggest a high-spin ground state for this complex. The magnetic moment of **(3.13)** decreases rapidly below 40 K, indicating a combination of ZFS and intermolecular antiferromagnetic interactions.

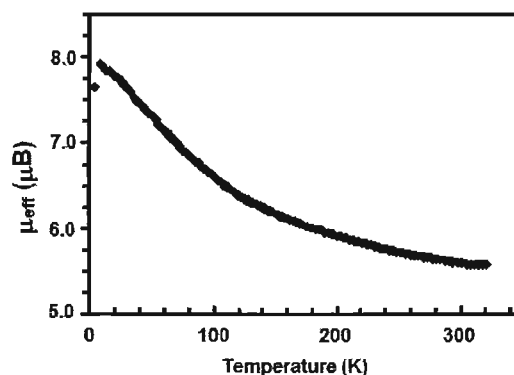


**Figure 3.08:** Variable temperature magnetic properties of **(3.14)** in a 5000 Oe magnetic field<sup>[121]</sup>

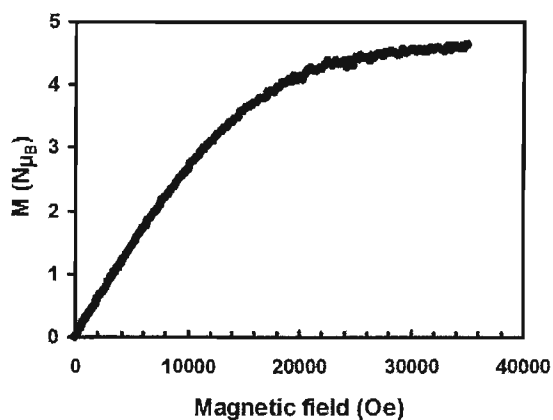


**Figure 3.09:** Reduced magnetization versus field data for (3.14) recorded at 5 K<sup>[121]</sup>

Complex (3.14) has very different variable temperature magnetic properties than either (3.11) or (3.13). The magnetic moment is significantly higher than anticipated for a magnetically isolated mononuclear iron(II) complex at room temperature (Figure 3.08). As the temperature is decreased a gradual increase in magnetic moment is observed, suggesting intermolecular ferromagnetic interactions may be operative. The magnetic moment reaches a plateau of 8.1  $\mu_B$  at nearly 8 K, and then slightly decreases. However, low temperature magnetization versus field experiments performed at 5 K provided no indication of ferromagnetic ordering, with a saturation magnetization of 4.6  $N\mu_B$  at 3.5 T, which is a typical value for high-spin iron(II) (Figure 3.09).

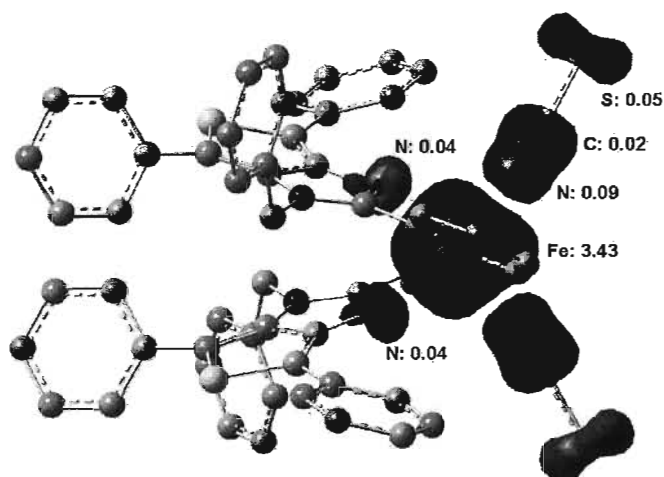


**Figure 3.10:** Calculated spin density distribution in (3.14) with natural population analysis derived atomic spin density shown for the most important contributors<sup>[121]</sup>

A possible pathway for magnetic exchange coupling was suggested in the molecular packing of (3.14), since close intermolecular S $\cdots$ S contacts were observed between coordinated thiocyanate ligands from adjacent molecules. To investigate this, DFT at the B3LYP/DZVP level was used to calculate the structure and spin density of complex (3.14), revealing significant spin delocalization (0.16) onto the coordinated thiocyanate ligands (Figure 3.10) and suggesting that the magnetic exchange pathway is that of a 1-D  $S = 2$  ferromagnetic chain. The experimental data was also fit to a Bonner-Fisher 1-D chain model ( $g = 2.13$  and  $J/k = +7.5$  K), which provides further evidence to support this claim and can be found elsewhere.<sup>[121]</sup>



v) Electronic absorption spectroscopy

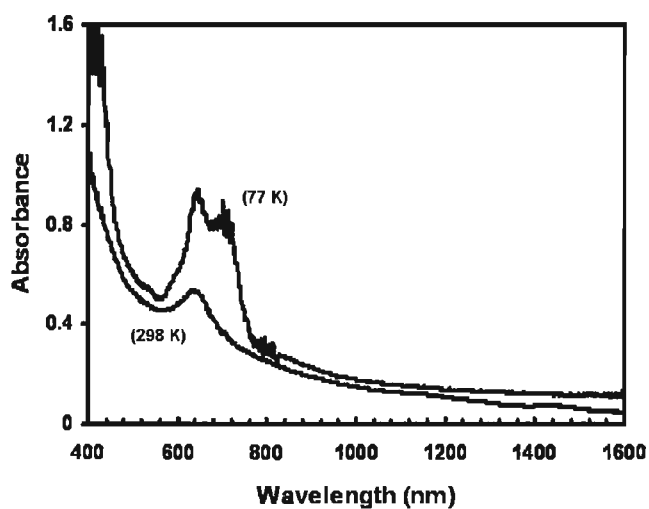


**Figure 3.11:** Variable temperature absorbance profile of (3.11) in ethanol<sup>[121]</sup>

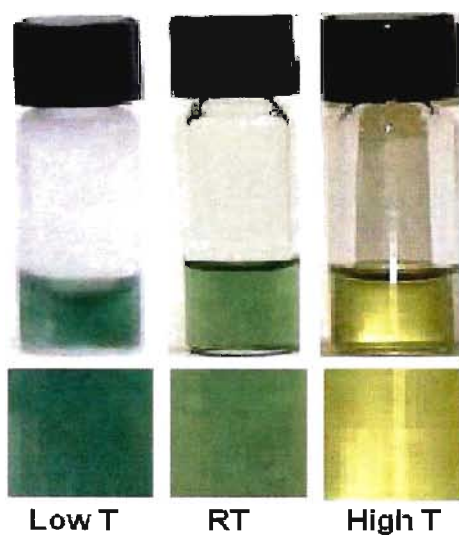


**Figure 3.12:** Solutions of (3.11) in ethanol at variable temperatures

The room temperature spectrum of (3.11) in ethanol features a weak absorption at 640 nm. However, upon cooling solutions of (3.11) to 77 K, a large increase in absorption intensity is observed along with the growth of a shoulder on the low energy side of the 640 nm absorption (Figure 3.11). The colour of the solution, pale green as observed at

room temperature, becomes dark green upon decreasing temperature to 77 K and light yellow upon heating to 330 K (**Figure 3.12**). These observations are in agreement with the magnetic data and suggest spin-crossover is occurring in solutions containing **(3.11)**. The new absorption feature centred at 700 nm is likely due to the band of the low-spin state of **(3.11)**. Ethanol solutions of complexes **(3.12)** and **(3.13)** exhibit absorption maxima at 650 nm ( $\epsilon = 400 \text{ M}^{-1}\text{cm}^{-1}$ ), with no evidence of temperature dependence in the absorption intensities.

vi) Electrochemistry

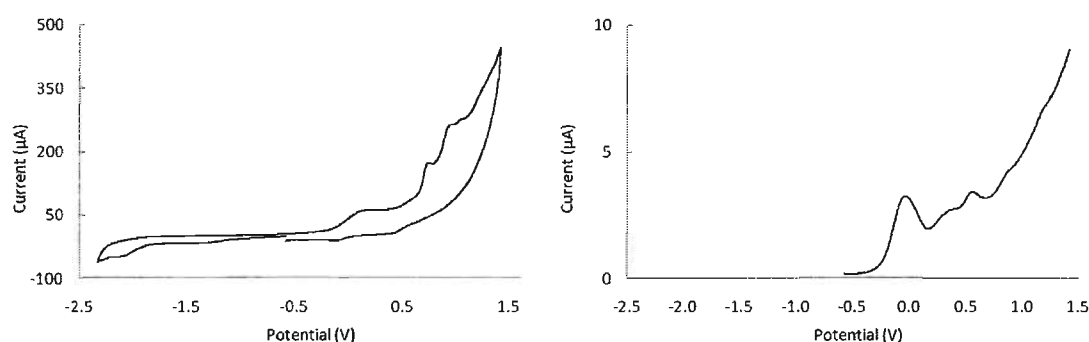


**Figure 3.13:** Cyclic (left) and differential pulse (right) voltammograms of **(3.13)**

---

**Table 3.02:** Electrochemical data for **(3.13)** in ACN

| Compound      | $E^{\circ}_{\text{ox}}$ (V) vs. fc | $E^{\circ}_{\text{ref}}$ (V) vs. fc |
|---------------|------------------------------------|-------------------------------------|
| <b>(3.13)</b> | +0.4, +0.8, +1.0, +1.3             | -0.1, -1.4, -2.1                    |

(Refer to section 8.04 for experimental details)

---

The electrochemical properties of complex **(3.13)** were investigated with cyclic voltammetry and feature a number of broad and irreversible processes versus ferrocene (**Figure 3.13**). During cathodic scans, the irreversible waves at potentials greater than -1.0 V are attributed to pyridine ring reductions. During anodic sweeps of **(3.13)**, an irreversible oxidation process centred at +0.4 V is observed and is likely attributed to the dehydrogenation of the NH bonds. Complex **(3.13)** also has a very broad irreversible oxidation at +1.3 V along with irreversible processes at +0.8, +1.0 V that are attributed to a combination of thienyl oxidation processes. Using differential pulse voltammetry, the iron(II) oxidation potential was determined to be -0.1 V versus ferrocene and observed along with the other oxidative events in the cyclic voltammogram. No indication of polymerization reactions were observed while attempting to electropolymerize complex **(3.13)** by repeated scanning over the terthienyl oxidation potential. Similar results were also observed for complex **(3.11)**. The irreversible oxidations at low potentials suggest that **(3.13)**, in addition to **(3.11)** and **(3.12)** are insufficiently stable for electrochemical reactions. Refer to **Table 3.02** for a list of redox events for compound **(3.13)**.

### 3.02 Substituted iron(II) ppi derivatives

#### i) Ligand synthesis

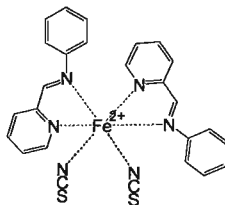
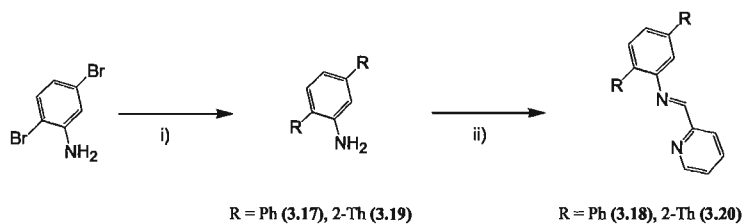


**Figure 3.14:** A diagram of  $\text{Fe}(\text{ppi})_2(\text{NCS})_2$  (**3.16**)

Our first attempts at generating an iron(II) spin-crossover complex bearing an electropolymerizable component resulted in a series of compounds with unique properties, however, their instability made them unsuitable for further reactions. Keeping with the same theme of modifying an existing spin-crossover compound, our target changed to derivatives of  $[\text{Fe}(\text{ppi})_2(\text{NCS})_2]$  [ppi = *N*-phenyl-2-pyridinaldimine] (**3.16**) because they could be easily structurally modified and were expected to have increased stability in comparison to the bispicen derivatives we previously synthesized (**Figure 3.14**).<sup>[122-124]</sup>



Reagents and conditions: (i) (**3.17**) 2-phenylboronic acid, (**3.19**) 2-thiopheneboronic acid, DME,  $\text{H}_2\text{O}$ , 10 mol %  $\text{Pd}(\text{PPh}_3)_4$ ,  $\text{K}_2\text{CO}_3$ , 95 °C, 72 h. (ii) 2-pyridinecarboxaldehyde, DCM, pentane.

**Scheme 3.06:** The synthesis of ligands (**3.18**) and (**3.20**)

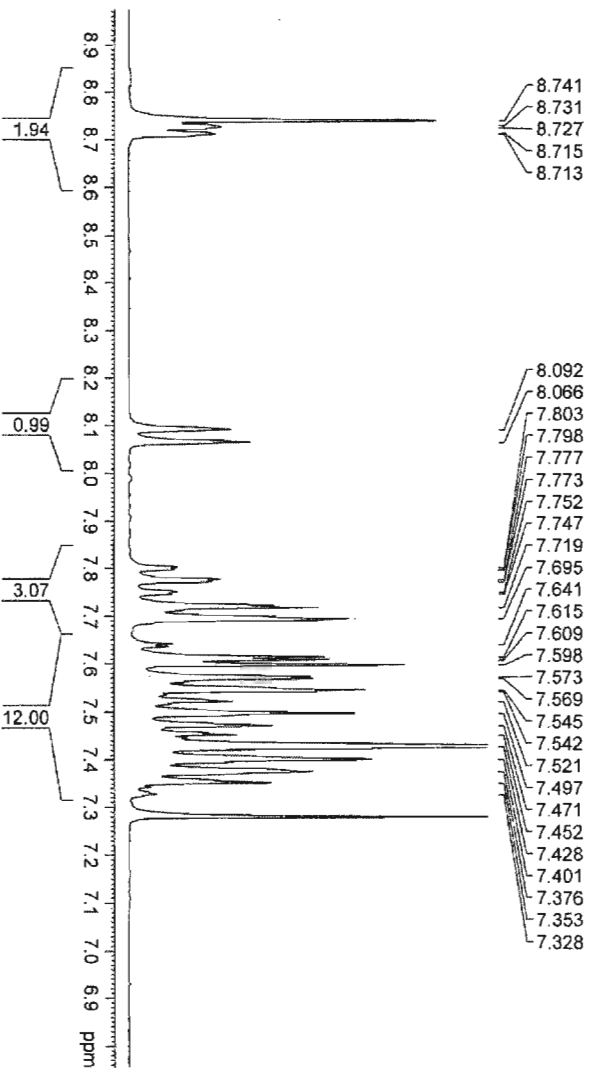


Figure 3.15:  $^1\text{H}$ -NMR spectrum of (3.18) in  $\text{CDCl}_3$

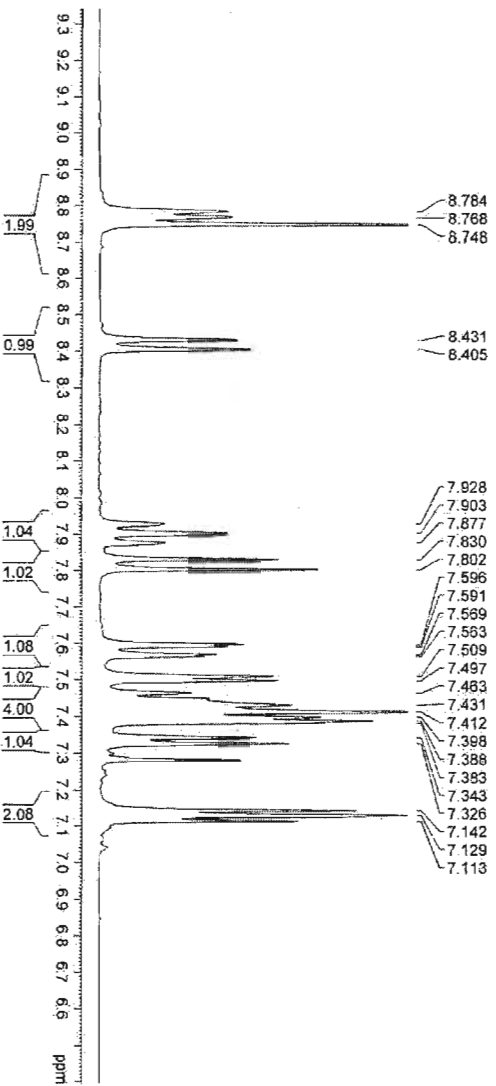
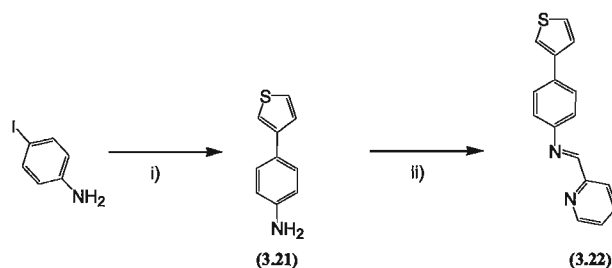
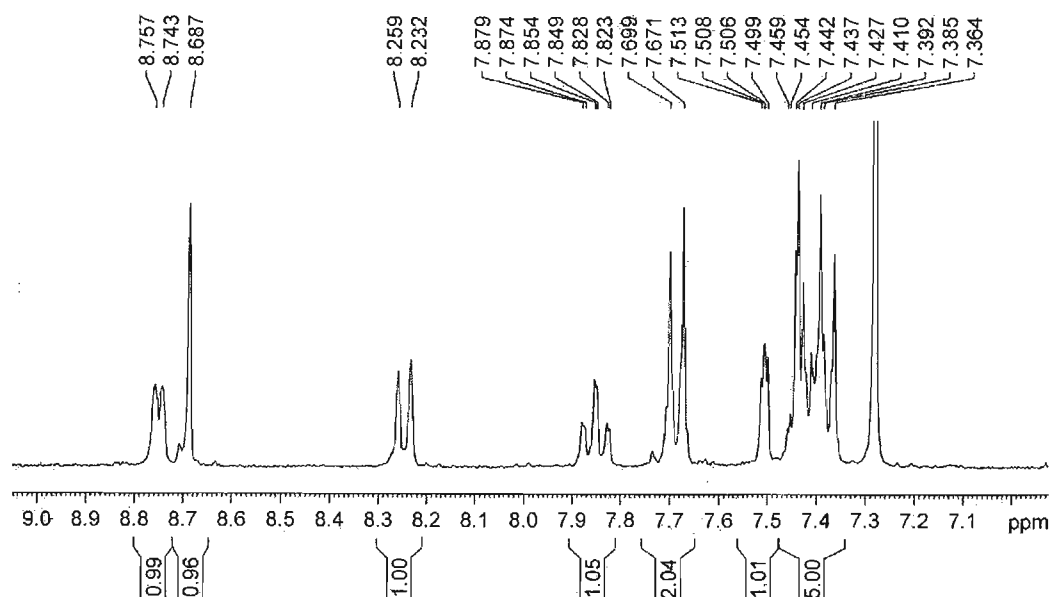


Figure 3.16:  $^1\text{H}$ -NMR spectrum of (3.20) in  $\text{CDCl}_3$



Reagents and conditions: (i) 3-thiopheneboronic acid, DME, H<sub>2</sub>O, 5 mol % Pd(PPh<sub>3</sub>)<sub>4</sub>, K<sub>2</sub>CO<sub>3</sub>, 95 °C, 72 h. (ii) 2-pyridinecarboxaldehyde, DCM, pentane.

**Scheme 3.07:** The synthesis of ligand (3.22)



**Figure 3.17:** <sup>1</sup>H-NMR spectrum of (3.22) in CDCl<sub>3</sub>

A diphenyl substituted ppi ligand was selected as the first target and was prepared in two steps from the commercially available reagent 2,5-dibromoaniline (**Scheme 3.06**). First a Suzuki-Miyaura cross-coupling reaction with phenylboronic acid was used to generate the 2,5-diphenyl compound (**3.17**), followed by a reaction with 2-pyridinecarboxaldehyde to give the ligand (**3.18**). Following this same methodology, 2-thiopheneboronic acid was also used in a coupling reaction with 2,5-dibromoaniline to generate the 2,5-dithienyl

precursor (3.19) and ligand (3.20) (Scheme 3.06). The monothienyl analogue was prepared from 4-iodoaniline, which was reacted with 3-thiopheneboronic acid and 2-pyridinecarboxaldehyde, affording compound (3.21) and ligand (3.22) (Scheme 3.07). The  $^1\text{H}$ -NMR spectra for ligands (3.18), (3.20) and (3.22) are shown in Figures 3.15 - 3.17, respectively, with the correct peak integration for their purported structures. In the spectrum for ligand (3.18), 17 peaks are observed around the aromatic region, which are consistent with the expected 13 terphenyl, 4 pyridyl protons of the ligand. Further downfield, at 8.74 ppm, a singlet is observed which is characteristic of the (deshielded) imine proton. For ligand (3.20), the 13 peaks observed around the aromatic of the spectrum are consistent with the expected 6 thienyl, 3 phenyl and 4 pyridyl protons of the ligand. The singlet at 8.78 ppm is characteristic of the imine proton. Similarly, for ligand (3.22), 11 peaks are observed around the aromatic region of the spectrum, which are consistent with the expected 3 thienyl, 4 phenyl and 4 pyridyl protons of the ligand. A singlet at 8.69 ppm is also observed which is characteristic of the imine proton.

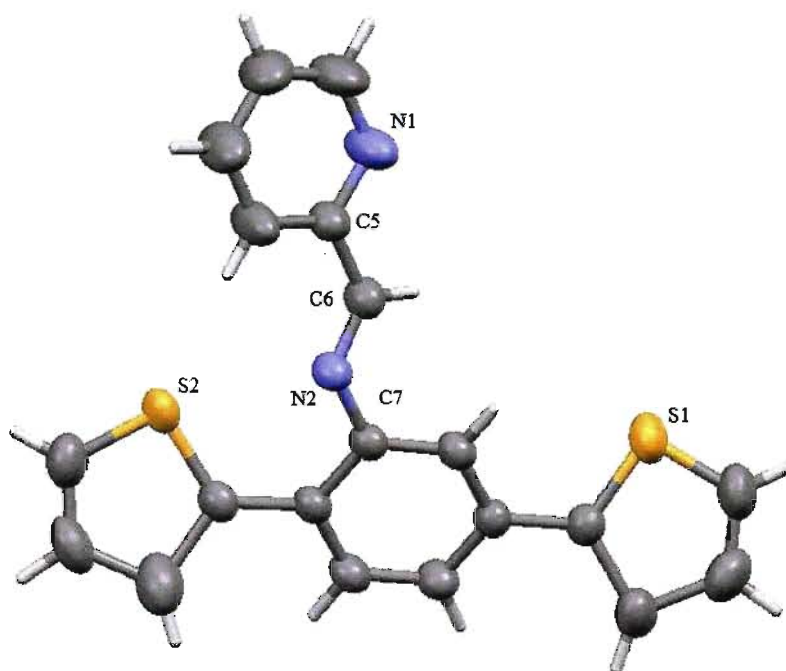


**Figure 3.18:** The molecular structure of **(3.20)** with thermal ellipsoids drawn at the 50 % probability level

**Table 3.03:** Selected bond distances and angles for **(3.18)**

| Atoms     | Distance (Å) | Atoms          | Angle (°) |
|-----------|--------------|----------------|-----------|
| C(6)-N(2) | 2.291(3)     | C(5)-C(6)-N(2) | 122.4(3)  |
|           |              | C(6)-N(2)-C(7) | 118.4(2)  |

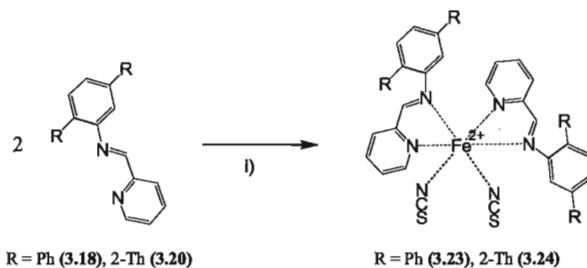
(standard deviations in the last digit are quoted in parenthesis)

Ligand **(3.20)** is more stable than our other thiophene bearing Schiff base ligands, **(2.07)** for example, and we were able to obtain single crystals suitable for X-ray diffraction experiments. An ORTEP diagram displays the molecular structure of the ligand (**Figure 3.18**) where each of the thiophene rings are disordered to a different extent between two



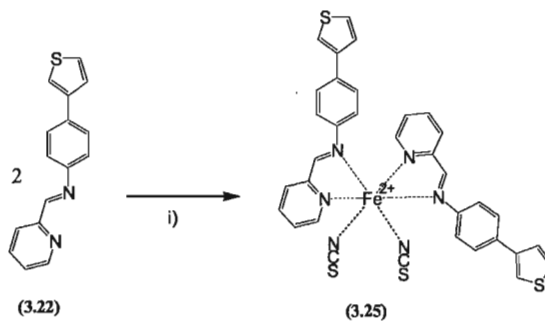
positions. The crystal structure is completely consistent with the anticipated Schiff base product and displays the imine bond between C(6) and N(2) (Table 3.03).

## ii) Coordination chemistry



Reagents and conditions: (i)  $\text{Fe(II)SO}_4 \cdot 7\text{H}_2\text{O}$ , KSCN, MeOH, 72 h.

**Scheme 3.08:** The synthesis of complexes (3.23) – (3.24)



Reagents and conditions: (i)  $\text{Fe(II)SO}_4 \cdot 7\text{H}_2\text{O}$ , KSCN, MeOH, 72 h.

**Scheme 3.09:** The synthesis of complex (3.25)

Iron(II) thiocyanate, prepared from hydrated iron(II) sulfate and KSCN, was used in the coordination of ligands (3.18), (3.20) and (3.22) to prepare complexes (3.23) – (3.25) (Schemes 3.08 - 3.09). The complexes are isolated as analytically pure powders and produced FAB mass spectra that all display a peak corresponding to the molecular cation. The FT-IR spectra for the complexes are also consistent with the proposed structures and

show the thiocyanate and imine stretching frequencies at approximately 2060 and 1593  $\text{cm}^{-1}$ , respectively.

iii) Structural properties

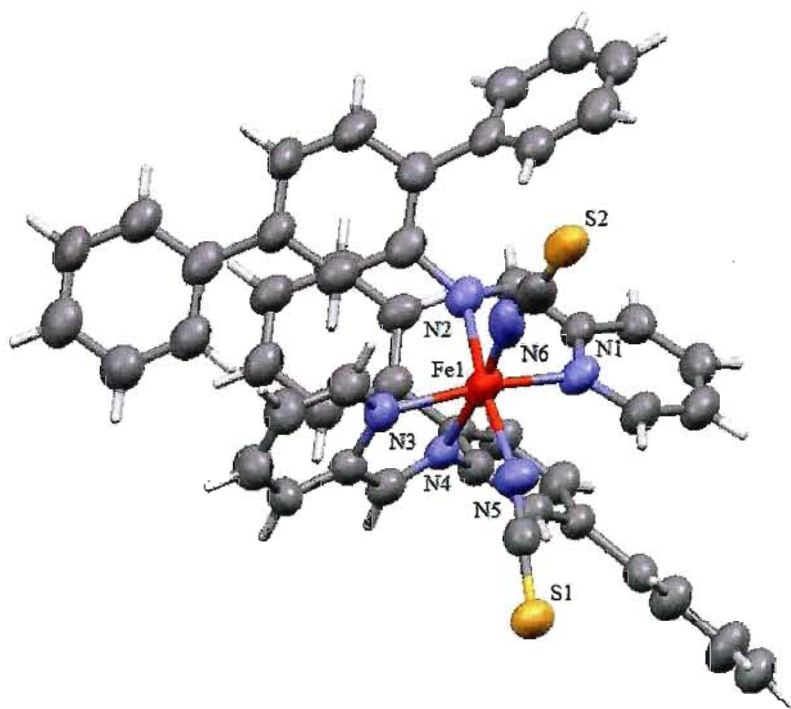


**Figure 3.19:** The molecular structure of (3.23) with thermal ellipsoids drawn at the 50 % probability level

---

**Table 3.04:** Selected bond distances and angles for **(3.23)**

| Atoms      | Distance (Å) | Atoms           | Angle (°) |
|------------|--------------|-----------------|-----------|
| Fe(1)-N(1) | 2.052(6)     | N(1)-Fe(1)-N(2) | 78.1(2)   |
| Fe(1)-N(2) | 2.097(5)     | N(1)-Fe(1)-N(4) | 91.7(2)   |
| Fe(1)-N(3) | 2.069(6)     | N(1)-Fe(1)-N(5) | 90.6(3)   |
| Fe(1)-N(4) | 2.119(5)     | N(1)-Fe(1)-N(6) | 96.6(3)   |
| Fe(1)-N(5) | 2.023(7)     | N(2)-Fe(1)-N(3) | 103.2(2)  |
| Fe(1)-N(6) | 1.99(1)      | N(2)-Fe(1)-N(4) | 88.5(2)   |
|            |              | N(2)-Fe(1)-N(6) | 92.1(3)   |
|            |              | N(3)-Fe(1)-N(4) | 76.6(2)   |
|            |              | N(3)-Fe(1)-N(5) | 86.8(3)   |
|            |              | N(3)-Fe(1)-N(6) | 95.0(3)   |
|            |              | N(4)-Fe(1)-N(5) | 86.8(3)   |
|            |              | N(5)-Fe(1)-N(6) | 94.3(3)   |
|            |              | N(1)-Fe(1)-N(3) | 168.2(2)  |
|            |              | N(2)-Fe(1)-N(5) | 167.6(3)  |
|            |              | N(4)-Fe(1)-N(6) | 171.5(3)  |

---

(standard deviations in the last digit are quoted in parenthesis)

---

Part of the appeal towards designing complex **(3.23)** stems from our anticipation that this complex would be stable enough to acquire single crystal structural information and to use its structure as a reference for the other complexes prepared in this series. Single crystals suitable for X-ray diffraction were grown from a solution of **(3.23)** in a mixture of methanol and dichloromethane, left to slowly evaporate. The expected iron *cis*-pseudo-octahedral coordination geometry is shown in an ORTEP diagram of the molecular structure of **(3.23)** (**Figure 3.19**). The iron centre is coordinated to two molecules of **(3.18)** through their donor nitrogen atoms, in addition to the nitrogen atoms of two thiocyanate anions. Coordinate bond lengths indicate the +2 oxidation state of the metal, with Fe-N lengths ranging from 1.99 to 2.12 Å (**Table 3.03**).

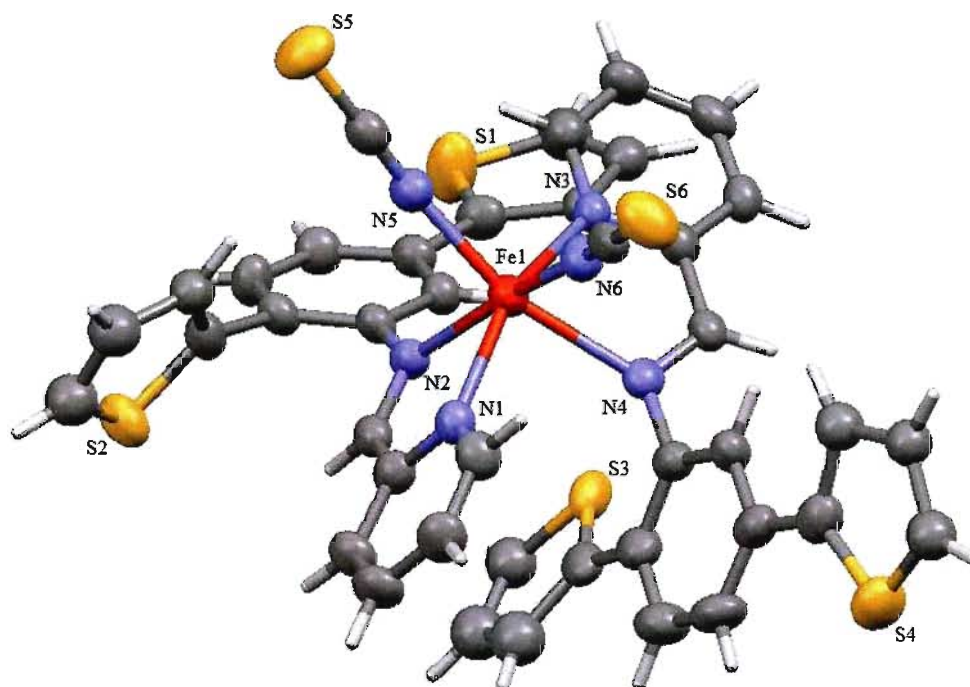


**Figure 3.20:** The molecular structure of (3.24) with thermal ellipsoids drawn at the 50 % probability level

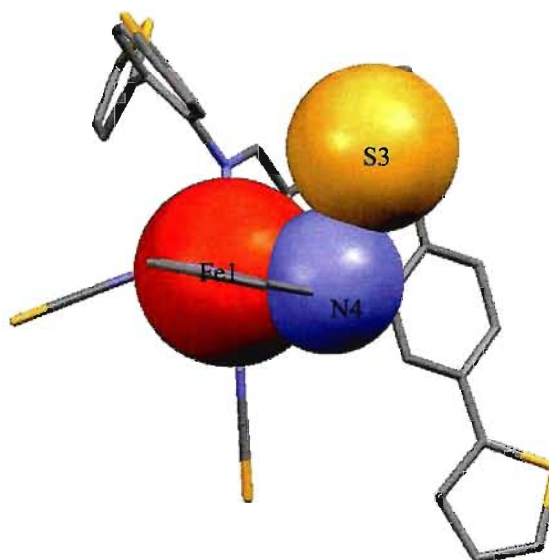


**Figure 3.21:** A space filling diagram showing the imine (N4)-thiophene (S3) contact of (3.24)

---

**Table 3.05:** Selected bond distances and angles for **(3.24)**

| Atoms      | Distance (Å) | Atoms           | Angle (°) |
|------------|--------------|-----------------|-----------|
| Fe(1)-N(1) | 2.188(3)     | N(1)-Fe(1)-N(2) | 74.9(1)   |
| Fe(1)-N(2) | 2.266(4)     | N(1)-Fe(1)-N(4) | 86.1(1)   |
| Fe(1)-N(3) | 2.186(4)     | N(1)-Fe(1)-N(5) | 109.4(2)  |
| Fe(1)-N(4) | 2.310(5)     | N(1)-Fe(1)-N(6) | 92.0(2)   |
| Fe(1)-N(5) | 2.063(5)     | N(2)-Fe(1)-N(3) | 97.2(1)   |
| Fe(1)-N(6) | 2.080(5)     | N(2)-Fe(1)-N(4) | 100.0(1)  |
|            |              | N(2)-Fe(1)-N(5) | 88.4(2)   |
|            |              | N(3)-Fe(1)-N(4) | 73.0(1)   |
|            |              | N(3)-Fe(1)-N(5) | 92.5(2)   |
|            |              | N(3)-Fe(1)-N(6) | 96.5(2)   |
|            |              | N(4)-Fe(1)-N(5) | 82.9(2)   |
|            |              | N(5)-Fe(1)-N(6) | 92.1(2)   |
|            |              | N(1)-Fe(1)-N(3) | 156.2(2)  |
|            |              | N(2)-Fe(1)-N(6) | 166.3(2)  |
|            |              | N(4)-Fe(1)-N(5) | 164.0(2)  |

---

(standard deviations in the last digit are quoted in parenthesis)

---

We were also able to acquire an X-ray crystal structure of complex **(3.24)**, from slowly evaporating mixtures of toluene and dichloromethane and many aspects of this structure were found to be similar to the terphenyl analogue **(3.23)**. The iron *cis*-pseudo-octahedral geometry, through the expected coordination of two ligands of **(3.20)** and anionic thiocyanate, is shown in an ORTEP diagram of the molecular structure of **(3.24)** (**Figure 3.20**). There are, however, some unique features in the crystal structure of **(3.24)**. Although each thiophene ring in the molecule is disordered to some extent, only the ring containing S3 is positioned inward towards the iron centre and, although disordered, occupies this position over 80 % of the time. The significance stems from the close (2.946 Å) thiophene S3...N4 imine contact (**Figure 3.21**), that results in an elongation of the Fe1...N4 bond by 2 % in comparison to the other Fe1...N2 imine

coordinate bond (**Table 3.05**). In comparison, the terphenyl complex **(3.23)** (as well as other similar derivatives) does not show significant difference between its two Fe $\cdots$ N(imine) coordinate bond lengths, which are also shorter than the Fe1 $\cdots$ N4 bond of **(3.24)**.

iv) Magnetic characterization

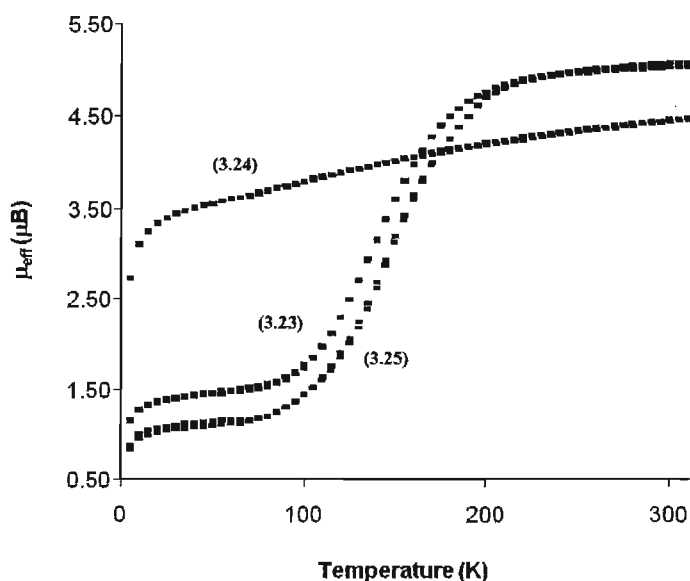


**Figure 3.22:** Variable temperature magnetic susceptibility measurements for complexes **(3.23)** - **(3.25)** in a 5000 Oe magnetic field

The variable temperature magnetic properties of **(3.23)** - **(3.25)** were analyzed with SQUID magnetometry and the data is presented as plots of the effective magnetic moment versus temperature (**Figure 3.22**). In powder samples of **(3.23)**, the variable temperature magnetic susceptibility data indicate a fairly abrupt spin transition without thermal hysteresis. At 320 K, the magnetic moment of **(3.23)** is 5.04  $\mu\text{B}$  and decreases with decreasing temperature to 1.2  $\mu\text{B}$  at 5 K, which is higher than anticipated for a

complete crossover to the low-spin state (theoretical value is 0  $\mu\text{B}$ ) and is likely caused by incomplete spin-crossover. Complex (3.25) has a nearly identical profile when compared to (3.23) except that the magnetic moment is closer to the theoretical value at low temperature (2 K). At 300 K, the magnetic moment of (3.24) is 4.78  $\mu\text{B}$  and is slightly lower than either (3.23) or (3.25), but is similar because it suggests a dominant population of the high-spin state. However, despite this initial similarity, the profile of the data becomes very different. Instead of an abrupt transition to the low-spin state a gradual decrease in magnetic moment is observed. The magnetic moment at 2 K is still 2.49  $\mu\text{B}$ , a curious value since it is not consistent with the other two complexes.

**Table 3.06:** Mössbauer data for (3.24) and (3.25)

| Compound | Temperature<br>(°C) | IS<br>(mm/s) | QS<br>(mm/s) | Site<br>(%) | Fe(II) Spin<br>State |
|----------|---------------------|--------------|--------------|-------------|----------------------|
| (3.24)   | 293                 | 0.97(1)      | 2.60(2)      | 68          | 2                    |
|          |                     | 0.32(3)      | 0.54(5)      | 32          | 0                    |
|          | 100                 | 1.103(3)     | 3.087(7)     | 80          | 1 or 2               |
|          |                     | 0.418(8)     | 0.78(2)      | 20          | 0                    |
|          | 5.6                 | 1.107(2)     | 3.088(5)     | 85          | 1 or 2               |
|          |                     | 0.42(1)      | 0.79(3)      | 15          | 0                    |
| (3.25)   | 293                 | 0.983(2)     | 2.731(3)     | 83          | 2                    |
|          |                     | 0.29(2)      | 0.32(2)      | 17          | 0                    |
|          | 100                 | 1.25(4)      | 2.8(1)       | 93          | 2                    |
|          |                     | 0.416(2)     | 0.807(3)     | 7           | 0                    |
|          | 5.6                 | 0.421(1)     | 0.815(2)     | >98         | 0                    |
|          |                     |              |              |             |                      |

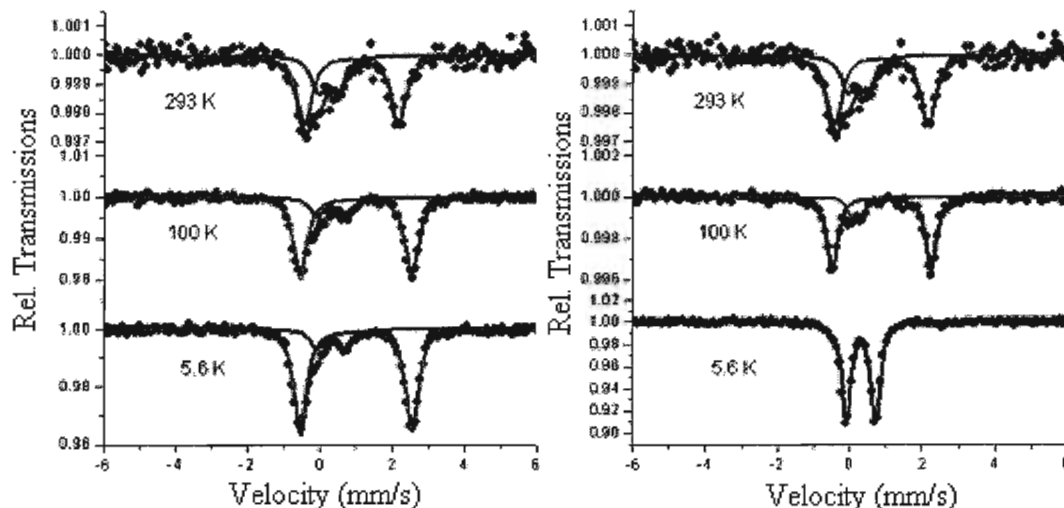


**Figure 3.23:** The Mössbauer spectra for complex (3.24) (left) and (3.25) (right) with experimental data (dots) fitted to theoretical lines

To confirm the observation of thermal spin-crossover in complex (3.24), the variable temperature Mössbauer properties of (3.24), and for comparison (3.25), have been investigated. For complex (3.25), the Mössbauer data in each case mirrors the variable temperature magnetic susceptibility data. At 293 K, the spectrum of (3.25) features two quadrupole doublets of significantly different intensity. The most intense doublet has Mössbauer parameters typical for high-spin iron(II) (Table 3.06), while the minor component features typical low-spin iron(II) parameters consistent with the variable temperature magnetic susceptibility data.<sup>125</sup> At 100 K, the intensity of the high-spin fraction is dramatically reduced, and the low-spin state is dominant (93 % of iron sites are low-spin at 100 K). At 5 K, the low-spin isomer is the only detectable component in the Mössbauer spectrum.



The spectrum of **(3.24)** at 293 K also features two quadrupole doublets, with the most intense component (68 %) featuring Mössbauer parameters consistent with high-spin iron(II) ( $S = 2$ ), and a minor component consistent with  $S = 0$  iron(II), which is in line with the data from variable temperature magnetic susceptibility measurements. However, further cooling produces a curious result. The Mössbauer spectrum at 100 K also features two quadrupole doublets, with the minor component exhibiting Mössbauer parameters consistent with  $S = 0$  iron(II), but the relative percentage of  $S = 0$  iron(II) sites has actually decreased upon cooling, which is opposite to what is expected for a typical spin-crossover, like that observed for **(3.25)**. Also of note, the value of  $\chi_m T$  at 100 K is much less ( $\chi_m T = 1.79 \text{ cm}^3 \text{ K mol}^{-1}$ ) than the expected value for a sample containing 80 %  $S = 2$  iron(II) (the theoretical value of  $\chi_m T$  is  $2.4 \text{ cm}^3 \text{ K mol}^{-1}$ , assuming a  $g$  value of 2). Between 100 and 5 K, the Mössbauer spectrum changes very little, with the intensity of the major doublet at 100 K increasing slightly at the expense of the minor doublet. Based on these observations, we speculate that complex **(3.24)** is possibly undergoing a spin-crossover to an unusual  $S = 1$  state, in addition to some small fraction of  $S = 0$  iron(II), suggesting that the energies of the  $S = 2$ , 1, and 0 states in **(3.24)** are very similar. There are no reports of pseudo-octahedral complexes undergoing such spin crossovers; however,  $S = 1$  states are more common in some 5-coordinate iron(II) complexes.<sup>8</sup> To further investigate these unusual results, variable temperature magnetization and EPR experiments are in progress, in addition to DFT calculations to help identify the relative energies of the  $S = 2$ , 1, or 0 states for complex **(3.24)**.

v) Electronic absorption spectroscopy

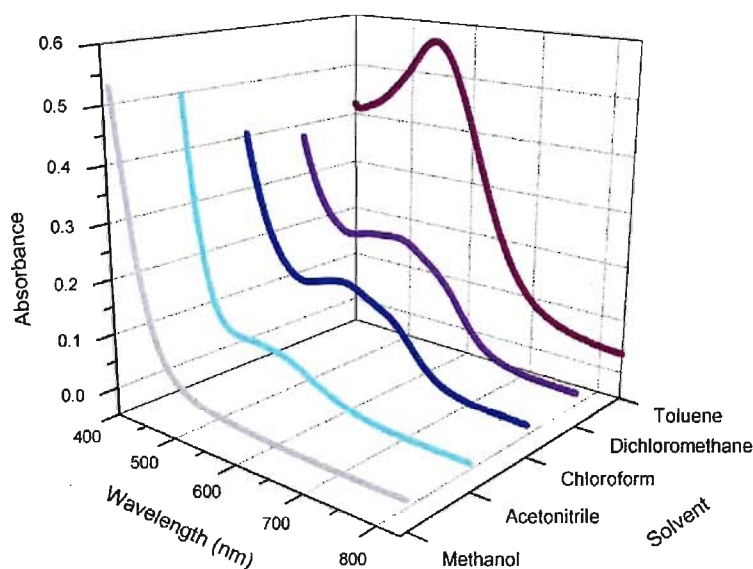


**Figure 3.24:** Solvatochromism exhibited by (3.23)

The room temperature spectra of (3.23) and (3.25) in dichloromethane feature absorption maximums at 621 nm ( $\epsilon = 1510 \text{ M}^{-1}\text{cm}^{-1}$ ) and 630 nm ( $\epsilon = 1690 \text{ M}^{-1}\text{cm}^{-1}$ ) respectively. The absorption profile of (3.24) features a maximum at 560 nm ( $\epsilon = 1850 \text{ M}^{-1} \text{ cm}^{-1}$ ) and is more intense and at higher energy in comparison to the other two complexes. All three compounds (3.23) – (3.25) feature vibrant solvatochromism. The most dramatic example, complex (3.23), is displayed in Figure 3.23 and changes from purple to colourless as the solvent polarity is increased. Also, solutions of (3.24) in dichloromethane are green initially, but after adding the electrolyte  $\text{N}(\text{C}_4\text{H}_9)_4\text{PF}_6$  used for electrochemical experiments, will appear red.

vi) Electrochemistry

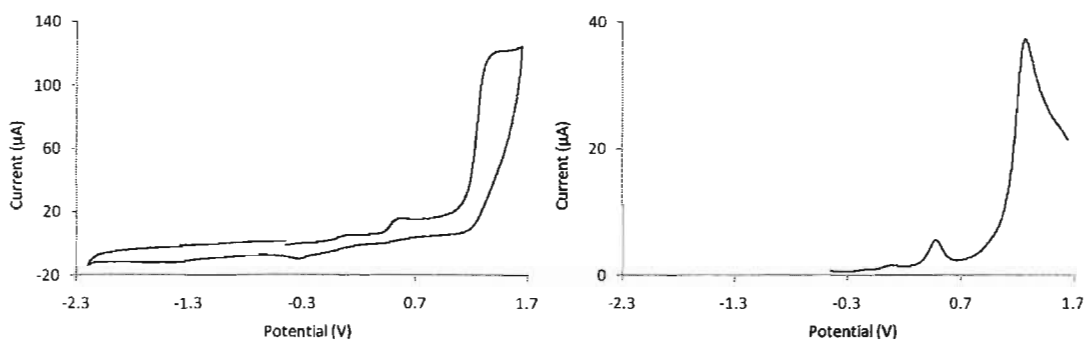


**Figure 3.25:** Cyclic (left) and differential pulse (right) voltammograms of (3.23)

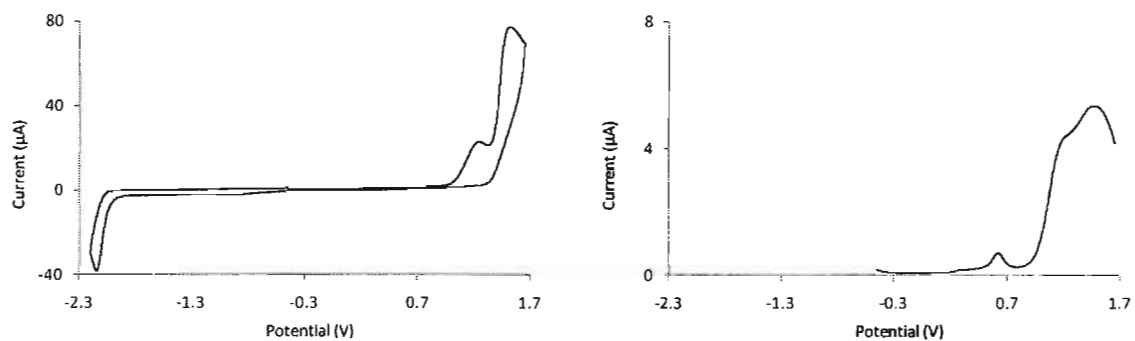


**Figure 3.26:** Cyclic (left) and differential pulse (right) voltammograms of (3.18)

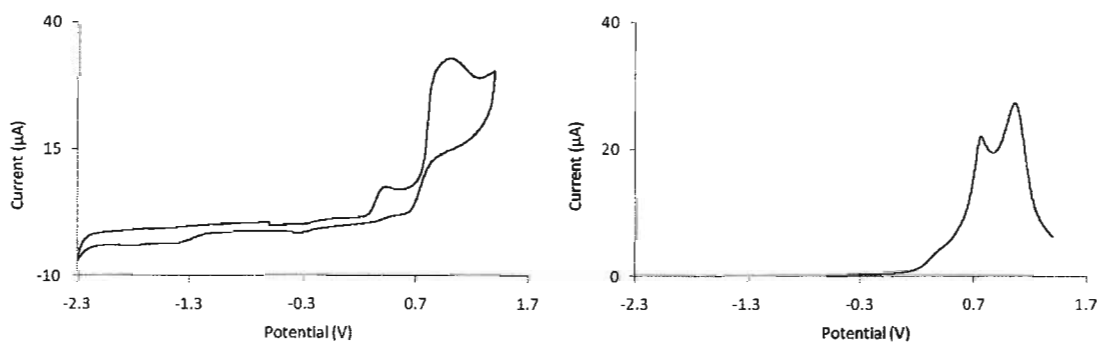


**Figure 3.27:** Cyclic (left) and differential pulse (right) voltammograms of (3.24)

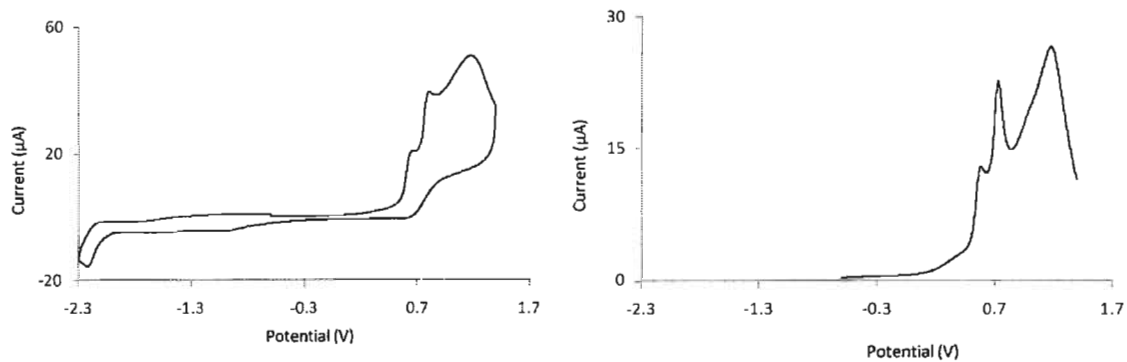


**Figure 3.28:** Cyclic (left) and differential pulse (right) voltammograms of (3.20)

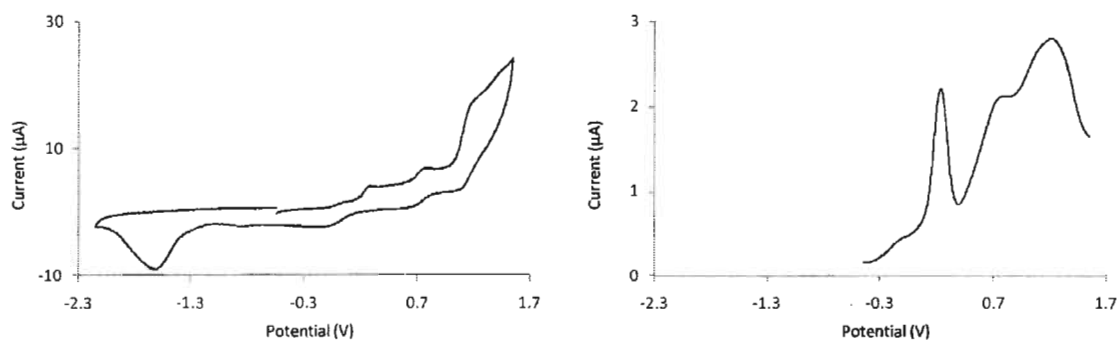


**Figure 3.29:** Cyclic (left) and differential pulse (right) voltammograms of (3.25)

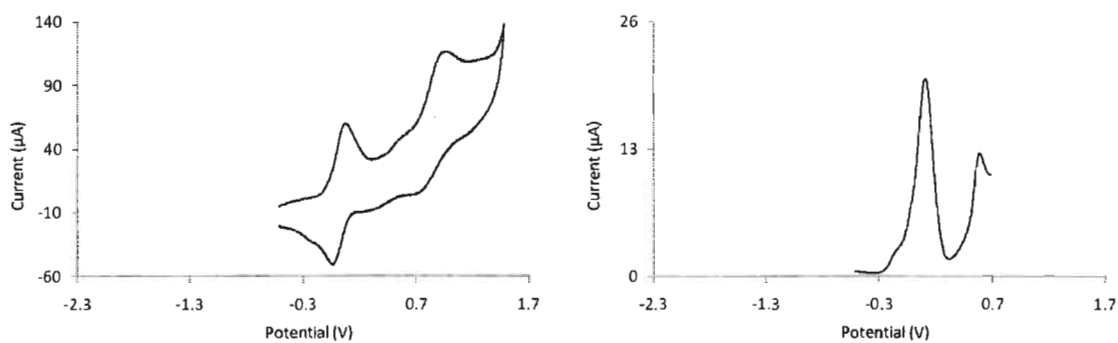


**Figure 3.30:** Cyclic (left) and differential pulse (right) voltammograms of (3.16)

---

**Table 3.07:** Electrochemical data for derivatives of **(3.16)** in DCM

| Compound      | $E^{\circ}_{\text{ox}}$ (V) vs. fc | $E^{\circ}_{\text{ref}}$ (V) vs. fc |
|---------------|------------------------------------|-------------------------------------|
| <b>(3.16)</b> | +0.6, +0.9                         | 0.0                                 |
| <b>(3.18)</b> | +0.6, +1.2, +1.5                   | -0.9, -1.5, -2.1                    |
| <b>(3.20)</b> | +0.6, +0.7, +1.2                   | -1.0, -1.6, -2.2                    |
| <b>(3.23)</b> | +0.5, +1.3                         | 0.0, -1.0, -1.4                     |
| <b>(3.24)</b> | +0.4, +0.8, +1.0                   | -0.2, -0.8, -1.6                    |
| <b>(3.25)</b> | +0.6, +1.2                         | 0.0, -0.8, -1.6                     |

---

(Refer to section **8.04** for experimental details)

---

The electrochemical properties of the complexes **(3.23)** – **(3.25)** have been investigated using cyclic and differential pulse voltammetry (**Figures 3.24, 3.26 and 3.28** respectively). In the cathodic sweeps of complexes **(3.23)** – **(3.25)**, broad and irreversible oxidation waves below potentials of -1.3 V versus ferrocene are noted in the cyclic voltammograms. The same reductions are observed at slightly higher potentials in the voltammograms of the ligands **(3.18)** and **(3.20)** and are likely attributed to imine and pyridine reduction events (**Figures 3.25 and 3.27**). In the anodic sweep of complex **(3.23)**, the  $\text{Fe}^{2+/3+}$  redox couple is observed at around 0.0 V. At potentials above +0.3 V, several broad and irreversible oxidation waves are noted in the cyclic voltammogram. Deconvolution by differential pulse techniques suggests that there are at least two distinct oxidations occurring in **(3.23)**. These waves are also present in the voltammogram of the uncoordinated ligand **(3.18)** and can be ascribed to irreversible ligand centred oxidations in the metal complexes. The oxidation of the terphenyl component likely occurs at the most positive potential hindering efforts to electrochemically polymerize **(3.23)** by repeatedly scanning over this region. Ligand **(3.18)** features an additional irreversible

oxidation centred at +1.5 V, not observed in the voltammogram of **(3.23)**, resulting from a second phenyl oxidation. The  $\text{Fe}^{2+/3+}$  redox couple of complex **(3.24)** is slightly lower in comparison to **(3.23)** and is observed at around -0.2 V. At potentials above +0.3 V broad quasi-reversible waves are noted in the cyclic voltammogram. Deconvolution by differential pulse techniques suggests that there are several oxidations occurring in **(3.24)**. These waves are also present in the voltammogram of the uncoordinated ligand **(3.20)** and can be ascribed to ligand centred oxidations in the metal complex. The oxidation of the thienyl component likely has its origin at the lowest potential, making it a suitable candidate for electrochemical polymerization. For complex **(3.25)**, a very broad  $\text{Fe}^{2+/3+}$  redox couple is present in the cyclic voltammogram around 0.0 V. A quasi-reversible peak at +0.7 V and an irreversible process at higher potentials are also observed by both the cyclic and differential pulse techniques. The oxidation of the thienyl component likely occurs at +0.7 V, but despite its quasi-reversible nature efforts towards electropolymerization were not successful. As a reference, the parent compound  $[\text{Fe}(\text{ppi})_2(\text{SCN})_2]$  **(3.16)** was also prepared, primarily to assess the potential of the  $\text{Fe}^{2+/3+}$  redox couple. Using cyclic and differential pulse techniques the oxidation was found to occur at around 0.0 V versus ferrocene and is in good agreement with compounds **(3.23)** – **(3.25)** (Figure 3.29). Refer to Table 3.06 for a list of redox events for complexes **(3.23)** – **(3.25)** and their respective precursor compounds.

## vii) Summary

Complexes (3.23) - (3.25) are stable and display spin isomerisation consistent with spin-crossover, which is favourable. However, in terms of generating polymeric materials from these complexes, the electrochemical properties of (3.24) were found to better suited for our goal, in comparison to (3.23) and (3.25), because of the low oxidation potential of the terthienyl component.

### Notes:

*A version of this chapter has been accepted for publication.*

† Cheng, H.; Djukic, B.; Jenkins, H. A.; Gorelsky, S. I.; Lemaire, M. T. *Can. J. Chem.* **2010**, submitted for publication.

## Chapter 4: Cobalt(II) valence tautomers

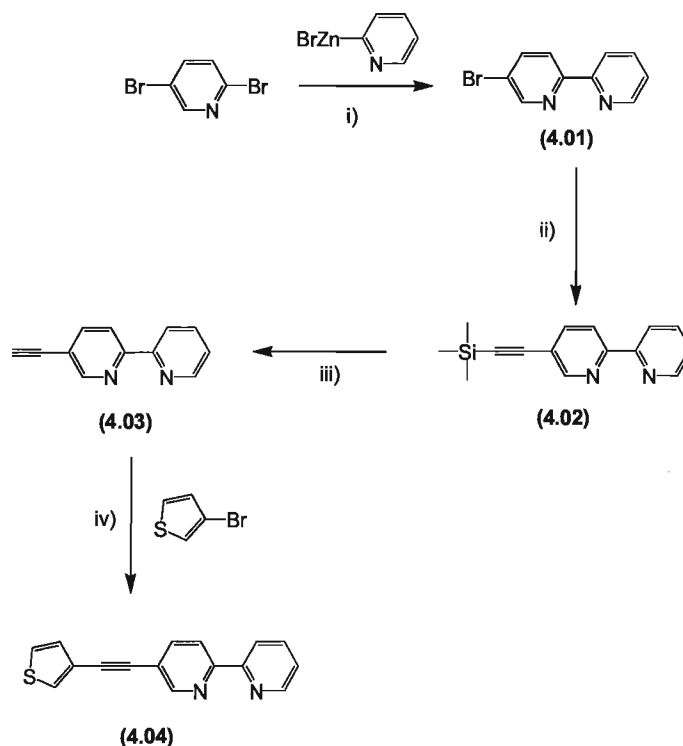
### 4.01 A valence tautomer bearing a thiophene substituent\*

#### i) Goals and objectives

Since Pierpont and Buchanan's discovery of valence tautomerism (VT) in cobalt complexes of the semiquinone radical anion, a large number of molecular complexes showing the hallmark features of VT, including cobalt–semiquinone intramolecular electron transfer coupled with a concomitant spin-crossover within the cobalt ion, have been reported. There are only a handful of published VT complexes featuring more than a single cobalt ion, including two VT coordination polymers, and VT metal–organic nanoparticles, which adds to the overall interest in the study of multi-metallic VT materials. Regarding our efforts towards the construction of complex hybrid materials that feature magnetic switching and electrical conductivity, we would also like to make use of the properties of the cobalt–semiquinone VT complexes and combine them with the conductive properties of conjugated polymers.<sup>[1,126-136]</sup>



ii) Ligand synthesis



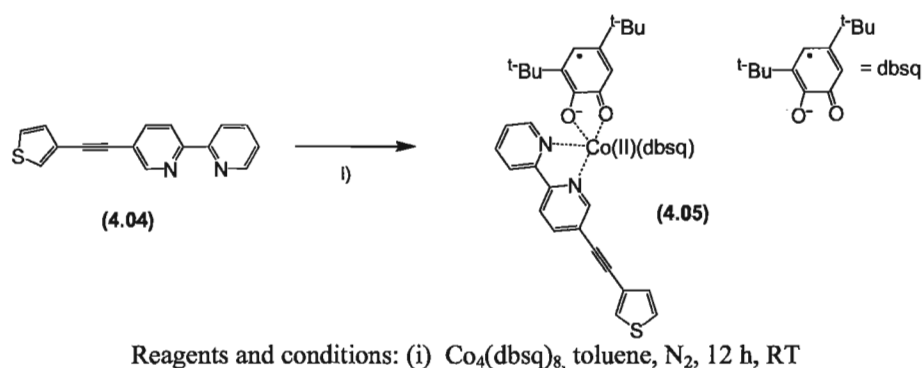
Reagents and conditions: (i)  $\text{Pd}(\text{PPh}_3)_4$ , THF,  $\text{N}_2$ , 24 h, RT (ii) TMS-acetylene,  $(i\text{-Pr})_2\text{NH}$ , 3 mol %  $\text{PdCl}_2(\text{PPh}_3)_2$ , 6 mol %  $\text{PPh}_3$ , 10 mol %  $\text{CuI}$ ,  $\text{N}_2$ , 12 h,  $105^\circ\text{C}$ . (iii)  $\text{KOH}$ ,  $\text{MeOH}$ ,  $\text{N}_2$ , 12 h, RT (iv)  $(i\text{-Pr})_2\text{NH}$ , 3 mol %  $\text{PdCl}_2(\text{PPh}_3)_2$ , 3 mol %  $\text{CuI}$ ,  $\text{N}_2$ , 12 h,  $105^\circ\text{C}$ .

**Scheme 4.01:** The synthesis of ligand **(4.04)**

A 3-ethynylthienyl substituted 2,2'-bipyridine ligand was prepared in four steps from the commercially available reagents 2,5-dibromopyridine and 3-bromothiophene (**Scheme 4.01**). An ethynyl spacer was also incorporated between these two units to help prevent steric congestion of the coordination complexes. 2-Pyridylzinc bromide solution was first used in a Negishi cross-coupling reaction with the 2,5-dibromopyridine providing **(4.01)**. A Sonogashira coupling between **(4.01)** and ethynyltrimethylsilane produced the protected acetylene precursor **(4.02)**. Deprotection of the acetylene group, followed by stirring overnight in a potassium fluoride solution, afforded **(4.03)**. Another Sonogashira

reaction between (4.03) and 3-bromothiophene afforded the ligand (4.04) that has been fully characterized. The  $^1\text{H}$ -NMR spectrum is consistent with the molecular structure displaying 10 peaks in the aromatic region that correspond to the 3 thienyl and 7 bipyridyl proton resonances.

iii) Coordination chemistry



**Scheme 4.02:** The synthesis of complex (4.05)

The ethynylthienyl-substituted derivative of 2,2'-bipyridine (4.04) was reacted with Pierpont's cobalt dbsq "tetramer" to produce complex (4.05) as an analytically pure powder (Scheme 4.02). Complex (4.05) is stable in the solid state, but decomposes in solution over a period of hours, even under dry and anaerobic conditions, which hindered our efforts to grow crystals suitable for X-ray diffraction. We are confident in the purported structure from other structural and analytical data including the FT-IR spectrum, FAB-MS and elemental analysis (including C, H, N and S).

iv) Magnetic characterization

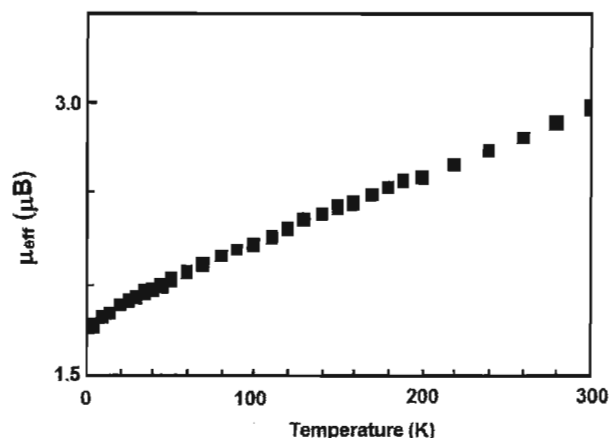


**Figure 4.01:** Variable temperature magnetic susceptibility plot for complex **(4.05)** in a 5000 Oe magnetic field<sup>[137]</sup>

Magnetic susceptibility measurements were carried out over the temperature range 2-300 K for complex **(4.05)** and the data are displayed as a plot of effective magnetic moment versus temperature (**Figure 4.01**). The profile of the data clearly suggests that valence tautomerism is operative within the complex as the magnetic moment of **(4.05)** at 2 K is 1.74  $\mu\text{B}$ , which is equal to the expected value for one unpaired electron residing in the lone coordinated dbsq ligand of the low temperature tautomer. Increasing the temperature results in a steady increase in magnetic moment, which approaches 3.0  $\mu\text{B}$  at 300 K but is less than expected for non-interacting  $S = 3/2$  cobalt(II) with two coordinated  $S = 1/2$  dbsq radicals (4.98  $\mu\text{B}$ ). The reduced moment likely results from a combination of antiferromagnetic coupling between cobalt and coordinated dbsq and the presence of some proportion of the cobalt(III)(dbsq)(dbcat) tautomer at this temperature.

v) Electronic absorption spectroscopy

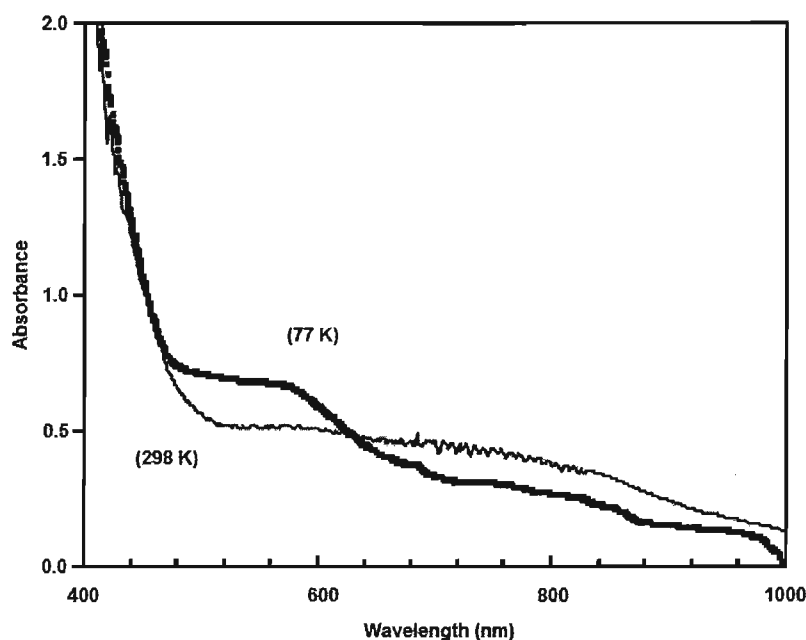


**Figure 4.02:** Variable temperature absorbance profile of **(4.05)**<sup>[137]</sup>

The electronic absorption properties of **(4.05)** were measured in an ethanol solution at 298 K, and as a frozen glass at 77 K (**Figure 4.02**). As is typical of cobalt-*bis*(semiquinone) valence tautomers, changes in temperature result in significant changes to the electronic spectrum. At 298 K, the Vis-NIR spectrum of complex **(4.05)** features broad absorptions across the visible region into the NIR. Typically, the higher temperature tautomer displays a cobalt(II)-to-semiquinone charge transfer absorption centred at approximately 800 nm. We observe a decrease in the absorbance of this band at 77 K, and an increase in the absorption of a band between 500 and 600 nm, consistent with the optical changes reported for other valence tautomers. The new, more strongly absorbing feature has a maximum absorbance at 580 nm and is characteristic of a catecholate-to-cobalt(III) charge transfer band, typical for the lower temperature

tautomer. The optical changes observed are all completely consistent with the purported valence tautomerism.

#### vi) Electrochemistry

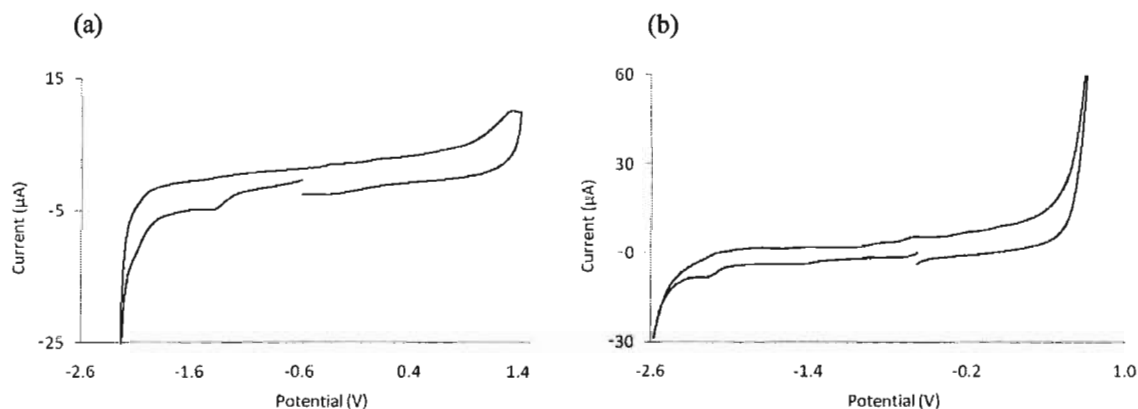


**Figure 4.03:** Cyclic voltammograms of (a) (4.04) and (b) (4.05)

**Table 4.01:** Electrochemical data for (4.04) in DCM (4.05) in DMF

| Compound | $E^{\circ}_{\text{ox}}$ (V) vs. fc | $E^{\circ}_{\text{red}}$ (V) vs. fc |
|----------|------------------------------------|-------------------------------------|
| (4.04)   | +0.8                               | -1.3                                |
| (4.05)   | +0.7                               | 0.0, -0.3, -0.7, -1.0, -2.3         |

(Refer to section 8.04 for experimental details)

The electrochemical properties of compounds (4.04) and (4.05) were studied by cyclic voltammetry in DCM and DMF solutions respectively. In the ligand (4.04), one quasi-reversible cathodic wave is observed at -1.3 V (versus fc) and is assigned to the reduction of the 2,2'-bipyridine substituent (Figure 4.03). Over anodic potentials, ligand (4.04)

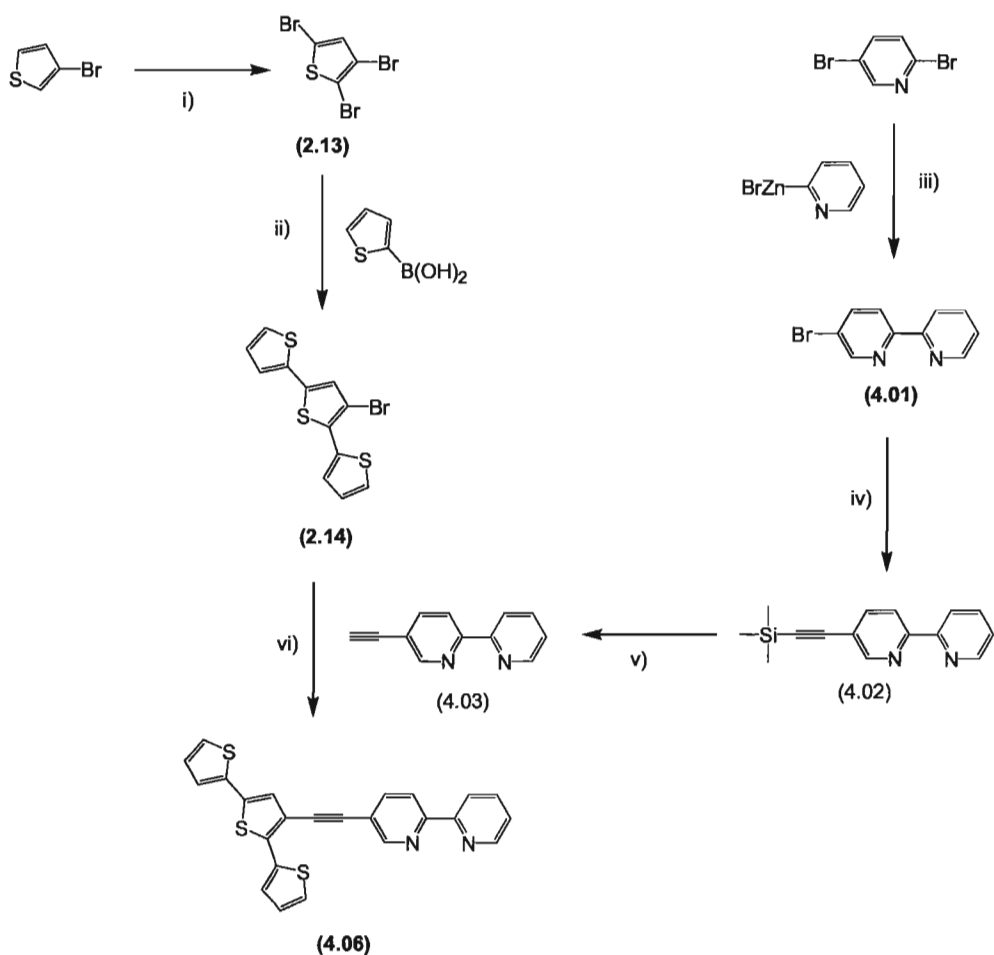
features an irreversible wave at +0.8 V, likely due to the oxidation of the thiophene ring. In the voltammogram of complex **(4.05)** a complex series of reduction processes are observed (**Figure 4.03**). At the most negative potentials two closely spaced waves are present and are attributed to the reduction of the 2,2'-bipyridine component. In comparison to the ligand **(4.04)**, these reductions occur at more negative potentials, but are typical for electronic changes that occur upon metal ion coordination. Several irreversible waves are observed between -1.1 and 0.0 V, which likely represent dbsq/dbcat and  $\text{Co}^{3+/2+}$  reduction events. Repeated cycles between 0 and +1.5 V in acetonitrile solutions of **(4.05)** did not result in electropolymerization. An increase in the peak current with increasing scan number and the deposition of an electroactive film on the working electrode were not observed. It is likely that the steric bulk of the  $[\text{Co}(\text{dbsq}_2)]$  substituent and high oxidation potential of the thiophene prevented electropolymerization. Refer to **Table 4.01** for a list of redox events for compounds **(4.04) - (4.05)**.

#### 4.02 A valence tautomer bearing a terthiophene substituent<sup>†</sup>

##### i) Extending the conjugation

A second VT target included a terthienyl analogue of **(4.05)** due to the anticipated lower oxidation potential of terthiophene and the reduction of steric interactions between bulky metal centres, both allowing for more efficient polymerization.

ii) Ligand synthesis



Reagents and conditions: (i)  $\text{Br}_2$ , 48 %  $\text{HBr}_{(\text{aq})}$ ,  $\text{Et}_2\text{O}$ , 50 °C. (ii) 2-thiopheneboronic acid, DME,  $\text{H}_2\text{O}$ , 10 mol %  $\text{PdCl}_2(\text{PPh}_3)_2$ ,  $\text{K}_2\text{CO}_3$ , 100 °C, 3 d. (iii)  $\text{Pd}(\text{PPh}_3)_4$ , THF,  $\text{N}_2$ , 12 h. (iv) TMS-acetylene,  $(i\text{-Pr})_2\text{NH}$ , 3 mol %  $\text{PdCl}_2(\text{PPh}_3)_2$ , 6 mol %  $\text{PPh}_3$ , 10 mol %  $\text{CuI}$ ,  $\text{N}_2$ , 12 h, 105 °C. (v)  $\text{KOH}$ ,  $\text{MeOH}$ ,  $\text{N}_2$ , 12 h. (vi) anhydrous DIPA, 3 mol %  $\text{PdCl}_2(\text{PPh}_3)_2$ , 3 mol %  $\text{CuI}$ ,  $\text{N}_2$ , 12 h, 105 °C.

**Scheme 4.03:** The synthesis of ligand (4.06)

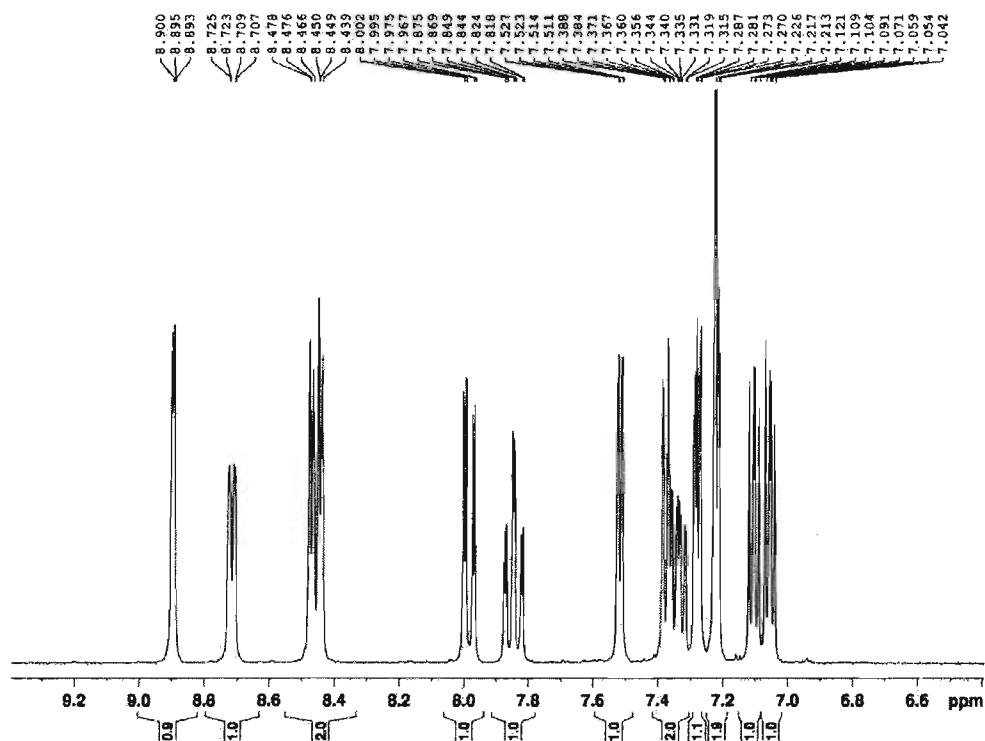
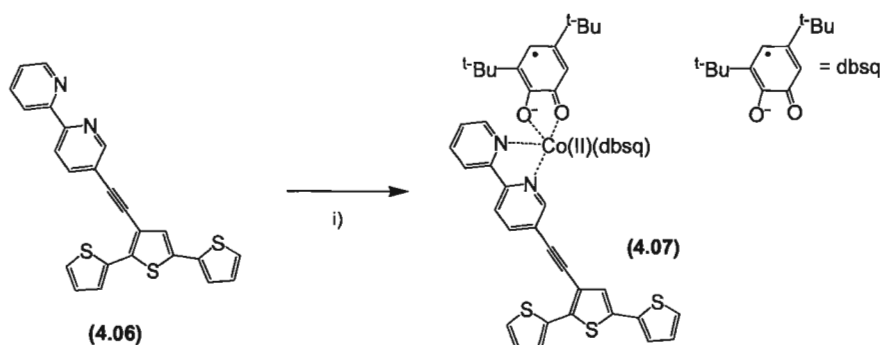


**Figure 4.04:**  $^1\text{H}$ -NMR spectrum of **(4.06)**

A 3-ethynylterthienyl substituted 2,2'-bipyridine ligand was prepared by a convergent synthesis using reagents **(2.14)** and **(4.03)** (described previously) in a Sonogashira cross-coupling to afford **(4.06)** (**Scheme 4.03**). Ligand **(4.06)** has been fully characterized and the  $^1\text{H}$ -NMR spectrum is displayed in **Figure 4.04**. The aromatic region contains 14 peaks in the aromatic region that correspond to the 7 terthienyl and 7 bipyridyl proton resonances.



iii) Coordination chemistry



Reagents and conditions: (i)  $\text{Co}_4(\text{dbsq})_8$ , toluene,  $\text{N}_2$ , 24 h, RT

**Scheme 4.04:** The synthesis of (4.07)

The terthienyl-substituted derivative of 2,2'-bipyridine (4.06) was reacted with Pierpont's cobalt dbsq "tetramer" to produce complex (4.07) as a dark green, analytically pure, powder (Scheme 4.04).<sup>[138]</sup> The stability of complex (4.07) is comparable to complex (4.05) in the solid state, but also decomposes in solution over a period of hours, even under dry and anaerobic conditions, again hindering our efforts to grow crystals suitable for X-ray diffraction. We are confident in the purported structure from other structural and analytical data, including the elemental analysis (C, H, N and S) and FAB-MS, which exhibits a peak corresponding to the ionized (4.07)<sup>+</sup> cation.

iv) Magnetic characterization

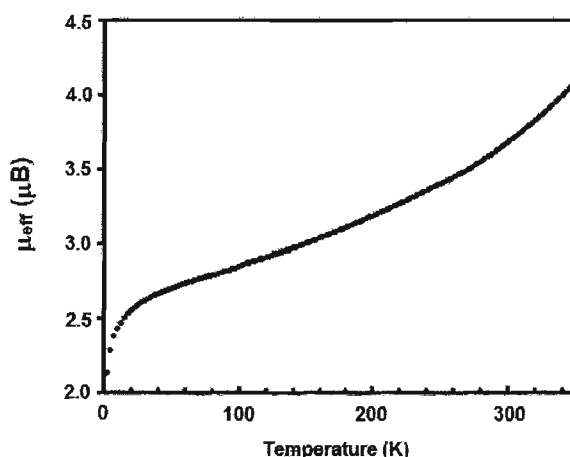


**Figure 4.05:** Variable temperature magnetic data of **(4.07)** in a 5000 Oe magnetic field<sup>[139]</sup>

Variable temperature magnetic data obtained from a powder sample of **(4.07)** confirm the presence of valence tautomerism in the solid state (**Figure 4.05**), with features that are typical for other reported and structurally related VT complexes. At the highest measured temperature (350 K), the effective magnetic moment observed from **(4.07)** is  $4.1 \mu_B$ , which indicates that the equilibrium favours the  $[(\text{dbsq})_2\text{Co}(\text{II})(\text{4.06})]$  tautomer at high temperature. With decreasing temperature, the moment gradually decreases to a final value of  $2.1 \mu_B$  at 2 K, indicating that at low temperature the equilibrium favours the expected  $[(\text{dbcat})(\text{dbsq})\text{Co}(\text{III})(\text{4.06})]$  tautomer. These observations are completely consistent with the magnetic properties observed in our other cobalt *bis*(semiquinone) VT complex **(4.05)**.

v) Electronic absorption spectroscopy

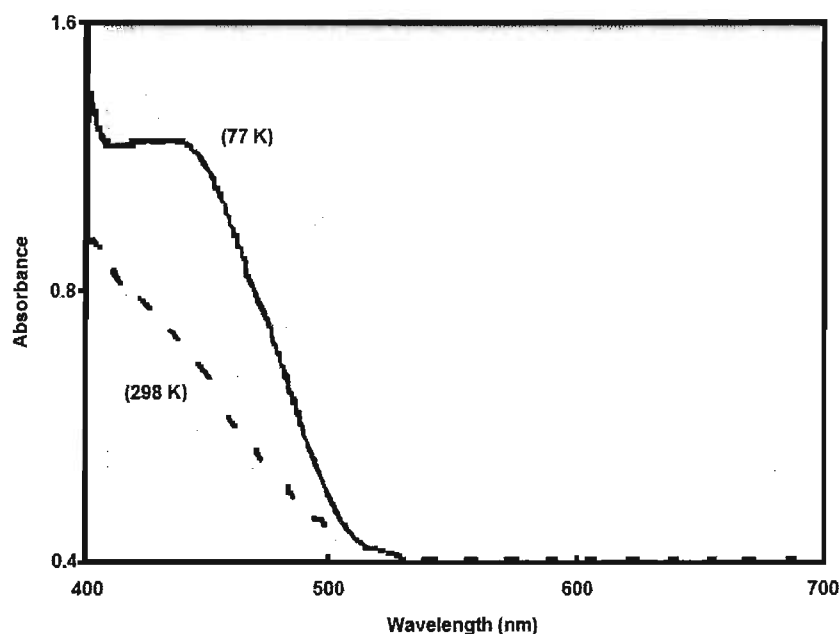


**Figure 4.06:** Variable temperature absorbance profile of (4.07) in ethanol<sup>[139]</sup>

In the absorbance spectrum of (4.07), a peak is observed in the visible region, between 400 and 600 nm, in ethanol at 298 K (**Figure 4.06**). As an ethanol glass at 77 K, the visible spectrum of (4.07) changes significantly, including an increase in absorbance between 400 and 600 nm, and the growth of a broad shoulder on the lower energy side of the 450 nm absorption. For comparison, in similar VT materials a MLCT band is typically centred at approximately 800 nm, as is observed in toluene spectra of (4.07). However, this absorption is not present in the room temperature spectrum of (4.07) in ethanol.<sup>[140]</sup>

## vi) Electrochemistry

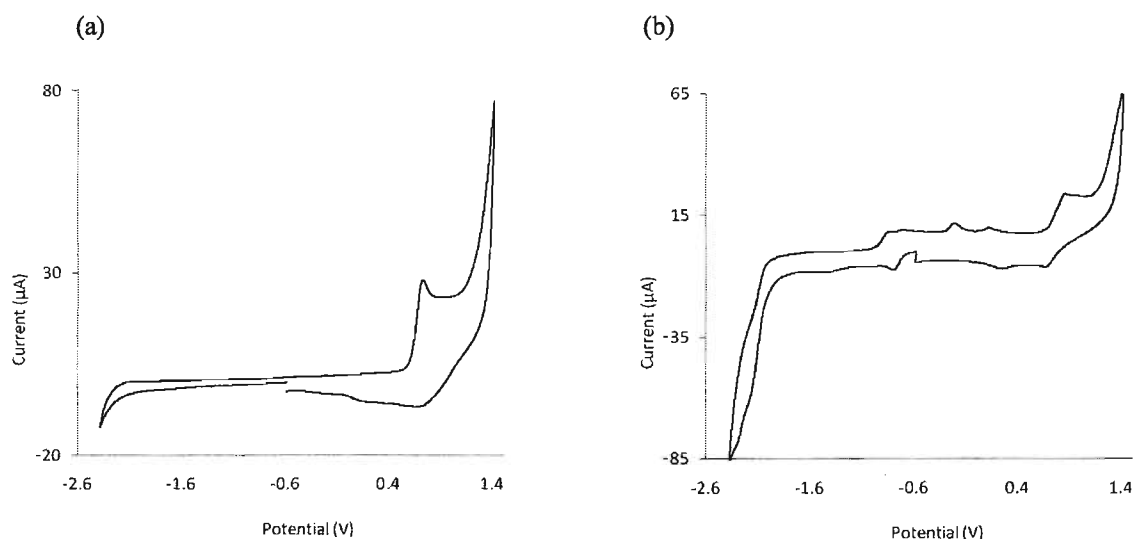


**Figure 4.07:** Cyclic voltammograms of (a) **(4.06)** and (b) **(4.07)**

**Table 4.02:** Electrochemical data for **(4.06)** and **(4.07)** in DCM

| Compound      | $E^{\circ}_{\text{ox}}$ (V) vs. fc | $E^{\circ}_{\text{ref}}$ (V) vs. fc |
|---------------|------------------------------------|-------------------------------------|
| <b>(4.06)</b> | +0.7                               | -                                   |
| <b>(4.07)</b> | +0.7                               | 0.0, -0.3, -0.7, -1.3, -2.2         |

(Refer to section 8.04 for experimental details)

The electrochemical properties of **(4.07)** were studied by cyclic voltammetry in dry and deoxygenated dichloromethane (**Figure 4.07**). A rich manifold of waves is present in the voltammogram, as is typical for cobalt–semiquinone coordination complexes. Of key interest, a quasi-reversible wave at +0.7 V (vs. ferrocene) is observed, which we can attribute to oxidation of the terthienyl substituent after comparison with the voltammogram of the ligand **(4.06)** (**Figure 4.07**). Refer to **Table 4.02** for a list of redox events for compounds **(4.06)** - **(4.07)**.

## vii) Summary

Complexes (4.05) and (4.07) exhibit valence tautomerism in the solid state, however, complex (4.05) did not undergo electropolymerization. As a result the electrochemical properties of (4.07) are better suited for further electropolymerization experiments because of the quasi-reversible nature of the terthienyl substituent.

### Notes:

*A version of this chapter has been published:*

\* O'Sullivan, T. J.; Djukic, B.; Dube, P. A.; Lemaire M. T. *Can. J. Chem.* **2009**, *87*, 533–538.

† O'Sullivan, T. J.; Djukic, B.; Dube, P. A.; Lemaire M. T. *Chem. Commun.*, **2009**, 1903-1905.

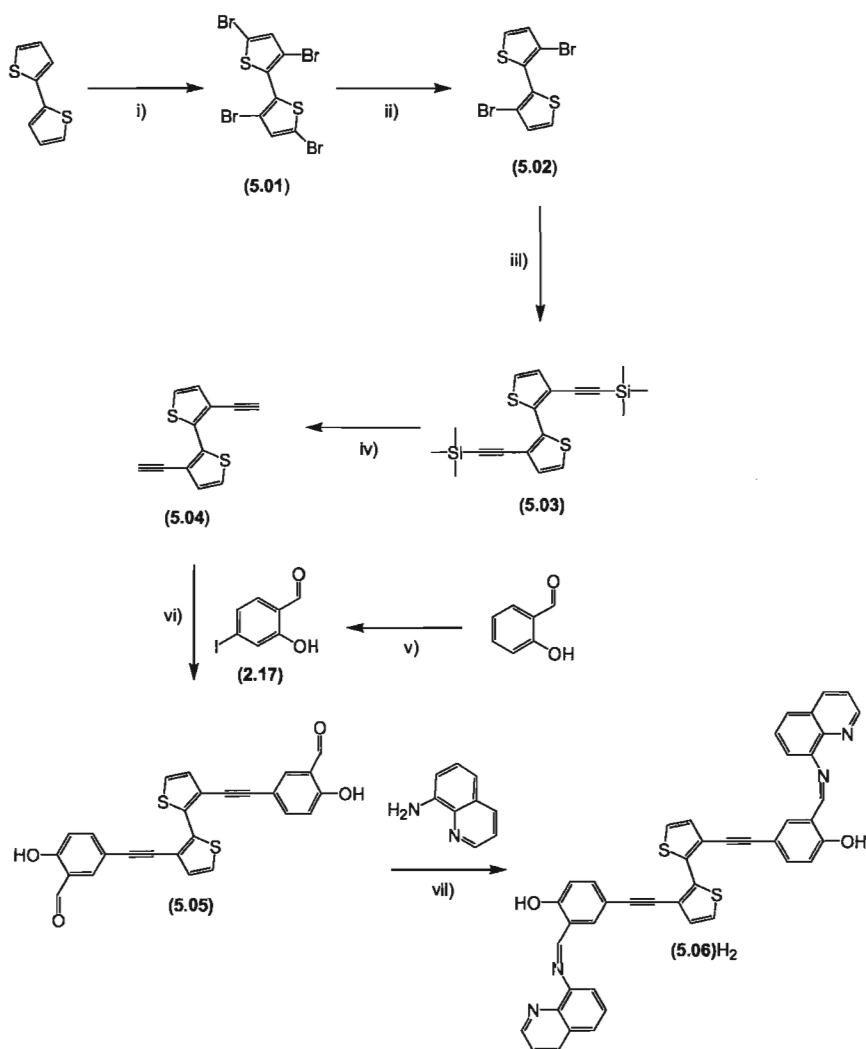
## Chapter 5: Bimetallic iron(III) spin-crossover complexes

### 5.01 Spin-crossover complexes containing a bridging *bis*-qsal ligand\*

#### i) Goals and objectives

Following the synthesis of the monometallic iron(III) SCO complex containing ligand **(2.19)** as a precursor to spin-crossover metallopolymer, we designed a bridging *bis*-qsal ligand containing a 2,2'-bithienyl linker as a logical extension of our thienyl-substituted SCO complexes. The complexes made from this ligand represent the first bimetallic qsal-type SCO materials and offer a new structural paradigm for the study of SCO in bimetallic iron(III) complexes.

ii) Ligand synthesis



Reagents and conditions: (i) Br<sub>2</sub>, CH<sub>3</sub>COOH, CHCl<sub>3</sub>, 100 °C, 24 h. (ii) Zn, EtOH, H<sub>2</sub>O, CH<sub>3</sub>COOH, HCl, 100 °C, 24 h. (iii) TMS-acetylene, DIPA, 6 mol % PPh<sub>3</sub>, 6 mol % PdCl<sub>2</sub>(PPh<sub>3</sub>)<sub>2</sub>, 6 mol % CuI, 95 °C, 20 h. (iv) MeOH, THF, KOH. (v) ICl, THF. (vi) THF, DIPA, 10 mol % PPh<sub>3</sub>, 10 mol % PdCl<sub>2</sub>(PPh<sub>3</sub>)<sub>2</sub>, 10 mol % CuI, 43 °C, 20 h. (vii) 8-aminoquinoline, THF, EtOH.

**Scheme 5.01:** The synthesis of (5.06)H<sub>2</sub>



**Figure 5.01:** The molecular structure of **(5.05)** with ellipsoids drawn at the 50 % probability level

**Table 5.01:** Selected bond distances and angles for **(5.05)**

| Atoms      | Distance (Å) | Atoms           | Angle (°) |
|------------|--------------|-----------------|-----------|
| C(5)-C(6)  | 1.201(3)     | C(9)-C(13)-O(1) | 124.4(2)  |
| C(13)-O(1) | 1.223(3)     |                 |           |

(standard deviations in the last digit are quoted in parenthesis)

Compound **(5.06)**H<sub>2</sub> was prepared in six steps from commercially available 2,2'-bithiophene (**Scheme 5.01**). Bromination of 2,2'-bithiophene generated 3,3',5,5'-tetrabromo-2,2'-bithiophene **(5.01)**, followed by a selective dehalogenation with zinc metal to produce the 3,3'-dibrominated product **(5.02)**. A Sonogashira coupling between **(5.02)** and ethynyltrimethylsilane provided **(5.03)**, which was deprotected with KOH to the rather unstable 3,3'-diethynyl-2,2'-bithiophene precursor **(5.04)**. Next, we used 5-iodosalicylaldehyde (**2.17**) in a Sonogashira reaction with **(5.04)** at 43 °C to afford the dialdehyde **(5.05)**, reproducibly and in good yield. Single crystals suitable for X-ray



analysis of compound **(5.04)** were obtained. An ORTEP diagram of the molecular structure displays the functionalized aldehyde precursor, salicylic acid, coupled to 2,2'-bithiophene through the acetylene bond of C(5) and C(6) (**Figure 5.01** and **Table 5.01**).

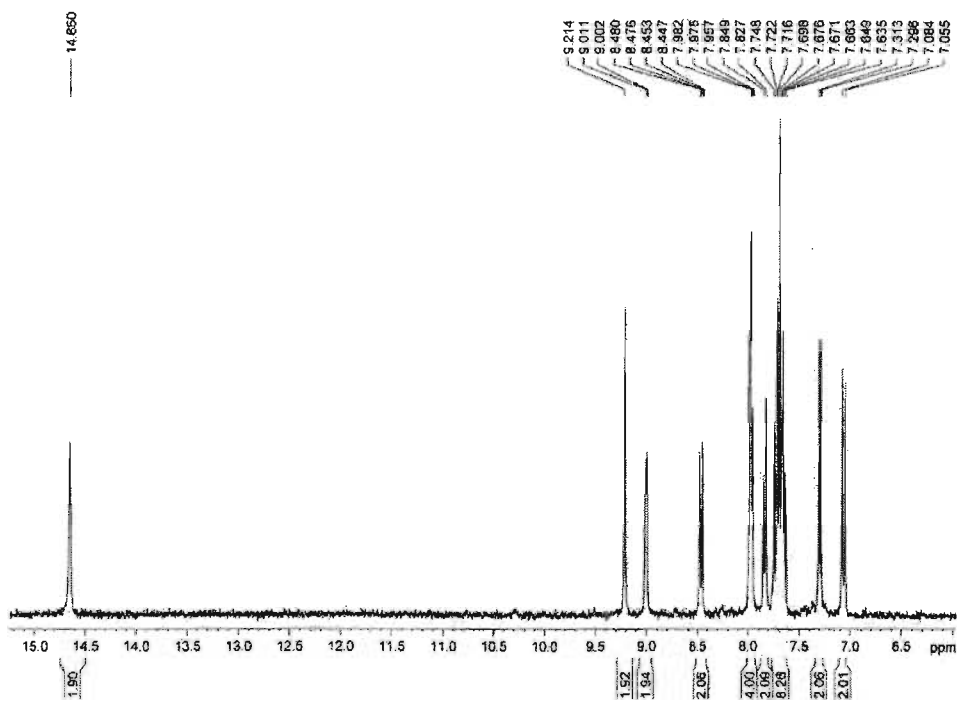
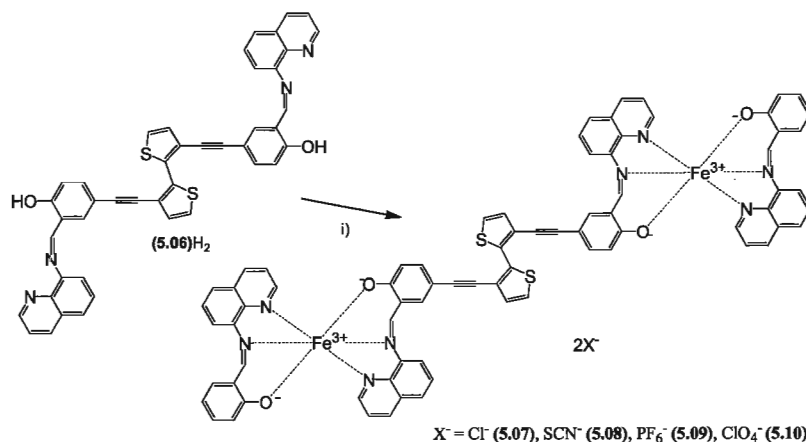


**Figure 5.02:**  $^1\text{H}$ -NMR spectrum of **(5.06)** $\text{H}_2$  in  $\text{CDCl}_3$

Compound **(5.06)** $\text{H}_2$  was isolated by reaction of **(5.05)** with four equivalents of 8-aminoquinoline, producing an orange, analytically pure solid after purification. Using less than four equivalents of 8-aminoquinoline resulted in an incomplete conversion to the diimine, which made the compound difficult to purify. Compound **(5.06)** $\text{H}_2$  was fully characterized but is unstable in solution or while stored as a solid. The  $^1\text{H}$ -NMR spectrum of **(5.06)** $\text{H}_2$  has hydroxyl and imine proton resonances at 14.7 ppm and 9.02 ppm respectively, similar to compounds **(2.01)**H, **(2.07)**H and **(2.19)**H, that are characteristic of the imine synthesis (**Figure 5.02**). Additionally, 22 peaks are observed in

the aromatic region of the spectrum, corresponding to the 4 bithienyl, 6 salicyl and 12 quinoline protons. The C=N imine absorption in the FT-IR spectrum is observed at  $1620\text{ cm}^{-1}$ .

### iii) Coordination chemistry



Reagents and conditions: (i) (**5.07**)  $\text{FeCl}_3 \cdot 6\text{H}_2\text{O}$ , (**2.01**), THF, MeOH; (**5.08**)  $\text{FeCl}_3 \cdot 6\text{H}_2\text{O}$ , (**2.01**),  $\text{NaPF}_6$ , THF, MeOH; (**5.09**)  $\text{FeCl}_3 \cdot 6\text{H}_2\text{O}$ , (**2.01**), KSCN, THF, MeOH; (**5.10**)  $\text{FeClO}_4 \cdot 6\text{H}_2\text{O}$ , THF, MeOH.

**Scheme 5.02:** The synthesis of *bis*-qsal complexes (**5.07**) – (**5.10**)

It was best to prepare bimetallic complexes containing ligand (**5.06**) after producing the ligand *in situ* from (**5.05**) rather than isolating the solid because of the instability of (**5.06**). The bimetallic iron(III) complex (**5.07**), containing two  $\text{Cl}^-$  counteranions, was prepared first by reaction of two equiv of  $\text{FeCl}_3 \cdot 6\text{H}_2\text{O}$  with (**5.06**) (Scheme 5.02). The addition of stoichiometric amounts of ligand (**2.01**) followed, in order to “cap” the available coordination sites on the iron centres. These steps produced an analytically pure powder that served as the starting point for the preparation of complexes (**5.08**) and (**5.09**). When attempting to generate the bimetallic complexes in one step, by combining

(**5.06**)H<sub>2</sub> with an iron(III) salt and 2 equiv of (**2.01**)H, we isolated a significant amount of [Fe(**2.01**)<sub>2</sub>]<sup>+</sup> with very little bimetallic product. Complexes (**5.08**) and (**5.09**), containing PF<sub>6</sub><sup>-</sup> and SCN<sup>-</sup> counteranions, respectively, were generated by metathesis of (**5.08**) with aqueous solutions containing an excess of NaPF<sub>6</sub> or KSCN. The perchlorate analogue (**5.10**) was prepared in a more direct manner by reacting (**5.06**) with Fe(ClO<sub>4</sub>)<sub>3</sub>·9H<sub>2</sub>O followed by addition of two equiv of (**2.01**)H. Complexes (**5.07**) - (**5.10**) are analytically pure powders that provide characteristic mass spectra, which include fragments of the molecular ion with either one or two counteranions removed. The complexes have very similar FT-IR spectra that all include the expected imine absorption around 1603 cm<sup>-1</sup>, which is shifted to lower energy in comparison to the same absorption in the uncoordinated ligand (**5.06**)H<sub>2</sub>. The only significant differences in the FT-IR spectra of (**5.07**) - (**5.10**) result from the absorptions of the different counteranions.

iv) Magnetic characterization

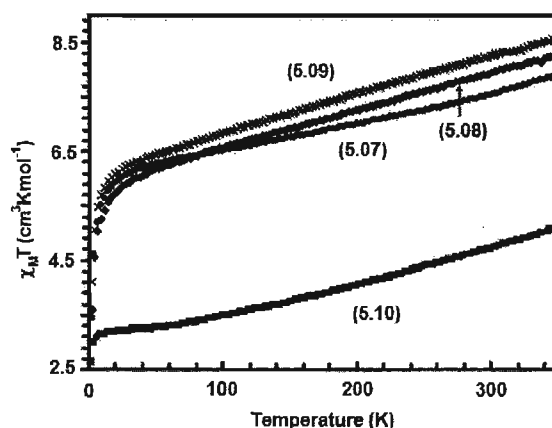


**Figure 5.03:** Variable temperature magnetic susceptibility of (**5.07**) - (**5.10**) in a 5000 Oe magnetic field<sup>[141]</sup>

Evidence for temperature dependent spin-crossover behaviour for each of the complexes is provided by variable temperature magnetic susceptibility, Mössbauer and ESR spectroscopy. First, we recorded magnetic susceptibility measurements on analytically pure powdered samples of **(5.07)** - **(5.09)** using a SQUID magnetometer between 2 - 350 K and found that their variable temperature magnetic properties are similar. For each complex, data are displayed as plots of  $\chi_M T$  versus  $T$ , and each plot features a very gradual decrease in  $\chi_M T$  with decreasing temperature toward 20 K, followed by a more rapid decrease between 20 K and 2 K (**Figure 5.03**). No hysteresis is observed upon warming from 2 K back to 350 K, which is typical behaviour for iron(III) spin-crossover systems. The  $\chi_M T$  values at 350 K for **(5.07)** – **(5.09)** are slightly less than the anticipated values for two high-spin ( $S = 5/2$ ) iron(III) ions in the absence of any magnetic coupling with a theoretical spin-only value of  $8.75 \text{ cm}^3\text{Kmol}^{-1}$ . The lower  $\chi_M T$  values that we observe at 350 K likely result from some proportion of the lower-spin isomer present at this temperature and are not the result of any intramolecular antiferromagnetic coupling (see Mössbauer). At the lowest measured temperature of 2 K,  $\chi_M T$  values for **(5.07)** - **(5.09)** indicate a lower spin state, but not the expected  $S = 1/2$  for each iron(III) atom in the low-spin state, which would have a theoretical value of  $0.75 \text{ cm}^3\text{Kmol}^{-1}$ . Rather, the  $\chi_M T$  values observed at 2 K are approximately  $3.5 \text{ cm}^3\text{Kmol}^{-1}$  at 2K and suggest an incomplete spin-crossover for each of **(5.07)** - **(5.09)**.

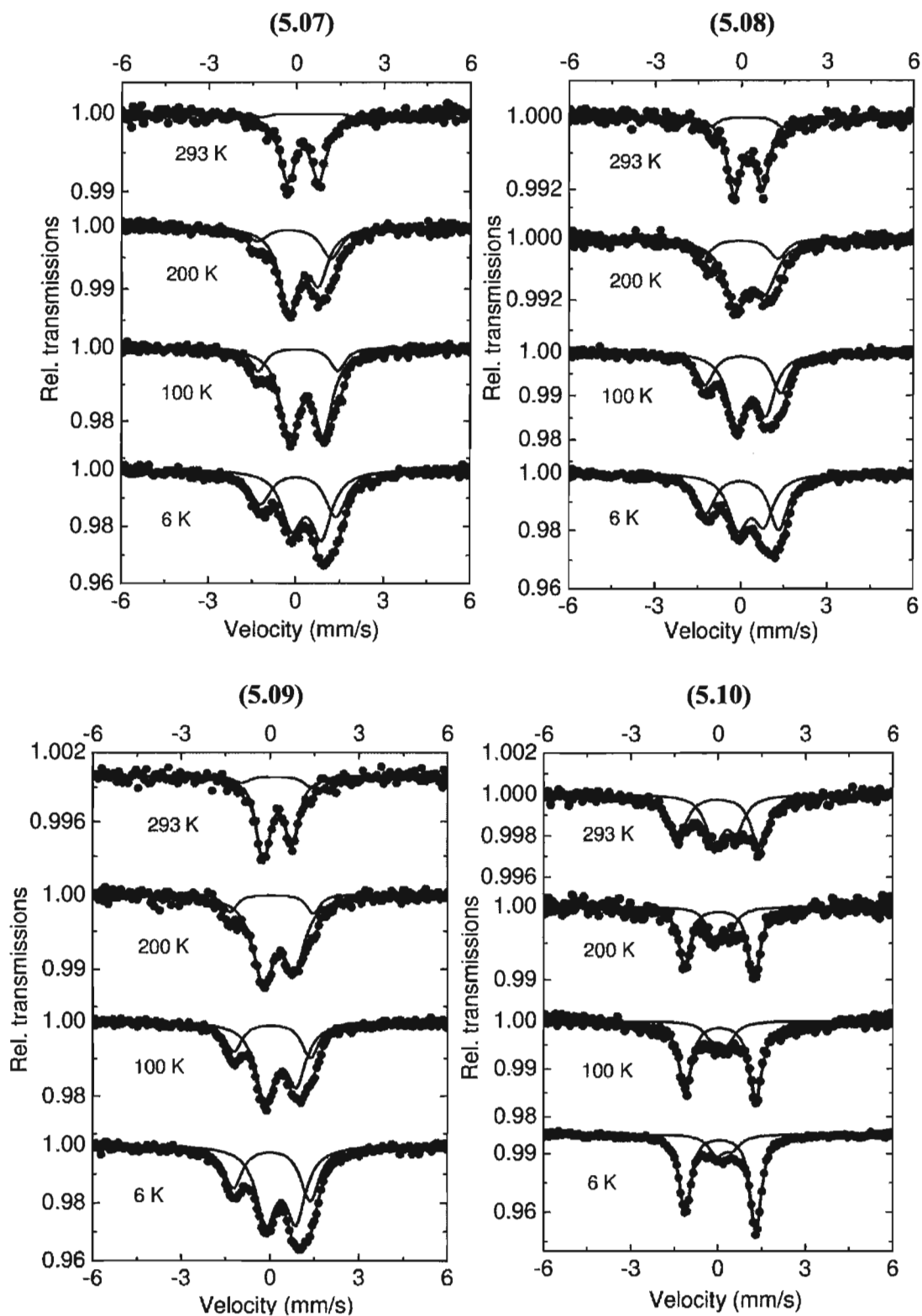


**Figure 5.04:** Variable temperature Mössbauer data for complexes (5.07) - (5.10), experimental data (dots) fitted to theoretical lines<sup>[141]</sup>

**Table 5.02: Mössbauer data for (5.07) - (5.10)**

| Compound | Temperature<br>(°C) | IS<br>(mm/s) | QS<br>(mm/s) | Site<br>(%) | Fe(III)<br>Spin State |
|----------|---------------------|--------------|--------------|-------------|-----------------------|
| (5.07)   | 293                 | 0.34(1)      | 1.07(1)      | 95          | 5/2                   |
|          |                     | 0.40(9)      | 3.2(4)       | 5           | 1/2                   |
|          | 200                 | 0.34(1)      | 0.96(2)      | 74          | 5/2                   |
|          |                     | 0.07(2)      | 2.48(3)      | 26          | 1/2                   |
|          | 100                 | 0.44(1)      | 1.08(1)      | 72          | 5/2                   |
|          |                     | 0.14(1)      | 2.58(3)      | 28          | 1/2                   |
|          | 6                   | 0.49(1)      | 1.01(5)      | 58          | 5/2                   |
|          |                     | 0.19(1)      | 2.59(5)      | 42          | 1/2                   |
| (5.08)   | 293                 | 0.35(1)      | 0.92(2)      | 88          | 5/2                   |
|          |                     | 0.31(7)      | 2.6(1)       | 12          | 1/2                   |
|          | 200                 | 0.43(3)      | 1.03(5)      | 80          | 5/2                   |
|          |                     | 0.11(4)      | 2.54(1)      | 20          | 1/2                   |
|          | 100                 | 0.47(1)      | 1.05(2)      | 69          | 5/2                   |
|          |                     | 0.18(1)      | 2.65(3)      | 31          | 1/2                   |
|          | 6                   | 0.47(2)      | 0.91(3)      | 58          | 5/2                   |
|          |                     | 0.17(1)      | 2.55(2)      | 42          | 1/2                   |
| (5.09)   | 293                 | 0.36(1)      | 0.96(1)      | 87          | 5/2                   |
|          |                     | 0.30(9)      | 2.4(1)       | 13          | 1/2                   |
|          | 200                 | 0.36(1)      | 0.93(2)      | 72          | 5/2                   |
|          |                     | 0.11(2)      | 2.53(4)      | 28          | 1/2                   |
|          | 100                 | 0.43(1)      | 0.98(1)      | 62          | 5/2                   |
|          |                     | 0.14(1)      | 2.57(2)      | 38          | 1/2                   |
|          | 6                   | 0.49(1)      | 1.01(5)      | 58          | 5/2                   |
|          |                     | 0.19(1)      | 2.59(5)      | 42          | 1/2                   |
| (5.10)   | 293                 | 0.26(2)      | 0.76(3)      | 45          | 5/2                   |
|          |                     | 0.13(1)      | 2.78(2)      | 56          | 1/2                   |
|          | 200                 | 0.25(3)      | 0.58(5)      | 30          | 5/2                   |
|          |                     | 0.16(1)      | 2.39(3)      | 70          | 1/2                   |
|          | 100                 | 0.16(4)      | 0.51(5)      | 23          | 5/2                   |
|          |                     | 0.19(1)      | 2.42(1)      | 77          | 1/2                   |
|          | 6                   | 0.33(2)      | 0.55(2)      | 20          | 5/2                   |
|          |                     | 0.20(1)      | 2.43(2)      | 80          | 1/2                   |

To help support our interpretation of the data from variable temperature magnetic susceptibility studies, we have also obtained Mössbauer spectra for complexes (5.07) – (5.09) at 293, 200, 100, and 6 K. The data are plotted for each complex (Figure 5.04)

and Mössbauer parameters for all complexes are listed in **Table 5.02**. As expected from the magnetic data, complexes **(5.07)** – **(5.09)** share similar Mössbauer properties and indicate the presence of two different sets of spin states in thermal equilibrium with one another. For **(5.07)** – **(5.09)** the Mössbauer spectra at 293 K each display a doublet with quadrupole splittings (0.92 mm/s – 1.07 mm/s) and isomer shifts (0.3 mm/s – 0.4 mm/s) that are typical for other reported monometallic high-spin iron(III) *bis*-qsal complexes. Another smaller component with Mössbauer parameters that suggest an  $S = 1/2$ ,  $1/2$  state is also observed at this temperature.<sup>[25,142-143]</sup> As the temperature decreases, the intensity of the high-spin doublet also decreases and is accompanied by an intensity increase in the low-spin doublet. The changes in the proportion of each state are small and occur slowly, reflecting the variable temperature magnetic data. At 6 K the Mössbauer spectrum of **(5.07)** indicates 58 % high-spin and 42 % low-spin components, which has a theoretical  $\chi_M T$  value of 5.39 cm<sup>3</sup>K mol<sup>-1</sup> that is similar to the value 5.2 cm<sup>3</sup>Kmol<sup>-1</sup> observed for magnetic susceptibility measurements at this temperature. Together, the variable temperature susceptibility and Mössbauer data suggest that over half of the iron(III) in **(5.07)** – **(5.09)** is in the high-spin state at low temperature. The mixed spin states can be interpreted in several ways, but a comparison of the coordinate bond lengths in the low temperature X-ray crystal structure of each complex would be required to make an accurate conclusion.

The variable temperature magnetic susceptibility profile for complex **(5.10)** is significantly different from those observed for **(5.07)** – **(5.09)**. The magnetic susceptibility data at 350 K,  $\chi_M T$  for **(5.10)** is 5.1 cm<sup>3</sup>Kmol<sup>-1</sup> and suggests a considerably

larger component of the iron(III) low-spin state at this temperature. At 293 K, the Mössbauer spectrum suggests that 55 % of the iron(III) is in the low spin state, which is mirrored by the  $\chi_M T$  value of  $4.7 \text{ cm}^3 \text{Kmol}^{-1}$  when compared to the anticipated  $4.3 \text{ cm}^3 \text{Kmol}^{-1}$  for this proportion. In the Mössbauer spectrum of (5.10), the doublet associated with the low-spin iron(III) increases in intensity and the high-spin doublet decreases with decreasing temperature. At 6 K, the data indicates 20 % high-spin and 80 % low-spin, which is again supported by the  $\chi_M T$  value of  $3.1 \text{ cm}^3 \text{Kmol}^{-1}$  observed at 6 K and is close to the expected value of  $2.4 \text{ cm}^3 \text{Kmol}^{-1}$ . The different magnetic properties observed from (5.10) are not unprecedented and likely have their origins in different structural properties compared with (5.07) – (5.09) that occur as a result of changing the counterions.<sup>[72,96-98]</sup>

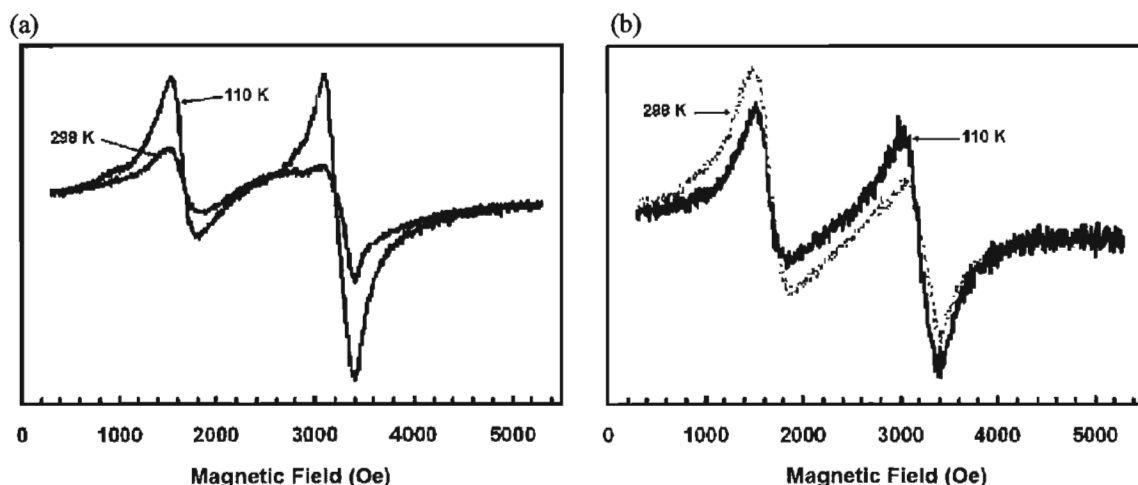


**Figure 5.05:** Powder ESR spectra of (a) (5.09) and (b) (5.10)<sup>[141]</sup>

ESR spectra were obtained from powder samples of each complex at 298 and 110 K, and reflect the magnetic susceptibility and Mössbauer analysis. ESR spectra for complex (5.09) are displayed beside (5.10) (Figure 5.05). For comparison, the spectra of (5.07)



and (5.08) are nearly identical to (5.09). The room temperature spectrum of (5.09) indicates the presence of both high-spin ( $g = 4.3$ ) and low-spin ( $g = 2.1$ ) iron(III). As the temperature is decreased to 110 K, the resonances become slightly more resolved and intense but still provide  $g$ -values that are similar to those observed in the room temperature spectrum and support the Mössbauer and magnetic susceptibility data presented previously. The broadness of the resonances is attributed to spin-spin interactions that have been observed for other iron(III) spin-crossover complexes.<sup>[144-145]</sup> The ESR spectra of complex (5.10) exhibit nearly identical peaks at each temperature, with only small intensity differences resulting from the small decrease in the proportion of the high-spin isomer between these temperatures.

#### v) Electrochemistry

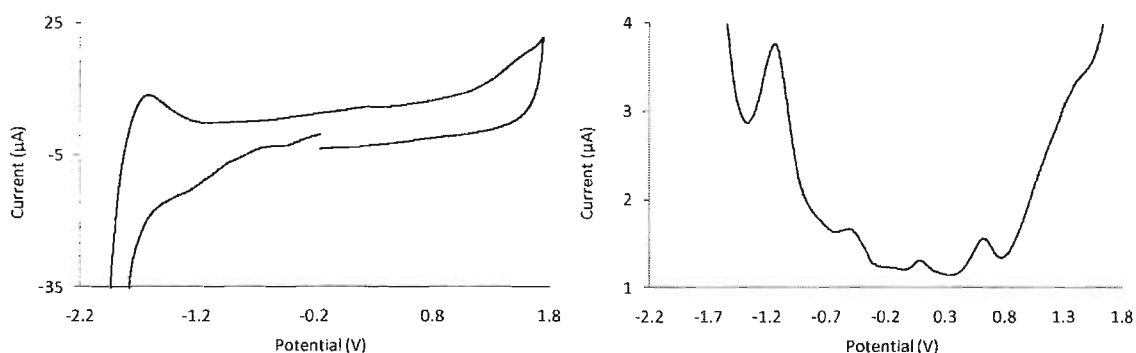


**Figure 5.06:** Cyclic (left) and differential pulse (right) voltammograms of (5.07)

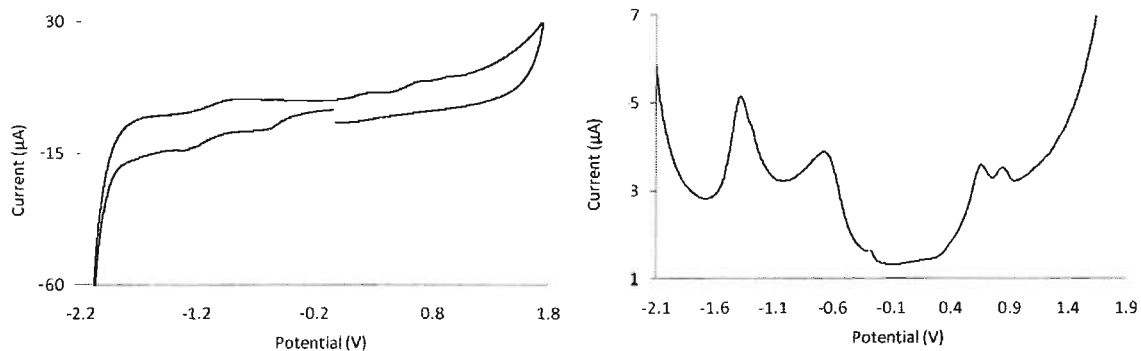


**Figure 5.07:** Cyclic (left) and differential pulse (right) voltammograms of (5.08)

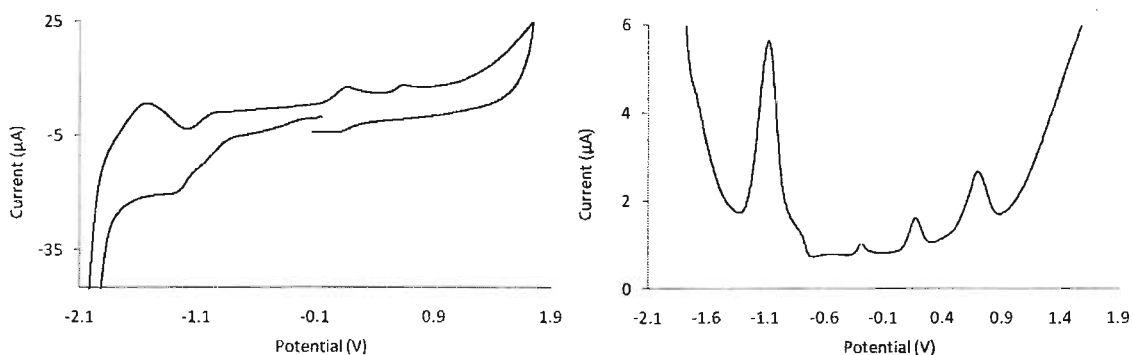


**Figure 5.08:** Cyclic (left) and differential pulse (right) voltammogram of (5.09)

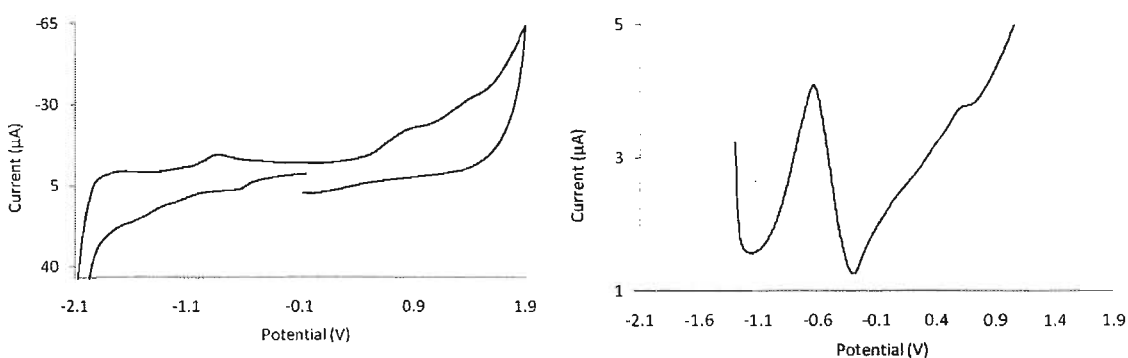


**Figure 5.09:** Cyclic (left) and differential pulse (right) voltammogram of (5.10)

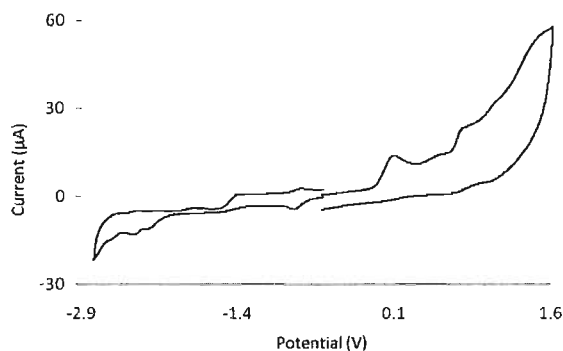


**Figure 5.10:** The cyclic voltammogram of **(5.06)**H<sub>2</sub>

**Table 5.03:** Electrochemical data for **(5.06)**H<sub>2</sub> – **(5.10)** in ACN

| Compound                     | E° <sub>ox</sub> (V) vs. fc | E° <sub>red</sub> (V) vs. fc |
|------------------------------|-----------------------------|------------------------------|
| <b>(5.06)</b> H <sub>2</sub> | +0.2, +0.6, +0.9, +1.2      | -0.7, -2.1, -2.3             |
| <b>(5.07)</b>                | +0.3, +0.8, +1.1            | -0.6                         |
| <b>(5.08)</b>                | +0.4, +0.6, +1.1            | -0.6                         |
| <b>(5.09)</b>                | +0.4, +0.9, +1.1            | -0.7                         |
| <b>(5.10)</b>                | +0.5, +1.1                  | -0.6                         |

(Refer to section 8.04 for experimental details)

The electrochemical properties of complexes **(5.07)** – **(5.10)** have been investigated using cyclic and differential pulse voltammetry and are very similar to those observed for the reported monometallic iron(III) complexes of ligand **(2.07)** (**Figures 5.06 – 5.09**). In the anodic sweep of complexes **(5.07)** - **(5.10)**, broad and irreversible oxidation waves above potentials of +0.1 V (versus fc) are noted in the cyclic voltammograms. Deconvolution by differential pulse techniques suggests that there are at least three distinct anodic processes in **(5.07)** - **(5.10)**, all at similar potentials in each complex. These waves are also present in the voltammogram of the uncoordinated ligand **(5.06)**H<sub>2</sub> and can be

ascribed to irreversible ligand based oxidations in the metal complexes (**Figure 5.10**). The oxidation of the 2,2'-bithienyl bridge likely occurs at the most positive of these oxidations, and we attempted to electrochemically polymerize (**5.07**) – (**5.10**) by repeatedly scanning over this region. No polymerization was observed, however, due to a combination of poor monomer solubility, steric congestion, and the high irreversible 2,2'-bithienyl oxidation potential. Ligand (**5.06**)H<sub>2</sub> features another irreversible oxidation centred at +0.2 V, which is not observed in the voltammograms of (**5.07**) – (**5.10**), and likely results from the oxidation of the hydroxyl group. Also, due to the instability of (**5.06**) in solution, it is possible that some of the observed waves in the voltammograms of complexes (**5.07**) – (**5.10**) could have originated from decomposition products. Over cathodic potentials, one quasi-reversible wave, representing iron(III) reduction, is centred at potentials around -0.6 V for (**5.07**) – (**5.10**). At more negative potentials, broad irreversible processes, likely due to the imine reduction, are observed. Refer to **Table 4.02** for a list of redox events for compounds (**5.06**)H<sub>2</sub> - (**5.10**).

#### vi) Summary

The bimetallic complexes (**5.07**) – (**5.10**) exhibited spin-crossover that was gradual and incomplete, similar to the iron(III) complexes of Chapter 2. Therefore, linking two spin-crossover components together through the bithiophene bridge did not adversely affect the magnetic properties. However, like the complexes made from ligand (**2.07**) in Chapter 2, complexes (**5.07**) – (**5.10**) are unsuitable for electrochemical polymerization.

**Notes:**

*A version of this chapter has been published.*

- \* Djukic, B.; Poddutoori, P. K.; Dube, P. A.; Seda, T.; Jenkins, H. A.; Lemaire, M. T.  
*Inorg. Chem.* **2009**, 48, 6109–6116

## Chapter 6: Polymeric materials

### 6.01 Conjugated polymers

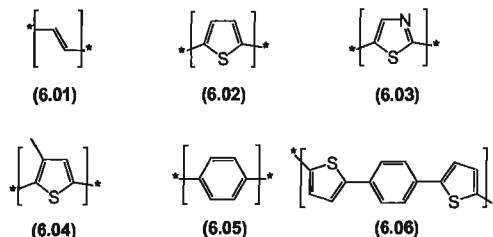


**Figure 6.01:** Conjugated polymers (i) polyacetylene (6.01), (ii) polythiophene (6.02), (iii) polythiazole (6.03), (iv) poly(3-methylthiophene) (6.04), (v) polyphenylene (6.05), (vi) poly(thiophene-phenylene-thiophene) (6.06)

Conjugated polymers are materials that feature an extended  $\pi$ -system along the polymer backbone and, generally, exhibit unique electronic properties, including high electrical conductivity when doped (*vide infra*), and electrochromism. Typical examples of  $\pi$ -conjugated polymers (6.01) – (6.06) are shown in **Figure 6.01**. Significant efforts have focused on the synthesis of conjugated polymers with pendant functional groups to enhance their physical properties.<sup>[146-148]</sup>

#### i) Electrical conductivity in conjugated polymers

Alan J. Heeger, Alan G. MacDiarmid and Hideki Shirakawa were awarded the Nobel Prize for Chemistry in 2000, for their discovery that electrical conductivity can be achieved within conjugated polymers. Electrical conductance ( $\sigma$ ) is measured in siemens (S) and expresses the ability of electricity to flow through a material. The conductance is the reciprocal of resistance and is determined through Ohm's law (Eq. 6.1) by applying a

known potential ( $U$ ) across the material and measuring the current ( $I$ ) that passes through it (Eq. 5).<sup>[149]</sup>

$$\sigma = I/U \quad (\text{Eq. 4})$$

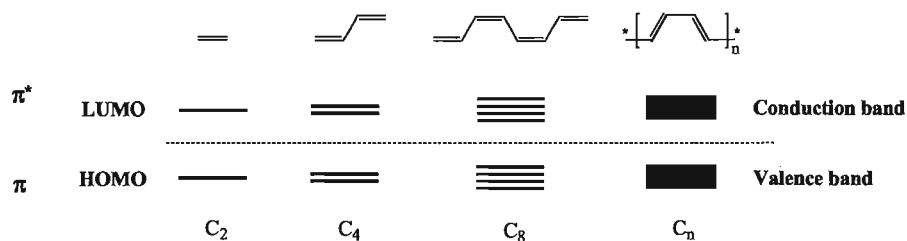


**Figure 6.02.** Energy band diagram for increasing lengths of (6.01)<sup>[150]</sup>

Conjugated  $\pi$ -bonds are a key aspect of the conductive properties of polymers because they allow electrons to become delocalized throughout the entire length of the polymeric chain. The  $\pi$  electrons are in the highest occupied molecular orbital (HOMO) of the polymer and have properties similar to the *valence band* in a solid-state semiconductor due to Peirels distortions and slightly non-degenerate energy levels along the chain (Figure 6.02). The lowest unoccupied molecular orbital (LUMO) of the polymer signifies the lowest energy level of the *conduction band* and the energy separation between the HOMO and the LUMO defines the *band gap*.<sup>[150]</sup>

Conjugation is not the only attribute of the polymer that results in conductivity because the electrons must also be able to travel freely through the polymer. Conductivity can be achieved by partial occupation of the valence band by removing an electron and introducing a hole in the LUMO where other electrons can travel. Electrons can also be

directly injected into the conduction band of the polymer and are free to accelerate under the influence of an applied electric field. The process of creating these partially filled bands and the charge carriers (hole and electron pairs) is called *doping* and also derives its name from an analogy to solid-state semiconductors.<sup>[151]</sup> Electrical conductivity can also be achieved through derivatization by reducing the energy gap separating the conduction and valence bands allowing for redistribution between electrons and holes at higher and lower energy levels.<sup>[152]</sup>

## ii) P-doped conducting polymers

Conducting polymers are said to be p-doped when a hole is introduced into the valence band. In 1977 Heeger, MacDiarmid and Shirakawa discovered that oxidation of polyacetylene (6.01) films with halogen vapour made them up to  $10^9$  times more conductive in comparison to non-oxidized polyacetylene films.<sup>[153-154]</sup> The doped form of polyacetylene can have electrical conductivity values exceeding  $10^5 \text{ Sm}^{-1}$ , which was higher than any previously known polymer. Teflon (6.07), a polymeric insulator, and silver, a metallic conductor, for comparison have conductivities of  $10^{-22} \text{ Sm}^{-1}$  and  $10^8 \text{ Sm}^{-1}$ , respectively. Since Heeger, MacDiarmid and Shirakawa's discovery, many p-doped conducting polymers have been reported, most notably polythiophene (6.02), which is used extensively in a variety of organic materials due to its stability.<sup>[155]</sup>



iii) N-doped conducting polymers

Conjugated polymers containing electron-withdrawing imine nitrogen atoms have electron-accepting properties and are highly susceptible to chemical and electrochemical reduction. In a process called n-doping, an electron is injected into the conduction band of the polymer and generates a charge carrier within the polymer chain.<sup>[156]</sup> For example, polythiazole (6.03) is an insulator in its undoped state with a low electrical conductivity,  $10^{-8} \text{ Sm}^{-1}$ , but upon reduction with sodium a significant increase in conductivity is observed producing a semiconducting material ( $10^{-1} \text{ Sm}^{-1}$ ).<sup>[157]</sup>

iv) Spectroscopic properties

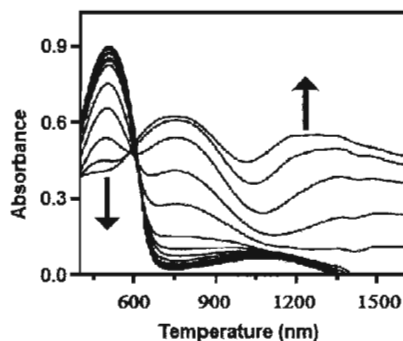


**Figure 6.03:** The spectroelectrochemistry of (6.04)<sup>[158]</sup>

Electrochemistry can be combined with optical spectroscopy to study the redox properties of many electroactive species, including conjugated polymers. Spectral measurements are often made using optically transparent electrodes that have been coated with a thin layer of the polymer film. The spectroscopic response from an oxidation or reduction process is measured directly through the electrode. Indium tin oxide (ITO)

coated glass containing a poly-3-methylthiophene (**6.04**) film displays a  $\pi$ - $\pi^*$  transition at 508 nm corresponding to the band gap of the polymer (**Figure 6.03**). With increased potential, lower energy charge carrier bands begin to appear at 800 nm and 1300 nm, while the absorbance of the initial  $\pi$ - $\pi^*$  transition is concurrently reduced. The polymer film can switch between a red reduced state at -0.2 V and a blue oxidized state at +0.5 V versus Ag/AgCl.<sup>[158]</sup>

## 6.02 Polymetallic materials

### i) Coordination polymers

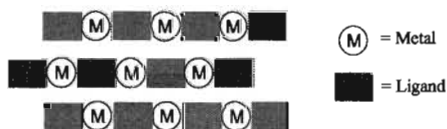


**Figure 6.04:** A general coordination polymer diagram

A coordination polymer is a metal coordination compound where ligands bridge between neighboring metal centres forming a continuous array of metal-ligand units (**Figure 6.04**). The nature of the bridging ligand can vary from halides to polyatomic ligands, including conjugated heterocycles like 4,4'-bipyridine (**1.18**). The diversity of the ligands results in a wide assortment of possible architectures with uniform, repetitious arrangements that span in 1, 2 or 3 dimensions. Although many coordination polymers have been prepared, particular relevance to our work includes those which also feature SCO. In particular, the 1-D chains formed from iron(II) featuring 1,2,4-triazole derivatives can exhibit room temperature spin transitions and wide thermal hystereses.

These covalently bridged SCO chains displayed enhanced cooperativity, physical properties and commercial viability.<sup>[88,159-160]</sup>

ii) Conjugated metallopolymer

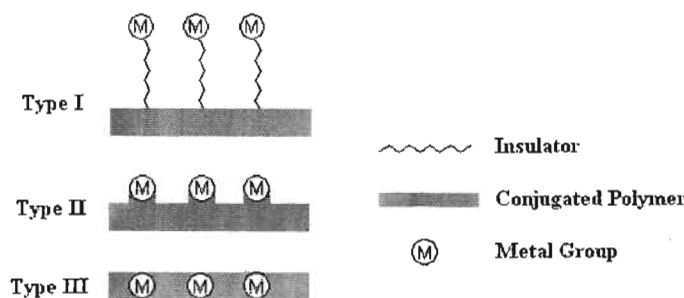


**Figure 6.05:** Type I - III conjugated metallopolymer<sup>[146]</sup>

Coupling transition metal complexes to  $\pi$ -conjugated polymers produces materials in which the unique (optical or magnetic) properties of the metal complex may be coupled to those of the conjugated backbone. In this approach, the polymer acts as a large polydentate ligand, creating polymetallic materials with uniform arrangements of metal centres. There are three main variations of conjugated metallopolymer, as classified by Wolf, each with an extended  $\pi$ -system along the polymer backbone as a common structural trait (**Figure 6.05**).<sup>[146]</sup> The extended  $\pi$ -system distinguishes them from the coordination polymers described previously.

### iii) Type I conjugated metallopolymers

Type I metallopolymers contain pendant metal centres linked to a conjugated organic backbone. The linker is electronically insulating and the metal ions/complexes are attached to the polymer molecule through the link by electrostatic interaction, coordination bond, or covalent bonding.<sup>[146]</sup>

### iv) Type II conjugated metallopolymers

In type II metallopolymers, the metal complexes constitute part of the polymers main chain by metal–ligand coordination or conjugated linkage between the ligand and polymer. Generally, the electronic interactions between the metals and polymer are stronger in comparison to pendant metal centres.<sup>[146]</sup>

### v) Type III conjugated metallopolymers

Type III metallopolymers contain the metal in the polymer backbone and the metal can become involved in electronic delocalization through  $d\pi$ – $p\pi$  overlap between the polymer  $\pi$  system and metal orbitals of appropriate symmetry. As a result the electronic interactions between the metal and backbone can become quite strong.<sup>[146]</sup>

### 6.03 Synthesis of conjugated polymers

#### i) Chemical synthesis

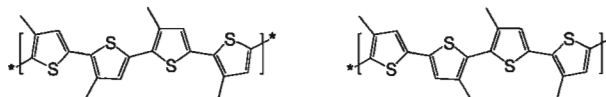
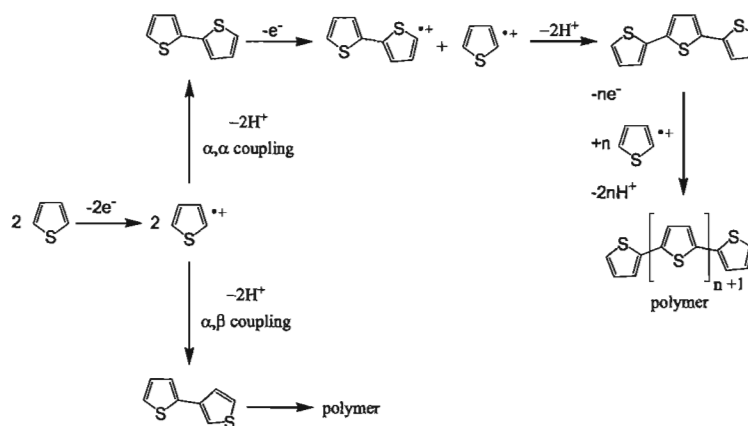


**Figure 6.06:** Conjugated polymers with higher (left) and lower (right) regioregularity

Chemical synthesis can be used to prepare conjugated polymers by oxidative coupling of monocyclic precursors. Polythiophenes, (6.02), (6.04) and (6.06), for example, are prepared by the oxidative polymerization of thiophene groups, using reagents like ferric chloride or iron(III) perchlorate as the oxidant.<sup>[161]</sup> Polymers with varying degrees of regioregularity are produced from this form of chemical oxidation (**Figure 6.06**). Regioregularity, where each repeating unit is derived from the same structural isomer of the monomer, can be improved by other methods including metal-catalyzed polymerization, analogous to Kumada, Negishi or Suzuki cross-couplings.<sup>[162-163]</sup>

#### ii) Electrochemical synthesis



**Scheme 6.01:** A mechanism for thiophene electropolymerization<sup>[165]</sup>

Electropolymerization is a method that was first used to prepare organic polymers such as polythiophene (6.02) but can also been used to prepare metal-containing conjugated polymers. Electropolymerization involves oxidation or reduction of a monomer at a potential that produces a reactive species, generally a radical-cation or radical-anion. These radicals undergo coupling to give first dimers, and subsequently, longer oligomers and polymers. The key requirement is that the resulting polymer and any components such as functional groups or metals incorporated into the polymer structure must be relatively stable at the potential required for polymerization. Monomers that electropolymerize at lower potentials are at an advantage because there is a reduced possibility for decomposition. As an example, the electropolymerization mechanism for five-membered heterocycles such as thiophene is shown in **Scheme 6.01**. Coupling can occur at the  $\alpha$  or  $\beta$  positions of the ring; however, the  $\alpha$  coupling is favored and leads to longer conjugation lengths. In many thiophene derivatives, the ratio of  $\alpha$  to  $\alpha$  and  $\alpha$  to  $\beta$  coupling upon electropolymerization is unknown. The polymer is obtained as a thin film, the thickness and morphology of which can be controlled by the electrochemical parameters (for example potential, current and deposition time). In addition, oxidative or reductive doping can be achieved *in situ* electrochemically, allowing these polymers to switch, easily, between more insulating and more conductive states.<sup>[153,164-165]</sup>

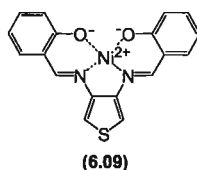


**Figure 6.07:** A diagram of Ni(saloth) (6.09)

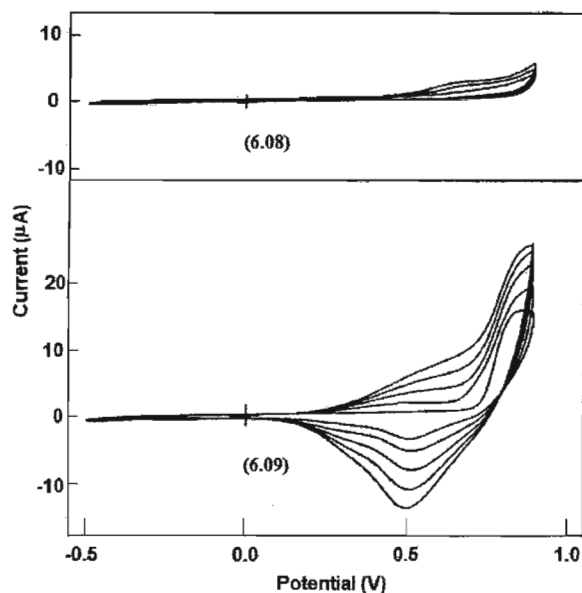


**Figure 6.08:** The cyclic voltammograms of **(6.08)** and **(6.09)**<sup>[166]</sup>

The investigation of the ligand salothH<sub>2</sub> [salothH<sub>2</sub> = *N,N'*-bis(salicylidene)-3,4-thiophenediamine] **(6.08)** and its nickel complex, [Ni(saloth)] **(6.09)** (**Figure 6.07**), are useful in illustrating electropolymerization through cyclic voltammetry (CV) (**Figure 6.08**). In the ligand **(6.08)**, the first CV scan possesses the largest change in current as the potential is increased. The subsequent scans show a continued ebbing of the current response and indicate that electropolymerization is not occurring. In contrast, **(6.09)** displays the common hallmarks of electropolymerization after repeated potential scans. The first scan exhibits a sharp monomer oxidation at +0.72 V and a reductive process at +0.50 V. During the second scan, a new oxidation appears at a lower potential (+0.55 V), which is attributed to the oxidation of the newly formed polythiophene derivative **(6.10)**. Continued scanning brings about an increase in current response with respect to the initial monomer oxidation. In addition to this increased electroactivity, a thick orange

film is observed on the surface of the electrode, which is also consistent with polymer formation.<sup>[166-169]</sup>

#### **6.04 Characterization techniques for conjugated metallopolymers**

Several characterization methods, encompassing aspects of structure, morphology and elemental composition are available for conjugated metallopolymers. In addition to UV-Vis and FT-IR spectroscopy, the techniques we have used for characterization include scanning electron microscopy (SEM), energy dispersive X-ray spectroscopy (EDX) and small angle x-ray scattering (SAXS).<sup>[170]</sup>

##### **i) Scanning electron microscopy**

Scanning Electron Microscopy (SEM) collects images of the sample surface by scanning it with a high-energy beam of electrons. The electrons interact with the atoms on the surface of the sample producing signals that contain information about the topography.<sup>[170]</sup>

##### **ii) Energy dispersive X-ray spectroscopy**

Energy dispersive X-ray spectroscopy (EDX) is an analytical technique used for the qualitative or quantitative elemental analysis of a sample by measuring the emission of X-rays that are characteristic of the atomic structure of the element. A high energy beam



of electrons is typically focused on a sample, which contains atoms in their ground electronic state. The incident beam can excite an electron in an inner shell of an atom, ejecting it from the shell and creating a hole. An electron from an outer, higher-energy, shell then fills the hole and the difference in energy between the higher-energy shell and the lower-energy shell is released in the form of an X-ray. The X-ray energy is characteristic of the unique atomic structure of the particular element under investigation. The quantity of X-rays at a given energy level is counted and this information can be used to identify the elemental composition of the specimen.<sup>[170]</sup>

### iii) Small angle X-ray scattering

Small-angle X-ray scattering (SAXS) is a technique where the scattering of X-rays by a sample is used for the determination of structural properties such as averaged particle size, shapes and characteristic distances of partially ordered materials. X-rays are directed at the sample with a low incident angle (near  $0^\circ$  and limited to a range of around  $1^\circ$ ) to create an intensity pattern based on the elastic scattering of the X-rays that correspond to the structural arrangement of the material. The advantage of SAXS experiments is that a crystalline sample is not needed. However, the random orientation of the material leads to a loss of information due to spatial averaging when compared to crystallography.<sup>[170]</sup>

## 6.05 Goals and objectives

Our current goal is the generation of polymeric materials from molecular spin-crossover complex (or VT) precursors that, from the previous work outlined in Chapters 2 - 4, we have identified as suitable for polymerization. We will use the techniques described in sections **6.01** – **6.04** to synthesize and characterize the polymers. Oxidative coupling will be used to link together the thiophene rings of our complexes to form conjugated polymers and will provide the first examples of electrically conductive metallopolymers containing spin-labile substituents.

## 6.06 Chemical polymerization of (2.10)\*

### i) Synthesis and characterization

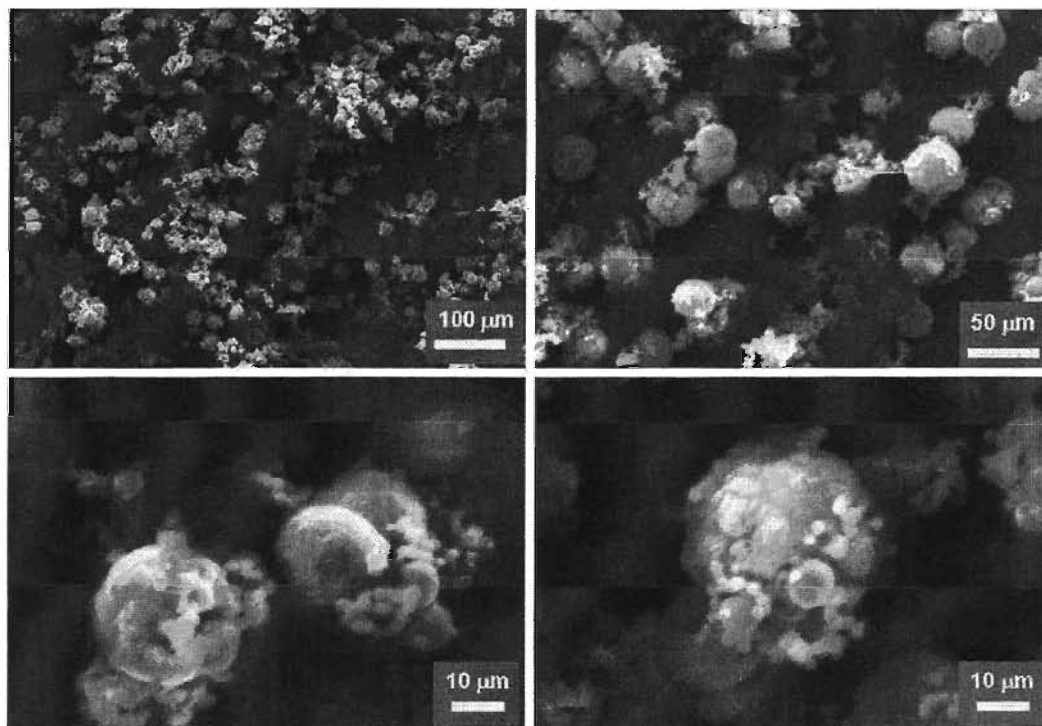
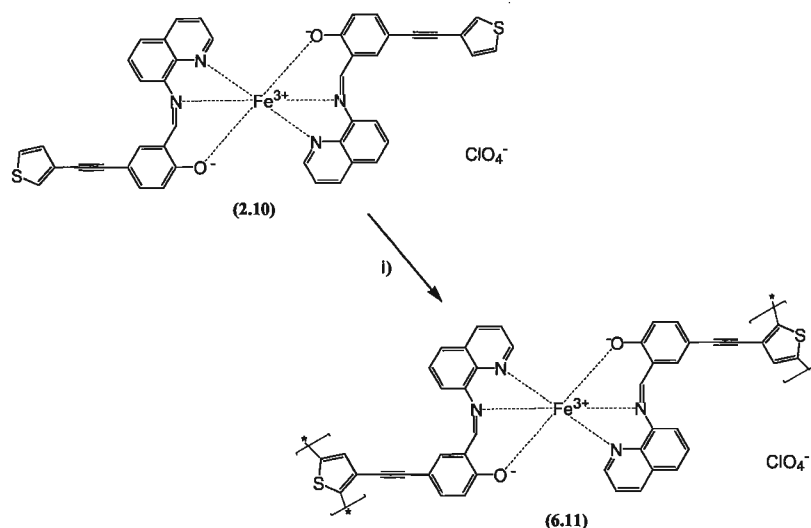


**Figure 6.09:** Purple microspheres of (6.11)<sup>[171]</sup>



Reagents and conditions: (i) CH<sub>3</sub>CN, 2 months

**Scheme 6.02:** The synthesis of (6.11)

An acetonitrile solution containing (2.10), a brown microcrystalline powder, and excess perchlorate anion was left open to air at room temperature. After several weeks, the dark purple spherical particles of (6.11), corroborated by SEM (**Figure 6.09**), were observed to form from the solution (note that similar formations, shown in Appendix 2, are also observed for solutions of (5.07) and (5.10)). Although the particles are not sized uniformly, their spherical shape is reminiscent of well-known polymer microspheres, which have been observed to deposit from solution during a precipitation polymerization mechanism (**Scheme 6.02**).<sup>[172-175]</sup> The FT-IR spectrum of (6.11) is nearly identical to (2.10), with very minor differences in absorbance intensity. Very slight energy differences for the C=N imine stretch of the coordinated ligand ( $\sim 2\text{ cm}^{-1}$ ) and Cl-O stretch of the perchlorate anion ( $\sim 4\text{ cm}^{-1}$ ), allows for the assertion that the structure of (6.11) is very similar to (2.10). Elemental analysis of (6.11) (including C, H, N, S and Fe analyses) is also consistent with the purported structure. Additionally, the solubilities of

(2.10) and (6.11) differ markedly, with (6.11) insoluble in common polar and non-polar solvents.

ii) Structural properties

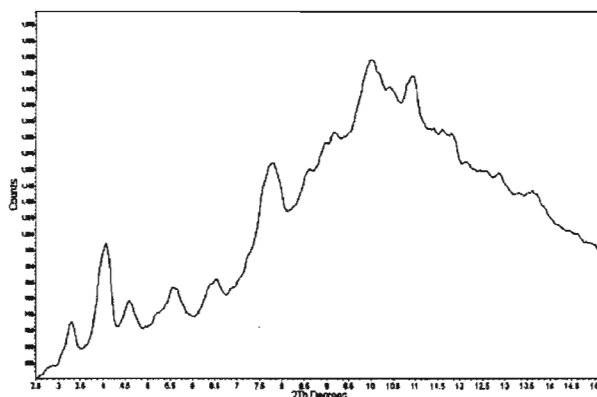


**Figure 6.10:** The X-ray powder diffraction pattern of (6.11)<sup>[171]</sup>

To obtain more detailed structural information, a PXRD profile of (6.11) has been obtained and the data acquired indicate that (6.11) is amorphous, but also suggests possible scattering features at very low angle (Figure 6.10). In contrast, the previously examined PXRD data of precursor (2.10) (Figure 2.09), clearly indicate the polycrystalline nature of this molecular complex.

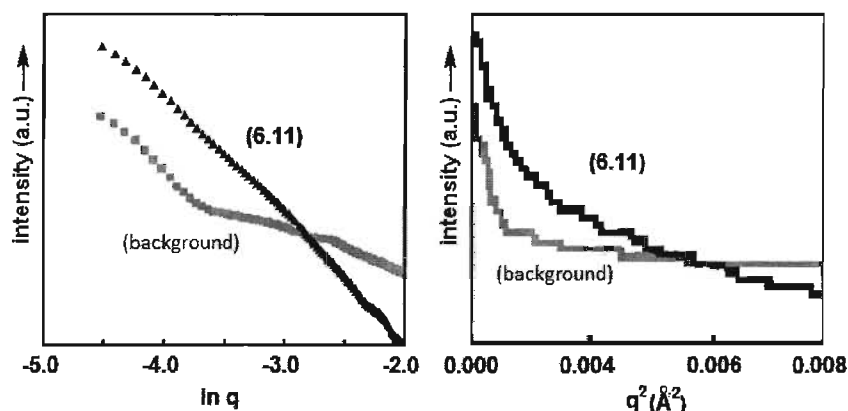


**Figure 6.11:** X-ray scattering (left) and Guinier (right) plots of **(6.11)**<sup>[171]</sup>

Further evidence for the purported macromolecular structure of **(6.11)** is obtained from small angle X-ray scattering (SAXS) experiments (**Figure 6.11**). Significant low angle scattering, above the background, from powder samples of **(6.11)** was observed. The low- $q$  data does not show an obvious Guinier region, which can be explained by the polydisperse nature of the particles, including very large particles, as is corroborated by the SEM images of **(6.11)**. The high- $q$  data clearly exhibits a linear (Porod's law) region with a slope of approximately -4 (a.u.), which indicates the presence of particles with well-defined surface features. The minimum particle size giving rise to the behaviour in the  $q$ -range analysed is about 70 Å.

iii) Electronic absorption spectroscopy

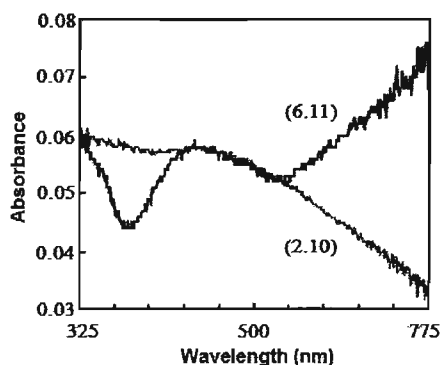


**Figure 6.12:** The reflectance spectrum of (2.10)<sup>[171]</sup>

Evidence suggesting (6.11) forms through polymerization of the thienyl substituents is demonstrated in the diffuse reflectance visible spectrum. The absorbance spectrum of (2.10), calculated from the reflectance profile, features a maximum at 470 nm that is similar to the spectrum of (2.10) in solution and results from a LMCT transition (Figure 6.12). The spectrum of (6.11) features a similar LMCT absorption band, in addition to another broad and more intense feature at a longer wavelength (>775 nm), which we ascribe to transitions between intergap states of the conjugated polythiophene backbone. The visible absorption data strongly supports our assertion that the polymer microspheres are generated by polymerization of the thiophene substituents.

iv) Magnetic characterization

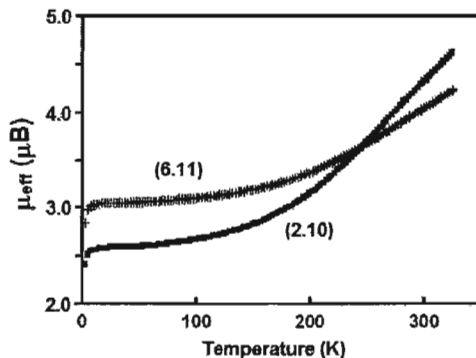


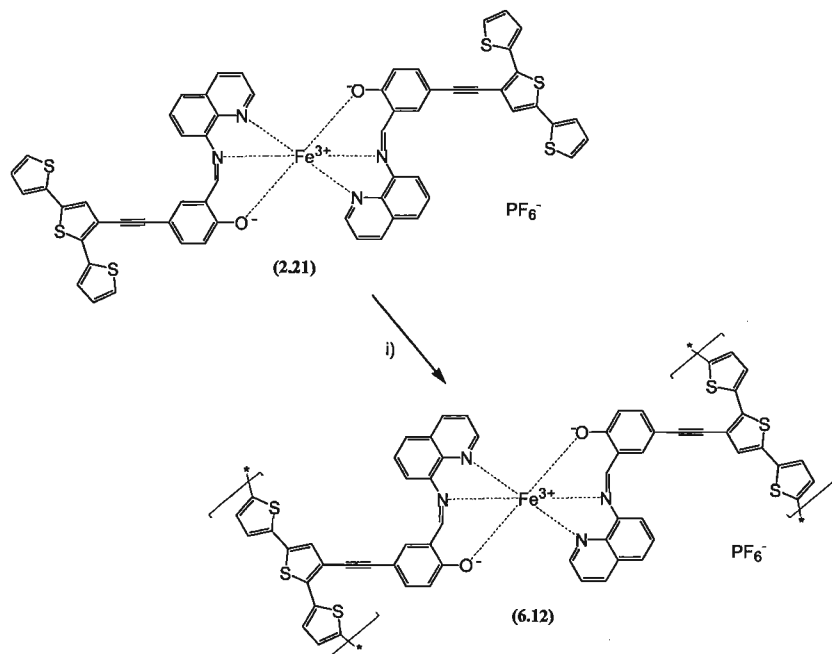
**Figure 6.13:** Variable temperature magnetic susceptibility data for **(6.11)** in a 5000 Oe magnetic field<sup>[171]</sup>

We have obtained variable temperature magnetic susceptibility data for **(6.11)**, which is presented along with the data obtained from **(2.10)** (**Figure 6.13**). For comparison, we have plotted the magnetic moment of **(6.11)** for one independent unit of the anticipated polymer structure, which helped to make clear the differences between the two data sets. At the highest recorded temperature (325 K), the magnetic moment of **(2.10)** is somewhat higher than the magnetic moment of **(6.11)** (4.6 vs. 4.2  $\mu\text{B}$ ). However, the data indicates that some component of the low-spin isomer is present in each sample at this temperature since the anticipated value for pure high-spin iron(III) is 5.9  $\mu\text{B}$ . The temperature dependent profile of the data is also different since **(2.10)** undergoes spin-crossover more rapidly than **(6.11)**. At the lowest measured temperature (2.5 K), the magnetic moment of **(6.11)** is now somewhat higher than **(2.10)** (2.8 vs. 2.4  $\mu\text{B}$ ), but both are consistent with magnetic moments observed at this temperature for other reported iron(III) spin-crossover complexes. The magnetic profile of complex **(6.11)**, like **(2.10)**, does not display thermal hysteresis.



## 6.07 Electrochemical polymerization of (2.21)<sup>†</sup>

### i) Synthesis and characterization



Reagents and conditions: (i) Bu<sub>4</sub>NPF<sub>6</sub>, CH<sub>3</sub>CN, N<sub>2</sub>

**Scheme 6.03:** The synthesis of (6.12)

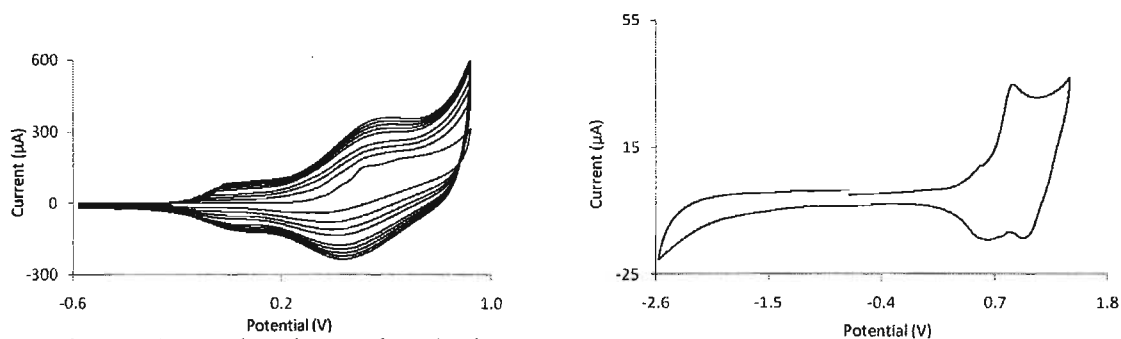


**Figure 6.14:** The electrochemical polymerization of (2.21) on an ITO substrate (left) and the cyclic voltammogram of (6.12) on a platinum button (right)

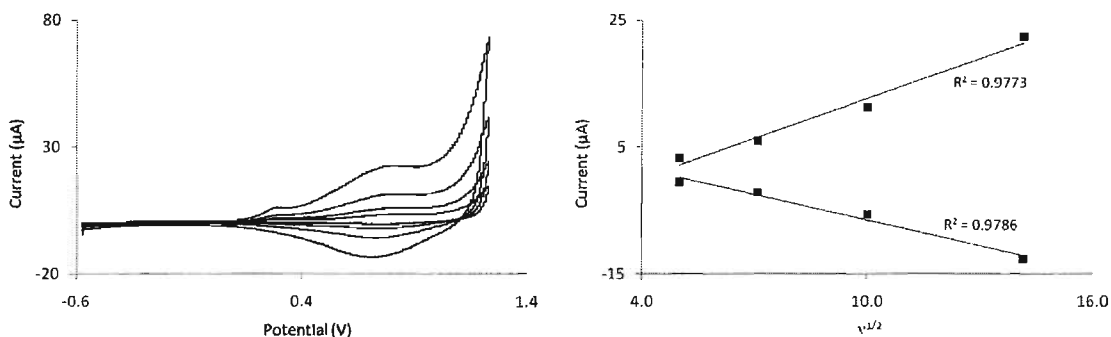
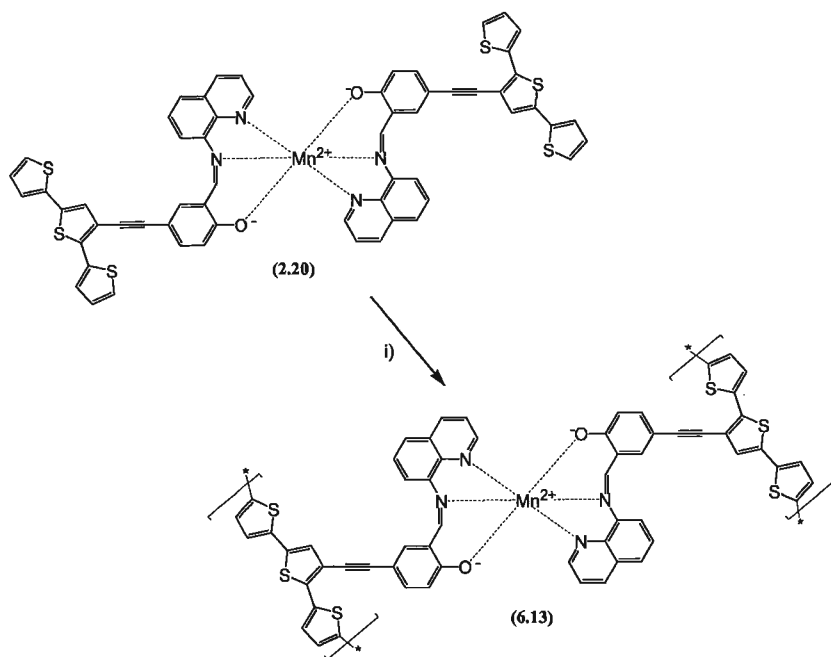


**Figure 6.15:** Current versus scan rate experiments for **(6.12)**

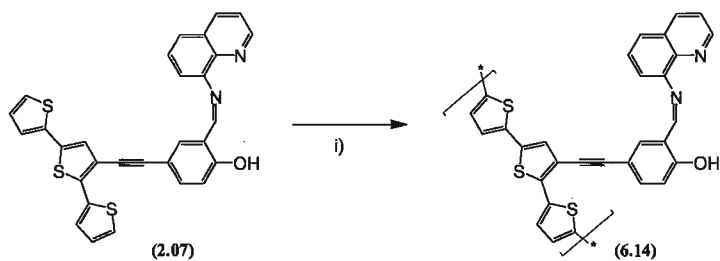
During the investigation of the electrochemical properties of complex **(2.21)** It was found that repeated scanning over a potential window of -0.5 to 1.0 V resulted in electropolymerization and the deposition of a transparent red film of **(6.12)** on a platinum button or ITO-coated glass working electrode (**Scheme 6.03** and **Figure 6.14**). The electrochemical properties of **(6.12)** were investigated after removal of the coated electrode from the solution, washing with acetonitrile, and then running cyclic voltammograms of the polymer in a fresh monomer free solution. The linear peak current dependence on the scan rate was observed and indicates the presence of an electroactive deposit on the working electrode (**Figure 6.15**). The elemental composition of the **(6.12)** film was determined by quantitative EDX spectroscopy. An average of 11 experiments indicate that the Fe:S and Fe:P ratios are in the range expected for the purported structure. In the electronic absorption spectrum of **(6.12)**, an absorption band with a maximum at 510 nm is observed. This absorption is assigned predominately to  $\pi - \pi^*$  transitions of the conjugated polythiophene, which obscure the expected LMCT band that is characteristic of iron(III) complexes. The FT-IR spectrum of **(6.12)** is very similar to the FT-IR spectrum of **(2.21)** and indicates that the polymeric structure was obtained

from electropolymerization without any structural alteration to the pendant iron coordination complex.



Reagents and conditions: (i) Bu<sub>4</sub>NPF<sub>6</sub>, DCM, N<sub>2</sub>

**Scheme 6.04:** The synthesis of (6.13)



Reagents and conditions: (i) Bu<sub>4</sub>NPF<sub>6</sub>, DCM, N<sub>2</sub>

**Scheme 6.05:** The synthesis of (6.14)

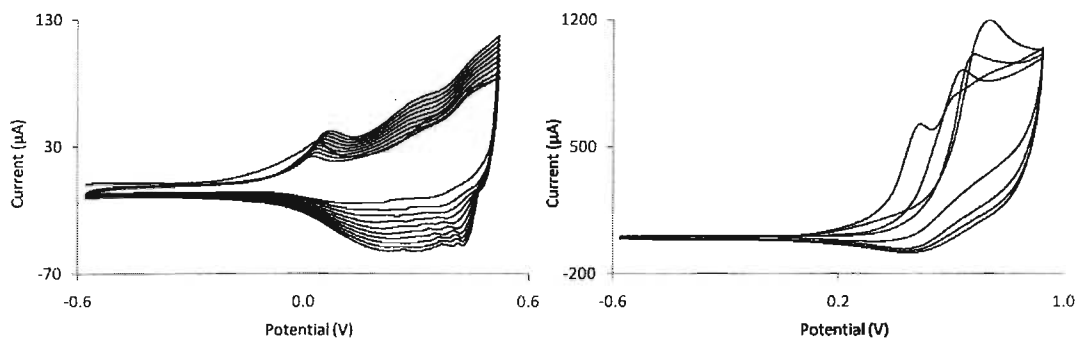


**Figure 6.16:** Electrochemical polymerization of (2.21) (left) and (2.07)H (right) on an ITO substrate

Polymers closely related to (6.12), a manganese(II) analogue (6.13) and the uncoordinated ligand (6.14), were also prepared by electrochemical synthesis to aid in the analysis of physical properties (Schemes 6.04 - 6.05 and Figure 6.16).

ii) Magnetic properties

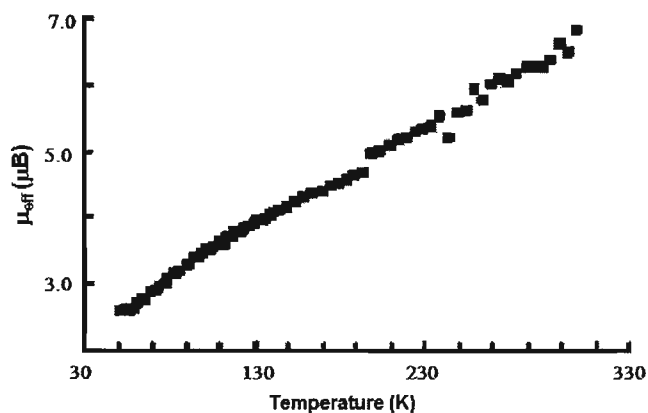


**Figure 6.17:** Variable temperature magnetic susceptibility data for (6.12) in a 15000 Oe magnetic field<sup>[118]</sup>

The variable temperature magnetic properties of **(6.12)** were investigated by SQUID magnetometry. Three independently prepared films of **(6.12)** were electrochemically generated on ITO-coated glass slides and then dried under vacuum for 24 h. The portion of the slide containing the film was cut and weighed, then loaded into a plastic straw and lowered into a SQUID magnetometer. The magnetic data were acquired from 330 to 60 K at a field of 1.5 T, collecting four DC scans for each temperature point with a wait of 60 s for temperature stability at each point (**Figure 6.17**). Following the experiment, the film was removed from the glass using DMSO, ethanol and gentle scrubbing with a tissue. The same piece of ITO-coated glass was loaded into the SQUID and an identical experiment was run so that the diamagnetic contribution to the susceptibility could be subtracted. The paramagnetic susceptibility of **(6.15)** was calculated based on the mass of the repeat unit of the polymer and the results are presented as a plot of the effective magnetic moment ( $\mu_{eff}$ ) versus temperature. At 330 K, the magnetic moment (6.8  $\mu_B$ ) is a little higher than the expected value for one high-spin iron(III) ion (5.9  $\mu_B$ ) and likely results from a polaronic spin contribution from the conducting polymer backbone. We observed a steady decrease in the magnetic moment with decreasing temperature, indicating that a gradual spin equilibrium is operative in **(6.12)**. At approximately 60 K, the magnetic moment per repeat unit is about 2.6  $\mu_B$ , which is greater than 1.73  $\mu_B$ , the anticipated value for one unpaired electron per complex, but is typical for low-spin iron(III) in other similar qsal-containing complexes. No thermal hysteresis in the magnetic properties was observed since the differences in magnetization values between warming and cooling modes at each temperature point were insignificant.

### iii) Variable temperature conductivity

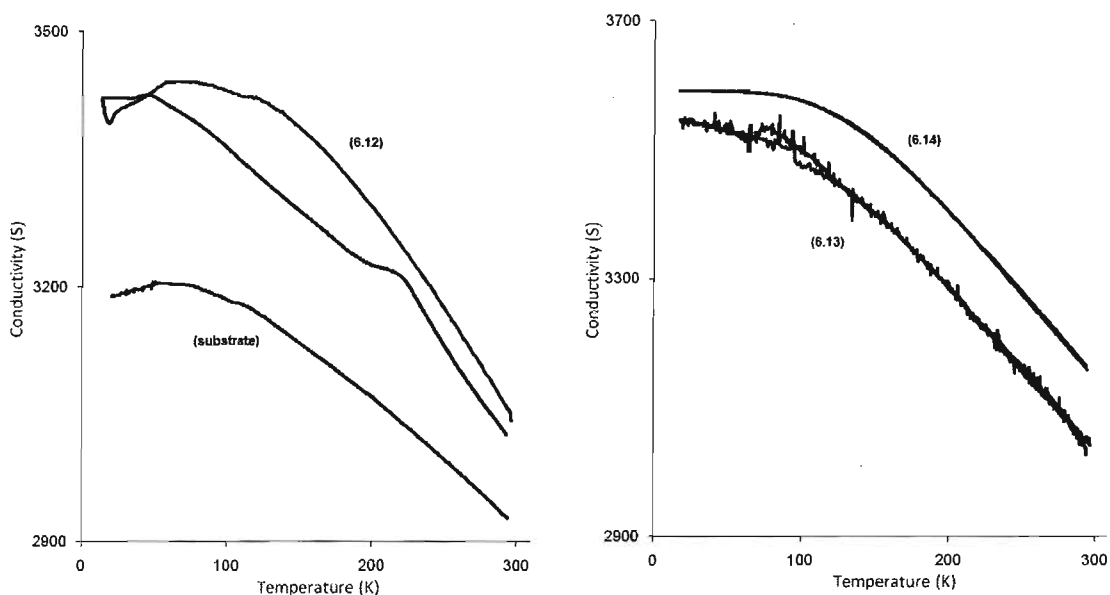


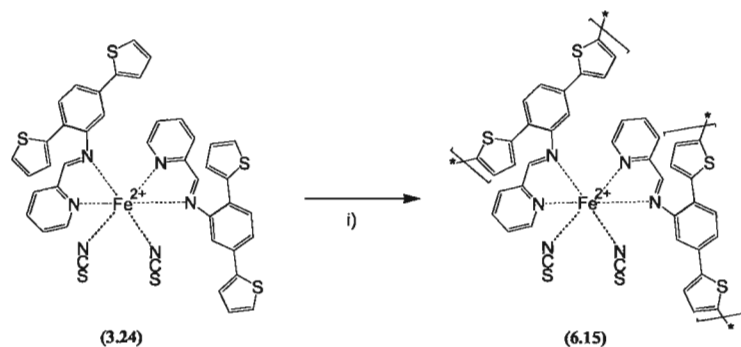
**Figure 6.18:** Variable temperature conductivity of electrodeposited films of **(6.12) - (6.14)**<sup>[118]</sup>

The variable temperature resistivity of electrodeposited films of **(6.12)** with an estimated thickness of 130 nm (Michelson interferometry was used to obtain the value) were also investigated on ITO-coated glass using the van der Pauw method.<sup>[176]</sup> Four contacts (gold wires) were applied to the film with silver paint and then the temperature dependent conductivity (reciprocal of resistivity) profile of the **(6.12)** film coated on ITO glass was collected. Profiles were collected by sweeping through the desired temperature range while simultaneously collecting data points **Figure 6.18**). During the cooling phase, data was collected between 300 K and 20 K over a period of 1.2 hours. The temperature was kept below 20 K for 20 minutes and then allowed to gradually rise back to ambient temperature over a period of 15 hours. The conductivity of the **(6.12)** film and the ITO-coated glass is significantly higher than the conductivity of the bare ITO-coated substrate,

which was measured after removal of the film. Based on a comparison between the (6.12) film and ITO coated glass versus the bare ITO-coated glass, we estimate the conductivity of (6.12) to be on the same order of magnitude as other poly(terthiophene) materials (approximately  $10\text{-}100\text{ Scm}^{-1}$ ).<sup>[153, 165, 176-177]</sup> Although the circuit gains a considerable amount of conductivity from the ITO substrate, the comparison indicates (6.12) is substantially more conductive than the other spin-crossover conductors that have been reported to date.<sup>[107-108]</sup> Curiously, we also observed large differences between cooling and warming measurements of the (6.12) coated ITO, that were not observed on the bare ITO glass slide. We decided to perform identical variable temperature resistivity experiments on a SCO free manganese(II) analogue of our iron(III) polymer and the polymer of the uncoordinated ligand, (6.13) and (6.14) respectively, to further investigate the apparent hysteretic conductivity profile of (6.12). The conductivity data acquired from (6.13) and (6.14) films are nearly identical, since upon cooling and warming, no large differences between the runs were observed.

## 6.08 Electrochemical polymerization of (3.24)

### i) Synthesis and characterization



Reagents and conditions: (i)  $\text{Bu}_4\text{NPF}_6$ , DCM,  $\text{N}_2$

**Scheme 6.06:** The synthesis of (6.15)

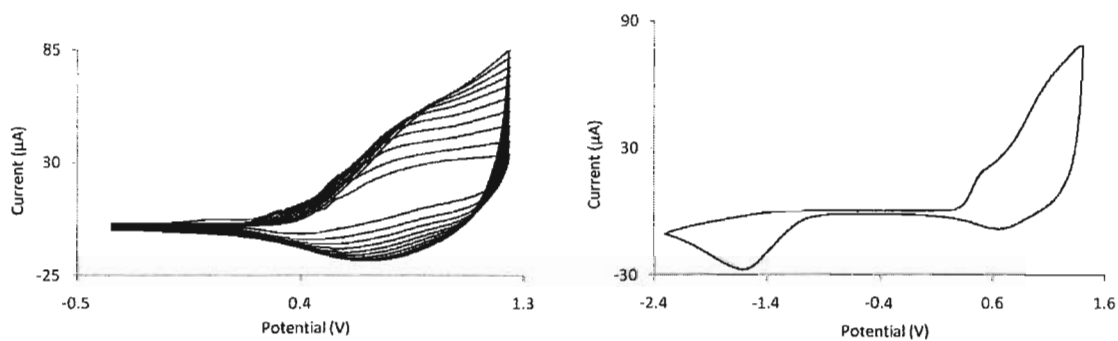


**Figure 6.19:** The electrochemical polymerization of (3.24) (left) and the cyclic voltammogram of (6.15) on a platinum button (right)

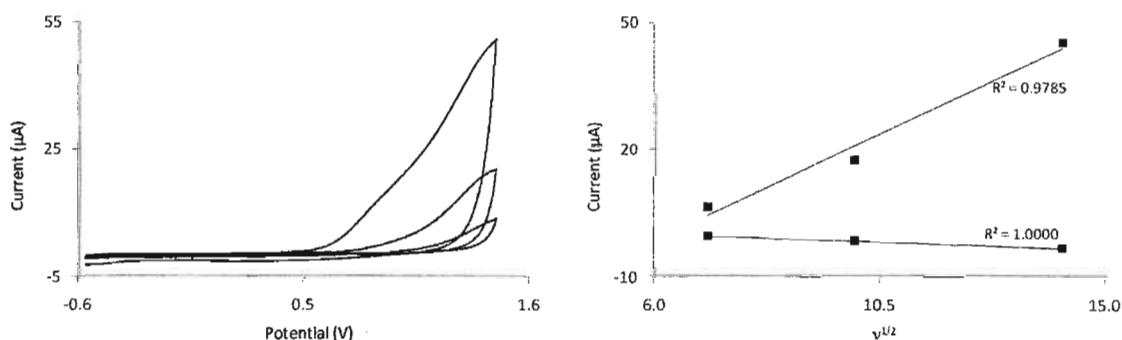


**Figure 6.20:** Current versus scan rate experiments for (6.12)



We decided to prepare an iron(II) spin-crossover metallopolymer next, to further examine the conductive properties of spin labile polymers. While studying the electrochemical properties of **(3.24)** in DCM by cyclic voltammetry, it was found that electropolymerization could be achieved by performing successive cycles, between -0.5 and +1.3 V versus ferrocene, to oxidize the thiophene groups (**Scheme 6.06** and **Figure 6.19**). Successful electropolymerization resulted in the deposition of a transparent orange film of **(6.15)** on a platinum button or ITO-coated glass working electrode. The electrochemical properties of **(6.15)** were investigated after removal of the coated electrode from the reaction solution, washing with DCM, and then running cyclic voltammograms of the polymer in a fresh monomer free solution (**Figure 6.20**). A linear peak current dependence on the scan rate was observed and indicates the presence of an electroactive deposit on the working electrode.

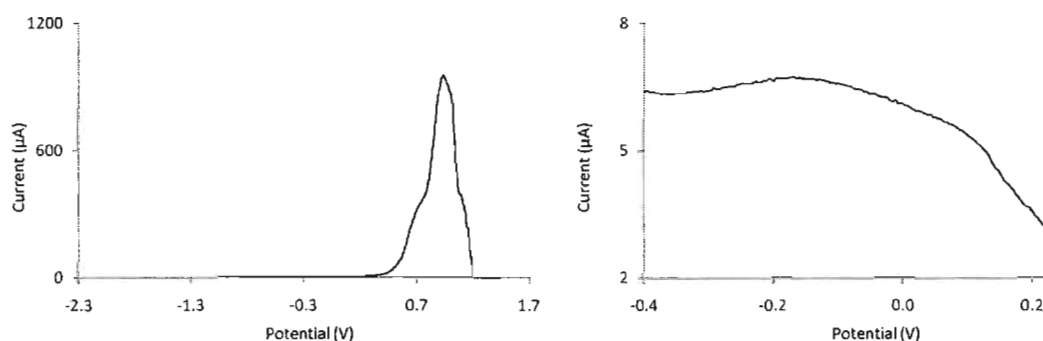


**Figure 6.21:** Differential pulse voltammograms of **(6.15)** (left) and the iron(II) oxidation of **(6.15)** (right)

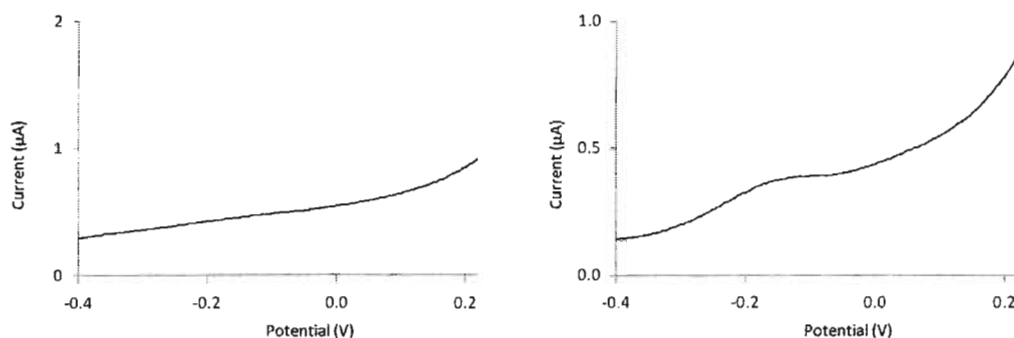


**Figure 6.22:** Differential pulse voltammograms polymer precursors **(3.20)** (left) and **(3.24)** (right)

Films of **(6.15)** were also carefully examined by differential pulse techniques, revealing large peaks beyond +0.5 V attributed to the thiophene oxidation, in addition to a smaller redox event, centred at approximately -0.1 V versus ferrocene (**Figure 6.21**). We ascribe this oxidation to the iron(II) metal centre due to its similar potential in comparison to complexes **(3.16)** (**Figure 3.29**) and **(3.24)** (**Figure 6.22**). The elemental composition of **(6.15)** was confirmed by EDX spectroscopy and verified that the Fe:S ratio is in the range expected for the purported structure. The FT-IR spectrum of **(6.15)** provided further structural corroboration of the polymer film because it is very similar to the FT-IR spectrum of **(3.24)** and verified that the polymeric structure included an imine-pendant iron coordination complex.

ii) Magnetic properties

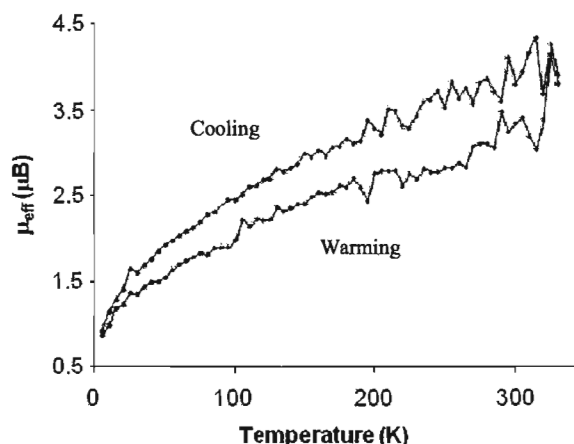


**Figure 6.23:** Variable temperature magnetic properties of **(6.15)** in a 15000 Oe field

The variable temperature magnetic properties of **(6.15)** were investigated by SQUID magnetometry, following a similar procedure to the analysis of **(6.12)**. The magnetic data were acquired from 330 to 5 K at a field of 1.5 T, allowing the temperature of the SQUID to stabilize before collecting measurements at each point (**Figure 6.23**). Following the experiment, the film was removed from the glass using DMSO, ethanol and gentle scrubbing with a tissue. The same piece of ITO-coated glass was loaded into the SQUID and an identical experiment was run so that the diamagnetic contribution to the susceptibility could be subtracted. The paramagnetic susceptibility of **(6.15)** was calculated based on the mass of the repeat unit of the polymer and the results are presented as a plot of the effective magnetic moment ( $\mu_{eff}$ ) versus temperature. At 330 K, the magnetic moment (3.9  $\mu_B$ ) is a lower than the expected value for one high-spin iron(II) ion. We observed a steady decrease in the magnetic moment with decreasing temperature, indicating that a gradual spin equilibrium is operative in **(6.15)**. At 5 K, the magnetic moment per repeat unit is about 0.9  $\mu_B$ , and is greater than anticipated for a

complete crossover to the low-spin state (theoretical value is 0  $\mu_B$ ). A slight difference in magnetic moment values was also observed between cooling and warming runs.

### iii) Electronic absorption spectroscopy

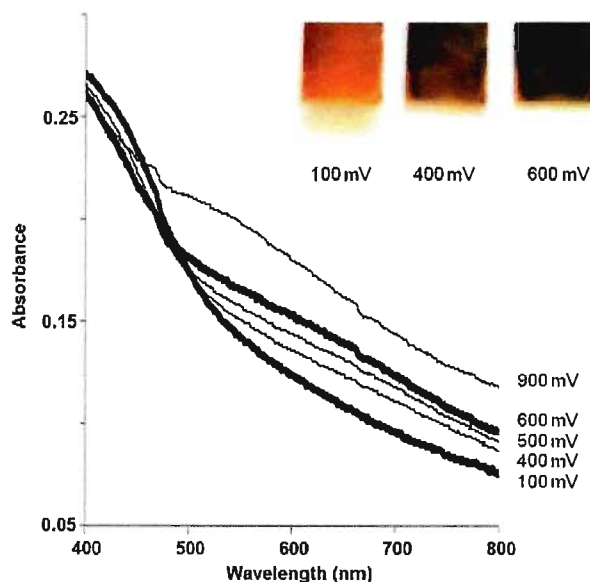


**Figure 6.24:** The spectroelectrochemical properties of (6.15)

In order to investigate the optical properties of (6.15), a film was electrochemically grown on an ITO electrode. The visible absorption spectra of (6.15) at room temperature features an absorption centred around 410 nm with a broad shoulder at lower energy that spans the visible spectrum (**Figure 6.24**). As the film is oxidized electrochemically, the low energy shoulder begins to grow in comparison to the maximum at 410 nm. In these spectra, the band observed at higher energy is  $\pi$ - $\pi^*$  in origin and the lower energy absorption results from transitions between intergap states of the polymer. The observed increase in absorbance of the low energy absorption is related to the doping level of the

polymer via electrochemical oxidation and is completely reversible up to potentials of 600 mV versus ferrocene.<sup>[179]</sup>

iv) Variable temperature conductivity

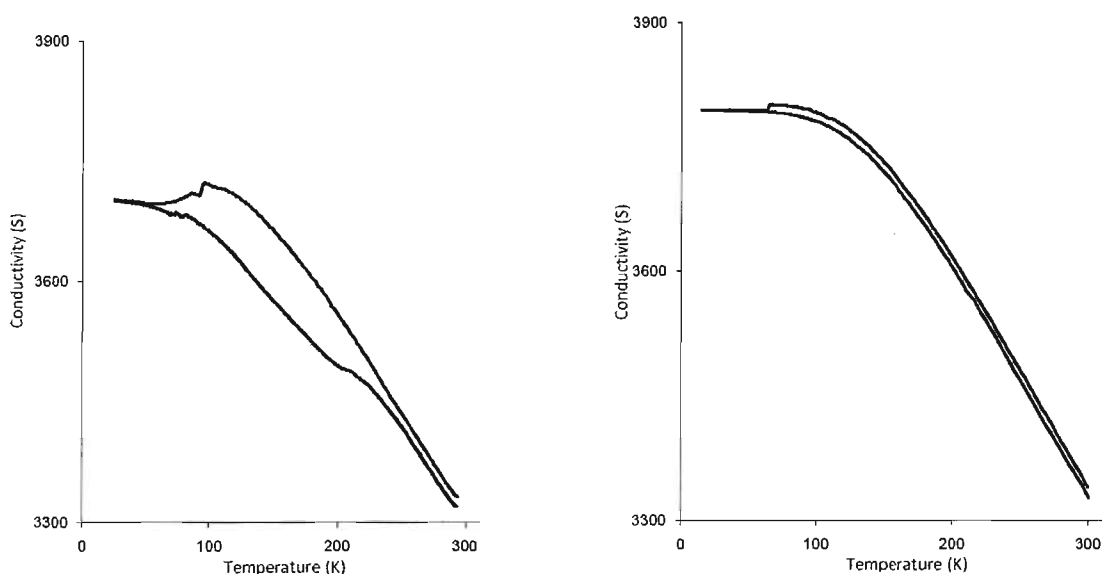


**Figure 6.25:** Variable temperature conductivity of polymer (6.15) measured by sweeping (left) and settling (right)

The variable temperature resistivity of electrodeposited films of (6.15) were investigated on ITO-coated glass using the four contact van der Pauw method. The temperature dependent conductivity (reciprocal of resistivity) profile of (6.15) coated on ITO glass was collected by sweeping through the desired temperature range while simultaneously collecting data points (Figure 6.25). The data collected for (6.15) was quite similar to (6.12), comparable in both the profile and magnitude. Upon observing the similarities between the two profiles, we investigated the possibility of a temperature dependent memory effect common to our polymers. Rather than sweeping through the data points, we decided it would be important to settle (pause) at each temperature, allowing the

temperature to stabilize and the system to reach equilibrium before collecting the data points. After the investigation, it was found that no sustainable memory effects were observed in (6.15) as a result of thermal perturbations.

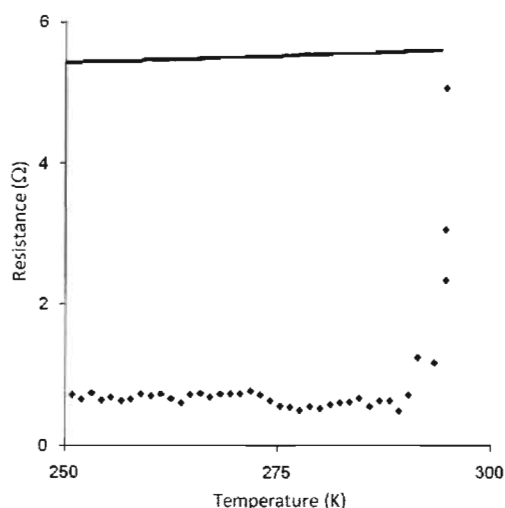
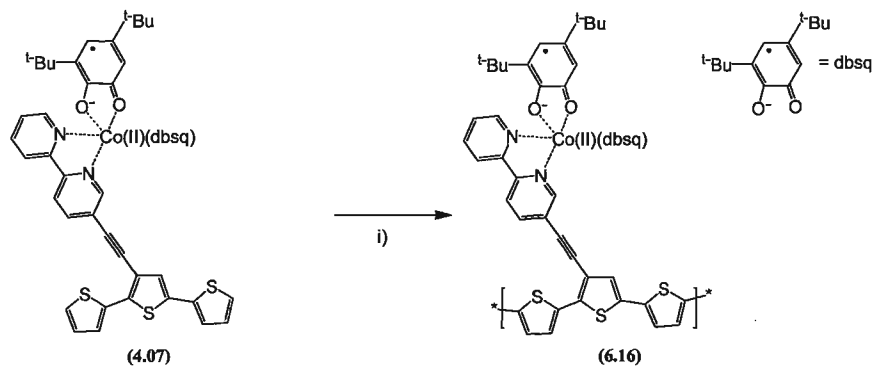


**Figure 6.26:** Variable temperature resistance of (6.15) measured before (solid line) and after (dotted line) oxidation

Poly (6.15) undergoes reversible electrochemical oxidation, and we were also interested in looking at the electron transport properties of the oxidized state. However, the electrochemically oxidized form of (6.15), although persistent under ambient conditions, was not suitable for assembly into our cryostat circuit. Thus, we turned to a chemical oxidation experiment, with molecular bromine, to examine this state with greater ease. Two contacts, 5 mm apart, were attached to the surface of the ITO supported polymer (6.15) and the resistance was measured versus the temperature. After collecting the profile of the neutral polymer, the sample was saturated with bromine and the film turned from orange to dark brown. The sample was placed under vacuum to remove residual bromine, and the resistance profile was collected again. The resistance of the oxidized polymer was found to be lower at all measured temperatures (Figure 6.26).

## 6.09 Electrochemical polymerization of (4.07)<sup>‡</sup>

### i) Synthesis and characterization



Reagents and conditions: (i)  $\text{Bu}_4\text{NPF}_6$ , DCM,  $\text{N}_2$

**Scheme 6.07:** The synthesis of (6.16)

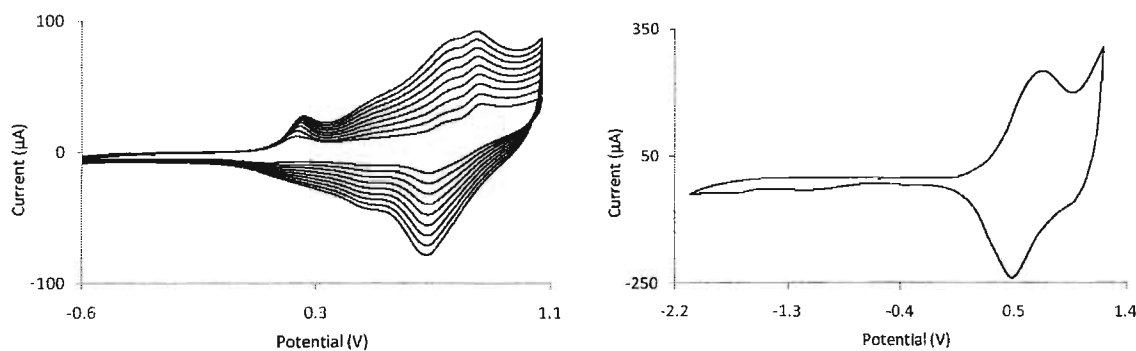


**Figure 6.27:** The electrochemical polymerization of (4.07) (left) and the cyclic voltammogram of (6.16) on a platinum button (right)

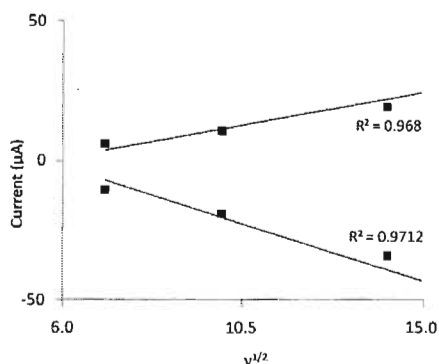
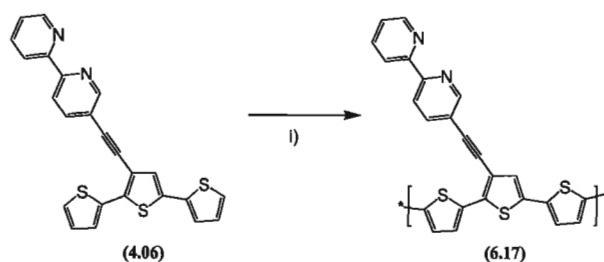


**Figure 6.28:** Current versus scan rate experiments for **(6.16)**

To further highlight the versatility of our approach in the development of multifunctional materials, we decided to also prepare the first conducting metallopolymer known to exhibit valence tautomerism. The electrochemical properties of **(4.07)** were studied by cyclic voltammetry in dry and deoxygenated DCM and electropolymerization was readily accomplished by performing successive cycles between -0.5 and 1.0 V versus ferrocene to oxidize the terthiophene groups (**Scheme 6.07** and **Figure 6.27**). Successful electropolymerization resulted in the deposition of a transparent red film of **(6.16)** on a platinum button or ITO-coated glass working electrode. The electrochemical properties of **(6.16)** were investigated after removal of the coated electrode from the solution, washing with DCM, and then running cyclic voltammograms of the polymer in a fresh monomer free solution. The linear peak current dependence on the scan rate was observed and indicates the presence of an electroactive deposit on the working electrode (**Figure 6.28**). The elemental composition of **(6.16)** was confirmed by EDX spectroscopy and indicated that the Co:S ratio is in the range expected for the purported structure. Phosphorus was also observed in the EDX spectrum of the polymer films,



which we attribute to the residual electrolyte trapped within the polymer film commonly observed in electrochemically generated films.<sup>[180]</sup>



Reagents and conditions: (i)  $\text{Bu}_4\text{NPF}_6$ , DCM,  $\text{N}_2$

**Scheme 6.08:** The synthesis of (6.17)

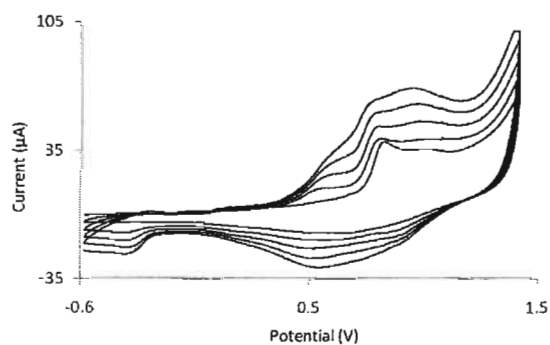


**Figure 6.29:** The electrochemical polymerization of (6.17)

A polymer of the uncoordinated ligand (6.17) was also prepared in an identical manner to aid in the analysis of the physical properties of (6.16) (Scheme 6.08 and Figure 6.29).

ii) Magnetic properties

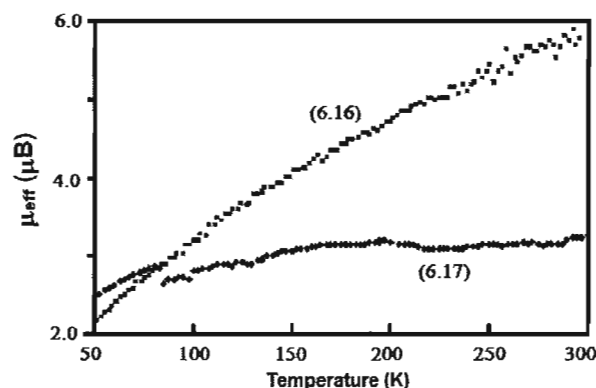


**Figure 6.30:** Variable temperature magnetic properties of **(6.16)** and **(6.17)** in a 15000 Oe field<sup>[139]</sup>

Evidence for the presence of valence tautomerism in **(6.16)** films was provided by variable temperature magnetic susceptibility experiments. A fresh film was grown on an ITO-coated glass slide, and that part of the slide containing the film was cut, loaded into a plastic straw and then lowered into a SQUID magnetometer. For a background subtraction, an identical experiment was performed on an equal mass of ITO-coated glass that was cut from the same slide containing **(6.16)**. The data obtained between 50 and 300 K are slightly noisy, owing in part to the very small mass (0.2 mg) of deposited film, but the general features of the plot strongly support our assertion that VT is operative in **(6.16)** (**Figure 6.30**). The magnetic values are based on the mass of the repeating unit, and vary between 2.1 and 6.0  $\mu\text{B}$ , for the lowest and highest temperatures of measurements, respectively. Additionally, we have ruled out the possibility that these magnetic changes observed in our films are the result of temperature-dependent polaronic spin concentration changes by repeating the above experiment with a film containing metal-free polymer **(6.17)**. After background subtraction, we observed a weak

paramagnetic response from (6.17) with little temperature dependence, which suggests that any contribution to the temperature dependent magnetic properties observed in (6.16) is negligible.

### iii) Electronic absorption spectroscopy

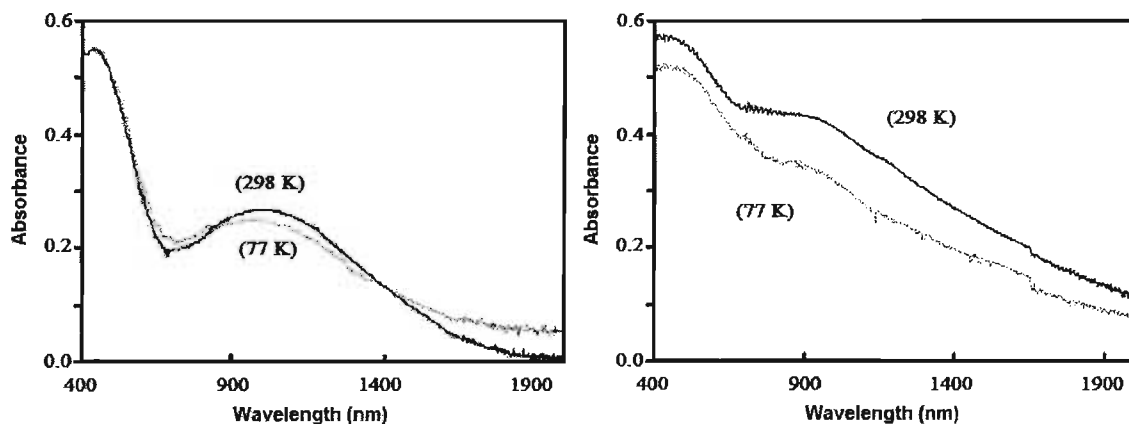


**Figure 6.31:** Variable temperature absorption profile of (6.16) (left) and (6.17) (right)<sup>[139]</sup>

Polymer (6.16) is insoluble in common organic solvents, and is very stable under ambient conditions (as determined by Vis-NIR spectroscopy, over a period of weeks). In order to investigate the optical properties of (6.16), a film was electrochemically grown on an ITO electrode. The metal-free polymer (6.17) was also generated on an ITO glass slide for comparison. The absorption spectra of (6.16) at 77 K and room temperature were collected and displayed modest temperature dependent properties (Figure 6.31). The room temperature spectrum of (6.16) features an absorption centred around 450 nm, and another broad absorption that falls into the NIR at 1000 nm, which are commonly observed in electrochemically generated polythiophenes. The higher energy band is  $\pi$ - $\pi^*$  in origin, and the lower energy absorption results from transitions to intergap states of the

polymer, a consequence of residual doping of polythiophene from the electropolymerization.<sup>[179]</sup> It is very likely that the lower energy absorption also obscures the cobalt(II)-to-dbsq charge transfer absorption, a MLCT band that is typically centred at approximately 800 nm in similar non-polymeric VT materials.<sup>[140]</sup> Upon cooling the film of **(6.16)** to 77 K, the absorbance of the long wavelength band decreases between 1400 and 800 nm, and a very modest increase in absorbance between 500 and 700 nm is observed. The absorbance changes are not mirrored in the Vis-NIR spectrum of the metal free polymer **(6.17)**, which is rather different from **(6.16)** because **(6.17)** absorbs less at 77 K than it does at 298 K over the entire measured wavelength range. From this observation we can rule out the possibility that the optical changes observed in **(6.16)** are the result of thermochromic changes to the polythiophene upon cooling. However, the optical changes we observed in **(6.16)** are too subtle to draw any conclusions regarding valence tautomerism in the polymer film. It is apparent that the contributions from absorption bands originating from transitions within the polymer chain obscure, at least partially, the typical charge transfer absorptions of cobalt–semiquinone valence tautomers.

iv) Variable temperature conductivity

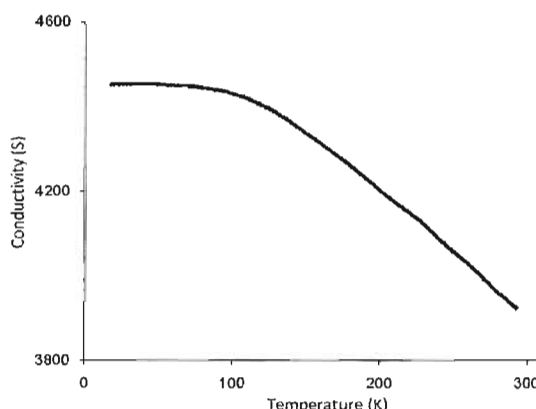


**Figure 6.32:** Variable temperature conductivity profile of (6.16)

The variable temperature resistivity of electrodeposited films of (6.16) were investigated on ITO-coated glass using the four contact van der Pauw method. The temperature dependent conductivity (reciprocal of resistivity) profile of the (6.16) film coated on ITO glass was collected by sweeping through the desired temperature range while simultaneously collecting data points (Figure 6.32). The conductivity of the (6.16) film and the ITO-coated glass is comparable to our other spin labile metallopolymer (6.12) and (6.14) and we estimate it to be on the same order of magnitude. The data was collected by sweeping, exactly like the conductivity experiments for (6.12) and (6.14), but we did not observe any significant differences between cooling and warming measurements. As the threshold level of conductivity is reached for (6.16) at around 110 K, a change in the slope of the conductivity profile is observed, as expected. Interestingly, a similar, although less steep change in slope is observed in the variable temperature magnetic profile.

**Notes:**

*A version of this chapter has been published.*

\* Djukic, B.; Singh, M. A.; Lemaire, M. T. *Synth. Met.* **2010**, *160*, 825-828.

† Djukic, B.; Lemaire, M. T. *Inorg. Chem.* **2009**, *48*, 10489–10491.

‡ O’Sullivan, T. J.; Djukic, B.; Dube, P. A.; Lemaire M. T. *Chem. Commun.*, **2009**, 1903-1905.

## Chapter 7: General conclusions

A new frontier in the field of magnetochemistry is the production of multifunctional materials. These materials feature two or more properties that are not naturally found associated with one another, including magnetic lability and conductivity. Conductive materials with labile magnetic states are typically generated by combining two independently prepared molecular precursors,  $[\text{Fe}(\text{qsal})_2]^+$  like spin-crossover cations and partially oxidized  $[\text{M}(\text{dmit})_2]^{n-}$  anions. However, these materials are typically weakly conducting. Our hybrid approach toward spin-crossover conductors is completely different because we focused on the preparation of conducting metallopolymer containing pendant spin-crossover complexes (or valence tautomers) attached directly to polythiophene derivatives. This design takes advantage of the inherent conducting properties of conjugated polymers, in addition to established synthetic methods, and their processability. The close spatial proximity of the spin labile and conducting components also augurs well for a stronger interaction between the magnetic and electron transport properties.

The first objective, described in Chapter 2, was to investigate derivatives of iron(III) qsal complexes, which were identified as an ideal starting point for the overall goals of this research. We modified the qsal ligand (**2.01**) by appending a thiophene ring to it through a conjugated bridge. The structurally modified (**2.01**) ligand was then used to make model complexes containing iron(III), to investigate the effect of thiophene ring substitution on the electronic or magnetic properties of the  $[\text{Fe}(\text{qsal})_2]^+$  cation. Three

iron(III) complexes with the appended ligand (2.07) were prepared. Characterization by variable temperature magnetic susceptibility, Mössbauer and ESR measurements revealed that structural modification of ligand (2.01) with an ethynylthienyl component is favourable because the iron(III) complexes generated still undergo spin-crossover. For complexes (2.08) and (2.10), a gradual and incomplete spin-crossover was observed between the  $S = 5/2$  and  $S = 1/2$  states. Complex (2.09) displays a rare  $S = 5/2$  to  $S = 3/2$  crossover that is also incomplete. An examination of the electrochemical properties of (2.08) – (2.10) followed and we did not observe electropolymerization through the appended thiophene rings. The initial results encouraged us to continue modifying the qsal ligand in an effort to make the electrochemical properties more amiable to polymerization. We attached a terthiophene component to (2.01) and prepared an iron(III) complex (2.20) bearing the modified ligand. Complex (2.20) has similar magnetic properties to the monothienyl iron(III) complexes formed from (2.07), with the occurrence of a gradual and incomplete spin-crossover. The electrochemical properties of (2.20) were enhanced in comparison to the monothienyl complexes, because the terthienyl oxidation occurs at a significantly lower oxidation potential, which is favourable for successful electrochemical polymerization.

Our second objective, discussed in chapters 3 and 4, was to design different kinds of spin labile monomers that we could use in subsequent electrochemical polymerization reactions. Since iron(II) spin-crossover complexes are considered the best example of molecular bistability, it seemed logical to incorporate an iron(II) spin-crossover complex into our conjugated polymers.<sup>[93]</sup> There are many examples of iron(II) complexes



exhibiting abrupt spin state transitions and thermal hysteresis, conferring the true bistability of these materials. Although new avenues for research with SCO materials are underway, no previous examples of iron(II) spin-crossover conductors have been reported to date. Our first efforts focused on three new thiophene containing “Toftlund-like” bispicen ligands (3.04), (3.07) and (3.10). Coordination of (3.04) and (3.10) with iron(II) *bis*(thiocyanate) resulted in the anticipated *cis*-pseudo-octahedral complexes (3.11) and (3.13) respectively. The complexes were characterized and featured incomplete spin-crossover in (3.11), or high-spin iron(II) in (3.13). Coordination of (3.07) with iron(II) *bis*(thiocyanate) produced a very unstable complex (3.12) that, in solution, undergoes a ligand-centred structural rearrangement to produce a stable complex (3.14). A similar rearrangement was also noted to occur for complex (3.12) as well, but only trace amounts of this rearranged product (3.15) could be isolated. Complex (3.14) features intriguing variable temperature magnetic properties and our analysis indicates that the temperature dependent magnetic behaviour of (3.14) is best described as a one-dimensional ferromagnetic chain with interchain antiferromagnetic interactions and/or ZFS at low temperatures, which reduces the magnetization. No indications of polymerization reactions were observed while attempting to electropolymerize complex (3.13). The irreversible oxidations observed at low potentials in the cyclic voltammogram (3.13), suggest that complexes (3.10) - (3.12) are insufficiently stable for electrochemical reactions.

The instabilities of the “Toftlund-like” complexes (3.10) - (3.13) caused us to explore another iron(II) spin-crossover system derived from  $[\text{Fe}(\text{ppi})_2(\text{NCS})_2]$  (3.16). Three

[Fe(ppi)<sub>2</sub>(NCS)<sub>2</sub>] derivatives were prepared containing 2',5'-diphenyl- (3.23), 2',5'-dithienyl- (2.24) and 4'-thienyl- (3.25) appendages. Complexes (3.23) and (3.24) were structurally characterized and upon comparison it was found that in (3.24) one imine (N4)-thiophene (S3) was causing an elongation of the Fe1...N4 coordinate bond. Characterization by variable temperature magnetic susceptibility measurements revealed that structural modification of complex (3.16) is favourable because the derivatives undergo spin-crossover. For complexes (3.23) and (3.25), an abrupt spin-crossover was observed between the  $S = 2$  and  $S = 0$  states. In contrast, the magnetic profile of complex (3.24) displays a more gradual slope to lower magnetic values. Further magnetic characterization of (3.24) and (3.25) resulted from Mössbauer spectroscopy. The Mössbauer spectra of complex (3.25) exhibits high- and low-spin fractions consistent with an  $S = 2$  to  $S = 0$  transition and is in agreement with the magnetic susceptibility measurements. The Mössbauer data for complex (3.24) also displays a temperature dependent mixture of spin isomers. With our current data, the transition in (3.24) is most consistent with an  $S = 2$  to  $S = 1$  crossover, with some thermal spin isomerisation of the  $S = 0$  state also observed. An examination of the electrochemical properties followed and we did not observe electropolymerization for complexes (3.23) and (3.25). Complex (3.24), with a terthiophene oxidation potential that was significantly lower than other oxidation events, was better suited for electrochemical polymerization reactions.

Cobalt(II) valence tautomers were selected as a third variation of the spin labile component to incorporate into our conjugated metallopolymer. We prepared two new derivatives of 2,2'-bipyridine ligands bearing thiophene (4.04) and terthiophene (4.06).

Reaction of these ligands with  $[\text{Co}_4(\text{dbsq})_8]$  resulted in monothienyl (**4.05**) and terthienyl (**4.07**) appended coordination complexes that, as demonstrated by variable temperature magnetic susceptibility and Vis-NIR experiments, exhibited valence tautomerism. Complex (**4.05**) served as a model to study the effects of thiophene substitution on the electronic or magnetic properties of the cobalt-*bis*(semiquinone) valence tautomers but did not undergo electropolymerization. The electrochemical properties of (**4.07**) were better suited for electropolymerization in comparison to (**4.05**) because of the quasi-reversible terthienyl oxidation.

Our third objective, discussed in Chapter 5, was to prepare bimetallic analogs of the iron(III) complexes made in Chapter 2, as a logical extension of our spin-crossover systems. Four bimetallic iron(III) spin-crossover complexes (**5.07**) – (**5.10**) were made from ligand (**5.06**), each having a different counteranion. The complexes were characterized with variable temperature magnetic susceptibility, Mössbauer, and EPR spectroscopy and had magnetic properties similar to the iron(III) complexes of Chapter 2. Since the observed spin-crossover remained gradual and incomplete, it was found that tethering two  $[\text{Fe}(\text{qsal})_2]^+$  components together through the bithiophene bridge did not adversely affect the magnetic properties.

Our hybrid approach toward synthesizing polymeric spin-crossover conductors is described in Chapter 6 and features four main variations including both chemical and electrochemical syntheses. The first adaption was an unexpected chemical formation of metallopolymeric microspheres (**6.11**) from acetonitrile solutions containing the

molecular spin-crossover precursor **(2.10)**. We characterized this metallopolymer using SEM, FT-IR, elemental analysis (including C, H, N, S, Fe analyses), small-angle X-ray scattering (SAXS) techniques, and PXRD. Of greatest significance, the polymeric spheres also exhibit spin-crossover observed by variable temperature magnetic susceptibility, conferring that **(6.11)** is the first spin-crossover microscale (or, due to the polydisperse particle size, nanoscale) material of its kind.

The remaining metallopolymers described in Chapter 6 were synthesized electrochemically. Polymer **(6.12)**, containing an iron(III) spin-crossover component, was electrochemically generated from **(2.21)** and was characterized by IR and EDX analysis, followed by variable temperature magnetic susceptibility measurements that confirmed spin-crossover is operative in the polymer film. The variable temperature conductivity measurements demonstrated that **(6.12)** is substantially more conductive than the other known spin-crossover conductors. We also observed large differences between cooling and warming conductivity measurements of **(6.12)** coated on ITO, that were not observed on the bare ITO glass slide or similar polymers **(6.13)** and **(6.14)** upon sweeping.

Our second spin labile metallopolymer **(6.15)**, containing an iron(II) spin-crossover component, was generated from **(3.24)**. Polymer **(6.15)** was characterized by IR and EDX analysis, followed by variable temperature magnetic susceptibility measurements that confirmed spin-crossover is operative in **(6.15)**. Variable temperature conductivity measurements verified that **(6.15)** is a semiconductor and, accordingly, the first spin-

crossover conductor containing an iron(II) spin labile component. The conductive properties of (6.15) are on the same order of magnitude as (6.12) and during sweeping measurements, display similar differences between cooling and warming conductivity values. A second conductivity experiment, where the temperature was allowed to stabilize before collecting the data points, revealed that no sustainable memory effects in (6.15) occurred as a result of thermal perturbations. Spectroelectrochemical results displayed vibrant changes in the optical properties of the oxidized film, in addition to demonstrating the stability of the oxidized state by its reversible nature. The oxidation of thin films of (6.15), by chemical methods, revealed a substantial decrease in electrical resistance after oxidation.

Our third example of a spin labile metallopolymer (6.16) features a cobalt-*bis*(semiquinone) valence tautomer and was made from complex (4.07). Polymer (6.16) was characterized by UV-Vis, NIR and EDX analysis, followed by variable temperature magnetic susceptibility measurements that confirmed that valence tautomerism is operative in the polymer film. Variable temperature conductivity measurements on thin films of (6.16), unlike (6.12) and (6.14), did not display significant differences in cooling and warming measurements upon sweeping. A change in the slope of both the variable temperature magnetic and conductivity profiles was also observed near 110 K.

The results obtained from these investigations have demonstrated that our hybrid metallopolymer approach toward spin-crossover conductors is advantageous due to the conducting properties of conjugated polymers. Considering the quantity of reported

magnetically labile complexes and variety of established synthetic methods for ligand design and polymerization, a vast expanse of potential research has been discovered. In particular, incorporating the spin labile component within the conjugated polymer backbone should be an active focus because interactions between the magnetic and electron transport properties may be further enhanced.

## **Chapter 8: Experimental**

### **8.01 General procedures**

All reagents were commercially available and used as received unless otherwise stated. Deaerated and anhydrous solvents were obtained from a Puresolve PS MD-4 solvent purification system, and all air and/or moisture sensitive reactions were carried out using standard Schlenk techniques, unless otherwise stated. Elemental analyses were obtained from Guelph Chemical Laboratories, Guelph, ON, Canada, Canadian Microanalytical Services, Ltd, Delta, BC, Canada and Atlantic Microlab, Inc. Norcross, GA, USA.

### **8.02 Instrumentation**

**FT-IR:** spectra were recorded on either a Shimadzu IRAffinity-1 or ThermoMattson RS-1 spectrometer as KBr discs or as evaporated films on NaCl plates.

**Interferometry:** Thickness of the polymer films were measured with a Michelson interferometer using a WILD M8 Stereomicroscope fitted with a LEITZ WETZLAR interferometer lens.

**ESR:** Electron spin resonance (ESR) spectra were recorded as powders in quartz tubes on a BrukerElexsys E580 pulsed and CW X-band (9 GHz) spectrometer, equipped with a liquid helium cryostat.

**Mass spectrometry:** EI and FAB spectra were obtained using a Kratos Concept 1S High Resolution E/B mass spectrometer. ESI spectra were obtained using a Bruker HCT Plus Proteineer LC-MS.

**Melting point:** A Stuart Scientific SMP10 apparatus was used to measure melting points.

**Mössbauer spectroscopy:** Analysis was performed using a constant-acceleration spectrometer (Wissel GMBH, Germany) in a horizontal transmission mode using a 50 mCi  $^{57}\text{Co}$  source and a Janis SHI-850-1 closed cycle helium refrigerator cryostat for variable temperature measurements.

**NMR:**  $^1\text{H}/^{13}\text{C}$ -NMR spectra were recorded on a Bruker Advance 300 MHz spectrometer with a 7.05 T Ultrashield magnet

**SAXS:** Transmission SAXS measurements were taken with a Cu  $K\alpha$  source, graphite monochromator, 3-slit shaping system, beam path evacuation to between 40–75 mT, with 1.1 m sample-detector separation. The detector used was a one-dimensional gas phase position sensitive detector with 101.6 mm active length (1024 channels) and semi-transparent Al beam stop. The angle calibration was determined by direct  $2\theta$  variation and monitoring of the location of the primary beam and confirmed through use of a silver behenate standard. The current setup yields a resolution of  $179.5 \pm 0.3$  channels/degree with a typical minimum angle ( $2\theta$ ) of approximately  $0.070^\circ$ . The minimum angle varied



slightly as the detector was moved periodically (perpendicular to the beam path) to allow monitoring of the direct beam (working with the minimum power of  $20 \text{ kV} \times 5 \text{ mA}$ ) for absorption/transmission measurements. Data acquisition was performed with  $35 \text{ kV} \times 38 \text{ mA}$  with the main beam placed behind the beam stop so that the edge of the beam stop defined the minimum accessible scattering angle. An extended line-shaped beam, approximately 10 mm height and 1.5 mm width at the sample position, was used to improve scattering statistics. Desmearing is done using the direct desmearing algorithm and correction for the geometry of the linear position sensitive detector is made on the background-corrected and desmeared data. The sample was mounted onto a single layer of Kapton tape with as even a distribution as possible over an area of about  $17 \text{ mm} \times 2.2 \text{ mm}$  and appeared to be uniformly opaque after sample loading. The Kapton tape support was mounted on an Al plate, 2 mm in thickness and having an aperture equal to that of the sample area. Transmission of the direct beam through the Kapton tape and the sample was measured at  $20 \text{ kV} \times 5 \text{ mA}$  for 5 s with 7 repeated exposures for statistical sampling. A transmission ratio of about 25 % (tape and sample relative to the tape alone) was seen indicating that the sample is a strong absorber/scatterer of X-rays at this energy. SAXS measurements on the bare Kapton tape used a 333 min exposure, and a 436 min exposure for the tape and sample experiments. The background and sample data were normalized according to counting time and measured transmission. The removal of a Kapton artifact peak that is seen at about  $0.070 \text{ \AA}^{-1}$  in the background data as well as in the raw sample data, was used to verify effective removal of background scattering

**SEM/EDX:** data was collected on a Pentafet EDS with a Link Systems detector (beryllium windows, 20 kV energy) at the CCEM, McMaster University, ON, CA. or an AMRAY 1600T SEM at Brock University. For EDS experiments the “apparent concentration” is calculated directly from the intensity of the characteristic X-ray peak before corrections for atomic number, absorbance, and fluorescence (ZAF).

**UV-Vis:** spectra were recorded on a Shimadzu 3600 UV-Vis-NIR spectrophotometer or ThermoSpectronic/Unicam UV-4 spectrophotometer. Room temperature spectra were acquired from solutions in appropriate solvents. Spectra at 77 K were obtained as ethanol glasses in 5 mm NMR tubes immersed in a transparent liquid nitrogen dewar. Polymer spectra were attained from solid samples through either absorbance or diffuse reflectance experiments pending on their opacity and using ITO and BaSO<sub>4</sub> as substrates respectively. Polymer spectra at 77 K were achieved by directly immersing the sample into the liquid nitrogen dewar. The molar absorptivity ( $\epsilon$ ) for experiments is reported in M<sup>-1</sup>cm<sup>-1</sup>, except when insolubility precluded an accurate determination.

### **8.03 Variable temperature magnetic susceptibility measurements**

Variable temperature magnetic susceptibility measurements were recorded on a superconducting quantum interference device (SQUID) magnetometer (Quantum Design MPMS) with a 5.5 T magnet (temperature range 1.8 to 400 K) in an appropriate external field of 0.5 T for bulk quantity samples or 1.5 T for polymer films. The samples were carefully weighed into gelatin capsules, which were loaded into plastic straw, and

attached to the sample transport rod. Diamagnetic corrections were made using Pascal's constants. Diamagnetic contributions from the straw, capsule and substrates were subtracted by running these free of sample. The samples analyzed were analytically pure with clear observation of SCO when indicated and the effects of possible magnetic impurities are negligible towards the overall scope of this project.

#### **8.04 Electrochemical experiments**

Electrochemical experiments were performed with a Bioanalytical Systems Inc. Epsilon electrochemical workstation. The supporting electrolyte in each experiment was dried in an oven at 115°C for 24 h before use. Compounds were dissolved in anhydrous solvent (ACN, DCM or DMF) and deaerated by sparging with N<sub>2</sub> gas for 20 minutes. Solution concentrations were approximately 10<sup>-3</sup> M unless otherwise stated. A typical three-electrode set-up was used including a platinum button (or ITO working electrode when indicated), silver wire reference electrode, and a platinum wire auxiliary electrode. Scan rates for CV experiments were 100 mV/s except for current versus scan rate experiments. Ferrocene was used in all cases as an internal standard and all potentials quoted are versus the ferrocene oxidation potential. Indium tin oxide (ITO) coated borosilicate glass cuvette slides (5-15 ohms) were purchased from Delta Technologies, LTD.

### **8.05 Electrical conductivity**

The cryostat consisted of a Lakeshore Cryotronics temperature controller (model DRC 91C), CTI-Cryogenics 8001 controller, 8003 compressor and a CTI-Cryogenics Cryo-Torr 8 high vacuum pump. The temperature dependence of the resistivity data was measured by a standard four probe dc technique and collected on MPMS MultiVu Application software (Revision 1.57 Build 075). The probes were made by adhering gold wires to the surface of the film with small amounts of silver paint or epoxy, and then soldering the wires to the cryostat sample holder. The film was carefully inspected to ensure that it contained no cracks and that the contact between the film, each gold wire and the cryostat sample holder remained uninterrupted. The sample holder was fitted into the cryostat sample chamber and then placed under vacuum. A current of 1.0-2.0 mA was applied to the circuit using a Keithly 224 programmable current source and then the variable temperature resistivity measurements were initiated. For temperature stabilization experiments, the same four probe technique was used but the data were collected and recorded on a superconducting quantum interference device (SQUID) magnetometer (Quantum Design MPMS) with a 5.5 T magnet.

### **8.06 X-ray structure determination and powder diffraction**

Crystals of suitable size were mounted on a glass fiber and data were collected on a SMART APEX II diffractometer located at the McMaster Analytical X-ray Diffraction Facility (MAX) (or a Nonius Kappa-CCD system located at the University of Toronto)

with Mo K $\alpha$  radiation ( $\lambda = 0.71073$  Å). Data were processed using APEX v2.2.0 (or Kappa-CCD) software and solved by direct methods (SHELXS-97).

X-ray powder diffraction data was obtained with a Bruker APEX II diffractometer using Mo K $\alpha$  radiation at 295 K and a detector-to-sample distance of 17 cm or a Bruker SMART 1K diffractometer, at 295 K, using Cu K $\alpha$  radiation, and a detector-to-sample distance of 5 cm. The powder was mounted in a glass slide and a 5 min still scan was recorded with the sample at  $\omega = 20^\circ$ . For comparison, the X-ray powder diffraction pattern of single crystals was calculated using the program Mercury 1.4.2.

### 8.07 Computation

All DFT calculations were performed using the Gaussian 03 package using the B3LYP hybrid functional and the DZVP basis set for all atoms and tight SCF convergence criteria were used for all calculations.<sup>[181-183]</sup> The converged wave functions were tested to verify that they correspond to the ground-state surface. The evaluation of atomic charges and spin densities was performed using the natural population analysis (NPA)<sup>[184-185]</sup> and the analysis of molecular orbitals in terms of fragment orbital contributions were carried out using the AOMix program<sup>[186]</sup>. Time-dependent DFT (TD-DFT) calculations at the B3LYP/DZVP level were performed to calculate the absorption spectra as described previously.<sup>[187]</sup>

## 8.08 Experimental for Chapter 2\*

### 1. Iron(III) qsal complexes

#### i) Ligand synthesis

#### (2.01)H: qsalH

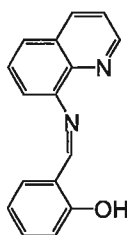
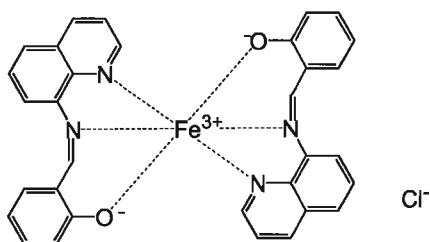


Figure 8.01: (2.01)H

(2.01)H was prepared by stirring 1 equivalent of 8-aminoquinoline with 1 equivalent of salicylaldehyde in MeOH and used *in situ* to produce the ligand (2.01) during coordination.  $^1\text{H}$ -NMR (300 MHz,  $\text{CDCl}_3$ ): 13.95 (br, 1H), 9.02 (dd, 1H,  $J = 4.2$ , 1.7 Hz), 8.95 (s, 1H), 8.22 (dd, 1H,  $J = 8.3$ , 1.7 Hz), 7.76 (dd, 1H,  $J = 8.0$ , 1.4 Hz), 7.60 (t, 1H,  $J = 7.5$  Hz), 7.53 (m, 3H), 7.11 (d, 1H,  $J = 8.2$  Hz), 6.99 (td, 1H,  $J = 7.4$ , 0.9 Hz) ppm. MS (EI +):  $m/z$  248 [ $\text{M}^+$ , 4.1 %], 203 [ $(\text{M} - \text{C}_7\text{H}_3\text{O})^+$ , 100 %].<sup>[188]</sup>

ii) Complex syntheses

**(2.02): [Fe(2.01)<sub>2</sub>]Cl**



**Figure 8.02: (2.02)**

0.417 g (3.40 mmol) salicylaldehyde was combined with 0.492 g (3.40 mmol) 8-aminoquinoline and stirred in MeOH (25 mL) for 10 minutes. 0.461 g (1.70 mmol) FeCl<sub>3</sub>·6H<sub>2</sub>O in MeOH (75 mL) was added to the flask. The solution was concentrated and cooled and the resulting solid was collected by vacuum filtration. Yield: 0.740 g (74 %). MS (ESI +, MeOH): *m/z* 550 [(M - Cl)<sup>+</sup>, 100 %]. FT-IR (KBr): 3430 (br, m), 3950 (w), 2924 (w), 1601 (s), 1580 (m), 1528 (s), 1500 (m), 1461 (w), 1425 (m), 1399 (m), 1380 (w), 1318 (m), 1210 (w), 1145 (w), 1088 (w), 1030 (w), 901 (w), 827 (w), 756 (m), 607 (w), 562 (w), 513 (w) cm<sup>-1</sup>.<sup>[189]</sup>

**(2.03): [Fe(2.01)<sub>2</sub>]I·H<sub>2</sub>O**

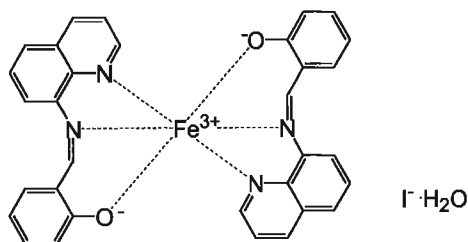


**Figure 8.03: (2.03)**

(**2.02**) (1.00 g, 1.70 mmol) was combined with KI (1.8 mmol, 0.37 g) in H<sub>2</sub>O (100 mL) and stirred for 24 hours. The resulting solid was collected by vacuum filtration, washed with water (50 mL) and pentane (50 mL). Yield: 1.1 g (91 %). MS (ESI +, MeOH): *m/z* 550 [(M - I)<sup>+</sup>, 100 %]. FT-IR (KBr): 3424 (br, w), 3036 (w), 3015 (w), 1601 (s), 1580 (m), 1528 (s), 1501 (m), 1460 (m), 1425 (m), 1400 (m), 1379 (m), 1298 (m), 1238 (w), 1205 (m), 1144 (s), 1084 (w), 1030 (w), 962 (w), 903 (w), 829 (m), 760 (s), 664 (w), 608 (w), 567 (w), 515 (w), 463 (w) cm<sup>-1</sup>. Elemental analysis: calculated (found)% for C<sub>32</sub>H<sub>22</sub>O<sub>2</sub>N<sub>4</sub>Fe; C, 55.27 (54.96); H, 3.48 (3.18); N, 8.06 (8.02).<sup>[189]</sup>

Concentrated solutions of (**2.02**) were prepared by combining 0.122 g (1.00 mmol) salicylaldehyde with 0.144 g (1.00 mmol) 8-aminoquinoline in 10 mL MeOH while stirring for 10 minutes. 0.135 g (0.500 mmol) FeCl<sub>3</sub>·6H<sub>2</sub>O in 20 mL MeOH was added to the flask, followed by 0.083 g (0.50 mmol) KI in an additional 10 mL MeOH. The solution was filtered and the solvent was left to slowly evaporate providing single crystals of Fe(qsal)<sub>2</sub>I.



## 2. Thienyl-substituted qsal complexes

### i) Ligand synthesis

#### (2.04): 5-(Ethynyltrimethylsilyl)salicylaldehyde

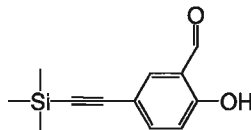
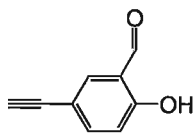


Figure 8.04: (2.04)

5-Bromosalicylaldehyde (4.65 g, 0.0231 mol),  $\text{PPh}_3$  (0.121 g, 2 mol %),  $\text{Pd}(\text{PPh}_3)_2\text{Cl}_2$  (0.324 g, 2 mol %), and  $\text{CuI}$  (0.132 g, 3 mol %) were combined with 150 mL of deaerated anhydrous diisopropylamine. Ethynyltrimethylsilane (2.50 g, 0.0254 mol) was added last, and the mixture was heated to reflux for 4 h. The reaction was concentrated under reduced pressure, combined with pentane (300 mL), and then filtered through a Celite pad. The solvent was removed by rotary evaporation to afford a light yellow powder. Yield: 4.95 g (99.8 %). Mp: 121–124 °C.  $^1\text{H}$ -NMR (300 MHz,  $\text{CDCl}_3$ ):  $\delta$  11.11 (s br, 1H), 9.87 (s, 1H), 7.73 (d, 1H,  $J = 2$  Hz), 7.64 (dd, 1H,  $J = 9, 2$  Hz), 6.97 (d, 1H,  $J = 9$  Hz), 0.27 (s, 9H) ppm.  $^{13}\text{C}$ -NMR (300 MHz,  $\text{CDCl}_3$ ):  $\delta$  196.0, 161.5, 140.1, 137.3, 120.3, 117.9, 115.1, 103.2, 93.2,  $-0.1$  ppm. MS (EI +):  $m/z$  218 [ $\text{M}^+$ , 29 %], 203 [ $(\text{M} - \text{CH}_3)^+$ , 100 %]. FT-IR (KBr): 3427 (m), 3206 (w), 2957 (w), 2878 (w), 2150 (m), 1668 (s), 1475 (s), 1377 (w), 1285 (s), 1245 (m), 1149 (s), 843 (s), 757 (m), 693 (m), 584 (w)  $\text{cm}^{-1}$ . Elemental analysis: calculated (found)% for  $\text{C}_{12}\text{H}_{14}\text{O}_2\text{Si}$ ; C, 66.03 (66.39); H, 6.47 (6.78).

**(2.05): 5-Ethynylsalicylaldehyde**



**Figure 8.05: (2.05)**

5-Ethynyltrimethylsilylsalicylaldehyde (**2.04**) (4.95 g, 0.0226 mol) was dissolved in THF (20 mL). Potassium hydroxide (1.27 g, 0.0226 mol) was dissolved in MeOH (10 mL) and added to the THF solution. The reaction mixture was stirred at room temperature overnight, and then the solvent was concentrated under reduced pressure. The residue was dissolved in  $\text{CHCl}_3$  and washed with 0.05 M HCl (400 mL) and distilled water (400 mL). The organic phase was dried over  $\text{MgSO}_4$ , filtered, and the solvent was removed by rotary evaporation to obtain a light yellow powder. Yield: 3.26 g (98 %). Mp: 115–118 °C.  $^1\text{H}$ -NMR (300 MHz,  $\text{CDCl}_3$ ):  $\delta$  11.15 (br s, 1H), 9.89 (s, 1H), 7.75 (d, 1H,  $J = 2$  Hz), 7.66 (d, 1H,  $J = 9, 2$  Hz), 7.00 (d, 1H,  $J = 9$  Hz), 3.06 (s, 1H) ppm.  $^{13}\text{C}$ -NMR (300 MHz,  $\text{CDCl}_3$ ):  $\delta$  196.0, 161.8, 140.2, 137.5, 120.4, 118.2, 114.0, 81.9, 76.8 ppm. MS (EI +):  $m/z$  146 [ $\text{M}^+$ , 100 %]. FT-IR (KBr): 3427 (w), 3273 (s), 3010 (w), 2886 (w), 1663 (s), 1580 (m), 1477 (s), 1377 (m), 1290 (s), 1201 (s), 1140 (m), 910 (w), 847 (m), 766 (m), 720 (w), 643 (m), 579 (w), 453 (w)  $\text{cm}^{-1}$ . Elemental analysis: calculated (found)% for  $\text{C}_9\text{H}_6\text{O}_2$ ; C, 73.95 (74.12); H, 4.14 (4.07).

**(2.06): 5-(3'-Ethynylthienyl)salicylaldehyde**

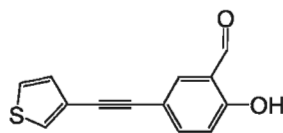


**Figure 8.06: (2.06)**

**(2.05)** (1.00 g, 6.84 mmol), 3-bromothiophene (1.12 g, 6.84 mmol),  $\text{PPh}_3$  (0.090 g, 5 mol %),  $\text{Pd}(\text{PPh}_3)_2\text{Cl}_2$  (0.240 g, 5 mol %), and  $\text{CuI}$  (0.065 g, 5 mol %) were added to anhydrous and deareated THF (50 mL) containing diisopropylamine (0.97 mL). The reaction was stirred under reflux for 20 h, cooled to room temperature, and then concentrated under reduced pressure. The residue was combined with pentane (300 mL), and then filtered through a Celite pad, concentrated to dryness, and the residue was dissolved in acetone. The solution was filtered, and concentrated to dryness again. The residue was dissolved in  $\text{CHCl}_3$  and washed with 0.05 M  $\text{HCl}$  (200 mL) and distilled water (200 mL). The organic phase was dried over  $\text{MgSO}_4$ , filtered, and the solvent was removed by rotary evaporation to afford a light yellow powder. Yield: 0.84 g (54 %). Mp: 95–95 °C.  $^1\text{H-NMR}$  (300 MHz,  $\text{CDCl}_3$ ):  $\delta$  11.13 (br s, 1H), 9.91 (s, 1H), 7.77 (d, 1H,  $J = 2$  Hz), 7.69 (dd, 1H,  $J = 9, 2$  Hz), 7.54 (d, 1H,  $J = 3$  Hz), 7.35 (dd, 1H,  $J = 5, 3$  Hz), 7.22 (d, 1H,  $J = 5$  Hz), 7.02 (d, 1H,  $J = 9$  Hz) ppm.  $^{13}\text{C-NMR}$  (300 MHz,  $\text{CDCl}_3$ ):  $\delta$  196.1, 161.4, 139.7, 138.8, 129.8, 128.7, 125.6, 121.9, 120.5, 118.2, 115.2, 87.0, 84.1 ppm. MS (EI +):  $m/z$  228 [ $\text{M}^+$ , 100 %]. FT-IR (KBr): 3427 (w), 3095 (w), 2921 (w), 2854 (w), 1656 (s), 1578 (w), 1480 (m), 1375 (w), 1286 (m), 1199 (w), 1115 (w), 957 (m), 867 (w), 801 (w), 742 (w), 686 (w), 624 (w), 575 (w), 521 (w), 446 (w)  $\text{cm}^{-1}$ . Elemental analysis: calculated (found)% for  $\text{C}_{13}\text{H}_8\text{SO}_2$ ; C, 68.41 (68.66); H, 3.54 (3.30).

**(2.07)H: theqsalH**

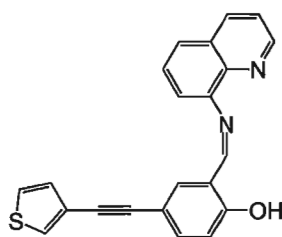


**Figure 8.07: (2.07)H**

**(2.06)** (0.293 g, 1.29 mmol) was dissolved in  $\text{CHCl}_3$  (0.4 mL) and added to a solution of 8-aminoquinoline (0.185 g, 1.29 mmol) in ethanol (50 mL). The solution was stirred at room temperature for 72 h and then filtered. The solvent was removed by rotary evaporation to afford the crimson oil of **(2.07)H**. Yield: 0.431 g (93 %).  $^1\text{H-NMR}$  (300 MHz,  $\text{CDCl}_3$ ):  $\delta$  14.45 (br s, 1H), 8.97 (dd, 1H,  $J = 4, 2$  Hz), 8.93 (s, 1H), 8.19 (dd, 1H,  $J = 8, 2$  Hz), 7.75 (dd, 1H,  $J = 8, 2$  Hz), 7.64–7.45 (m, 6H), 7.31 (dd, 1H,  $J = 8, 2$  Hz), 7.20 (d, 1H,  $J = 5$  Hz), 7.06 (d, 1H,  $J = 9$  Hz) ppm.  $^{13}\text{C-NMR}$ : The instability of **(2.07)** prevented the acquisition of a publishable  $^{13}\text{C-NMR}$  spectrum. HRMS (EI +) calculated for  $[\text{C}_{22}\text{H}_{14}\text{ON}_2\text{S}]^+$ : 354.08361 found 354.08269. FT-IR (KBr): 3427 (m), 3038 (w), 1619 (s), 1495 (s), 1384 (m), 1284 (m), 1244 (w), 1161 (w), 1084 (w), 1054 (w), 891 (w), 827 (m), 787 (m), 754 (w), 595 (w), 469 (w)  $\text{cm}^{-1}$ . Elemental analysis: calculated (found)% for  $\text{C}_{22}\text{H}_{14}\text{ON}_2\text{S}$ ; C, 74.56 (74.21); H, 3.99 (3.85); N, 7.91 (7.97). UV–Vis ( $\text{CHCl}_3$ ):  $\lambda_{\text{max}}$  ( $\epsilon$  ( $\text{M}^{-1} \text{cm}^{-1}$ )) = 500 nm (285).

ii) Complex syntheses

**(2.08): [Fe(2.07)<sub>2</sub>]PF<sub>6</sub>**

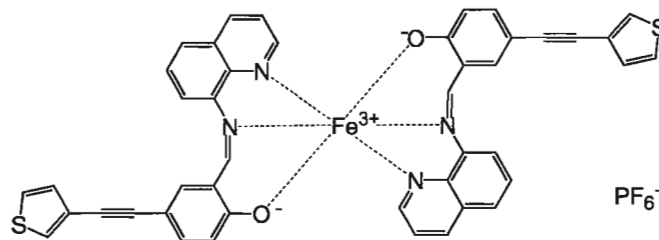


**Figure 8.08: (2.08)**

**(2.07)** (0.489 g, 1.38 mmol) was suspended in MeOH (40 mL), combined with Et<sub>3</sub>N (0.140 g, 1.38 mmol), and stirred for 10 min. FeCl<sub>3</sub>·6H<sub>2</sub>O (0.187 g, 0.690 mmol) was then added, and the solution was stirred for 1 h. An excess of NaPF<sub>6</sub> (0.406 g, 2.42 mmol) was added and the mixture was stirred overnight. Combining the mixture with distilled water (250 mL) resulted in a deep green microcrystalline precipitate that was filtered off, washed with water, pentane, and then dried. Yield: 0.624 g (89.7 %). MS (ESI +, CH<sub>3</sub>CN): *m/z* 762 [(M – PF<sub>6</sub>)<sup>+</sup>, 100 %]. FT-IR (KBr): 3052 (w), 2920 (w), 1606 (s), 1574 (m), 1504 (m), 1455 (m), 1375 (m), 1307 (m), 1164 (w), 1089 (w), 842 (vs), 780 (w), 557 (w), 511 (w) cm<sup>-1</sup>. Elemental analysis: calculated (found)% for C<sub>44</sub>H<sub>26</sub>O<sub>2</sub>N<sub>4</sub>S<sub>2</sub>FePF<sub>6</sub>; C, 58.23 (58.53); H, 2.89 (3.00); N, 6.17 (5.84). UV-Vis (CH<sub>3</sub>CN): λ<sub>max</sub> = 445 nm.

**(2.09): [Fe(2.07)<sub>2</sub>][SCN·2.5H<sub>2</sub>O]**

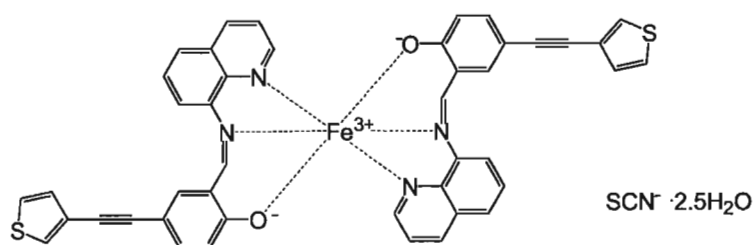


**Figure 8.09: (2.09)**

**(2.07)** (0.489 g, 1.38 mmol) was suspended in MeOH (40 mL), combined with  $\text{Et}_3\text{N}$  (0.140 g, 1.38 mmol), and stirred for 10 min.  $\text{FeCl}_3 \cdot 6\text{H}_2\text{O}$  (0.187 g, 0.690 mmol) was then added, and the solution was stirred for 1 h. An excess of KSCN (0.235 g, 2.42 mmol) was added and the mixture was stirred overnight. Combining the mixture with distilled water (250 mL) resulted in a deep green microcrystalline precipitate that were filtered off, washed with water, pentane, and then dried. Yield: 0.497 g (87.2 %). MS (ESI +,  $\text{CH}_3\text{CN}$ ):  $m/z$  762  $[(\text{M} - \text{NCS})^+, 100 \text{ \%}]$ . FT-IR (KBr): 3450 (m), 3052 (w), 2921 (w), 2053 (vs), 1607 (s), 1574 (s), 1503 (m), 1456 (s), 1376 (m), 1308 (m), 1164 (m), 1088 (w), 1038 (m), 927 (w), 828 (m), 782 (m), 677 (w), 547 (m), 511 (w)  $\text{cm}^{-1}$ . Elemental analysis: calculated (found)% for  $\text{C}_{45}\text{H}_{26}\text{O}_2\text{N}_5\text{S}_3\text{Fe} \cdot 2.5 \cdot \text{H}_2\text{O}$ ; C, 62.43 (62.91); H, 3.61 (3.18); N, 8.08 (7.45). UV-Vis ( $\text{CH}_3\text{CN}$ ):  $\lambda_{\text{max}} = 455 \text{ nm}$ .

**(2.10): [Fe(2.07)<sub>2</sub>](ClO<sub>4</sub>)**

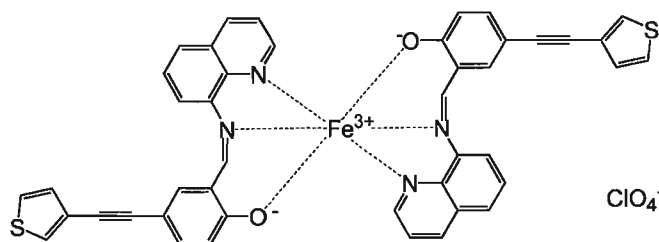


**Figure 8.10: (2.10)**

**(2.07)** (0.397 g, 1.12 mmol) was dissolved in DCM (10 mL), and a half-equivalent of Fe(ClO<sub>4</sub>)<sub>3</sub>·6H<sub>2</sub>O (0.20 g, 0.56 mmol) dissolved in CH<sub>3</sub>CN (15 mL) was added at room temperature in air. A dark precipitate formed immediately in the solution, to which an additional 25 mL of CH<sub>3</sub>CN was added. The mixture was stirred for 2 h, and the dark maroon precipitate was isolated by vacuum filtration, washed with water, pentane, and dried. Yield: 0.34 g (71 %). MS (ESI +, CH<sub>3</sub>CN): *m/z* 762 [(M – ClO<sub>4</sub>)<sup>+</sup>, 100 %]. FT-IR (KBr): 3098 (w), 3063 (w), 1605 (s), 1573 (s), 1527 (m), 1503 (s), 1454 (m), 1397 (m), 1376 (m), 1306 (m), 1241 (w), 1190 (w), 1093 (vs), 829 (m), 782 (m), 760 w), 622 (m), 548 (w), 512 (w) cm<sup>-1</sup>. Elemental analysis: calculated (found)% for C<sub>44</sub>H<sub>26</sub>O<sub>6</sub>N<sub>4</sub>S<sub>2</sub>FeCl; C, 61.29 (61.25); H, 3.04 (3.01); N, 6.50 (6.31). UV-Vis (CHCl<sub>3</sub>): λ<sub>max</sub> (ε (M<sup>-1</sup> cm<sup>-1</sup>)) = 450 nm (4100). UV-Vis (BaSO<sub>4</sub>): λ<sub>max</sub> = 475 nm.

**(2.11): [Mn(2.07)<sub>2</sub>]**

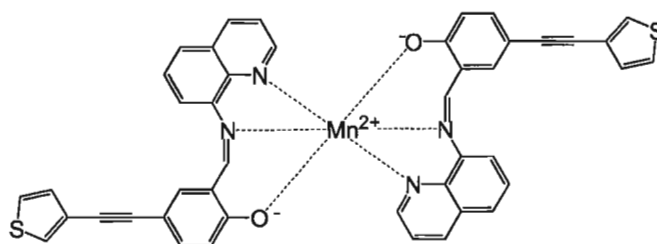


**Figure 8.11: (2.11)**

8-aminoquinoline 20.3 mg, 0.141 mmol was added to a solution of **(2.07)** (32.2 mg, 0.141 mmol) in DCM (10 mL) and stirred for 30 minutes.  $\text{Mn}(\text{C}_2\text{H}_3\text{O}_2)_2 \cdot 4\text{H}_2\text{O}$  (17.3 mg, 0.0706 mmol) was dissolved in MeOH (10 mL) and added to the solution, which was stirred for an additional 30 minutes and then filtered. Slow evaporation of the solvent under aerobic conditions provided single crystals suitable for X-ray diffraction. Yield: 41.0 mg (77 %). MS (ESI +,  $\text{CH}_3\text{CN}$ ):  $m/z$  762 [ $(\text{M})^+$ , 30 %]. FT-IR (KBr): 3300 (br, s), 2962 (w), 2921 (w), 2852 (w), 2195 (w), 1603 (s), 1584 (m), 1499 (s), 1457 (s), 1402 (m), 1339 (w), 1275 (w), 1237 (w), 1157 (m), 1120 (w), 1089 (w), 1063 (w), 865 (w), 823 (w), 781 (w), 622 (w), 502 (w)  $\text{cm}^{-1}$ . Elemental analysis: calculated (found)% for  $\text{C}_{44}\text{H}_{26}\text{O}_2\text{N}_4\text{S}_2\text{Mn}$ ; C, 69.38 (68.97); H, 3.45 (3.15); N, 7.36 (7.11). UV-Vis ( $\text{CH}_3\text{CN}$ ):  $\lambda_{\text{max}}$  ( $\epsilon$  ( $\text{M}^{-1} \text{cm}^{-1}$ )) = 485 nm ( $1.5 \times 10^4$ ).



**(2.12): [Fe(2.07)<sub>2</sub>]·C<sub>3</sub>H<sub>6</sub>O·1.5H<sub>2</sub>O**

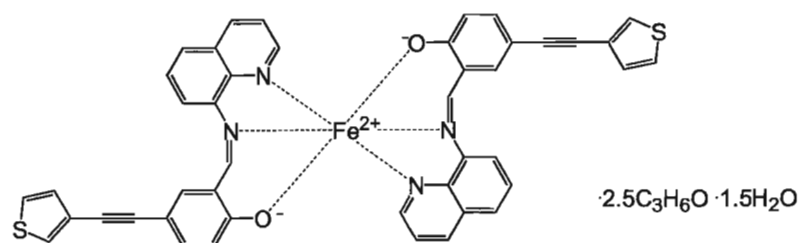


**Figure 8.12: (2.12)**

**(2.10)** (40 mg, 0.046 mmol) was stirred in acetone (20 mL) for 0.5 h. The solution was filtered and divided into two equal portions, which were left to stand open to air at room temperature. Black plate crystals formed by slow evaporation. MS (ESI +, CH<sub>3</sub>CN): 762 [M<sup>+</sup>, 100 %]. FT-IR (KBr): 3063 (w), 2961 (w), 2922 (w), 2851 (w), 1605 (s), 1573 (s), 1504 (s), 1454 (m), 1376 (m), 1314 (m), 1260 (m), 1203 (m), 1164 (m), 1129 (m), 1088 (m), 825 (s), 777 (s), 623 (w), 551 (w), 511 (w) cm<sup>-1</sup>. Elemental analysis: calculated (found)% for C<sub>47</sub>H<sub>32</sub>O<sub>4.5</sub>N<sub>4</sub>S<sub>2</sub>Fe; C, 66.83 (64.76); H, 4.18 (3.99); N, 6.63 (6.04). UV-Vis (CHCl<sub>3</sub>): λ<sub>max</sub> (ε (M<sup>-1</sup> cm<sup>-1</sup>)) = 445 nm (4400).

### 3. Terthienyl-substituted qsal complexes

#### i) Ligand synthesis

**(2.13): 2,3,5-tribromothiophene**

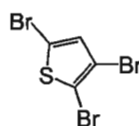


**Figure 8.13: (2.13)**

3-bromothiophene (6.00 g, 36.8 mmol) was added to a mixture of 48 %  $\text{HBr}_{(\text{aq})}$  (10.8 mL) and  $\text{Et}_2\text{O}$  (9.6 mL) and cooled to 5 °C. Bromine (11.6 g, 72.5 mmol) was dissolved in 48 %  $\text{HBr}_{(\text{aq})}$  and added to the solution of 3-bromothiophene while maintaining the temperature of 5 °C. The mixture was then heated for 3 hours at 50 °C, extracted in  $\text{Et}_2\text{O}$  and passed through a small column of alumina using  $\text{Et}_2\text{O}$  as the eluent. Yield: 11.6 g (98 %).  $^1\text{H-NMR}$  (300 MHz,  $\text{CDCl}_3$ ):  $\delta$  6.90 ppm (s, 1H). MS (EI +):  $m/z$  326  $[\text{M}(^{81}\text{Br}_2^{79}\text{Br})^+, 100]$ , 322  $[\text{M}(^{81}\text{Br}^{79}\text{Br}_2)^+, 100]$ .<sup>[190]</sup>

**(2.14): 3'-Bromo-2,2':5',2''-terthiophene**

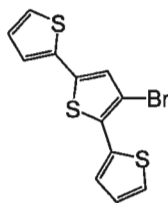


**Figure 8.14: (2.14)**

9.12 g (28.4 mmol) of (2.13) was added to a round bottom flask and then combined with anhydrous 1,2-dimethoxyethane (270 mL) and a 1.0 M aqueous solution of  $\text{K}_2\text{CO}_3$  (200 mL). The mixture was purged by  $\text{N}_2$  sparging for 0.5 h, followed by the addition of 2-thienylboronic acid (8.00 g, 62.5 mmol) and 10 mol % (with respect to 2,3,5-tribromothiophene)  $\text{PdCl}_2(\text{PPh}_3)_2$  (3.18 g, 2.75 mmol). The reaction mixture was heated at 95 °C for 72h. The reaction contents were combined with  $\text{H}_2\text{O}$  (400 mL) and extracted into DCM (400 mL). The organic extracts were combined, dried over  $\text{MgSO}_4$ , concentrated (not to dryness) by rotary evaporation, and then pentane was added to precipitate out reaction by-products, which were removed by gravity filtration. The

filtrate was concentrated to dryness and the crude product was purified by column chromatography (SiO<sub>2</sub>) using hexane as eluent to obtain of vibrant yellow oil. Yield: 4.27 g (46 %). <sup>1</sup>H-NMR (300 MHz, CDCl<sub>3</sub>): δ 7.50 (d, 1H, *J* = 4 Hz), 7.39 (d, 1H, *J* = 5 Hz), 7.28 (d, 1H, *J* = 5 Hz), 7.21 (d, 1H, *J* = 4 Hz), 7.14 (m, 2H), 7.07 (m, 1H) ppm. <sup>13</sup>C-NMR (300 MHz, CDCl<sub>3</sub>): δ 135.8, 135.7, 134.4, 130.9, 128.2, 127.8, 127.5, 126.7, 126.2, 125.5, 124.5, 108.0 ppm. MS (EI +): *m/z* 328 [M(<sup>81</sup>Br)<sup>+</sup>, 100], 326 [M(<sup>79</sup>Br)<sup>+</sup>, 100]. HRMS (EI +) calculated for C<sub>12</sub>H<sub>7</sub>SBr (325.88933), found 325.89021.<sup>[190]</sup>

**(2.15): 3'-(3-hydroxy-3-methylbut-1-ynyl)-2,2':5',2''-terthiophene**

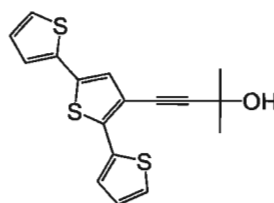


**Figure 8.15: (2.15)**

The following procedure is a modified version of Shin and co-workers. **(2.14)** (2.90 g, mmol) was dissolved in diisopropyl amine (50 mL) and sparged with N<sub>2</sub> for 0.5 h. Pd(PPh<sub>3</sub>)<sub>2</sub>Cl<sub>2</sub> (187 mg, 0.240 mmol) and CuI (51 mg, 0.26 mmol) were added to the solution containing **(2.14)**. After refluxing for 24 h, the reaction mixture was concentrated by rotary evaporation and diluted into H<sub>2</sub>O. The organics were extracted into DCM, passed through a Celite pad, dried over MgSO<sub>4</sub> and concentrated to dryness. The residue was dissolved in a minimal amount of hexane and chromatographed on silica gel using a 5:1 mixture of hexane-ethylacetate as the eluent to give a yellow oil. Yield: 2.1 g (70 %). <sup>1</sup>H-NMR (300 MHz, CDCl<sub>3</sub>): δ 7.46 (dd, 1H, *J* = 3.6, 0.9 Hz), 7.32 (dd,

1H,  $J = 5.1, 0.9$  Hz), 7.24 (dd, 1H,  $J = 5.1, 0.9$  Hz), 7.16 (dd, 1H,  $J = 3.6, 0.9$  Hz), 7.10 (s, 1H), 7.07 (dd 1H,  $J = 5.1, 3.6$  Hz) 7.03 (dd 1H,  $J = 5.1, 3.6$  Hz), 2.50 (br, 1H), 1.7 (s, 6H) ppm. MS (EI +):  $m/z$  330 [ $M^+$ , 14 %], 312 [ $(M-CH_3)^+$ , 18 %], 272 [ $(M-C_3H_6O)$ , 100 %].<sup>[191]</sup>

**(2.16): 3'-(Ethynyl)-2,2':5',2''-terthiophene**

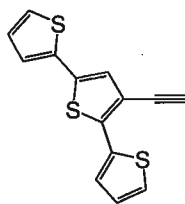


**Figure 8.16: (2.16)**

The following procedure is a modified version of Shin and co-workers. **(2.15)** (350 mg, 1.1 mmol) is added to a mixture of MeOH (45 mL) and Toluene (20 mL) and sparged with  $N_2$  for 1 h. Potassium hydroxide (5.0 g, 89 mmol) is then added and the mixture is heated to 100 °C. After confirmation of the disappearance of the starting material by  $^1H$ -NMR (2 d), the solution is extracted with DCM and chromatographed on silica gel using hexane as the eluent to give a yellow oil. Yield: 230 mg (80 %).  $^1H$ -NMR (300 MHz,  $CDCl_3$ ):  $\delta$  7.58 (dd, 1H,  $J = 3.7, 1.0$  Hz), 7.34 (dd, 1H,  $J = 5.1, 1.0$  Hz), 7.28 (m, 1H), 7.21 (dd, 1H,  $J = 3.7, 1.1$ ), 7.17 (s, 1H), 7.10 (dd, 1H,  $J = 5.0, 3.7$ ), 7.07 (dd, 1H,  $J = 5.1, 3.8$ ) ppm. MS (EI +):  $m/z$  272 [ $M^+$ , 100 %].<sup>[191]</sup>

**(2.17): 5-Iodosalicylaldehyde**

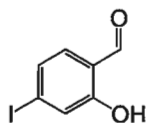


**Figure 8.17: (2.17)**

The following procedure is a modified version of Pauls and co-workers. A 1.0 M solution of iodine monochloride in dry THF (100 mL) was added to a flask containing a mixture of salicylaldehyde (12.2 g, 0.100 mol) and I<sub>2</sub> (25.4 g, 0.100 mol). The reaction was stirred at room temperature for 48 h, and then added to a saturated aqueous solution of Na<sub>2</sub>SO<sub>3</sub> (1 L). The solution was stirred at room temperature as the purple color gradually disappeared, and the THF was completely evaporated resulting in a precipitate that was filtered, washed with water, and dried providing a white solid. Yield: 23 g (94 %). <sup>1</sup>H-NMR (300 MHz, CDCl<sub>3</sub>): δ 10.97 (br s, 1H), 9.85 (s, 1H), 7.87 (d, 1H, *J* = 2 Hz), 7.80 (dd, 1H, *J* = 9, 2 Hz), 6.83 (d, 1H, *J* = 9 Hz) ppm. MS (EI +): *m/z* 248 [M<sup>+</sup>, 100 %].<sup>[192]</sup>

**(2.18): 3'-(5-ethynylsalicylaldehyde)-2,2':5',2''-terthiophene**

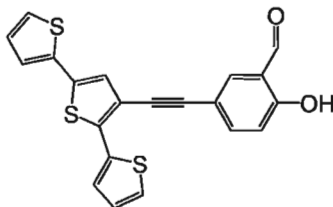


**Figure 8.18: (2.18)**

(**2.16**) (0.915 g, 3.36 mmol) was dissolved in anhydrous THF (100 mL) and purged by N<sub>2</sub> sparging for 0.5 h. In the following order, triethylamine (0.70 mL, 4.9 mmol), Pd(PPh<sub>3</sub>)<sub>2</sub>Cl<sub>2</sub> (77 mg, 0.10 mmol), CuI (34 mg, 0.17 mmol), PPh<sub>3</sub> (29 mg, 0.11 mmol) and (**2.17**) (1.19 g, 4.80 mmol) were added to the THF solution containing (**2.16**). After refluxing for 5 d, the reaction mixture was concentrated by rotary evaporation and diluted into H<sub>2</sub>O. The organics were extracted into DCM, passed through a Celite pad, dried over MgSO<sub>4</sub> and concentrated to dryness. The residue was dissolved in a minimal amount of warm CHCl<sub>3</sub> and the product precipitated in pentane (50 mL). The product was washed with small amounts of pentane and cold methanol to afford a yellow solid. Yield: 0.56 g (42 %). Mp: 146-147 °C. <sup>1</sup>H-NMR (300 MHz, CDCl<sub>3</sub>): δ 11.19 (s, <sup>1</sup>H), 9.94 (s, 1H), 7.81 (d, 1H, *J* = 1 Hz), 7.75 (dd, 1H, *J* = 5, 1 Hz), 7.50 (d, 1H, *J* = 1 Hz), 7.37 (d, 1H, *J* = 2 Hz), 7.29 (d, 1H, *J* = 3 Hz), 7.23 (d, 1H, *J* = 2 Hz), 7.20 (s, 1H), 7.12-7.08 (m, 3H) ppm. <sup>13</sup>C-NMR (300 MHz, CDCl<sub>3</sub>): δ 196.2, 161.6, 139.6, 138.5, 136.8, 136.1, 135.7, 134.3, 128.0, 127.3, 126.8, 125.9, 125.6, 125.2, 124.3, 120.6, 118.3, 117.4, 115.1, 92.4, 84.7 ppm. MS (EI +): *m/z* 392 [*M*<sup>+</sup>, 100 %]. FT-IR (KBr): 3449 (w), 2922 (w), 2853 (w), 1655 (s), 1584 (w), 1457 (w), 1384 (w), 1282 (w), 1176 (m), 1140 (m), 831 (w), 685 cm<sup>-1</sup> (s). Elemental analysis: calculated (found)% for C<sub>21</sub>H<sub>12</sub>O<sub>2</sub>S<sub>3</sub>; C, 64.26 (64.37); H, 3.08 (2.88).

**(2.19)H: theqsalH**

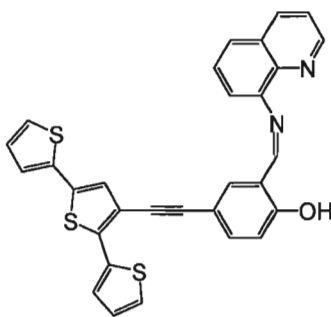


**Figure 8.19: (2.19)H**

**(2.18)** (0.21 g, 0.54 mmol) was dissolved in  $\text{CHCl}_3$  (25 mL) and purged with  $\text{N}_2$  for 0.5 h. 8-aminoquinoline (0.077 g, 0.54 mmol) was added to the solution of **(2.18)**, and the deep red mixture was stirred at room temperature under  $\text{N}_2$  for 24 h. The solution was concentrated to dryness by rotary evaporation to afford **(2.19)H**, pure and in near quantitative yield. **(2.19)H** is unstable and was not generally isolated, but used directly in coordination reactions (we isolated pure **(2.19)H** for characterization).  $^1\text{H}$ -NMR (300 MHz,  $\text{CDCl}_3$ ):  $\delta$  14.45 (s, 1H), 9.00 (m, 2H), 8.22 (d, 1H,  $J = 8$  Hz), 7.79 – 7.48 (m, 7 H), 7.36 – 6.93 (m, 7H) ppm.  $^{13}\text{C}$ -NMR: The instability of **(2.19)H** prevented the acquisition of a publishable  $^{13}\text{C}$ -NMR spectrum. MS (MALDI-TOF  $-$ ):  $m/z$  517 [(M – H) $^-$ , 80 %], 491 [(M – CO) $^-$ , 78 %] 391 [(M –  $\text{C}_9\text{H}_6\text{N}$ ) $^-$ , 100 %]. FT-IR (KBr): 3447 (br, s), 2953 (m), 2922 (s), 2853 (m), 1654 (m), 1618 (s), 1559 (w), 1458 (w), 1261 (w), 1083 (w), 872 (w), 789 (w), 693 (w)  $\text{cm}^{-1}$ . Elemental analysis: calculated (found)% for  $\text{C}_{30}\text{H}_{18}\text{N}_2\text{OS}_3$ ; C, 69.47 (69.14); H, 3.50 (3.16); N, 5.40 (5.11).

ii) Complex syntheses

**(2.20): [Fe(2.19)<sub>2</sub>]PF<sub>6</sub>**

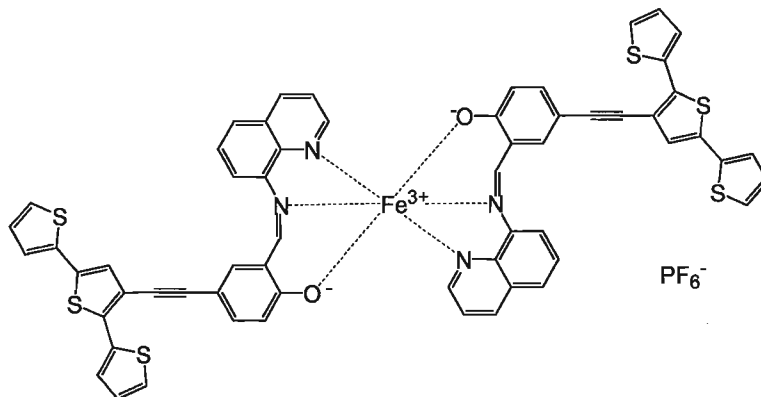


**Figure 8.20: (2.20)**

**(2.18)** (0.21 g, 0.54 mmol) was dissolved in CHCl<sub>3</sub> (25 mL) and purged with N<sub>2</sub> for 0.5 h. 8-aminoquinoline (0.077 g, 0.54 mmol) was added, and the deep red mixture was stirred at room temperature under N<sub>2</sub> for 24 h (generating ligand **(2.19)** *in situ*). FeCl<sub>3</sub>·6H<sub>2</sub>O (0.073 g, 0.27 mmol) in MeOH (10 mL) was added to the solution of **(2.18)**, resulting in a solution color change from red to brown. The brown solution was stirred for 4 h, and then concentrated by rotary evaporation to remove the CHCl<sub>3</sub> completely. MeOH (50 mL) and THF (50 mL) were added to the concentrated solution, followed by the addition of solid NaPF<sub>6</sub> (0.318 g, 1.89 mmol). The mixture was stirred for 8 h, subsequently added to an aqueous solution (500 mL) of NaPF<sub>6</sub> (0.200 g, 1.19 mmol), and stirred overnight. The brown-green precipitate was collected by vacuum filtration, washed with water, and then pentane. Yield: 250 mg (76 %). MS (ESI +, CH<sub>3</sub>CN): *m/z* 1090 [(M – PF<sub>6</sub>)<sup>+</sup>, 100 %]. FT-IR (KBr): 3420 (br, m), 2920 (w), 1603 (s), 1575 (m), 1524 (m), 1503 (m), 1451 (w), 1378 (m), 1319 (m), 1214 (w), 1191 (w), 1165 (w), 1088 (w), 831 (s), 696 (m), 542 (w),



512  $\text{cm}^{-1}$  (w)  $\text{cm}^{-1}$ . Elemental analysis: calculated (found)% for  $\text{C}_{60}\text{H}_{34}\text{N}_4\text{O}_2\text{S}_6\text{FePF}_6$ ; C, 58.30 (58.13); H, 2.77 (2.93); N, 4.53 (4.84).

**(2.21):  $[\text{Mn}(\mathbf{2.19})_2]$**

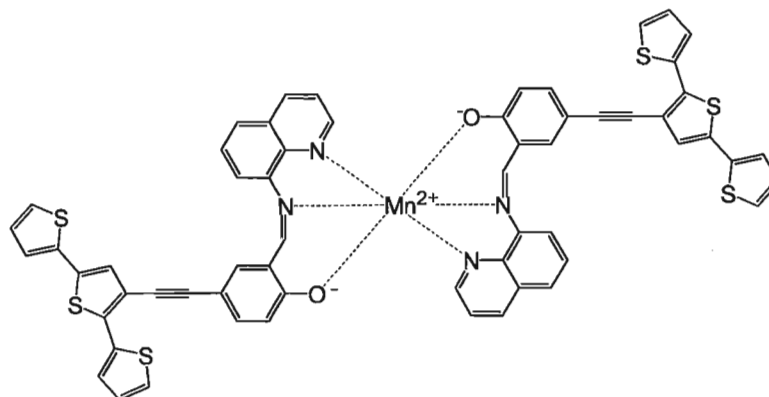


**Figure 8.21: (2.21)**

8-aminoquinoline (5.5 mg, 0.038 mmol) was added to a solution of **(2.18)** (15 mg, 0.038 mmol) in DCM (5 mL) deaerated with  $\text{N}_2$  gas and stirred for 30 minutes. A solution of  $\text{Mn}(\text{C}_2\text{H}_2\text{O}_2)_2 \cdot 4\text{H}_2\text{O}$  (4.7 mg, 0.019 mmol) in MeOH (10 mL) was added to the DCM solution, which was stirred for an additional 30 minutes and then dried by vacuum affording an orange solid. Yield: 20 mg (98 %). MS (FAB +): 1090  $[(\text{M} + \text{H})^+]$ , 3 %, 572  $[(\text{M} - \text{C}_{30}\text{H}_{18}\text{N}_2\text{OS}_3)^+]$ , 65 %. FT-IR (KBr): 3460 (w), 2959 (m), 2924 (m), 2853 (m), 2195 (w), 1607 (m), 1506 (m), 1464 (m), 1402 (w), 1375 (m), 1335 (w), 1261 (s), 1092 (s), 1022 (s), 798 (s), 748 (w), 686  $\text{cm}^{-1}$  (w)  $\text{cm}^{-1}$ .

## 8.09 Experimental for Chapter 3<sup>†</sup>

### 1. Bispicen derivatives

#### i) Thiophene derivative

#### (3.02): 2,5-dibromo-3,4-dinitrothiophene

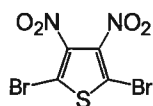


**Figure 8.22: (3.02)**

Concentrated  $\text{H}_2\text{SO}_4$  (40 mL) was added to a 3-neck round bottom flask and then purged with  $\text{N}_2$  for 30 minutes while being cooled in an ice bath. 2,5-dibromothiophene (10.7 g, 44.4 mmol) was added slowly, maintaining a temperature below 20 °C. Concentrated  $\text{HNO}_3$  (7 mL) was then added to the round bottom flask dropwise to keep the temperature under 30 °C. Following the addition, the mixture was stirred for an additional 3 h and then poured over ice (160 g). After the ice had melted, a solid residue was recovered by vacuum filtration, washed with water producing and recrystallized from MeOH to provide a light yellow powder. Yield: 7.64 g (52 %).  $^{13}\text{C}$ -NMR (600 MHz,  $\text{CDCl}_3$ ):  $\delta$  140.3, 113.4 ppm. MS (EI +):  $m/z$  332 [ $\text{M}^+$ , 100 %].<sup>[120]</sup>

**(3.03): 3,4-diaminothiophene·2HCl**

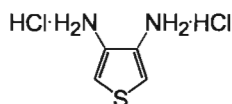


**Figure 8.23: (3.03)**

Concentrated HCl (25 mL) was added to a 3-neck round bottom flask, which was then degassed by sparging with N<sub>2</sub> for 30 minutes. **(3.02)** (1.28 g, 3.80 mmol) was added and the reaction mixture was then cooled in an ice bath. Tin (3.19 g, 26.9 mmol) was added slowly while maintaining a temperature of 25-30 °C. The flask was then stirred until all the tin metal was consumed and then cooled to 3 °C overnight. The resulting precipitate was recovered by vacuum filtration and washed with diethyl ether and affording a white solid. Yield: 0.640 g (83 %). <sup>1</sup>H-NMR (300 MHz, CDCl<sub>3</sub>): δ 6.16 (s, 2H), 3.36 (br, 4H) ppm. MS (EI +): *m/z* 114 [(M-2HCl)<sup>+</sup>, 100 %].<sup>[120]</sup>

**(3.04): *N,N'*-bis(2-pyridylmethyl)-3,4-diaminothiophene**

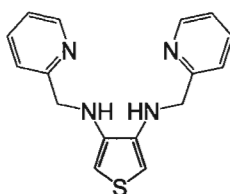


**Figure 8.24: (3.04)**

**(3.03)** (0.20 g, 1.1 mmol) was added to an oven-dried 3-neck round bottom flask fitted with a reflux condenser and flushed with N<sub>2</sub> for 5 minutes. In a separate flask, sodium hydroxide (0.086 g, 2.2 mmol) was dissolved in methanol (20 mL) and sparged with N<sub>2</sub> for 20 minutes and then transferred by syringe into the flask containing **(3.03)**. The

mixture was stirred for 30 minutes, followed by the addition of 2-pyridinecarboxaldehyde (0.24 g, 2.3 mmol) and then the mixture was heated to reflux for 1.5 h (in the absence of light). The solution was removed from the heating mantle while NaBH<sub>4</sub> (0.21 g, 5.7 mmol) was added in small portions and then the reflux was continued for an additional for 14 hours. The solvent was removed by rotary evaporation and the residue was extracted into DCM and dried with MgSO<sub>4</sub>. The solution was passed through a Celite pad and then concentrated by rotary evaporation combined with pentane (50 mL), filtered and dried. The residue was chromatographed with neutral alumina, using 2:1 hexane-EtOAc followed by 1:2 hexane-EtOAc as the eluents, providing bright yellow oil. Yield: 0.053g (17 %). <sup>1</sup>H-NMR (300 MHz, CDCl<sub>3</sub>): δ 8.60 (d, 2H, *J* = 4.5Hz), 7.67 (td, 2H, *J* = 7.5, 1.8Hz), 7.39 (d, 2H, *J* = 7.8Hz), 7.21 (dd, 2H, *J* = 5.2, 1.8Hz), 6.01 (s, 2H), 4.45 (m, 6H) ppm. <sup>13</sup>C-NMR (600 MHz, CDCl<sub>3</sub>): δ 158.5, 149.3, 139.5, 136.7, 122.2, 121.8, 97.6, 51.4 ppm. MS (FAB +): *m/z* 297 [(M<sup>+</sup>, 100 %)], 93 [(M-C<sub>10</sub>H<sub>10</sub>N<sub>3</sub>S)<sup>+</sup>, 62 %]. HRMS (EI +) calculated for [C<sub>16</sub>H<sub>16</sub>N<sub>4</sub>S]<sup>+</sup>: 296.10951, found 296.10957. FT-IR (KBr): 3447 (br, s), 3105 (m), 2960 (w), 2923 (m), 2851 (w), 1594 (s), 157 (m), 1436 (m), 1261 (w), 1097 (br, w), 801 (w), 757 (m) cm<sup>-1</sup>.

ii) Diphenylthiophene derivative

**(3.05): 3,4-dinitro-2,5-diphenylthiophene**

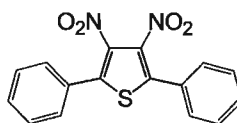


**Figure 8.25: (3.05)**

Phenylboronic acid (0.20 g, 1.7 mmol) was added to a Schlenk flask and flushed with N<sub>2</sub> gas for 5 minutes. 1,2-dimethoxyethane (5 mL) and water (1.8 mL) were added to the reaction flask, which was then sparging with N<sub>2</sub> for 30 minutes. K<sub>2</sub>CO<sub>3</sub> (0.50 g, 3.6 mmol), **(3.02)** (0.10 g, 0.60 mmol), Pd(PPh<sub>3</sub>)<sub>4</sub> (0.040 g, 0.040 mmol) were added to the flask, and the mixture was heated to 65 °C under nitrogen for 13 hours. The reaction mixture was washed with water and extracted with DCM, dried with MgSO<sub>4</sub>, and concentrated to dryness. The residue was chromatographed over silica gel using 1:3 DCM: hexane as the eluent giving a yellow powder. Yield: 0.16 g (80 %). Mp: 145-147 °C. <sup>1</sup>H-NMR (300 MHz, CDCl<sub>3</sub>): δ 7.54 (m, 10H) ppm. <sup>13</sup>C-NMR (600 MHz, CDCl<sub>3</sub>): δ 140.8, 136.8, 130.9, 129.3, 129.1, 128.1 ppm. MS (EI +): *m/z* 326 [M<sup>+</sup>, 100 %]. HRMS (EI +) calculated for [C<sub>16</sub>H<sub>10</sub>N<sub>2</sub>O<sub>4</sub>S]<sup>+</sup>: 326.03613, found 326.03557. FT-IR (KBr): 3448 (br, m), 3059 (w), 1963 (w), 1542 (s), 1524 (s), 1448 (m), 1395 (s), 1327 (s), 1261 (m), 1079 (m), 902 (m), 748 (s), 691 (s) cm<sup>-1</sup>. Elemental analysis: calculated (found)% for C<sub>16</sub>H<sub>10</sub>N<sub>2</sub>O<sub>4</sub>S; C, 58.94 (57.43); H, 3.09 (3.71); N, 8.58 (7.81).

**(3.06): 3,4-diamino-2,5-diphenylthiophene·2HCl**

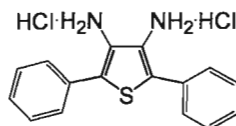


**Figure 8.26: (3.06)**

**(3.05)** (0.33 g, 1.0 mmol) in absolute ethanol (30 mL) and concentrated HCl (60 mL) was added tin metal (3.63 g, 30.6 mmols) in small portions and stirred at room temperature

for 15 h. The resulting precipitate was collected by vacuum filtration and washed with H<sub>2</sub>O to afford a pale yellow solid. Yield: 0.24 g (71 %). Mp: 205-207 °C. <sup>1</sup>H-NMR (300 MHz, CDCl<sub>3</sub>): δ 7.56 (m, 4H), 7.45 (m, 4H), 7.30 (m, 2H), 3.67 (br, 4H) ppm. <sup>13</sup>C-NMR (600 MHz, CDCl<sub>3</sub>): δ 134.4, 133.2, 129.1, 127.6, 126.7, 116.5 ppm. MS (FAB+): *m/z* 266 [(M-2HCl)<sup>+</sup>, 100 %]. HRMS (EI +) calculated for [C<sub>16</sub>H<sub>14</sub>N<sub>2</sub>S]<sup>+</sup>: 266.08777, found 266.08880. FT-IR (KBr): 3330 (m, d), 3047 (w), 2920 (w), 2848 (w), 1616 (m), 1595 (m), 1523 (m), 1489 (m), 1429 (s), 1313 (w), 970 (m), 754 (s), 703 (m), 621 (w), 573 (w) cm<sup>-1</sup>. Elemental analysis: calculated (found)% for C<sub>16</sub>H<sub>16</sub>N<sub>2</sub>SCl<sub>2</sub>; C, 72.22 (70.01); H, 5.30 (5.35); N, 10.52 (9.93).

**(3.07): *N,N'*-bis(2-pyridylmethyl)-3,4-diamino-2,5-diphenylthiophene**

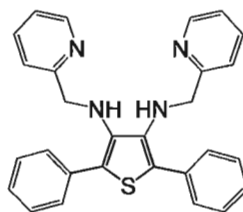


**Figure 8.27: (3.07)**

**(3.06)** (0.12 g, 0.35 mmol) was added to an oven-dried 3-neck round bottom flask fitted with a reflux condenser that was flushed with N<sub>2</sub> for 5 minutes. In a separate flask, potassium hydroxide (0.040 g, 0.69 mmol) was dissolved in methanol (20 mL), sparged with N<sub>2</sub> for 20 minutes and then transferred via syringe into the flask containing **(3.03)**. The mixture was stirred for 30 minutes followed by the addition of 2-pyridinecarboxaldehyde (0.22 g, 2.1 mmol) and then refluxed for 1 h and protected (in the absence of light). The reaction was then cooled down to RT followed by adding 20

eq. of NaBH<sub>4</sub> (0.26 g, 6.9 mmol), and then refluxed at 75 °C for 1 h under an atmosphere of nitrogen. The reaction mixture was diluted into Na<sub>2</sub>CO<sub>3</sub> solution (pH = 9.5), extracted into diethyl ether, dried over MgSO<sub>4</sub> and concentration by rotary evaporation. The residue was chromatographed over neutral alumina using DCM as the eluent and concentrated to dryness affording 0.12 g of **(3.07)**, which was used directly in coordination reaction due to instability. <sup>1</sup>H-NMR (300 MHz, CDCl<sub>3</sub>): δ 8.52 (m, 2H), 7.59 (m, 16H), 4.31 (m, 6H) ppm.

iii) Terthiophene derivative

**(3.08): 3',4'-dinitro-2,2':5',2''-terthiophene**

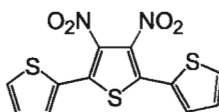


**Figure 8.28: (3.08)**

Thiophene-2-boronic acid (3.29 g, 25.7 mmol) was added to a Schlenk flask and flushed with N<sub>2</sub> gas for 5 minutes. 1,2-dimethoxyethane (5 mL) and water (1.8 mL) were added to the reaction flask and then sparged with N<sub>2</sub> for 30 minutes. Potassium carbonate (0.25 g, 1.8 mmol), **(3.02)** (3.1 g, 9.3 mmol) and Pd(PPh<sub>3</sub>)<sub>4</sub> (0.65 g, 0.56 mmol) were added to the flask and the mixture was refluxed at 100 °C for 8 h. The reaction mixture was washed with water and extracted into DCM, dried with MgSO<sub>4</sub> and concentrated to dryness. The residue was chromatographed over silica gel using 1:3 DCM: hexane as eluent giving a yellow solid. Yield: 0.050 g (48 %). <sup>1</sup>H-NMR (300 MHz, CDCl<sub>3</sub>): δ 7.62

(dd, 2H,  $J = 5.1, 0.9$  Hz), 7.57 (dd, 2H,  $J = 3.6, 0.9$  Hz), 7.20 (dd, 2H,  $J = 5.1, 3.6$  Hz) ppm. MS (FAB +):  $m/z$  338 [ $M^+$ , 100 %].<sup>[193]</sup>

**(3.09): 3',4'-diamino-2,2':5',2''-terthiophene·2HCl**

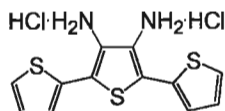


**Figure 8.29: (3.29)**

**(3.08)** (0.27 g, 0.80 mmol) in absolute ethanol (30 mL) and concentrated HCl (60 mL) was combined with 30 eq. of tin metal (2.84 g, 24.0 mmol) in small portions. The resulting mixture was stirred at room temperature for 15 h. The resulting precipitate was collected by vacuum filtration and washed with H<sub>2</sub>O affording a yellow solid. Yield: 0.28 g (88 %). <sup>1</sup>H-NMR (300 MHz, CDCl<sub>3</sub>) =  $\delta$  7.30 (dd, 2H,  $J = 4.8, 1.5$  Hz), 7.11 (m, 4H), 3.76 (br, 4H), ppm. MS (FAB +):  $m/z$  278 [(M-2HCl)<sup>+</sup>, 100 %].<sup>[193]</sup>

**(3.10): *N,N'*-bis(2-pyridylmethyl)-3,4-diamino-2,2':5',2''-terthiophene**

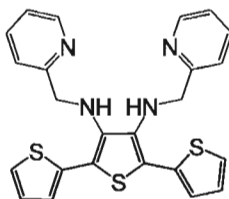


**Figure 8.30: (3.10)**

**(3.09)** (0.10 g, 0.28 mmol) was added to an oven-dried 3-neck round bottom flask fitted with a reflux condenser. The apparatus was then flushed with N<sub>2</sub> for 5 minutes. 2 eq. of



KOH (0.032 g, 0.57 mmol) was dissolved in methanol (20 mL) in a round bottom flask and degassed by sparging with N<sub>2</sub> for 20 minutes. Under a nitrogen atmosphere, the solution was transferred by syringe into a 3-neck round bottom flask. The mixture was stirred for 30 minutes followed by the addition of 6 eq. of 2-pyridinecarboxaldehyde (0.18 g, 0.16 mL, 1.7 mmol). The reaction mixture was refluxed for 1 h and protected from light by covering with foil. The reaction was then cooled to RT, followed by adding 20 eq. of NaBH<sub>4</sub> (0.22 g, 5.7 mmol), and then refluxed at 75 °C for 1 h under an atmosphere of nitrogen. The reaction mixture was diluted into NaHCO<sub>3</sub> solution (pH = 9.5) and extracted into diethyl ether. The organic extracts were combined and dried over MgSO<sub>4</sub>. The reaction mixture was diluted into water and extracted into diethyl ether. Organic extracts were combined, washed with saturated NaCl solution, and dried over MgSO<sub>4</sub>. Concentration by rotary evaporation provided 0.10 g (76 %) of pure brown-yellow oil, which required no further purification. <sup>1</sup>H-NMR (300 MHz, CDCl<sub>3</sub>) δ 8.51 (d, 2H, *J* = 4.8Hz), 7.64 (m, 2H), 7.26 (m, 4H), 7.17 (m, 4H), 7.06 (m, 2H), 4.92 (br, 2H), 4.38 (s, 4H) ppm. <sup>13</sup>C-NMR (600 MHz, CDCl<sub>3</sub>) δ 159.0, 149.1, 138.7, 136.5, 135.7, 127.2, 125.2, 124.9, 122.1, 116.1, 52.6 ppm. MS (FAB +): *m/z* 461 [M<sup>+</sup>, 52 %], 369 [(M-C<sub>6</sub>H<sub>6</sub>N)<sup>+</sup>, 100 %]. FT-IR (KBr): 3428 (s), 2922 (s), 2853 (m), 1593 (m), 1466 (br, m), 1431 (m), 1402 (m), 1219 (br, m), 1148 (m), 1045 (br, m), 691 (s) cm<sup>-1</sup>. Elemental analysis: calculated (found)% C<sub>24</sub>H<sub>20</sub>N<sub>4</sub>S<sub>3</sub>; C: 62.61 (62.61), H: 4.38 (5.57) N: 12.16 (8.50).

iv) Complex syntheses

**(3.11): [Fe(3.04)(NCS)<sub>2</sub>]**

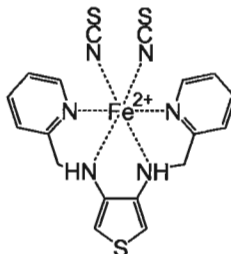


**Figure 8.31: (3.11)**

**(3.04)** (0.025 g, 0.080 mmol) was added to a flask flushed with N<sub>2</sub> gas, followed by the addition of methanol (8 mL). The solution was sparged with N<sub>2</sub> gas for 10 minutes and then iron(II) tetrafluoroborate (0.028 g, 0.080 mmol) was added. The mixture was stirred for 0.5 h, followed by the addition of KSCN (0.033 g, 0.34 mmol) dissolved in H<sub>2</sub>O (10mL) and sparged with N<sub>2</sub> gas for 10 minutes. The flask containing **(3.04)** was stirred overnight, gradually forming a green precipitate which was isolated by vacuum filtration, washed with water, methanol and then dried. Yield: 0.032 g (80 %). MS (FAB +): *m/z* 468 [M<sup>+</sup>, 17 %], 410 [(M-SCN)<sup>+</sup>, 100 %], 351 [(M-2SCN)<sup>+</sup>, 99 %]. FT-IR (KBr): 3448 (br, s), 3159 (br, m), 2920 (m), 2060 (br, s), 1603 (m), 1425 (m), 787 (m), 762 (m) cm<sup>-1</sup>. Elemental analysis: calculated (found)% for C<sub>18</sub>H<sub>16</sub>N<sub>6</sub>S<sub>3</sub>Fe; C, 46.16 (46.85); H, 3.44 (3.04); N, 17.93 (16.62). UV-Vis (MeOH): λ<sub>max</sub> = 640 nm.

**(3.12): [Fe(3.07)(NCS)<sub>2</sub>]**

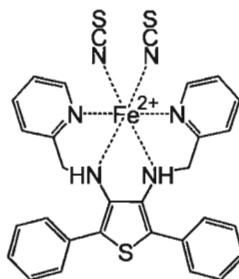


**Figure 8.32: (3.12)**

**(3.07)** (0.10 g, 0.22 mmol) was added to a flask flushed with N<sub>2</sub> gas, followed by the addition of methanol (10 mL). The solution was sparged with N<sub>2</sub> gas for 10 minutes and then iron(II) tetrafluoroborate (0.080 g, 0.22 mmol) was added. The mixture was stirred for 0.5 h, followed by the addition of KSCN (0.090 g, 0.89 mmol) dissolved in H<sub>2</sub>O (10mL) and sparged with N<sub>2</sub> gas for 10 minutes. The flask containing **(3.04)** was stirred overnight, gradually forming a green precipitate which was isolated by vacuum filtration, washed with water, methanol and then dried. Yield: 0.069 g (50 %). MS (FAB +): *m/z* 620 [*M*<sup>+</sup>, 3 %], 562 [(*M*-SCN)<sup>+</sup>, 18 %], 503 [(*M*-2SCN)<sup>+</sup>, 17 %]. FT-IR (KBr): 3424 (br, m), 3194 (br, w), 2921 (m), 2851 (w), 2071 (s), 1602 (w), 1508 (w), 1261 (w), 1102 (m), 1018 (m), 802 (m), 757 (m), 698 (m) cm<sup>-1</sup>. Elemental analysis: calculated (found)% for C<sub>30</sub>H<sub>24</sub>N<sub>6</sub>S<sub>3</sub>Fe; C, 58.07 (59.21); H, 3.90 (4.97); N, 13.54 (11.00). UV-Vis (MeOH): λ<sub>max</sub> = 650 nm.

**(3.13): [Fe(3.10)(NCS)<sub>2</sub>]**

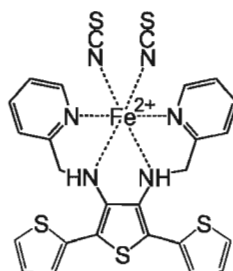


**Figure 8.33: (3.13)**

**(3.10)** (0.12 g, 0.25 mmol) was added to a flask flushed with N<sub>2</sub> gas, followed by the addition of methanol (10 mL). The solution was sparged with N<sub>2</sub> gas for 10 minutes and then iron(II) tetrafluoroborate (0.085 g, 0.25 mmol) was added. The mixture was stirred for 0.5 h, followed by the addition of KSCN (0.10 g, 1.0 mmol) dissolved in H<sub>2</sub>O (10mL) and sparged with N<sub>2</sub> gas for 10 minutes. The flask containing **(3.04)** was stirred overnight, gradually forming a green precipitate which was isolated by vacuum filtration, washed with water, methanol and then dried. Yield: 0.090 g (57 %). MS (FAB +): *m/z* 632 [*M*<sup>+</sup>, 13 %], 578 [(*M*-SCN)<sup>+</sup>, 5 %]. FT-IR (KBr): 3425 (br, m), 3222 (w), 3107 (w), 3075 (w), 2921 (w), 2851 (w), 2081 (s), 2063 (s), 1602 (m), 1572 (w), 1484 (w), 1440 (w), 1411 (m), 1232 (w), 1101 (w), 899 (w), 760 (w), 697 (m) cm<sup>-1</sup>. Elemental analysis: calculated (found)% for C<sub>26</sub>H<sub>20</sub>N<sub>6</sub>S<sub>5</sub>Fe; C, 49.37 (49.30); H, 3.19 (2.94); N, 13.29 (12.86).

**(3.14): [Fe(C<sub>56</sub>H<sub>40</sub>N<sub>8</sub>S<sub>2</sub>)(NCS)<sub>2</sub>]**

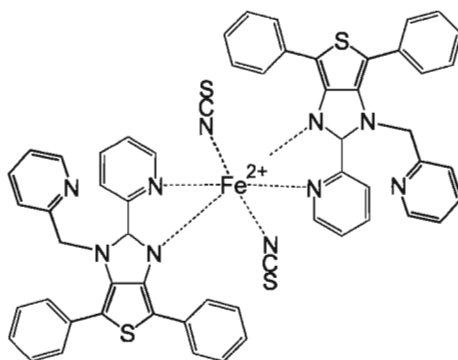


**Figure 8.34: (3.14)**

**(3.12)** (20 mg) was recrystallized in 1:1 MeOH/DCM (4 mL) to produce red-black crystals over a period of 2 weeks. FT-IR (KBr): 2961 (m), 2922 (m), 2855 (m), 2060 (s), 1628 (m), 1597 (w), 1470 (w), 1437 (w), 1261 (m), 1096 (s), 1024 (s), 802 (s), 754 (m), 694 (m) cm<sup>-1</sup>. MS (FAB +): *m/z* 1002 [(M-SCN)<sup>+</sup>, 8 %], 445 [(C<sub>28</sub>H<sub>21</sub>N<sub>4</sub>S)<sup>+</sup>, 100 %], 353 [(C<sub>22</sub>H<sub>15</sub>N<sub>3</sub>S)<sup>+</sup>, 52 %]. Elemental analysis: calculated (found)% for C<sub>58.5</sub>H<sub>41</sub>N<sub>10</sub>S<sub>4</sub>FeCl; C, 63.86 (63.90); H, 3.78 (N/A, small sample size prevented account measure of H %); N, 12.63 (12.13).

**(3.15) [Fe(C<sub>48</sub>H<sub>32</sub>N<sub>8</sub>S<sub>6</sub>)(NCS)<sub>2</sub>]**

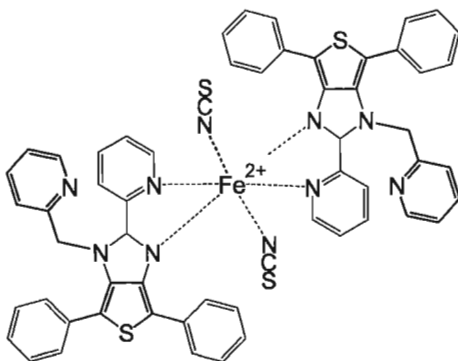


**Figure 8.35: (3.15)**

(3.14) (20 mg) of was added to 1:1 MeOH/DCM (4mL) to produce a red-black powder over a period of 2 weeks. MS (FAB +):  $m/z$  1086  $[(M-SCN)^+, 1.6 \%, 457 [(M-C_{26}H_{16}N_6S_5Fe)^+, 100 \%]$ .

## 2. Substituted “ppi” complexes

### i) $[Fe(ppi)_2(NCS)_2]$ synthesis

(3.16):  $[Fe(ppi)_2(NCS)_2]$

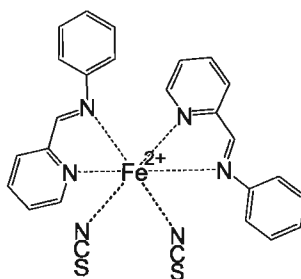


**Figure 8.36: (3.16)**

The ligand 2-pyridinalphenylimine (ppi) was prepared by stirring analine (0.093 g, 1.0 mmol) with 2-pyridinecarboxaldehyde (0.107 g, 1.00 mmol) in MeOH (5 mL) for 1 hour while sparging with  $N_2$ . In a separate flask, a solution of KSCN (0.131 g, 1.35 mmol) in  $H_2O$  (10 mL) was sparged with  $N_2$  gas for 0.5 hours, combined with  $Fe(II)SO_4 \cdot 7H_2O$  (0.139 g, 1.00 mmol), stirred for 0.5 hours and added to the flask containing the ppi ligand. The resulting blue precipitate was collected by vacuum filtration and washed with water, pentane and then dried. Yield: 230 mg (87 %). MS (FAB +):  $m/z$   $[(M)^+, 11 \%, [(M-SCN)^+, 78 \%, [(M-2SCN)^+, 56 \%, [(M-C_{13}H_{10}N_3S)^+, 100 \%]$ . FT-IR (NaCl): 3059

(w), 2962 (w), 2058 (s), 1591 (br, m), 1487 (m), 1441 (w), 1362 (w), 1302 (w), 1261 (w), 1198 (w), 1155 (w), 1014 (w), 922 (w), 743 (s), 549 (w)  $\text{cm}^{-1}$ .<sup>[122]</sup>

i) Diphenyl-substitued ppi ligand synthesis

**(3.17): 2,5-diphenylaniline**

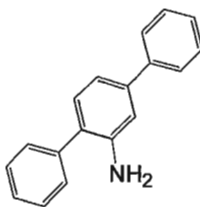


**Figure 8.37: (3.17)**

2,5-dibromoaniline (0.74 g 3.4 mmol) was added to a round bottom flask and then combined with anhydrous 1,2-dimethoxyethane (100 mL) and a 1.0 M aqueous solution of  $\text{K}_2\text{CO}_3$  (30 mL). The mixture was purged by  $\text{N}_2$  sparging for 0.5 h, followed by the addition of 2-thienylboronic acid (0.83 g, 6.8 mmol) and  $\text{Pd}(\text{PPh}_3)_4$  (0.39 g, 0.34 mmol). The reaction mixture was heated at 95 °C for 72h. The reaction contents were combined with  $\text{H}_2\text{O}$  (200 mL) containing 20 g NaCl and extracted into DCM (200 mL). The organic extracts were combined, dried over  $\text{MgSO}_4$ , concentrated (not to dryness) by rotary evaporation, dissolved in hexanes and then filtered through Celite. The filtrate was concentrated to dryness to obtain a white solid. Yield: 480 mg (65 %). Mp: 186-187 °C.  $^1\text{H}$ -NMR (300 MHz,  $\text{CDCl}_3$ ):  $\delta$  7.69 (m, 10H), 7.29 (d, 1H,  $J = 5.9$  Hz), 7.15 (d, 1H,  $J = 6.3$  Hz), 7.05 (s, 1H) ppm.  $^{13}\text{C}$ -NMR (600 MHz,  $\text{CDCl}_3$ ):  $\delta$  143.9, 141.6, 141.1, 139.3, 130.9, 129.1, 128.9, 128.7, 127.30, 127.28, 127.1, 126.8, 117.7, 114.3 ppm. MS (EI +):

$m/z$  245 [ $M^+$ , 100 %]. HRMS (EI +) calculated for  $[C_{18}H_{15}N]^+$ : 245.12045, found 245.12008. FT-IR (NaCl): 3448 (m), 3374 (m), 3018 (w), 1611 (s), 1555 (m), 1477 (m), 1408 (m), 1311 (w), 1259 (w), 1219 (w), 1148 (w), 1069 (w), 1011 (w), 860 (w), 812 (w), 756 (s), 698 (s)  $cm^{-1}$ .

**(3.18): *N'*-(2,2':5',2''-terphenyl)-2-pyridinalimine**

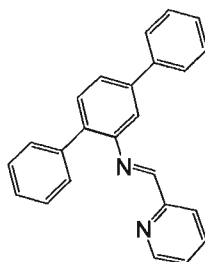


**Figure 8.38: (3.18)**

**(3.17)** (170 mg, 0.69 mmol) was dissolved in 0.5 mL of DCM and added dropwise to a solution of pentane containing 2-pyridinecarboxaldehyde (100 mg, 0.93 mmol). The solution was concentrated to 10 mL and cooled. The resulting white precipitate was washed with cool pentane and dried under vacuum. Yield: 190 mg (83 %). Mp: 119-121 °C.  $^1H$ -NMR (300 MHz,  $CDCl_3$ ):  $\delta$  8.74 (s, 1H), 8.73 (d, 1H,  $J$  = 4.9 Hz), 8.09 (d, 1H,  $J$  = 7.9 Hz), 7.80 (m, 3H), 7.64 (m, 12H) ppm.  $^{13}C$ -NMR (600 MHz,  $CDCl_3$ ):  $\delta$  161.1, 154.9, 149.6, 149.1, 141.5, 140.3, 139.1, 136.7, 134.7, 130.9, 130.3, 128.9, 127.8, 127.7, 127.1, 127.0, 125.4, 125.1, 121.9, 117.4 ppm. MS (EI +):  $m/z$  334 [ $M^+$ , 62 %], 256 [ $(M - C_5H_4N)^+$ , 100 %]. HRMS (EI +) calculated for  $[C_{24}H_{18}N_2]^+$ : 334.14700, found 334.14756. FT-IR (NaCl): 3055m, 2920m, 2857w, 1629m, 1589m, 1472s, 1438, 1386, 1263, 1182, 1080 (w), 1034 (w), 991 (w), 901 (m), 837 (w), 756 (s), 698 (s)  $cm^{-1}$ .



Elemental analysis: calculated (found)% for  $C_{24}H_{18}N_2$ ; C, 86.20 (85.75); H, 5.43 (5.07); N, 8.38 (8.48).

ii) Dithienyl-substitued ppi ligand synthesis

**(3.19): 2,5-dithienylaniline**

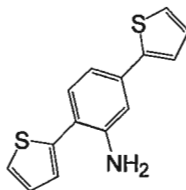


**Figure 8.39: (3.19)**

2,5-dibromoaniline (0.453 g 2.16 mmol) was added to a round bottom flask and then combined with anhydrous 1,2-dimethoxyethane (34 mL) and a 1.0 M aqueous solution of  $K_2CO_3$  (17 mL). The mixture was purged by  $N_2$  sparging for 0.5 h, followed by the addition of 2-thienylboronic acid (0.829 g, 6.48 mmol) and  $Pd(PPh_3)_4$  (0.25 g, 0.22 mmol). The reaction mixture was heated at 95 °C for 72h. The reaction contents were combined with  $H_2O$  (200 mL) containing 20 g NaCl and extracted into DCM (200 mL). The organic extracts were combined, dried over  $MgSO_4$ , concentrated (not to dryness) by rotary evaporation, dissolved in hexanes and then filtered through Celite. The filtrate was concentrated to dryness to obtain an orange oil. Yield: 310 mg (55 %).  $^1H$ -NMR (300 MHz,  $CDCl_3$ ):  $\delta$  7.42 (m, 3H), 7.34 (dd, 1H,  $J = 5, 0.5$  Hz), 7.30 (dd, 1H,  $J = 3.5, 0.8$  Hz), 7.20 (dd, 1H,  $J = 3.6, 1.5$  Hz), 7.18 (m, 2H), 7.08 (d, 1H,  $J = 1.6$  Hz), 4.12 (br, 2H) ppm.  $^{13}C$ -NMR (600 MHz,  $CDCl_3$ ):  $\delta$  144.4, 144.2, 140.9, 135.0, 131.5, 128.1, 127.8,

125.9, 125.4, 124.9, 123.3, 119.4, 116.5, 113.2 ppm. MS (EI +):  $m/z$  257 [ $M^+$ , 100 %]. HRMS (EI +) calculated for  $[C_{14}H_{11}NS_2]^+$ : 257.03329, found 257.03344. FT-IR (NaCl): 3443 (br, w), 2924 (s), 2857 (w), 1612 (s), 1552(w), 1483 (m), 1427 (w), 1308 (w), 1260 (w), 1198 (w), 1088 (w), 1049 (w), 949 (w), 839(w), 804 (s), 698 (s), 447 (w)  $cm^{-1}$ .

**(3.20): *N*-(2,5-di(2-thienyl)phenyl)-2-pyridinalimine**

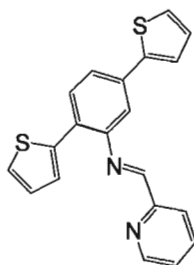


**Figure 8.40: (3.20)**

**(3.19)** (250 mg, 0.95 mmol) was dissolved in 2 mL of DCM and added dropwise to a solution of hexane (4 mL) containing 2-pyridinecarboxaldehyde (150 mg, 1.40 mmol). The resulting yellow precipitate was collected by vacuum filtration, washed with cool pentane and dried. Yield: 190 mg (58 %). Mp: 155-158 °C.  $^1H$ -NMR (300 MHz,  $CDCl_3$ ):  $\delta$  8.78 (d, 1H,  $J$  = 4.7), 8.74 (s, 1H), 8.43 (d, 1H,  $J$  = 7.8), 7.93 (t, 1H,  $J$  = 7.7), 7.83 (d, 1H,  $J$  = 8.2), 7.60 (dd, 1H,  $J$  = 8.2, 1.6), 7.51 (d, 1H,  $J$  = 3.7), 7.46 (m, 4H), 7.34 (d, 1H,  $J$  = 5.0), 7.14 (m, 2H) ppm.  $^{13}C$ -NMR (600 MHz,  $CDCl_3$ ):  $\delta$  161.2, 154.6, 149.7, 147.6, 143.4, 140.0, 136.8, 134.3, 128.4, 128.2, 127.6, 127.5, 126.8, 125.9, 125.4, 125.2, 124.2, 123.4, 122.5, 115.9 ppm. MS (EI +):  $m/z$  346 [ $M^+$ , 62 %], 268 [ $(M-C_5H_4N)^+$ , 100 %]. HRMS (EI +) calculated for  $[C_{20}H_{14}N_2S_2]^+$ : 346.05984, found 346.06023. FT-IR (NaCl): 3063 (w), 2916 (w), 1620 (m), 1582 (w), 1464 (m), 1431 (m),

1402 (w), 1352 (w), 1211 (w), 1119 (w), 978 (w), 897 (w), 874 (w), 852 (w), 817 (s), 781 (w), 700 (s), 617 (w), 478 (w)  $\text{cm}^{-1}$ . Elemental analysis: calculated (found)% for  $\text{C}_{20}\text{H}_{14}\text{N}_2\text{S}_2$ ; C, 69.35 (69.80); H, 4.07 (3.69); N, 8.09 (8.11).

iii) Thienyl-substituted ppi ligand synthesis

**(3.21): 4-thienylaniline**

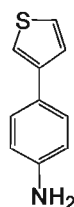


**Figure 8.41: (3.21)**

4-iodoaniline (0.219 g 1.00 mmol) was added to a round bottom flask and then combined with anhydrous 1,2-dimethoxyethane (15 mL) and a 1.0 M aqueous solution of  $\text{K}_2\text{CO}_3$  (10 mL). The mixture was purged by  $\text{N}_2$  sparging for 0.5 h, followed by the addition of 2-thienylboronic acid (0.127 g, 1.00 mmol) and  $\text{Pd}(\text{PPh}_3)_4$  (0.058 g, 0.050 mmol). The reaction mixture was heated at 95  $^\circ\text{C}$  for 72h. The reaction contents were combined with  $\text{H}_2\text{O}$  (200 mL) containing 20 g NaCl and extracted into DCM (200 mL). The organic extracts were combined, dried over  $\text{MgSO}_4$ , concentrated (not to dryness) by rotary evaporation, dissolved in hexanes and then filtered through Celite. The hexanes were then discarded and the Celite pad containing **(3.21)** was washed with  $\text{CHCl}_3$ , concentrated and then combined with pentane. A red precipitate that appeared instantly was removed by filtration, followed by concentrating the pentane solution to 10 mL and

collecting a yellow solid precipitate. Yield: 55 mg (31 %). Mp: 96-98 °C.  $^1\text{H-NMR}$  (300 MHz,  $\text{CDCl}_3$ ):  $\delta$  7.45 (d, 2H,  $J = 8.5$  Hz), 7.41 (m, 3H), 6.67 (d, 2H,  $J = 8.5$  Hz), 3.72 (br, 2H) ppm.  $^{13}\text{C-NMR}$  (600 MHz,  $\text{CDCl}_3$ ):  $\delta$  145.6, 142.4, 127.5, 126.7, 126.1, 125.8, 118.0, 115.3 ppm. MS (EI +):  $m/z$  175 [ $\text{M}^+$ , 100 %]. HRMS (EI +) calculated for  $[\text{C}_{10}\text{H}_9\text{NS}]^+$ : 175.04557, found 175.04594. FT-IR (NaCl): 3406 (br, s), 3314 (m), 3093 (w), 2922 (w), 1618 (s), 1497 (m), 1267 (m), 1196 (m), 1126 (w), 1094 (w), 837 (m), 777 (s), 698 (m), 628 (m), 565 (m), 511 (m)  $\text{cm}^{-1}$ .

**(3.22): *N*-(4-(3-thienyl)phenyl)-2-pyridinalimine**

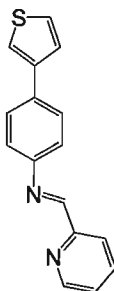


**Figure 8.42: (3.22)**

(3.21) (50 mg, 0.29 mmol) was dissolved in 1 mL of DCM and added dropwise to a solution of pentane (10 mL) containing 2-pyridinecarboxaldehyde (34 mg, 0.31 mmol). The solution was concentrated to 3 mL by slow evaporation. The resulting yellow precipitate was collected by vacuum filtration, washed with cool pentane and dried. Yield: 63 mg (84 %). Mp: 117-120 °C.  $^1\text{H-NMR}$  (300 MHz,  $\text{CDCl}_3$ ):  $\delta$  8.76 (d, 1H,  $J = 4.2$  Hz), 8.69 (s, 1H), 8.26 (d, 1H,  $J = 7.9$  Hz), 7.88 (td, 1H,  $J = 7.6, 1.7$  Hz), 7.70 (d, 2H,  $J = 8.5$  Hz), 7.51 (m, 1H), 7.46 (m, 5H) ppm.  $^{13}\text{C-NMR}$  (600 MHz,  $\text{CDCl}_3$ ):  $\delta$  160.2, 154.6, 149.8, 141.7, 136.7, 134.5, 127.8, 127.2, 126.3, 126.2, 125.1, 121.9, 121.7, 120.2

ppm. MS (EI +):  $m/z$  264 [ $M^+$ , 100 %]. HRMS (EI +) calculated for  $[C_{16}H_{12}N_2S]^+$ : 264.70212, found 264.07204. FT-IR (NaCl): 3435 (br, m), 3065 (w), 2920 (w), 1622 (br, m), 1472 (m), 1423 (m), 1350 (w), 1261 (m), 1202 (m), 1101 (br, m), 1034 (m), 833 (w), 783 (s), 538 (m)  $cm^{-1}$ . Elemental analysis: calculated (found)% for  $C_{16}H_{12}N_2S$ ; C, 72.71 (71.94); H, 4.58 (4.72); N, 10.60 (9.89).

iv) Complex synthesis

**(3.23):  $[Fe(3.18)_2(NCS)_2]$**

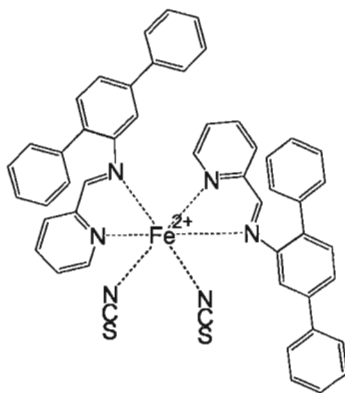


**Figure 8.43: (3.23)**

A solution of KSCN (201 mg, 2.06 mmol) in MeOH (50 mL) is sparged with  $N_2$  gas for 0.5 hours, combined with  $Fe(II)SO_4 \cdot 7H_2O$  (81 mg, 0.29 mmol). The mixture was stirred for an additional 0.5 hours and then combined with **(3.18)** (190 mg, 0.57 mmol). The solution was stirred under an atmosphere of nitrogen for 3 days, concentrated to 20 mL and cooled in an ice bath. The resulting blue precipitate was collected by vacuum filtration and washed with water, pentane and then dried. Yield: 210 mg (85 %). MS (FAB +):  $m/z$  840 [ $(M)^+$ , 3.0 %], 782 [ $(M - SCN)^+$ , 24 %], 448 [ $(M - C_{25}H_{18}N_3S)^+$ ,

100 %]. FT-IR (NaCl): 2963 (m), 2918 (m), 2850 (m), 2060 (s), 1591 (br, m), 1471 (m), 1440 (w), 1261 (s), 1098 (s), 1020 (s), 800 (s), 700 (m)  $\text{cm}^{-1}$ . Elemental analysis: calculated (found)% for  $\text{C}_{51}\text{H}_{37}\text{N}_6\text{S}_2\text{FeCl}$ ; C, 68.67 (68.93); H, 4.22 (4.68); N, 9.51 (9.34). Note: residual crystallization solvent in the sample analyzed. UV-Vis (DCM):  $\lambda_{\text{max}}$  ( $\epsilon$  ( $\text{M}^{-1} \text{cm}^{-1}$ )) = 621 nm (1510).

**(3.24):  $[\text{Fe}(\mathbf{3.20})_2(\text{NCS})_2]$**

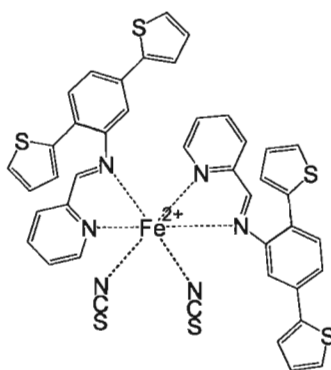


**Figure 8.44: (3.24)**

A solution of KSCN (73 mg, 0.75 mmol) in  $\text{H}_2\text{O}$  (10 mL) is sparged with  $\text{N}_2$  gas for 0.5 hours, combined with  $\text{Fe}(\text{II})\text{SO}_4 \cdot 7\text{H}_2\text{O}$  (69 mg, 0.25 mmol). The mixture was stirred for an additional 0.5 hours and then added to a flask containing **(3.20)** (170 mg, 0.50 mmol) in MeOH (50 mL), which was also sparged with  $\text{N}_2$  gas for 0.5 hours. The solution was stirred under an atmosphere of nitrogen for 3 days, concentrated to 20 mL and cooled in an ice bath. The resulting green-blue precipitate was collected by vacuum filtration and washed with water, pentane and then dried. Yield: 220 mg (65 %). MS (FAB +):  $m/z$  864  $[(\text{M})^+]$ , 2.8 %, 806  $[(\text{M} - \text{SCN})^+]$ , 27 %, 460  $[(\text{M} - \text{C}_{21}\text{H}_{14}\text{N}_3\text{S}_3)^+]$ , 100 %. FT-IR (NaCl): 3400 (br, w), 3066 (w), 2924 (w), 2852 (w), 2054 (s), 1625 (br, m), 1593 (s),

1483 (m), 1439 (m), 1301 (w), 1211 (w), 1120 (w), 955 (w), 910 (w), 817 (m), 773 (w), 698 (s)  $\text{cm}^{-1}$ . Elemental analysis: calculated (found)% for  $\text{C}_{57}\text{H}_{46}\text{N}_6\text{S}_5\text{FeCl}_2$ ; C, 60.38 (60.41); H, 3.72 (3.46); N, 7.41 (7.48). Note: residual crystallization solvent in the sample analyzed. UV-Vis (DCM):  $\lambda_{\text{max}}$  ( $\epsilon$  ( $\text{M}^{-1} \text{cm}^{-1}$ )) = 560 nm (1850).

**(3.25):  $[\text{Fe}(\mathbf{3.22})_2(\text{NCS})_2]$**

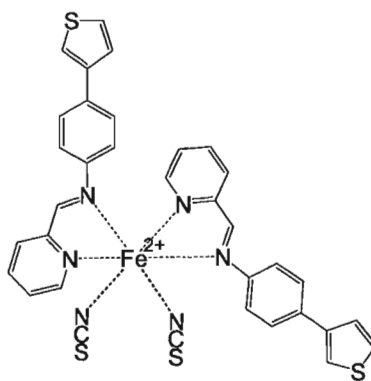


**Figure 8.45: (3.25)**

A solution of KSCN (93 mg, 0.96 mmol) in MeOH (50 mL) was sparged with  $\text{N}_2$  gas for 0.5 hours, combined with  $\text{Fe}(\text{II})\text{SO}_4 \cdot 7\text{H}_2\text{O}$  (130 mg, 0.47 mmol). The mixture was stirred for an additional 0.5 hours and then combined with **(3.22)** (250 mg, 0.95 mmol). The solution was stirred under an atmosphere of nitrogen for 3 days, concentrated to 20 mL and cooled in an ice bath. The resulting green precipitate was collected by vacuum filtration and washed with water, pentane and then dried. Yield: 310 mg (94 %). MS (FAB +):  $m/z$  700 [ $(\text{M})^+$ , 10 %], 642 [ $(\text{M} - \text{SCN})^+$ , 60 %], 378 [ $(\text{M} - \text{C}_{17}\text{H}_{12}\text{N}_3\text{S}_2)^+$ , 100 %]. FT-IR (NaCl): 3092 (w), 2064 (s), 2037 (s), 1589 (br, m), 1487 (w), 1433 (w), 1354 (w), 1300 (w), 1258 (w), 1200 (m), 1150 (w), 1105 (w), 1015 (w), 962 (w), 904 (w), 853 (w), 785 (m), 731 (w), 689 (w), 629 (w), 554 (w)  $\text{cm}^{-1}$ . Elemental analysis:

calculated (found)% for  $C_{34}H_{24}N_6S_5Fe$ ; C, 58.29 (58.31); H, 3.45 (3.12); N, 12.00 (11.92). UV-Vis (DCM):  $\lambda_{max}$  ( $\epsilon$  ( $M^{-1} cm^{-1}$ )) = 630 nm (1690).

## 8.10 Experimental for Chapter 4<sup>†</sup>

### 1. A thienyl-substituted valence tautomer

#### i) Ligand synthesis

#### (4.01): 5-bromo-2,2'-bipyridine

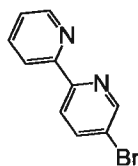


Figure 8.46: (4.01)

(4.01) was prepared following the procedure reported by Fang and Hanan. 2,5-dibromopyridine (1.95 g, 0.00830 mol) and  $Pd(PPh_3)_4$  (0.27 g, 0.25 mmol) were added successively to a flask which was flushed with  $N_2$  gas. A solution of 0.5 M pyridyl zinc bromide in THF (25 mL) was syringed into the flask, and the mixture was stirred for 24 hours. The reaction mixture was added to a solution of 0.2 M EDTA and 1 M  $Na_2CO_3$  to extract the product from its zinc ion. Organics were extracted using  $Et_2O$  (50mL), dried with  $Na_2SO_4$ , and concentrated by rotary evaporation. The final product was eluted from an alumina column using 10:1 hexanes:EtOAc and once concentrated was a white crystalline solid. Yield: 1.8 g (94 %).  $^1H$ -NMR (300 MHz,  $CDCl_3$ ):  $\delta$  8.75 (d, 1H,  $J$  =



2.2), 8.70 (d, 1H,  $J = 5.5$ ), 8.41 (d, 1H,  $J = 8.0$ ), 8.36 (d, 1H,  $J = 8.4$ ), 7.98 (dd, 1H,  $J = 8.5, 2.4$ ), 7.87 (td, 1H,  $J = 7.7, 1.74$ ), 7.37 (m, 1H) ppm. MS (FAB +):  $m/z$  235  $[(M(^{79}\text{Br})^+, 100\%)]$ , 237  $[(M(^{81}\text{Br})^+, 100\%)]$ .<sup>[194]</sup>

**(4.02): 5-(trimethylsilylethynyl)bipyridine**

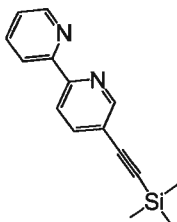


**Figure 8.47: (4.02)**

The following is a modified version of the procedure reported by Ziessel and co-workers. **(4.01)** (1.00 g, 4.39 mmol),  $\text{PdCl}_2(\text{PPh}_3)_2$  (92 mg, 0.13 mmol),  $\text{PPh}_3$  (69 mg, 0.26 mmol), and  $\text{CuI}$  (83 mg, 0.48 mmol) were added successively to a flask which was flushed with  $\text{N}_2$  gas. Anhydrous  $N,N$ -diisopropylamine (90 mL) was syringed into the flask, and the mixture was stirred while sparging for 0.5 hours. Ethynyltrimethylsilane (0.579 g, 6.58 mmol) was then added and the reaction mixture was refluxed for 20 hours. The solvent was evaporated and the residue was dissolved in chloroform and combined with pentane, precipitating impurities that were removed by gravity filtration. The filtrate was passed through a Celite pad and concentrated. The residue was dissolved in acetone, filtered and concentrated to afford **(4.02)**. Yield: 1.1 g (96 %).  $^1\text{H-NMR}$  (300 MHz,  $\text{CDCl}_3$ ):  $\delta$  8.75 (d, 1H,  $J = 2$  Hz), 8.70 (d, 1H,  $J = 5$  Hz), 8.40 (m, 2H), 7.84 (m, 2H), 7.33 (m, 1H), 0.29 (s, 9H) ppm. MS (EI +):  $m/z$  252  $[\text{M}^+, 100\%]$ .<sup>[195]</sup>

**(4.03): 5-ethynyl-2,2'-bipyridine**

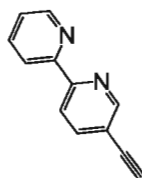


**Figure 8.48: (4.03)**

Deprotection of **(4.02)** (1.891g, 7.492 mmol) was accomplished by stirring it in MeOH (120 mL) containing KF (0.870 g, 15.0 mmol) at RT overnight. Crude **(4.03)** was purified by flash chromatography (SiO<sub>2</sub>) eluting with DCM/MeOH to give a dark brown solid. Yield: 1.32 g (98 %). <sup>1</sup>H-NMR (300 MHz, CDCl<sub>3</sub>): δ 8.79 (s, 1H), 8.71 (d, 1H, *J* = 3.3 Hz), 8.42 (m, 2H), 7.94 (m, 2H), 7.33 (m, 1H), 3.30 (s, 1H) ppm. MS (EI +): *m/z* 180 [M<sup>+</sup>, 100 %].<sup>[195]</sup>

**(4.04): 5-(3'-ethynylthienyl)bipyridine (thebipy)**

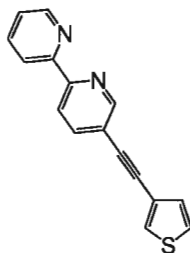


**Figure 8.49: (4.04)**

A solution of 3-bromothiophene (0.100 mL, 1.06 mmol) in anhydrous *N,N*-diisopropylamine (20 mL) was deaerated by sparging with N<sub>2</sub> gas for 0.5 hours. PdCl<sub>2</sub>(PPh<sub>3</sub>)<sub>2</sub> (37 mg, 0.053 mmol), PPh<sub>3</sub> (14 mg, 0.053 mmol), CuI (10 mg, 0.053 mmol) and **(4.03)** (0.230 g, 1.28 mmol) were added successively. The mixture was

refluxed overnight until the starting materials were consumed, as verified by TLC. The crude product was passed through a pad of Celite, and the filtrate was washed with brine ( $3 \times 50$  mL), and then dried with sodium sulfate. After concentration, the crude product was recrystallized from warm acetone/water (5:1) to provide a yellow solid. Yield: 0.26 g (92 %). Mp: 141 °C.  $^1\text{H-NMR}$  (300 MHz,  $\text{CDCl}_3$ ):  $\delta$  8.82 (s, 1H), 8.71 (d, 1H,  $J = 2$  Hz), 8.43 (t, 2H,  $J = 3.4$  Hz), 7.94 (dd, 1H,  $J = 4$ , 1 Hz), 7.85 (td, 1H,  $J = 4$ , 1 Hz), 7.62 (d, 1H,  $J = 1$  Hz), 7.35 (m, 2H), 7.26 (d, 1H,  $J = 2$  Hz) ppm.  $^{13}\text{C-NMR}$  (600 MHz,  $\text{CDCl}_3$ ):  $\delta$  155.5, 154.7, 151.5, 149.3, 139.2, 137.0, 129.8, 129.4, 125.6, 123.9, 121.7, 121.3, 120.3, 120.3, 88.6, 85.9 ppm. MS (FAB +):  $m/z$  262 [ $\text{M}^+$ , 100 %]. FT-IR (KBr): 3405 (br, m), 3702 (m), 2920 (w), 2205 (m), 1717 (w), 1586 (m), 1541 (m), 1457 (s), 1433 (m), 1366 (m), 1126 (w), 1090 (w), 1019 (m), 854 (m), 784 (s), 739 (w), 623 (m)  $\text{cm}^{-1}$ . Elemental analysis: calculated (found)% for  $\text{C}_{16}\text{H}_{10}\text{N}_2\text{S}$ ; C, 73.27 (72.96); H, 3.85 (4.07); 10.69 (10.35).

## ii) Complex synthesis

### (4.05): $[\text{Co}(\text{dbsq})_2(4.04)]$

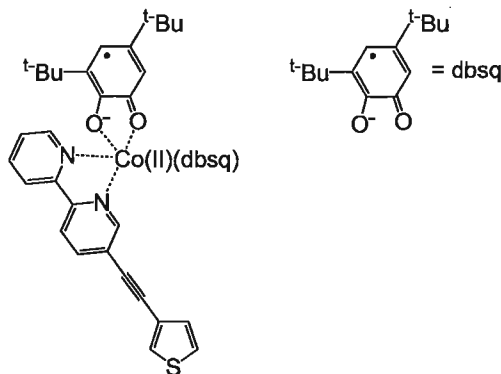


Figure 8.50: (4.05)

**(4.04)** (0.0600 g, 0.229 mmol) was added to a solution of  $\text{Co}_4(\text{dbsq})_8$  (0.11 g, 0.057 mmol) in anhydrous and deaerated toluene (20 mL) and the mixture was stirred for 5 hours at room temperature while under nitrogen. The solution was concentrated by half, and cooled in ice-water producing a precipitate that was isolated by vacuum filtration, washed with cold toluene, and dried to afford purple crystals. Yield: 0.13 g (71 %). MS (FAB +):  $m/z$  541  $[(\text{M}-\text{C}_6\text{H}_5\text{O}_2)^+, 100 \text{ \%}]$ , 321  $[(\text{M}-\text{C}_{12}\text{H}_{10}\text{O}_4)^+, 55 \text{ \%}]$ . FT-IR (KBr): 3447 (br, m), 3042(w), 2955(s), 2902(m), 2864(m), 2361(w), 2210(m), 1570(m), 1464(s), 1440(s), 1356(m), 1283(s), 1242(s), 1204(w), 984(m), 841(m), 791(m)  $\text{cm}^{-1}$ . Elemental analysis: calculated (found)% for  $\text{C}_{44}\text{H}_{50}\text{N}_2\text{SO}_4\text{Co}$ ; C, 67.44 (67.14); H, 3.03 (5.64); N, 10.39 (10.15); S, 4.20 (3.95). UV-Vis (MeOH):  $\lambda_{\text{max}} = 389 \text{ nm}$ .

## 2. A terthienyl-substituted valence tautomer

### i) Ligand synthesis

#### **(4.06): 3'-(5-ethynylbipyridine)-2,2':5',2''-terthiophene**

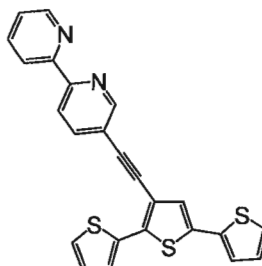


**Figure 8.51: (4.06)**

**(4.03)** (0.681 g, 3.78 mmol) and **(2.14)** (0.825 g, 2.52 mmol) were dissolved in deaerated and anhydrous *N,N*-diisopropylamine (65 mL).  $\text{PdCl}_2(\text{PPh}_3)_2$  (0.053 g, 0.076 mmol) and CuI (0.014 g, 0.074 mmol) were added to the reaction mixture, which was refluxed for 60 h. The reaction mixture was concentrated and passed through a pad of Celite. The filtrate was then extracted into  $\text{CHCl}_3$  ( $3 \times 60$  mL), washed with brine, dried over magnesium sulfate, filtered, and concentrated to dryness. The crude product was flash chromatographed over neutral alumina using 10:1 hexanes:EtOAc as the eluent to provide a brilliant yellow solid. Yield: 0.64 g (59 %). Mp: 143-145 °C.  $^1\text{H}$ -NMR (300 MHz,  $\text{CDCl}_3$ ) = d 8.90 (d, 1H,  $J = 3$  Hz), 8.72 (dd, 1H,  $J = 6, 3$  Hz), 8.48 (dd, 2H,  $J = 9, 3$  Hz), 7.98 (dd, 1H,  $J = 9, 3$  Hz), 7.85 (td, 1H,  $J = 9, 3$  Hz), 7.52 (dd, 1H,  $J = 6, 3$  Hz), 7.34 (m, 5H), 7.10 (dd, 1H,  $J = 9, 3$  Hz), 7.06 (dd, 1H,  $J = 9, 3$  Hz) ppm.  $^{13}\text{C}$ -NMR ( $\text{CDCl}_3$ ) = d 155.4, 154.9, 151.4, 149.3, 139.2, 139.0, 137.0, 136.0, 135.5, 134.4, 128.0, 127.3, 126.7, 126.1, 125.8, 125.2, 124.3, 124.0, 121.3, 120.4, 120.2, 117.1, 91.2, 89.3 ppm. MS (EI +):  $m/z$  426 [ $\text{M}^+$ , 100 %]. FT-IR (KBr) = 3425 (br, s), 3061 (w), 2922 (m), 2853 (w), 2201 (w), 1637 (w), 1588 (m), 1541 (w), 1452 (s), 1432 (m), 1364 (w), 1228 (w), 1089 (w), 1022 (w), 859 (w), 805 (m), 792 (m), 742 (m), 684 (s), 649 (w), 458 (w)  $\text{cm}^{-1}$ . Elemental analysis: calculated (found)% for  $\text{C}_{24}\text{H}_{14}\text{N}_2\text{S}_3$ ; C, 67.58 (67.91); H, 3.31 (3.55); N, 6.57 (6.22).

ii) Complex synthesis

**(4.07): [Co(dbsq)<sub>2</sub>(4.06)]**

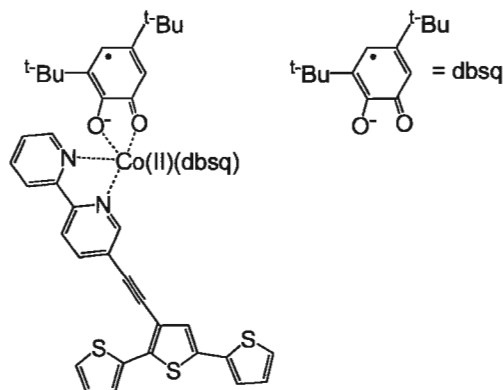


**Figure 8.52: (4.07)**

**(4.06)** (0.150 g, 0.469 mmol) was added to a solution of  $\text{Co}_4(\text{dbsq})_8$  (0.175 g, 0.0880 mmol) in anhydrous and deaerated toluene (15 mL) and the mixture was stirred overnight at room temperature while under nitrogen. The solution was concentrated by half, and cooled in ice-water producing a precipitate that was isolated by vacuum filtration, washed with cold toluene, and dried to afford a dark green solid. Yield: 0.160 g (43 %). MS (FAB +):  $m/z$  926 [ $\text{M}^+$ , 50 %], 911 [ $(\text{M} - \text{CH}_3)^+$ , 100 %]. FT-IR (KBr): 3448 (br, m), 3071 (m), 2952 (s), 2902 (m), 2862 (m), 2202 (m), 1577 (m), 1490 (s), 1467 (s), 1355 (m), 1281 (w), 1243 (s), 1157 (w), 1093 (w), 1028 (w), 983 (m), 903 (w), 844 (w), 826 (w), 694 (m), 494 (w)  $\text{cm}^{-1}$ . Elemental analysis: calculated (found)% for  $\text{C}_{52}\text{H}_{54}\text{N}_2\text{S}_3\text{O}_4\text{Co}$ ; C, 67.44 (67.14); H, 5.88 (5.64); N, 3.03 (3.00); S, 10.39 (10.15). UV-Vis (MeOH):  $\lambda_{\text{max}} = 450 \text{ nm}$ .

## 8.11 Experimental for Chapter 5<sup>8</sup>

### 1. Bimetallic qsal complexes

#### i) Ligand synthesis

##### (5.01): 3,3',5,5'-tetrabromo-2,2'-bithiophene

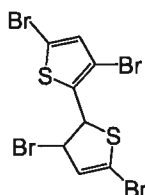
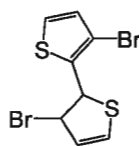


Figure 8.53: (5.01)

Bromine (19.6 g, 123 mmol) was added dropwise over 1.5 h to a solution of 2,2'-bithiophene (5.57, 33.5 mmol) in glacial acetic acid (20 mL) and chloroform (45 mL) while maintaining a temperature of 5-15 °C. The mixture was stirred at room temperature for 5 h and then refluxed for 24 h. The reaction was then cooled, quenched by the addition of an aqueous 10 % KOH solution (50 mL), extracted with  $\text{CHCl}_3$  and then dried with  $\text{MgSO}_4$ . Recrystallization from ethanol provided off white crystals. Yield: 15.3 g (95 %).  $^1\text{H-NMR}$  ( $\text{CDCl}_3$ ): 7.07 (s, 2H) ppm. MS (EI +):  $m/z$  481  $[(\text{M}({}^{79}\text{Br}_2{}^{81}\text{Br}_2)^+, 100 \%)]$ .<sup>[196-197]</sup>

**(5.02): 3,3'-dibromothiophene**



**Figure 8.54: (5.02)**

(5.01) (12.5 g, 25.9 mmol) was added over a period of 0.5 h to a refluxing dispersion of anhydrous zinc powder (6.5 g, 0.1 mol) in 130 mL of ethanol containing 13 mL H<sub>2</sub>O, 31 mL glacial acetic acid and 2.6 mL concentrated hydrochloric acid. After refluxing for an additional 2 h, the mixture was cooled to room temperature, filtered, and washed with ethanol. The filtrate was collected and the solvent was removed. The residue was dissolved in Et<sub>2</sub>O, extracted with an aqueous 5 % sodium bicarbonate solution, and dried over MgSO<sub>4</sub>. The solvent was removed and the product was recrystallized from hexanes to give colourless crystals. Yield 6.7 g (79 %). <sup>1</sup>H-NMR (CDCl<sub>3</sub>): 7.44 (d, 2H, *J* = 5.2 Hz), 7.11 (d, 2H, *J* = 5.2 Hz) ppm. MS (EI +): *m/z* 324 [(M(<sup>79</sup>Br<sup>81</sup>Br)<sup>+</sup>, 100 %].<sup>[195-196]</sup>

**(5.03): 3,3'-bis(trimethylsilylethynyl)-2,2'-bithiophene**

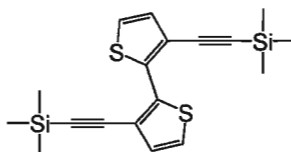


**Figure 8.55: (5.03)**

(5.02) (2.405 g, 7.400 mmol), PPh<sub>3</sub> (0.117 g, 0.447 mmol), Pd(PPh<sub>3</sub>)<sub>2</sub>Cl<sub>2</sub> (0.313 g, 0.447 mmol), and CuI (0.085 g, 0.45 mmol) were combined with deaerated anhydrous diisopropylamine (50 mL). Ethynyltrimethylsilane (2.23 g, 22.7 mmol) was then added to



the mixture which was then heated to 95 °C for 20 h. The reaction was concentrated under reduced pressure, combined with pentane (300 mL), and filtered through a Celite pad. The filtrate was washed with distilled water, and the organic phase was dried with MgSO<sub>4</sub> and filtered. The solvent was removed by rotary evaporation to afford a crystalline yellow solid. Yield: 2.62 g (98 %). Mp: 84-85 °C. <sup>1</sup>H-NMR (CDCl<sub>3</sub>): 7.17 (d, 2H, *J* = 5 Hz), 7.06 (d, 2H, *J* = 5 Hz), 0.25 (s, 18H) ppm. <sup>13</sup>C-NMR (CDCl<sub>3</sub>): δ 139.0, 130.6, 123.8, 119.3, 101.5, 100.7, -0.4 ppm. MS (EI +): *m/z* 358 [M<sup>+</sup>, 36 %], 73 [(M - C<sub>15</sub>H<sub>13</sub>S<sub>2</sub>Si)<sup>+</sup>, 100 %]. FT-IR (KBr): 3087 (w), 2954 (m), 2897 (w), 2147 (s), 1493 (w), 1359 (w), 1239 (m), 1081 (w), 950 (m), 886 (m), 844 (s), 756 (m), 712 (s), 634 (m), 433 (w) cm<sup>-1</sup>. Elemental analysis: calculated (found)% for C<sub>12</sub>H<sub>14</sub>O<sub>2</sub>Si; C, 60.32 (59.96); H, 6.20 (6.19).

**(5.04): 3,3'-dithienyl-2,2'-bithiophene**

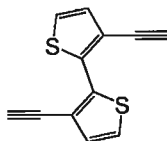


**Figure 8.56: (5.04)**

**(5.03)** (1.00 g, 2.79 mmol) was dissolved in a deaerated mixture of dry tetrahydrofuran and EtOH (100 mL). Potassium hydroxide (0.328 g, 5.86 mmol) was added to the solution. The reaction mixture was stirred at room temperature overnight, H<sub>2</sub>O (20 mL) was added, and the solvent was concentrated under reduced pressure. The residue was dissolved in DCM and washed with distilled water (300 mL). The organic phase was dried over MgSO<sub>4</sub>, filtered, and the solvent was removed by rotary evaporation to obtain

a brown oil that was sufficiently pure to proceed immediately with the next step.  $^1\text{H}$ -NMR ( $\text{CDCl}_3$ ):  $\delta$  7.23 (d, 1H,  $J = 5$  Hz), 7.12 (d, 1H,  $J = 5$  Hz), 3.35 (s, 1H) ppm. MS (EI +):  $m/z$  214 [ $\text{M}^+$ , 100 %]. HRMS (EI +) calculated for  $[\text{C}_{12}\text{H}_6\text{S}_2]^+$ : 213.99110 found 213.99102.

**(5.05): 3,3'-bis(5-ethynylsalicylaldehyde)-2,2'-bithiophene**

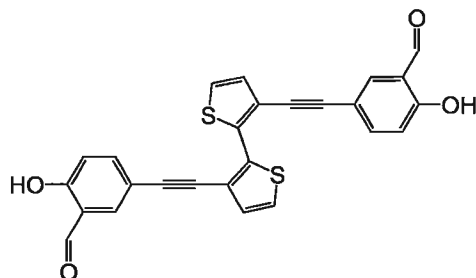


**Figure 8.57: (5.05)**

**(5.04)** (0.597 g, 2.79 mmol), **(2.17)** (1.52 g, 6.14 mmol),  $\text{PPh}_3$  (0.073 g, 0.28 mmol),  $\text{Pd}(\text{PPh}_3)_2\text{Cl}_2$  (0.196 g, 0.280 mmol), and  $\text{CuI}$  (0.053 g, 0.28 mmol) were added to anhydrous and deaerated THF (100 mL) containing diisopropylamine (0.9 mL). The reaction was stirred at 43 °C for 20 h, cooled to room temperature, and concentrated under reduced pressure. The residue was combined with  $\text{CHCl}_3$  (100 mL), filtered through a Celite pad with DCM (400 mL), and washed with 0.5 M HCl (400 mL). The organic phase was dried over  $\text{MgSO}_4$ , filtered, and the solvent was removed by rotary evaporation. The solution was concentrated (25 mL) and added dropwise to pentane (500 mL), resulting in a precipitate that was collected by vacuum filtration. The precipitate was washed with pentane (25 mL), ice cold methanol (15 mL), and dried to afford a yellow powder. Yield: 1.84 g (77 %). Mp: >200 °C.  $^1\text{H}$ -NMR ( $\text{CDCl}_3$ ):  $\delta$  11.13 (br s,

2H), 9.89 (s, 2H), 7.77 (d, 2H,  $J = 2$  Hz), 7.72 (dd, 2H,  $J = 9, 2$  Hz), 7.28 (d, 2H,  $J = 5$  Hz), 7.26 (d, 2H,  $J = 5$  Hz), 7.01 (d, 2H,  $J = 9$  Hz) ppm.  $^{13}\text{C}$ -NMR ( $\text{CDCl}_3$ ):  $\delta$  196.1, 161.6, 139.5, 138.1, 136.7, 130.4, 124.4, 120.6, 119.2, 118.3, 115.3, 93.6, 85.2 ppm. MS (EI +):  $m/z$  452 [ $\text{M}^+$ , 100 %]. HRMS (EI +) calculated for  $[\text{C}_{26}\text{H}_{14}\text{O}_4\text{S}_2]^+$ : 454.03335 found 454.03347. FT-IR (KBr): 3424 (w), 3080 (w), 2924 (w), 2852 (w), 1655 (s), 1614 (w), 1580 (w), 1503 (m), 1476 (m), 1372 (w), 1282 (m), 1261 (m), 1222 (w), 1186 (w), 1137 (w), 906 (w), 879 (w), 844 (w), 766 (w), 723 (w), 705 (w), 684 (w), 636 (w)  $\text{cm}^{-1}$ . Elemental analysis: calculated (found)% for  $\text{C}_{26}\text{H}_{14}\text{O}_4\text{S}_2 \cdot \text{H}_2\text{O}$ ; C, 66.10 (65.94); H, 3.42 (3.38).

**(5.06) $\text{H}_2$ : bis-qsalH**

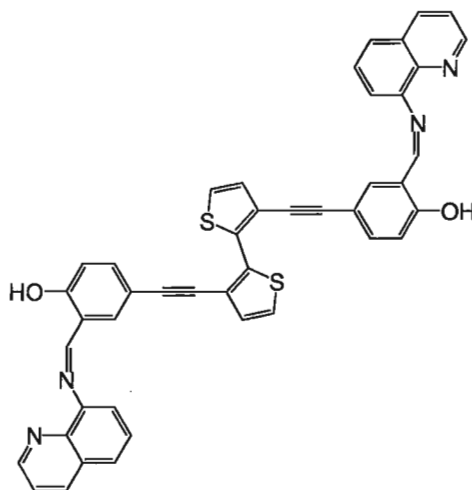


**Figure 8.58: (5.06) $\text{H}_2$**

(5.05) (0.150 g, 0.330 mmol) was dissolved in a THF (15 mL) and added to a solution of 8-aminoquinoline (0.185 g, 1.29 mmol) in ethanol (15 mL). The solution was deaerated and stirred at room temperature for 24 h. The mixture was then concentrated under

reduced pressure and dissolved in  $\text{CHCl}_3$  (1.0 mL) and precipitated into warm hexane (15 mL). The solid was collected by vacuum filtration, washed with hexanes, and dried to give an orange solid. Yield: 0.166 g (71 %). Mp:  $>200^\circ\text{C}$ .  $^1\text{H}$ -NMR ( $\text{CDCl}_3$ ):  $\delta$  14.66 (br, 2H), 9.21 (s, 2H), 9.01 (d, 2H,  $J = 3$  Hz), 8.48 (dd, 2H,  $J = 8.5, 1.5$  Hz), 7.98 (m, 4H), 7.85 (d, 2H,  $J = 7$  Hz), 7.75 (m, 8H), 7.31 (d, 2H,  $J = 5$  Hz), 7.08 (d, 2H,  $J = 8.5$  Hz) ppm.  $^{13}\text{C}$ -NMR: The instability of **(5.06)** $\text{H}_2$  prevented the acquisition of a publishable  $^{13}\text{C}$ -NMR spectrum. MS (FAB +):  $m/z$  707  $[(\text{M} + \text{H})^+]$ , 8.8 %. HRMS (FAB +) calculated for  $[\text{C}_{44}\text{H}_{27}\text{O}_2\text{N}_4\text{S}_2]^+$ : 707.15755 found 707.13532. FT-IR (KBr): 3449 (w), 3096 (w), 2925 (w), 2853 (w), 1620 (s), 1482 (w), 1385 (w), 1285 (w), 1121 (w), 1083 (w), 886 (w), 826 (w), 792 (w), 716 (w), 635 (w), 595 (w)  $\text{cm}^{-1}$ . Elemental analysis: calculated (found)% for  $\text{C}_{44}\text{H}_{26}\text{O}_2\text{N}_4\text{S}_2$ ; C, 74.77 (74.50); H, 3.71 (3.62); N, 7.93 % (7.69).

ii) complex syntheses

**(5.07): [(Fe(2.01))<sub>2</sub>(5.06)]Cl<sub>2</sub>**

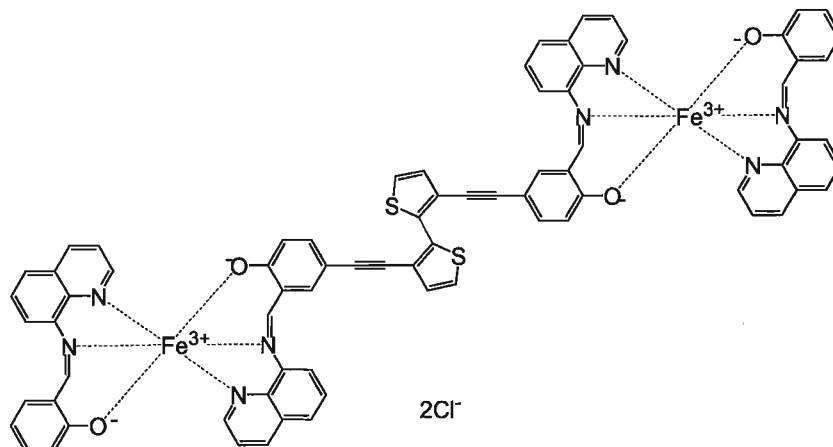


**Figure 8.59: (5.07)**

**(5.05)** (0.681 g, 1.50 mmol) was dissolved in deaerated THF (30 mL), combined with 8-aminoquinoline (0.432 g, 3.00 mmol), and stirred for 24 h. FeCl<sub>3</sub>·6H<sub>2</sub>O (0.810 g, 3.00 mmol) was added to the mixture, and the solution was stirred for 2 h. The resulting precipitate was washed with water, pentane, dried and suspended in MeOH (20 mL). 8-aminoquinoline (0.389 g, 2.70 mmol) and salicylaldehyde (0.329 g, 2.70 mmol) in MeOH (10 mL) were added to the suspension. The mixture was stirred overnight, washed with water, pentane, and dried, affording a brown powder. Yield: 1.62 g (78 %). MS (MALDI +): *m/z* 1310 [(M – 2Cl)<sup>+</sup>, 0.8 %], 1063 [(M – C<sub>16</sub>H<sub>11</sub>N<sub>2</sub>OCl<sub>2</sub>)<sup>+</sup>, 1.6 %], 550 [(M – C<sub>44</sub>H<sub>24</sub>N<sub>4</sub>O<sub>2</sub>S<sub>2</sub>FeCl<sub>2</sub>)<sup>+</sup>, 27 %], 303 [(M – C<sub>60</sub>H<sub>35</sub>N<sub>6</sub>O<sub>3</sub>S<sub>2</sub>FeCl<sub>2</sub>)<sup>+</sup>, 100 %]. FT-IR (KBr): 3421 (w), 3049 (w), 2924 (w), 2856 (w), 2191 (w), 1603 (s), 1574 (s), 1525 (s), 1504 (s), 1456 (m), 1396 (w), 1375 (m), 1307 (m), 1240 (w), 1194 (w), 1147 (w), 1130 (w), 1086 (w), 972 (w), 930 (w), 883 (w), 829 (m), 760 (w), 708 (w), 633 (w), 542 (w), 511 (m),

457 (w)  $\text{cm}^{-1}$ . Elemental analysis: calculated (found)% for  $\text{C}_{76}\text{H}_{46}\text{N}_8\text{O}_4\text{S}_2\text{Fe}_2\text{Cl}_2$ ; C, 65.83 (66.04); H, 2.99 (3.36); N, 8.00 (8.11).

**(5.08):  $[(\text{Fe}(2.01))_2(5.06)](\text{SCN})_2 \cdot 2\text{KCl}$**

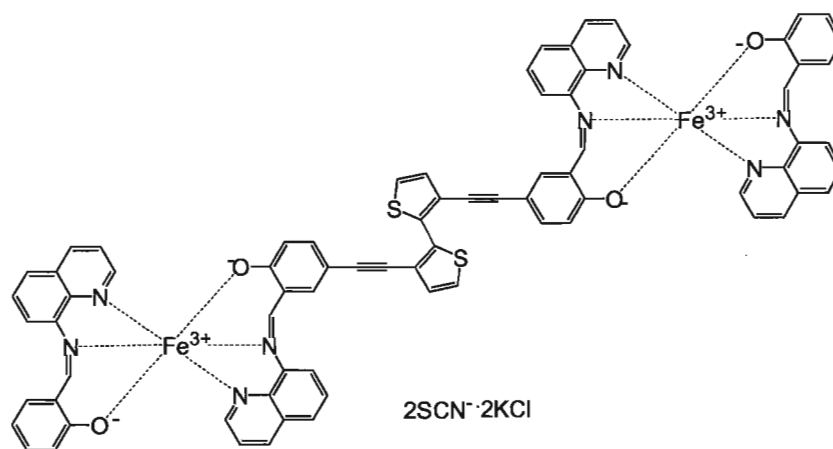


**Figure 8.60: (5.08)**

**(5.07)** (0.150 g, 0.109 mmol) was suspended in MeOH (30 mL), and an excess of KSCN (0.042 g, 0.43 mmol), was added. The mixture was stirred overnight and then combined with distilled water (250 mL), which resulted in a brown precipitate that was filtered, washed with water, pentane, and dried. Yield 0.13 g (85 %). MS (FAB +):  $m/z$  1368  $[(\text{M} - \text{SCN})^+]$ , 1.2 %, 1310  $[(\text{M} - \text{S}_2\text{C}_2\text{N}_2)^+]$ , 4.8 %, 1063  $[(\text{M} - (\text{C}_{18}\text{H}_{11}\text{N}_4\text{OS}_2))^+]$ , 8.7 %, 550  $[(\text{M} - \text{C}_{46}\text{H}_{24}\text{N}_6\text{O}_2\text{S}_4\text{Fe})^+]$ , 100 %. FT-IR (KBr): 3410 (w), 3051 (w), 2924 (w), 2852 (w), 2195(w), 2038 (s), 1602 (s), 1574 (s), 1525 (s), 1504 (s), 1458 (s), 1429 (w), 1396 (w), 1377 (m), 1308 (m), 1240 (w), 1194 (w), 1147 (w), 1068 (w), 972 (w), 931 (w), 883 (w), 829 (m), 785 (w), 758 (w), 719 (w), 634 (w), 542 (w), 511 (w), 463 (w), 414 (w)  $\text{cm}^{-1}$ . Elemental analysis: calculated (found)% for  $\text{C}_{78}\text{H}_{46}\text{N}_{10}\text{O}_4\text{S}_4\text{Fe}_2 \cdot 2\text{KCl}$ ; C, 60.49 (60.49); H, 3.25 (2.96); N, 7.24 (7.99).

**(5.09): [(Fe(2.01))<sub>2</sub>(5.06)](PF<sub>6</sub>)<sub>2</sub>**

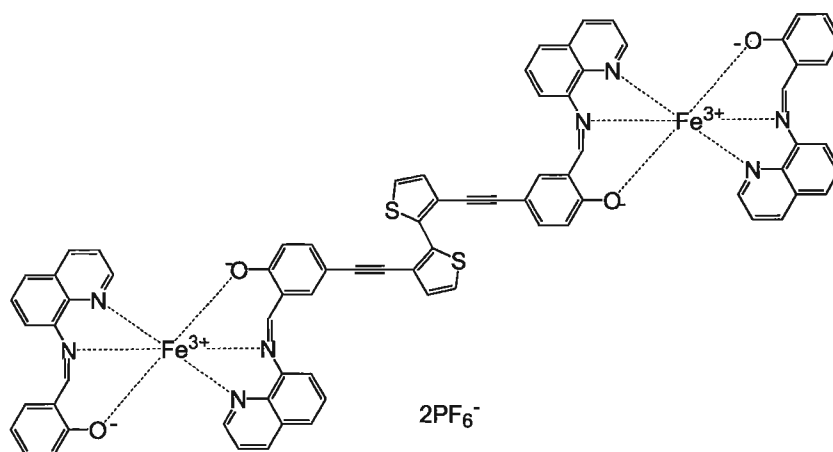


**Figure 8.61: (5.09)**

**(5.07)** (0.150 g, 0.109 mmol) was suspended in MeOH (30 mL), and an excess of NaPF<sub>6</sub> (0.073 g, 0.43 mmol) was added. The mixture was stirred overnight and then combined with distilled water (250 mL), which resulted in a brown precipitate that was filtered, washed with water, pentane, and dried. Yield 0.16 g (89 %). MS (FAB +): *m/z* 1455 [(M – PF<sub>6</sub>)<sup>+</sup>, 1.6 %], 1310 [(M – P<sub>2</sub>F<sub>12</sub>)<sup>+</sup>, 4.1 %], 1063 [(M – C<sub>16</sub>H<sub>11</sub>N<sub>2</sub>OP<sub>2</sub>F<sub>12</sub>)<sup>+</sup>, 6.5 %], 550 [(M – C<sub>44</sub>H<sub>24</sub>N<sub>4</sub>O<sub>2</sub>S<sub>2</sub>FeP<sub>2</sub>F<sub>12</sub>)<sup>+</sup>, 100 %]. FT-IR (KBr): 3419 (w), 3066 (w), 2924 (w), 2852 (w), 2193 (w), 1604 (s), 1576 (s), 1525 (s), 1504 (s), 1458 (s), 1398 (w), 1377 (m), 1309 (m), 1242 (w), 1194 (w), 1149 (w), 1088 (w), 972 (w), 931 (w), 843 (s), 787 (w), 760 (w), 721 (w), 634 (w), 557 (m), 512 (w), 463 (w) cm<sup>-1</sup>. Elemental analysis: calculated (found)% for C<sub>76</sub>H<sub>46</sub>N<sub>8</sub>O<sub>4</sub>S<sub>2</sub>Fe<sub>2</sub>P<sub>2</sub>F<sub>12</sub>; C, 57.00 (57.34); H, 2.90 (2.66); N, 7.00 (6.69).

**(5.05)** (0.274 g, 0.604 mmol) was dissolved in deaerated THF (60 mL), combined with 8-aminoquinoline (0.174 g, 1.21 mmol), and stirred for 24 h.  $\text{Fe}(\text{ClO}_4)_2 \cdot 6\text{H}_2\text{O}$  (429 g, 1.21 mmol) was added, and the solution was stirred for 2 h. The resulting precipitate was washed with water, pentane, dried, and then suspended in MeOH (30 L). 8-aminoquinoline (0.115 g, 0.799 mmol) and salicylaldehyde (0.097 g, 0.80 mmol) in MeOH (10 mL) were added to the suspension. The mixture was stirred overnight, washed with water, pentane, and dried to give a brown powder. Yield: 0.36 g (39 %). MS (MALDI +):  $m/z$  1410  $[(\text{M} - \text{ClO}_4)^+, 0.5 \text{ \%}]$ , 1008  $[(\text{M} - \text{C}_{16}\text{H}_{11}\text{N}_2\text{O}_5\text{FeCl}_2)^+, 6.6 \text{ \%}]$  550  $[(\text{M} - \text{C}_{44}\text{H}_{24}\text{N}_4\text{O}_{10}\text{S}_2\text{FeCl}_2)^+, 97 \text{ \%}]$ . FT-IR (KBr): 3447 (br w), 3071 (w), 2923 (w), 2851 (w), 2195 (w), 1603 (s), 1574 (s), 1525 (s), 1505 (s), 1457 (s), 1397 (m), 1378 (m), 1308 (m), 1242 (w), 1194 (w), 1089 (s), 973 (w), 884 (w), 832 (m), 790 (w), 760 (w), 729 (w), 622 (m), 547 (w), 512 (w), 460 (w), 415 (w)  $\text{cm}^{-1}$ . Elemental analysis: calculated (found)% for  $\text{C}_{76}\text{H}_{46}\text{N}_8\text{O}_{12}\text{S}_2\text{Fe}_2\text{Cl}_2$ ; C, 60.44 (60.30); H, 3.07 (2.91); N, 7.42 (7.10).



## 8.12 Experimental for Chapter 6<sup>ll</sup>

### 1. Chemical polymerization

#### i) Iron(III) microspheres

#### (6.11): poly(2.10)

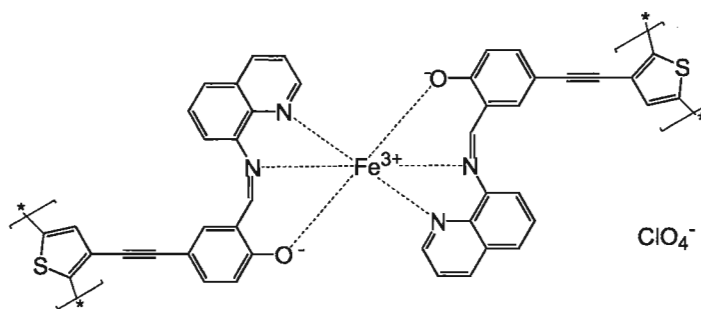


Figure 8.63: (6.11)

An acetonitrile solution containing (2.10) and excess  $\text{ClO}_4^-$  was left open to air at room temperature and purple microspheres of (6.11) were deposited after nearly 2 months. FT-IR (KBr): 3423 (br, m), 2921 (w), 2854 (w), 1607 (s), 1574 (m), 1529 (m), 1455 (m), 1397 (w), 1378 (w), 1317 (w), 1166 (w), 1090 (s), 926 (w), 832 (w), 784 (w), 623 (m), 549 (w), 513 (w)  $\text{cm}^{-1}$ . Elemental analysis: calculated (found)% for  $\text{C}_{44}\text{H}_{22}\text{O}_6\text{N}_4\text{S}_2\text{FeCl}$ ; C, 61.58 (61.16); H, 2.59 (3.04); N, 6.53 (6.28); S, 7.46 (7.07); Fe, 6.51 (7.00). UV-Vis ( $\text{BaSO}_4$ ):  $\lambda_{\text{max}} = 470 \text{ nm}, >775 \text{ nm}$ .

## 2. Electrochemical polymerization

### i) Iron(III) spin-crossover related polymers

#### (6.12): poly(**2.21**)

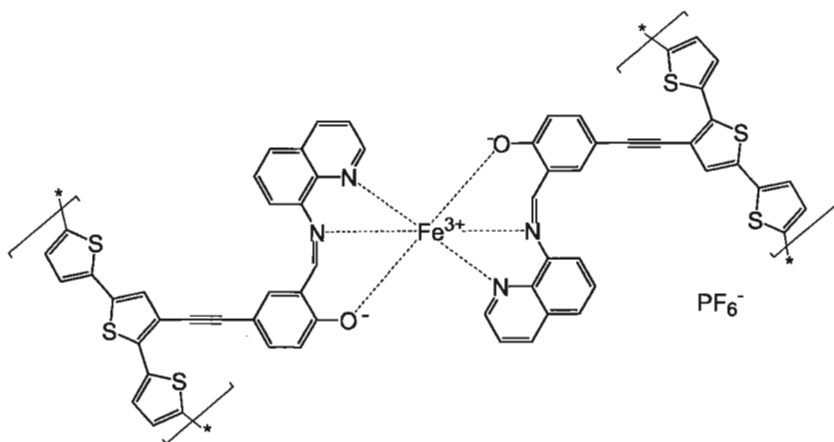


**Figure 8.64: (6.12)**

Monomer (**2.21**) was dried under vacuum at 55 °C for 72 h before use. (**2.21**) (25 mg, 0.020 mmol) was combined with anhydrous  $\text{CH}_3\text{CN}$  (20 mL) containing approximately 0.7 M  $\text{Bu}_4\text{NPF}_6$ . The solution was stirred, while sparging with  $\text{N}_2$  (0.5 h), to generate a saturated solution of (**2.21**) (the solubility of (**2.21**) in  $\text{CH}_3\text{CN}$  is poor). A small quantity of the solution (2 mL) was carefully filtered into a sealed,  $\text{N}_2$  purged electrochemical cell. The electropolymerization of (**2.21**) was carried out at a scan rate of 100 mV/s, over a potential range of -0.5 to +1.0 V (vs. fc); 10 scans over this potential window were performed. A brilliant red film was deposited on an indium tin oxide (ITO) coated glass slide (or a platinum button in some instances). FT-IR (KBr): 3435 (m), 2922 (w), 2853

(w), 1604 (s), 1574 (s), 1523 (m), 1503 (m), 1449 (m), 1374 (m), 1305 (m), 1189 (w), 1087 (w), 842 (s), 691 (m), 556 (m), 512 (w)  $\text{cm}^{-1}$ . UV-Vis (ITO):  $\lambda_{\text{max}} = 510 \text{ nm}$ .

Table 8.01: EDX analysis for **(6.12)**

| Iron to sulfur ratio ( $\text{Fe}_{\text{atom}} \% / \text{S}_{\text{atom}} \%$ ) |               |       |       |
|---|---------------|-------|-------|
| <b>(6.12): polymer</b>  | (0.151)       |       |       |
| <b>(2.21): monomer</b>  | (0.152)       |       |       |
| Theoretical   | (0.167)       |       |       |
| Compound:   | <b>(6.12)</b> |       |       |
| Element   | Fe            | S     | P     |
| Weight (%)  | 10.49         | 71.72 | 17.69 |
| Atom (%)  | 11.68         | 77.29 | 11.03 |
| Apparent concentration (%)  | 13.61         | 73.64 | 14.24 |
| ZAF factor  | 1.08          | 0.96  | 0.75  |
| 3 sigma standard deviation  | 3.05          | 4.36  | 3.85  |
| Compound:   | <b>(2.21)</b> |       |       |
| Element   | Fe            | S     | P     |
| Weight (%)  | 19.95         | 64.59 | 9.49  |
| Atom (%)  | 10.76         | 70.77 | 12.55 |
| Apparent concentration (%)  | 10.68         | 66.27 | 19.34 |
| ZAF factor  | 1.54          | 1.40  | 1.32  |
| 3 sigma standard deviation  | 1.53          | 2.13  | 1.87  |

**(6.13): poly(2.20)**

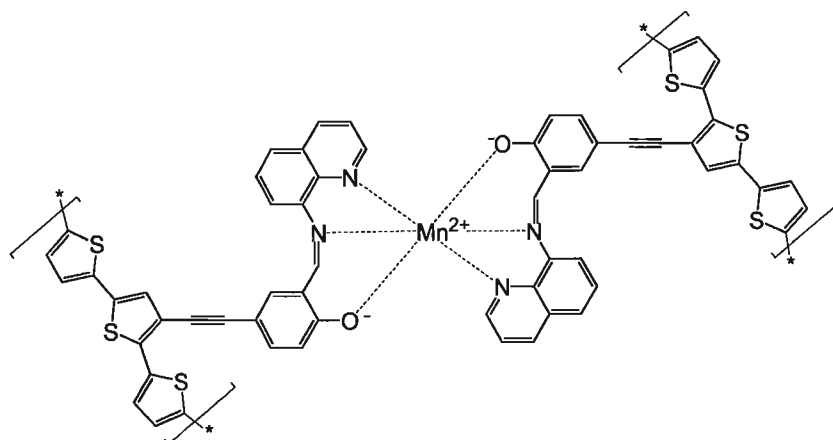


**Figure 8.65: (6.13)**

**(2.19)** (0.0015 g, 3.8  $\mu$ mol) was dissolved in DCM (2 mL) previously purged with  $N_2$  for 0.5 h. 8-aminoquinoline (0.0006 g, 4  $\mu$ mol) was added, and the mixture was stirred at room temperature under  $N_2$  for 1 hour (generating ligand **(2.20)** *in situ*). The supporting electrolyte  $Bu_4NPF_6$  (0.554 g, 1.41 mmol) was added and the sample was subjected to four oxidative sweeps at a scan rate of 100 mV/s over a potential range of -0.5 to +1.0 V (vs. fc). An orange film was collected on the surface of an ITO electrode with a thickness of 150 nm. UV-Vis (ITO):  $\lambda_{max} = 510$  nm.

**(6.14): poly(2.22)**

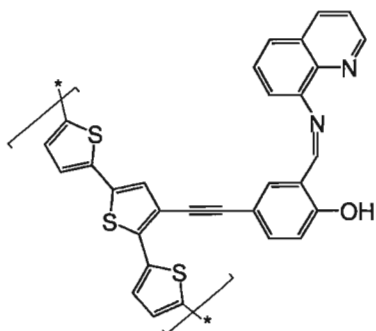


**Figure 8.66: (6.14)**

Monomer **(2.22)** was dried under vacuum at 55 °C for 72 h before use. **(2.22)** (1.0 mg, 0.92  $\mu\text{mol}$ ) was dissolved in anhydrous DCM (1 mL) containing 0.7 M supporting electrolyte ( $\text{Bu}_4\text{NPF}_6$ ) and subjected to four oxidative sweeps at a scan rate of 100 mV/s over a potential range of -0.5 to +1.0 V (vs. fc). An orange film was collected on the surface of the ITO electrode with a thickness of 250 nm. FT-IR (KBr): 3350 (br, s), 2968 (m), 2938 (w), 2881 (w), 1645 (br, m), 1475 (m), 1387 (w), 1108 (br, m), 1070 (br, m), 1037 (br, m), 839 (s), 738 (w), 670 (w), 626 (w), 558 (m)  $\text{cm}^{-1}$ .

ii) Iron(II) spin-crossover conjugated polymer

(6.15): poly(3.24)

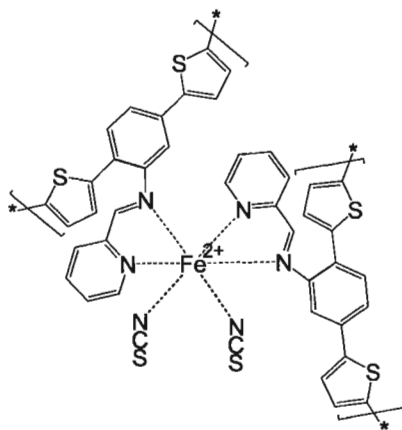


Figure 8.67: (6.15)

Monomer (3.24) was dried under vacuum at room temperature for 72 h before use. (3.24) (0.004 g, 5  $\mu\text{mol}$ ) was dissolved in anhydrous DCM (2 mL) containing 0.5 M supporting electrolyte ( $\text{Bu}_4\text{NPF}_6$ ) and sparged with  $\text{N}_2$  gas for 20 minutes. The solution was then subjected to successive oxidative sweeps at a scan rate of 100 mV/s over a potential range of -0.5 to +1.0 V (vs. fc). An orange film was collected on the surface of the ITO (or Platinum) electrode. IR (KBr): 3449 (br, s), 2961 (w), 2924 (w), 2855 (w), 3667 (m), 1630 (br, s), 1464 (w), 1400 (w), 1261 (w), 1099 (br, w), 1024 (br, w), 845 (br, m), 804 (w), 673 (w), 559 (w)  $\text{cm}^{-1}$ . UV-Vis (ITO):  $\lambda_{\text{max}} = 410 \text{ nm}$ .

Table 8.02: EDX analysis for **(6.15)**

| Iron to sulfur ratio (Fe <sub>atom</sub> % : S <sub>atom</sub> %) |         |       |
|---|---------|-------|
| (6.15): polymer   | (0.179) |       |
| (3.24): monomer   | (0.160) |       |
| Theoretical   | (0.167) |       |
| Compound: polymer (6.16)  |         |       |
| Element   | Fe      | S     |
| Weight (%)  | 22.50   | 78.25 |
| Atom (%)  | 13.76   | 86.24 |
| Apparent concentration (%)  | 16.83   | 83.17 |
| ZAF factor  | 0.75    | 1.03  |
| 3 sigma standard deviation  | 4.02    | 4.22  |
| Compound: monomer (4.07)  |         |       |
| Element   | Fe      | S     |
| Weight (%)  | 23.73   | 76.27 |
| Atom (%)  | 15.15   | 84.85 |
| Apparent concentration (%)  | 22.42   | 77.58 |
| ZAF factor  | 0.75    | 0.81  |
| 3 sigma standard deviation  | 3.05    | 3.42  |

iii) Cobalt(II) valence tautomer related polymers

(6.16): poly(4.07)

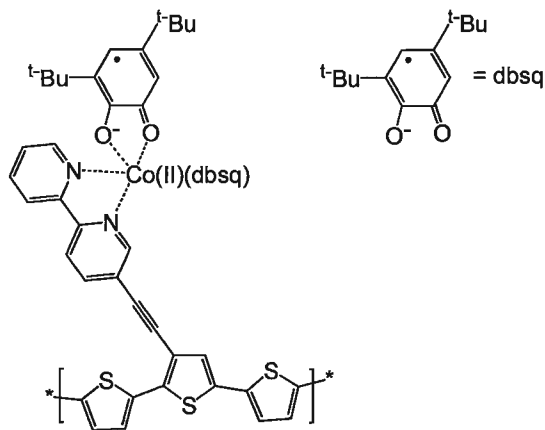


Figure 8.68: (6.16)

Monomer (4.07) was dried under vacuum at room temperature for 72 h before use. (4.07) (0.003 g, 3  $\mu$ mol) was dissolved in anhydrous DCM (3 mL) containing 0.7 M supporting electrolyte ( $\text{Bu}_4\text{NPF}_6$ ) and sparged with  $\text{N}_2$  gas for 20 minutes. The solution was then subjected to successive oxidative sweeps at a scan rate of 100 mV/s over a potential range of -0.5 to +1.0 V (vs. ferrocene). A red film was collected on the surface of the ITO (or platinum) electrode. NIR (ITO):  $\lambda_{\text{max}} = 1000$  nm. UV-Vis (ITO):  $\lambda_{\text{max}} = 450$  nm.



Table 8.03: EDX analysis for **(6.16)**

| Cobalt to sulfur ratio (Co <sub>atom</sub> % / S <sub>atom</sub> %) |         |        |        |
|---|---------|--------|--------|
| (6.16): polymer   | (0.363) |        |        |
| (4.07): monomer   | (0.343) |        |        |
| Theoretical   | (0.333) |        |        |
| Compound: polymer (6.16)  |         |        |        |
| Element   | Co      | S      | P      |
| Weight (%)  | 12.47   | 18.71  | 5.23   |
| Atom (%)  | 3.75    | 10.34  | 2.99   |
| Apparent concentration (%)  | 22.08   | 44.94  | 12.78  |
| ZAF factor  | 0.667   | 0.904  | 0.920  |
| 3 sigma standard deviation  | 1.5776  | 0.9849 | 0.4995 |
| Compound: monomer (4.07)  |         |        |        |
| Element   | Co      | S      |        |
| Weight (%)  | 20.49   | 32.52  |        |
| Atom (%)  | 7.13    | 20.80  |        |
| Apparent concentration (%)  | 28.02   | 61.30  |        |
| ZAF factor  | 0.685   | 0.944  |        |
| 3 sigma standard deviation  | 2.7615  | 1.7592 |        |

(6.17): poly(4.06)

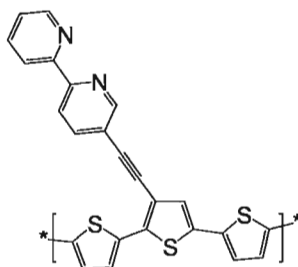


Figure 8.69: (6.17)

Monomer (4.06) was dried under vacuum at room temperature for 72 h before use. (4.03) (0.001 g, 3  $\mu$ mol) was dissolved in anhydrous DCM (2 mL) containing 0.7 M supporting electrolyte ( $\text{Bu}_4\text{NPF}_6$ ) and sparged with  $\text{N}_2$  gas for 20 minutes. The solution was then subjected to successive oxidative sweeps at a scan rate of 100 mV/s over a potential range of -0.5 to +1.0 V (vs. fc). A purple film was collected on the surface of the ITO electrode. NIR (ITO):  $\lambda_{\text{max}} = 950$  nm. UV–Vis (ITO):  $\lambda_{\text{max}} = 450$  nm.

#### Notes:

*A version of this chapter has been published.*

\* (a) Djukic, B.; Dube, P. A.; Razavi, F.; Seda, T.; Jenkins, H. A.; Britten, J. F.; Lemaire, M. T. *Inorg. Chem.* **2009**, *48*, 699–707.

(b) Djukic, B.; Lemaire, M. T. *Inorg. Chem.* **2009**, *48*, 10489–10491.

† (a) O’Sullivan, T. J.; Djukic, B.; Dube, P. A.; Lemaire M. T. *Can. J. Chem.* **2009**, *87*, 533–538.

(b) O’Sullivan, T. J.; Djukic, B.; Dube, P. A.; Lemaire M. T. *Chem. Commun.*, **2009**, 1903–1905.

§ Djukic, B.; Poddutoori, P. K.; Dube, P. A.; Seda, T.; Jenkins, H. A.; Lemaire, M. T. *Inorg. Chem.* **2009**, *48*, 6109–6116.

|| (a) Djukic, B.; Singh, M. A.; Lemaire, M. T. *Synth. Met.* **2010**, *160*, 825–828.

(b) Djukic, B.; Lemaire, M. T. *Inorg. Chem.* **2009**, *48*, 10489–10491.

(c) O’Sullivan, T. J.; Djukic, B.; Dube, P. A.; Lemaire M. T. *Chem. Commun.*, **2009**, 1903-1905.

*A version of this chapter has been accepted for publication.*

† Cheng, H.; Djukic, B.; Jenkins, H. A.; Gorelsky, S. I.; Lemaire, M. T. *Can. J. Chem.* **2010**, submitted for publication.

## References

- [1] Sato, O.; Tao, J.; Zhang, Y.-Z. *Angew. Chem. Int. Ed.* **2007**, 46, 2152-2187.
- [2] Real, J. A.; Gaspar, A. B.; Muñoz, M. C.; *Dalton Trans.* **2005**, 2062–2079.
- [3] Li, W.-K.; Zhou, G.-du.; Mak, T. C. W. *Advanced Structural Inorganic Chemistry*; Oxford University Press: New York, **2008**.
- [4] Müller, U. *Inorganic Structural Chemistry, 2nd ed.*; Wiley: Hoboken N.J., **2007**.
- [5] Wiberg, N.; Holleman, A. F.; Wiberg, E. *Inorganic Chemistry, 1st English ed.*; Academic Press: New York, **2001**.
- [6] Cambi, L.; Szego, L. *Ber. Dtsch. Chem. Ges.* **1931**, 64, 2591 –2598.
- [7] Ladd, M. F. C. *Introduction to Physical Chemistry, 3rd ed.*; Cambridge University Press: New York:, **1998**.
- [8] Gülich, P.; Goodwin, H.A. *Spin-crossover in Transition Metal Compounds, Vol. I*: Springer; New York, **2004**.
- [9] Mabbs, F. E.; Machin, D. J. *Magnetism and Transition Metal Complexes, Dover ed.*; Dover Publications: New York, **2008**.
- [10] Mehn, M. P.; Brown, S. D.; Paine, T. K.; Brennessel, W. W.; Cramer, C. J.; Peters, J. C.; Que, L. Jr. *Dalton Trans.* **2006**, 1347 – 1351.
- [11] Börzel, H.; Comba, P.; Pritzkow, H.; Sickmüller, A. F. *Inorg. Chem.*, **1998**, 37, 3853–3857.
- [12] Carretta, P.; Lascialfari, A. *NMR-MRI,  $\mu$ SR, and Mössbauer Spectroscopies in Molecular Magnets*; Springer: New York, **2007**.
- [13] Parish, R. V. *NMR, NQR, EPR, and Mössbauer Spectroscopy in Inorganic Chemistry*; E. Horwood: New York, **1990**.
- [14] Buchen, T.; Toftlund, H.; Gülich, P. *Chem. Eur. J.* **1996**, 2, 1129-1133.
- [15] Scott, R. A.; Lukehart, C. M. *Applications of Physical Methods to Inorganic and Bioinorganic Chemistry*; Wiley: Hoboken N.J., **2007**.
- [16] Günzler, H.; Williams, A. *Handbook of Analytical Techniques*; Wiley-VCH: New York, **2001**.

- [17] Conti, A. J.; Chadha, R. K.; Sena, K. M.; Rheingold A. L.; Hendrickson, D.N. *Inorg. Chem.* **1993**, 32, 2670-2680.
- [18] Emeléus, H. J.; Sharpe, A. G. *Advances in inorganic chemistry and radiochemistry*; Academic Press, Inc.: New York, 1970.
- [19] Nihei, M.; Shiga, T.; Maeda, Y.; Oshio, H. *Coord. Chem. Rev.*, **2007**, 251, 2606–2621.
- [20] Sorai, M.; *Heat Capacity Studies of Spin-crossover Systems*; Springer: Berlin, **2004**.
- [21] Gütllich, P.; Garcia, Y.; Goodwin, H. A.; *Chem. Soc. Rev.* **2000**, 29, 419–427.
- [22] Rodgers, G, E. *Descriptive Inorganic, Coordination, and Solid-State Chemistry, 2nd Ed.*; Brooks/Cloe; Toronto, **2002**.
- [23] Allen, J. P. *Biophysical Chemistry*; Wiley-Blackwell: Hoboken N.J., **2008**.
- [24] Gütllich, P.; Hauser, A.; Spiering, H. *Angew. Chem., Int. Ed.*, **1994**, 33, 2024–2054.
- [25] Takahashi, K.; Cui, H.-B.; Okano, Y.; Kobayashi, H.; Mori, H.; Tajima, H.; Einaga Y.; Sato, O. *J. Am. Chem. Soc.*, **2008**, 130, 6688–6689.
- [26] Di Varia, M.; Midollini, S.; Sacconi, L. *Inorg. Chem.* **1981**, 20, 3430-3435.
- [27] Yatsimirskii, K. B. *Theor. Exp. Chem.* **1971**, 4, 466-469.
- [28] Real, J. A.; Gaspar, A. B.; Niel, V.; Muñoz, M. C. *Coord. Chem. Rev.* **2003**, 236, 121-141.
- [29] Baker, W. A. Jr.; Bobonich, H. M. *Inorg. Chem.* **1964**, 3, 1184–1188.
- [30] König, E.; Madeja, K. *Chem. Commun.* **1966**, 3, 61-62.
- [31] Nihei, M.; Tahira, H.; Takahashi, N.; Otake, Y.; Yamamura, Y.; Saito, K.; Oshio H. *J. Am. Chem. Soc.*, **2010**, 132, 3553–3560.
- [32] Kitchen, J. A. Jameson, G. N. L. Tallon J. L. Brooker S. *Chem. Commun.*, **2010**, 46, 3200-3202.
- [33] Kosaka, W.; Nomura, K.; Hashimoto, K.; Ohkoshi, S.-i. *J. Am. Chem. Soc.*, **2005**, 127, 8590–8591.
- [34] Reger, D. L.; Gardinier, J. R.; Gemmill, W. R.; Smith, M. D.; Shahin, A. M.; Long, G. J.; Rebbouh, L.; Grandjean, F. *J. Am. Chem. Soc.*, **2005**, 127, 2303–2316.

- [35] Fujigaya, T.; Jiang, D.-L.; Aida, T. *J. Am. Chem. Soc.*, **2005**, *127*, 5484–5489.
- [36] Chang, H. R. ; McCusker, J. K. ; Toftlund, H. ; Wilson, S. R. ; Trautwein, A. X. ; Winkler, H. ; Hendrickson, D. N. *J. Am. Chem. Soc.*, **1990**, *112*, 6814–6827.
- [37] Neville, S. M.; Halder, G. J.; Chapman K. W.; Duriska M. B.; Moubaraki B.; Murray K. S.; Kepert C. J. *J. Am. Chem. Soc.*, **2009**, *131*, 12106–12108.
- [38] Forestier, T.; Kaiba, A.; Pechev, S.; Denux, D.; Guionneau, P.; Etrillard, C.; Daro, N.; Freysz, E.; Létard, J.-F. *Chem. Eur. J.* **2009**, *15*, 6122 – 6130.
- [39] Amooore, J. J. M.; Neville, S. M.; Moubaraki, B.; Iremonger, S. S.; Murray, K. S.; Létard, J.-F.; Kepert, C. J.; *Chem. Eur. J.* **2010**, *16*, 1973 – 1982.
- [40] Weber, B.; Bauer, W.; Obel, J. *Angew. Chem. Int. Ed.* **2008**, *47*, 10098 –10101.
- [41] Arai, M.; Kosaka, W.; Matsuda, T.; Ohkoshi, S.-i. *Angew. Chem.* **2008**, *120*, 6991 –6993.
- [42] Gandolfi, C.; Moitzi, C.; Schurtenberger, P.; Morgan, G. G.; Albrecht, M.; *J. Am. Chem. Soc.* **2008**, *130*, 14434–14435.
- [43] Reed, C. A.; Guiset F. *J. Am. Chem. Soc.* **1996**, *118*, 3281–3282.
- [44] Hayami, S.; Gu, Z.-z.; Shiro, M.; Einaga, Y.; Fujishima, A.; Sato O. *J. Am. Chem. Soc.* **2000**, *122*, 7126–7127.
- [45] Tweedle, M. F.; Wilson, L. J. *J. Am. Chem. Soc.* **1976**, *98*, 4824–4834.
- [46] Kunze, K. R.; Perry, D. L.; Wilson, L. J. *Inorg. Chem.* **1977**, *16*, 594–599.
- [47] Maeda, Y.; Tsutsumi, N.; Takashima, Y.; *Inorg Chem.* **1984**, *23*, 2440-2447.
- [48] Cox, M.; Darken, J.; Fitzsimmons, B. W.; Smith, A. W.; Larkworthy, L. F.; Rogers, K. A. *Chem Commun.* **1970**, *2*, 105-106.
- [49] Cox. M.; Darken, J.; Fitzsimmons, B. W.; Smith, A. W.; Larkworthy, L. F.; Rogers, K. A. *Dalton Trans.* **1972**, 1192-1195.
- [50] Floquet, S.; Boillot, M.-L.; Rivière, E.; Varret, F.; Boukheddaden, K.; Morineau, D.; Négrier, P. *New J. Chem.* **2003**, *27*, 341-348.
- [51] Sour, A.; Boillot, M.-L.; Rivière, E.; Lesot, P.; *Eur. J. Inorg. Chem.* **1999**, 2117-2119.
- [52] Hirose, S.; Hayami, S.; Maeda, Y. *Bull. Chem. Soc. Jpn.* **2000**, *73*, 2059-2066.
- [53] Gütlich, P.; McGarvey, B. R.; Kläui, W. *Inorg. Chem.* **1980**, *19*, 3704–3706.

- [54] Eberspach, W.; El Murr, N.; Kläui, W. *Angew. Chem. Int. Ed.* **1982**, *21*, 915-916.
- [55] Navon, G.; Kläui, W. *Inorg. Chem.* **1984**, *23*, 2722-2725.
- [56] Kläui, W.; Eberspach, W.; Güthlich, P. *Inorg. Chem.* **1987**, *26*, 3977-3982.
- [57] Halepoto, D. M.; Holt, D. G. L.; Larkworthy, L. F.; Leigh, G. L.; Povey, D. C.; Smith, G. W. *Chem. Comm.* **1989**, *16*, 1322-1323.
- [58] Halepoto, D. M.; Holt, D. G. L.; Larkworthy, L. F.; Povey, D. C.; Smith, G. W. *Polyhedron* **1989**, *8*, 1821-1822.
- [59] Sim, P. G.; Sinn, E. *J. Am. Chem. Soc.* **1981**, *103*, 241-243.
- [60] Garcia, Y.; Kahn, O.; Ader, J. P.; Buzdin, A.; Meurdesoif, Y.; Guillot, M. *Phys. Lett. A* **2000**, *271*, 145-154.
- [61] Nakano, M.; Matsubayashi, G.; Matsuo, T. *Adv. Quantum Chem.* **2003**, *44*, 617-630.
- [62] Nakano, M.; Matsubayashi, G.; Matsuo, T. *Phys. Rev. B* **2002**, *66*, 212412.
- [63] Kaustov, L.; Tal, M. E.; Shames, A. I.; Gross, Z. *Inorg. Chem.* **1997**, *36*, 3503-3511.
- [64] Kimura, S.; Narumi, Y.; Kindo, K. *Phys. Rev. B* **2002**, *72*, 064448.
- [65] Pierpont, C. G.; Buchanan, R. M.; *Coord. Chem. Rev.* **1981**, *38*, 45-87.
- [66] Güthlich, P.; Dei, A.; *Angew. Chem.* **1997**, *109*, 2852-2857.
- [67] Halcrow, M. A. *Chem. Soc. Rev.* **2008**, *37*, 278 – 289.
- [68] McGarvey, J. J.; Lawthers, I. *Chem. Commun.* **1982**, *16*, 906-907.
- [69] Létard, J. F. J. *Mater. Chem.* **2006**, *16*, 2550-2559.
- [70] Decurtins, S.; Güthlich, P.; Köhler, C.P.; Spiering, H.; Hauser, A. *Chem. Phys. Lett.* **1984**, *105*, 1-4.
- [71] Güthlich, P.; Hauser A. *Coord. Chem. Rev.* **1990**, *97*, 1-22.
- [72] Hayami, S.; Hiki, K.; Kawahara, T.; Maeda, Y.; Urakami, D.; Inoue, K.; Ohama, M.; Kawata, S.; Sato, O. *Chem. Eur. J.* **2009**, *15*, 3497-3508.
- [73] Schenker, S. Hauser, A. *J. Am. Chem. Soc.* **1994**, *116*, 5497-5498.
- [74] Juhasz, G.; Hayami, S.; Sato, O.; Maeda, Y. *Chem. Phys. Lett.*, **2002**, *364*, 164-170.

- [75] Gütlich, P.; Ksenofontov, V.; Gaspar, A. B. *Coord. Chem. Rev.*, **2005**, *249*, 1811–1829.
- [76] Ganguli, P.; Gütlich, P.; Müller, E. W. *Inorg. Chem.* **1982**, *21*, 3429–3433
- [77] Ewald, H.; Martin, R. L.; Sinn, E.; White, A. H. *Inorg. Chem.* **1969**, *8*, 1837–1846.
- [78] Gaspar, A. B.; Muñoz, M. C.; Moliner, N.; Ksenofontov, V.; Levchenko, G. G.; Gütlich, P.; Real, J. A. *Monatsh. Chem.* **2003**, *134*, 285–294.
- [79] Gaspar, A. B.; Muñoz, M. C.; Moliner, N.; Ksenofontov, V.; Levchenko, G. G.; Gütlich, P.; Real J. A. *Molecular Magnets: Recent Highlights* **2003**, 169–178.
- [80] Gallois, B.; Real, J. A.; Hauw, C.; Zarembovitch, J. *Inorg. Chem.*, **1990**, *29*, 1152–1158.
- [81] Real, J. A.; Gallois, B.; Granier, T.; Suez-Panama, F.; Zarembowitch, J. *Inorg. Chem.*, **1992**, *31*, 4972–4979.
- [82] Mueller, E. W.; Ensling, J.; Spiering, H.; Gütlich, P. *Inorg. Chem.*, **1983**, *22*, 2074–2078.
- [83] Letard, J.-F.; Real, J. A.; Moliner, N.; Gaspar, A. B.; Capes, L.; Cador, O.; Kahn, O. *J. Am. Chem. Soc.* **1999**, *121*, 10630–10631.
- [84] Nakano, K.; Suemura, N.; Kawata, S.; Fuyuhiko, A.; Yagi, T.; Nasu, S.; Morimoto, S.; Kaizaki, S. *Dalton Trans.* **2004**, 982–988.
- [85] Ksenofontov, V.; Gaspar, A. B.; Niel, V.; Reiman, S.; Real, J. A.; Gütlich, P. *Chem. Eur. J.* **2004**, *10*, 1291–1298.
- [86] Amooore, J. J. M.; Kepert, C. J.; Cashion, J. D.; Moubaraki, B.; Neville, S. M.; Murray, K. S. *Chem. Eur. J.* **2006**, *12*, 8220–8227.
- [87] Yoneda, K.; Adachi, K.; Hayami, S.; Maeda, Y.; Katada, M.; Fuyuhiko, A.; Kawata, S.; Kaizaki, S. *Chem. Commun.* **2006**, 45–47.
- [88] Murray, K. S. *Eur. J. Inorg Chem.* **2008**, *20*, 3101–3121.
- [89] Ortega-Villar, N. Thompson, A. L. Muñoz, M. C. Ugalde-Saldívar, V. M. Goeta, A. E. Moreno-Esparza, R. Real J. A. *Chem. Eur. J.* **2005**, *11*, 5721–5734.
- [90] Breuning, E.; Ruben, M.; Lehn, J. M.; Renz, F.; Garcia, Y.; Ksenofontov, V.; Gütlich, P.; Wegelius, E.; Rissanen, K. *Angew. Chem. Int. Ed.* **2000**, *39*, 2504–2507.
- [91] Hanan, G. S.; Schubert, U. S.; Volkmer, D.; Rivière, E.; Lehn, J.-M.; Kyritsakas, N.; Fischer, J. *Can. J. Chem.* **1997**, *75*, 169–182.



- [92] Zhong, Z.; J. Tao, J.; Yu, Z.; Dun, C.; Liu, Y.; You, X. *Dalton Trans.* **1988**, 327-328.
- [93] Kahn, O.; Martinez, C. J.; *Science* **1998**, 279, 44-48.
- [94] Bousseksou, A.; Molnár, G.; Matouzenko, G. *Eur. J. Inorg. Chem.* **2004**, 4353-4369.
- [95] Létard, J.; Guionneau, P.; Codjovi, E.; Lavastre, O.; Bravic, G.; Chasseau, D.; Kahn, O.; *J. Am. Chem. Soc.* **1997**, 119, 10861–10862.
- [96] Hayami, S.; Kawahara, T.; Juhasz, G.; Kawamura, K.; Uehashi, K.; Sato, O.; Maeda, Y. *J. Radioanal. Nucl. Chem.* **2003**, 255, 443-447.
- [97] Hayami, S.; Gu, Z.-z.; Yoshiki, H.; Fujishima, A.; Sato, O. *J. Am. Chem. Soc.* **2001**, 123, 11644–11650.
- [98] Real, J. A.; Bolvin, H.; Bousseksou, A.; Dworkin, A.; Kahn, O.; Varret, F.; Zarembowitch, J. *J. Am. Chem. Soc.* **1992**, 114, 4650-4658.
- [99] Krober, J.; Codjovi, E.; Kahn, O.; Grolibre, F.; Jay, C. *J. Am. Chem. Soc.* **1993**, 115, 9810-9811.
- [100] Sorai, M.; Ensling, J.; Hasselbach, K. M.; Gütlich, P. *Chem. Phys.* **1977**, 20, 197–208.
- [101] Nakamoto, T.; Bhattacharjee, A.; Sorai, M. *Bull. Chem. Soc. Jpn.* **2004**, 77, 921 – 932.
- [102] Cavallini, M.; Bergenti, I.; Milita, S.; Ruani, G.; Salitros, I.; Qu, Z.-R.; Chandrasekar, R.; Ruben M. *Angew. Chem. Int. Ed.* **2008**, 47, 8596 –8600.
- [103] Gamez, P.; Costa, J. S.; Quesada, M.; Aromí, G. *Dalton Trans.* **2009**, 38, 7845-7853.
- [104] Gaspar, A.B.; Ksenofontov, V.; Seredyuk, M.; Gütlich, P. *Coord. Chem. Rev.* **2005**, 249, 2661-2676.
- [105] Coronado, E.; Galán-Mascarós, J. R. *J. Mater. Chem.* **2005**, 15, 66–74.
- [106] Faulmann, C.; Dorbes, S.; Garreau de Bonneval, B.; Molnár, G.; Bousseksou, A.; Gomez-Garcia, C. J.; Coronado, E.; Valade, L. *Eur. J. Inorg. Chem.* **2005**, 3261–3270.
- [107] Dorbes, S.; Valade, L.; Real, J. A.; Faulmann, C. *Chem. Commun.*, **2005**, 69-71.
- [108] Takahashi, K.; Cui, H.-B.; Okano, Y.; Kobayashi, H.; Einaga, Y.; Sato, O. *Inorg. Chem.* **2006**, 45, 5739–5741.

- [109] Takahashi, K.; Kawakami, T.; Gu, Z.-z.; Einaga, Y.; Fujishima, A.; Sato, O. *Chem. Commun.*, **2003**, 2374-2375.
- [110] Sato, O.; Kawakami, T.; Kimura, M.; Hishiya, S.; Kubo, S.; Einaga Y. *J. Am. Chem. Soc.* **2004**, *126*, 13176-13177.
- [111] Djukic, B.; Dube, P. A.; Razavi, F.; Seda, T.; Jenkins, H. A.; Britten, J. F.; Lemaire, M. T. *Inorg. Chem.* **2009**, *48*, 699-707.
- [112] Neya, S.; Takahashi, A.; Ode, H.; Hoshino, T.; Hata, M.; Ikezaki, A.; Ohgo, Y.; Takahashi, M.; Hiramatsu, H.; Kitagawa, T.; Furutani, Y.; Kandori, H.; Funasaki, N.; Nakamura, M. *Eur. J. Inorg. Chem.* **2007**, *20*, 3188-3194.
- [113] Neya, S.; Takahashi, A.; Ode, H.; Hoshino, T.; Ikezaki, A.; Ohgo, Y.; Takahashi, M.; Furutani, Y.; Lorenz-Fonfria, V. A.; Kandori, H.; Hiramatsu, H.; Kitagawa, T.; Teraoka, J.; Funasaki, N.; Nakamura, M. *Bull. Chem. Soc., Jpn.* **2008**, *81*, 136-141.
- [114] Nakamura, M. *Coord. Chem. Rev.* **2006**, *250*, 2271-2294
- [115] Ohgo, Y.; Chiba, Y.; Hashizume, D.; Uekusa, H.; Ozeki, T.; Nakamura, M. *Chem. Commun.* **2006**, 1935-1937
- [116] Dunand-Sauthier, M.-N. C.; Deronzier, A. *J. Electroanal. Chem.* **1997**, *428*, 65-71.
- [117] Wolf, M. O.; Y. Zhu, Y.; *Adv. Mater.* **2000**, *12*, 599-601.
- [118] Djukic, B.; Lemaire, M. T. *Inorg. Chem.* **2009**, *48*, 10489–10491.
- [119] Toftlund, H.; Pedersen, E.; Yde-Andersen, S. *Acta Chem. Scand.* **1984**, *38A*, 693-697.
- [120] Kenning, D. D.; Mitchell, K. A.; Calhoun, T. R.; Funfar, M. R.; Sattler, D. J.; Rasmussen, S. C. *J. Org. Chem.* **2002**, *67*, 9073-9076.
- [121] Cheng, H.; Djukic, B.; Jenkins, H. A.; Gorelsky, S. I.; Lemaire, M. T. *Can. J. Chem.* **2010**, accepted for publication.
- [122] Wei, H. H.; Kao, S. P.; Jean, Y. C. *Transition Met. Chem.* **1986**, *11*, 405-408.
- [123] Zhi, Y. H. H.; Spiering, H.; Gütllich, P. *Transition Met. Chem.* **1996**, *21*, 472-473.
- [124] Wei, H.-H.; Hsiao, C.-S. *J. Inorg. Nucl. Chem.* **1981**, *43*, 2299-2300.
- [125] Kao, S. P.; Jean, Y. C.; Wei, H. H. *Hyperfine Interact.* **1986**, *28*, 711-714.

- [126] Buchanan, M.; Pierpont, C. G. *J. Am. Chem. Soc.* **1980**, *102*, 4951–4957.
- [127] Evangelio, E.; Ruiz-Molina, D. *Eur. J. Inorg. Chem.* **2005**, 2957 – 2971.
- [128] Shultz D. A. *Magnetism Molecules to Materials II*: Wiley-VCH; Weinheim, **2001**, 281–306.
- [129] Jung O.-S. Pierpont and C. G., *J. Am. Chem. Soc.*, **1994**, *116*, 2229–2230.
- [130] Bodnar, S. H.; Caneschi, A.; Dei, A.; Shultz, D. A.; Sorace, L. *Chem. Commun.*, **2001**, 2150–2151.
- [131] Carbonera, C.; Dei, A.; Létard, J.-F. ; Sangregorio, C.; Sorace, L. *Angew. Chem., Int. Ed.* **2004**, *43*, 3136–3138.
- [132] Tao, J.; Maruyama, H.; Sato, O. *J. Am. Chem. Soc.*, **2006**, *128*, 1790–1791.
- [133] Bin-Salamon, S.; Brewer, S. H.; Depperman, E. C.; Franzen, S.; Kampf, J. W.; Kirk M. L.; Kumar, R. K.; Lappi, S.; Peariso, K.; Preuss K. E.; Shultz, D. A. *Inorg. Chem.*, **2006**, *45*, 4461–4467.
- [134] Hearn, N. G. R.; Korčok, J. L.; Paquette, M. M.; Preuss, K. E. *Inorg. Chem.*, **2006**, *45*, 8817–8819.
- [135] Bin-Salamon, S. Brewer, S. Franzen, S. Feldheim, D. L. Lappi S. Shultz, D. A. *J. Am. Chem. Soc.*, **2005**, *127*, 5328–5329.
- [136] Imaz, I.; Maspocho, D.; Rodríguez-Blanco, C.; Pérez-Falcón, J. M.; Campo, J.; Ruiz-Molina, D. *Angew. Chem. Int. Ed.* **2008**, *47*, 1857–1860.
- [137] O’Sullivan, T. J.; Djukic, B.; Dube, P. A.; Lemaire M. T. *Can. J. Chem.* **2009**, *87*, 533–538.
- [138] Buchanan, R. M.; Fitzgerald, B. J.; Pierpont, C. G. *Inorg. Chem.* **1979**, *18*, 3439–3444.
- [139] O’Sullivan, T. J.; Djukic, B.; Dube, P. A.; Lemaire M. T. *Chem. Commun.*, **2009**, 1903–1905.
- [140] Adams, D. M. Noodleman L. Hendrickson, and D. N. *Inorg. Chem.* **1997**, *36*, 3966–3984.
- [141] Djukic, B.; Poddutoori, P. K.; Dube, P. A.; Seda, T.; Jenkins, H. A.; Lemaire, M. T. *Inorg. Chem.* **2009**, *48*, 6109–6116.

- [142] Faulman, C.; Dorbes, S.; Lampert, S.; Jacob, K.; Garreau de Bonneval, B.; Molnar, G.; Bousseksou, A.; Real, J. A.; Valade, L. *Inorg. Chim. Acta* **2007**, *360*, 3870–3878.
- [143] Dickinson, R. C.; Baker, W. A. Jr.; Collins, R. L. *J. Inorg. Nucl. Chem.* **1977**, *39*, 1531–1533.
- [144] Simaan, A. J.; Boillot, M.-L.; Riviere, E.; Boussac, A.; Girerd, J.-J. *Angew. Chem. Int. Ed.* **2000**, *39*, 196–198.
- [145] Tang, J.; Costa, J. S.; Smulders, S.; Molnár, G.; Bousseksou, A.; Teat, S. J.; Li, Y.; van Albada, G. A.; Gamez, P.; Reedijk, J. *Inorg. Chem.* **2009**, *48*, 2128–2135.
- [146] Wolf, M. O. *J. Inorg. Organomet. Polym. Mater.* **2006**, *16*, 189–199.
- [147] Chen, C.-P.; Chan, S.-H.; Chao, T.-C.; Ting, C.; Ko, B.-T. *J. Am. Chem. Soc.* **2008**, *130*, 12828–12833.
- [148] Yamamoto, T.; Lee, B.-L.; Suganuma, H.; Sasaki, S. *Polym. J.* **1998**, *30*, 853–856.
- [149] Floyd, T. L. *Principles of Electric Circuits, 6th Ed.*; Prentice Hall: Upper Saddle River N.J., **1999**.
- [150] Aldissi, M. *Inherently conducting polymers: processing, fabrication, applications, limitations*; Noyes Data Corp.; Park Ridge N.J., **1989**.
- [151] Pomerantz, Z.; Levi, M. D.; Salitra, G.; Demadrille, R.; Fisyuk, A.; Zaban, A.; Aurbacha, D.; Pronb, A. *Phys. Chem. Chem. Phys.* **2008**, *10*, 1032–1042.
- [152] Mehrez, H.; Svizhenko, A.; Anantram, M. P.; Elstner, M.; Frauenheim, T. *Phys. Rev. B* **2005**, *71*, 155421.
- [153] Roncali J. *Chem. Rev.* **1992**, *92*, 711–738.
- [154] Chiang, C. K.; Druy, M. A.; Gau, S. C.; Heeger, A. J.; Louis, E. J.; MacDiarmid, A. G.; Park, Y. W.; Shirakawa, H. *J. Am. Chem. Soc.* **1978**, *100*, 1013–1015.
- [155] Woo, C. H.; Thompson, C. B.; Kim, B. J.; Toney, M. F.; Fréchet, J. M. J. *J. Am. Chem. Soc.* **2008**, *130*, 16324–16329.
- [156] Yamamoto, T.; Sugiyama, K.; Kushida, T.; Inoue, T.; Kanbara T. *J. Am. Chem. Soc.* **1996**, *118*, 3930–3937.
- [157] Maruyama, T.; Suganuma, H.; Yamamoto, T. *Synth. Met.* **1995**, *74*, 183–185.
- [158] Alkan, S.; Cutler, C.A.; Reynolds J.R. *Adv. Funct. Mater.* **2003**, *13*, 331–336.

- [159] Garcia, Y.; Van Koningsbruggen, P.; Lapouyade, R.; Fournés, L.; Rabardel, L.; Kahn O.; Ksenofontov V.; Levchenko G.; Gütllich, P. *Chem. Mater.* **1998**, *10*, 2426–2433.
- [160] Garcia, Y.; Niel V.; Muñoz C.; Real J. A. *Top. Curr. Chem.* **2004**, *233*, 229–257.
- [161] Ruckenstein, E.; Park, J. S. *Synth. Met.* **1991**, *44*, 293–306.
- [162] Yamamoto, T.; Sanechika, K.; Yamamoto, A. *J. Polym. Sci., Part C: Polym. Lett.* **1980**, *18*, 9–12.
- [163] Chen, T. A.; Rieke R. D. *J. Am. Chem. Soc.*, **1992**, *114*, 10087–10088.
- [164] Tourillon, G.; Garnier, F. J. *Electroanal. Chem.* **1982**, *135*, 173–178.
- [165] Wolf, M. *Adv. Mater.* **2001**, *13*, 545–553.
- [166] Reddinger, J. L.; Reynolds J. R. *Chem. Mater.*, **1998**, *10*, 1236–1243.
- [167] Reddinger, J. L.; Reynolds J. R. *Synth. Met.* **1997**, *84*, 225–226.
- [168] Reddinger, J. L.; Reynolds J. R. *Macromolecules*, **1997**, *30*, 673–675.
- [169] Stott, T. L.; Wolf, M. O. *Coord. Chem. Rev.* **2003**, *246*, 89–10.
- [170] Goldstein, J. I.; Newbury, D. E.; Echlin, P.; Joy, D. C.; Lyman, C. E.; Lifshin, E.; Sawyer, L. C.; Michael, J. R. *Scanning Electron Microscopy and X-Ray Microanalysis*; Springer: New York, **2003**.
- [170] Glatter, O.; Kratky O. *Small Angle X-ray Scattering*; Academic Press: London, **1982**.
- [171] Djukic, B.; Singh, M. A.; Lemaire, M. T. *Synth. Met.* **2010**, *160*, 825–828.
- [172] Takekoh, R.; Li, W.-H.; Burke, N. A. D.; Stöver, H. D. H. *J. Am. Chem. Soc.* **2006**, *128*, 240–244.
- [173] Downey, J. S.; McIsaac, G.; Frank, R. S.; Stöver, H. D. H. *Macromolecules*, **2001**, *34*, 4534–4541.
- [174] Goh, E. C. C.; Stöver, H. D. H. *Macromolecules*, **2002**, *35*, 9983–9989.
- [175] Kulbaka, K.; Cheng, A.; Bartole, A.; Greenberg, S.; Resendes, R.; Coombs, N.; Safa-Sefat, A.; Burke, N.; Greedan, J. E.; Stöver, H. D. H.; Ozin, G. A.; Manners, I. *J. Am. Chem. Soc.* **2002**, *124*, 12522–12534.
- [176] Van der Pauw, L. J. *Philips Res. Rep.* **1958**, *13*, 1–9.

- [177] Roncali, J. *Chem. Rev.* **1997**, 97, 173-206.
- [178] Kingsborough, R. P.; Swager, T. M. *J. Am. Chem. Soc.* **1999**, 121, 8825-8834.
- [179] Patil, A. O.; Heeger, A. J.; Wudl, F. *Chem. Rev.*, **1988**, 88, 183-200.
- [180] Clot, O.; Wolf, M. O.; Patrick, B. O. *J. Am. Chem. Soc.* **2000**, 122, 10456-10457.
- [181] Frisch, M. J.; Trucks, G. W.; Schlegel, H. B.; Scuseria, G. E.; Robb, M. A.; Cheeseman, J. R.; Montgomery, Jr., J. A.; Vreven, T.; Kudin, K. N.; Burant, J. C.; Millam, J. M.; Iyengar, S. S.; Tomasi, J.; Barone, V.; Mennucci, B.; Cossi, M.; Scalmani, G.; Rega, N.; Petersson, G. A.; Nakatsuji, H.; Hada, M.; Ehara, M.; Toyota, K.; Fukuda, R.; Hasegawa, J.; Ishida, M.; Nakajima, T.; Honda, Y.; Kitao, O.; Nakai, H.; Klene, M.; Li, X.; Knox, J. E.; Hratchian, H. P.; Cross, J. B.; Bakken, V.; Adamo, C.; Jaramillo, J.; Gomperts, R.; Stratmann, R. E.; Yazyev, O.; Austin, A. J.; Cammi, R.; Pomelli, C.; Ochterski, J. W.; Ayala, P. Y.; Morokuma, K.; Voth, G. A.; Salvador, P.; Dannenberg, J. J.; Zakrzewski, V. G.; Dapprich, S.; Daniels, A. D.; Strain, M. C.; Farkas, O.; Malick, D. K.; Rabuck, A. D.; Raghavachari, K.; Foresman, J. B.; Ortiz, J. V.; Cui, Q.; Baboul, A. G.; Clifford, S.; Cioslowski, J.; Stefanov, B. B.; Liu, G.; Liashenko, A.; Piskorz, P.; Komaromi, I.; Martin, R. L.; Fox, D. J.; Keith, T.; Al-Laham, M. A.; Peng, C. Y.; Nanayakkara, A.; Challacombe, M.; Gill, P. M. W.; Johnson, B.; Chen, W.; Wong, M. W.; Gonzalez, C.; Pople, J. A. Gaussian, Inc., Wallingford CT, **2004**.
- [182] Becke, A. D. *J. Chem. Phys.* **1993**, 98, 5648-5652.
- [183] Lee, C.; Yang, W.; Parr, R. G. *Phys. Rev. B* **1988**, 37, 785-789.
- [184] Godbout, N.; Salahub, D. R.; Andzelm, J.; Wimmer, E. *Can. J. Chem.* **1992**, 70, 560-571.
- [185] Reed, A. E.; Curtiss, L. A.; Weinhold, F. *Chem. Rev.* **1988**, 88, 899-926.
- [186] Gorelsky, S. I. *version 6.46 ed.*; University of Ottawa: Ottawa, **2010**.
- [187] Gorelsky, S. I.; Lever, A. B. P. *J. Organomet. Chem.* **2001**, 635, 187-196.
- [188] Oshio, H.; Kitazaki, K.; Mishiro, J.; Kato, N.; Maeda, Y.; Takashima, Y. *Dalton Trans.* **1987**, 1341 – 1347.
- [189] Dickenson, R. C.; Baker, W. A.; Collins, R. L. *J. Inorg. Nucl. Chem.* **1977**, 39, 1531-1533.
- [190] Kagan, J.; Liu, H. *Synth. Met.* **1996**, 82, 75-81.
- [191] Kim, D. H.; Kang, B. S.; Lim, S. M.; Bark, K.-M.; Kim, B. G.; Shiro, M.; Shim, Y.-B.; Shin, S. C. *Dalton Trans.* **1998**, 1893-1898.

- [192] Choi-Sledeski, Y. M.; McGarry, D. G.; Green, D. M.; Mason, H. J.; Becker, M. R.; Davis, R. S.; Ewing, W. R.; Dankulich, W. P.; Manetta, V. E.; Morris, R. L.; Spada, A. P.; Cheney, D. L.; Brown, K. D.; Colussi, D. J.; Chu, V.; Heran, C. L.; Morgan, S. R.; Bentley, R. G.; Leadley, R. J.; Maignan, S.; Guilloteau, J.-P.; Dunwiddie, C. T.; Pauls, H. W. *J. Med. Chem.* **1999**, *42*, 3572–3587.
- [193] Kitamura, C.; Tanaka, S.; Yamashita, Y. *Chem. Mater.* **1996**, *8*, 570–578.
- [194] Fang, Y.-Q.; Hanan, G. S. *Synlett.* **2003**, 852-855.
- [195] Grosshenny, V.; Romero, F. M.; Ziessel, R. *J. Org. Chem.* **1997**, *62*, 1491-1500.
- [196] Facchetti, A.; Yoon, M.-H.; Stern, C. L.; Hutchison, G. R.; Ratner, M. A.; Marks, T. J. *J. Am. Chem. Soc.* **2004**, *126*, 13480–13501.
- [197] Yu, W.-L.; Meng, H.; Pei, J.; Huang, W.; Li, Y.; Heeger, A. J.; *Macromolecules* **1998**, *31*, 4838–4844.

## Appendix A: Crystallographic parameters

Table A.1: Crystal data and structure refinement for (2.03)

|                                   |   |                       |
|-----------------------------------|---|-----------------------|
| Empirical formula                 | $C_{32}H_{22}FeIN_4O_2$                     |                       |
| Formula weight                    | 677.29                                      |                       |
| Temperature                       | 296(2) K                                    |                       |
| Wavelength                        | 0.71073 Å                                   |                       |
| Crystal system                    | Orthorhombic                                |                       |
| Space group                       | Pnna  |                       |
| Unit cell dimensions              | $a = 13.044(2)$ Å                           | $\alpha = 90^\circ$ . |
|                                   | $b = 16.405(3)$ Å                           | $\beta = 90^\circ$ .  |
|                                   | $c = 12.652(2)$ Å                           | $\gamma = 90^\circ$ . |
| Volume                            | $2707.4(8)$ Å <sup>3</sup>                  |                       |
| Z                                 | 4   |                       |
| Density (calculated)              | 1.662 Mg/m <sup>3</sup>                     |                       |
| Absorption coefficient            | 1.735 mm <sup>-1</sup>                      |                       |
| F(000)                            | 1348  |                       |
| Crystal size                      | 0.24 x 0.18 x 0.12 mm <sup>3</sup>          |                       |
| Theta range for data collection   | 2.03 to 26.48°.                             |                       |
| Index ranges                      | -16 ≤ h ≤ 16, -20 ≤ k ≤ 20, -15 ≤ l ≤ 15    |                       |
| Reflections collected             | 18971                                       |                       |
| Independent reflections           | 2797 [R(int) = 0.0876]                      |                       |
| Completeness to theta = 26.48°    | 99.7 %                                      |                       |
| Absorption correction             | Numerical                                   |                       |
| Max. and min. transmission        | 0.8241 and 0.6808                           |                       |
| Refinement method                 | Full-matrix least-squares on F <sup>2</sup> |                       |
| Data / restraints / parameters    | 2797 / 0 / 226                              |                       |
| Goodness-of-fit on F <sup>2</sup> | 1.000                                       |                       |
| Final R indices [I > 2σ(I)]       | R1 = 0.0438, wR2 = 0.0859                   |                       |
| R indices (all data)              | R1 = 0.0874, wR2 = 0.1014                   |                       |
| Largest diff. peak and hole       | 0.595 and -0.346 e.Å <sup>-3</sup>          |                       |



---

Table A.3: Crystal data and structure refinement for **(2.11)**

|  |  |                              |
|--|--|------------------------------|
| Empirical formula                      | $\text{C}_{44}\text{H}_{26}\text{MnN}_4\text{O}_2\text{S}_2$       |                              |
| Formula weight                         | 761.75   |                              |
| Temperature                            | 173(2) K   |                              |
| Wavelength                             | 0.71073 Å  |                              |
| Crystal system                         | Monoclinic   |                              |
| Space group                            | P21/c  |                              |
| Unit cell dimensions                   | $a = 14.516(5)$ Å  | $\alpha = 90^\circ$ .        |
|  | $b = 19.636(8)$ Å  | $\beta = 103.766(6)^\circ$ . |
|  | $c = 12.673(4)$ Å  | $\gamma = 90^\circ$ .        |
| Volume                                 | $3509(2)$ Å <sup>3</sup>   |                              |
| Z                                      | 4  |                              |
| Density (calculated)                   | $1.442$ Mg/m <sup>3</sup>  |                              |
| Absorption coefficient                 | $0.541$ mm <sup>-1</sup>   |                              |
| F(000)                                 | 1564   |                              |
| Crystal size                           | $0.15 \times 0.11 \times 0.02$ mm <sup>3</sup>                     |                              |
| Theta range for data collection        | $2.18$ to $25.00^\circ$ .  |                              |
| Index ranges                           | $-17 \leq h \leq 17$ , $-14 \leq k \leq 23$ , $-15 \leq l \leq 14$ |                              |
| Reflections collected                  | 23226  |                              |
| Independent reflections                | 6165 [ $R(\text{int}) = 0.2018$ ]                                  |                              |
| Completeness to $\theta = 25.00^\circ$ | 99.9 %   |                              |
| Absorption correction                  | None   |                              |
| Max. and min. transmission             | 0.9893 and 0.9242  |                              |
| Refinement method                      | Full-matrix least-squares on $F^2$                                 |                              |
| Data / restraints / parameters         | 6165 / 0 / 479   |                              |
| Goodness-of-fit on $F^2$               | 0.956  |                              |
| Final R indices [ $I > 2\sigma(I)$ ]   | $R1 = 0.0678$ , $wR2 = 0.1145$                                     |                              |
| R indices (all data)                   | $R1 = 0.2103$ , $wR2 = 0.1685$                                     |                              |
| Largest diff. peak and hole            | $0.352$ and $-0.348$ e.Å <sup>-3</sup>                             |                              |

---

---

Table A.2: Crystal data and structure refinement for **(2.12)**

|                                   |  |                   |
|-----------------------------------|--|-------------------|
| Empirical formula                 | C <sub>47</sub> H <sub>32</sub> FeN <sub>4</sub> O <sub>4.5</sub> S <sub>2</sub> |                   |
| Formula weight                    | 844.74   |                   |
| Temperature                       | 296(2) K   |                   |
| Wavelength                        | 0.71073 Å  |                   |
| Crystal system                    | Monoclinic   |                   |
| Space group                       | P21/n  |                   |
| Unit cell dimensions              | a = 14.504(6) Å  | α = 90°.          |
|                                   | b = 17.778(7) Å  | β = 109.377(10)°. |
|                                   | c = 16.911(8) Å  | γ = 90°.          |
| Volume                            | 4113(3) Å <sup>3</sup>   |                   |
| Z                                 | 4  |                   |
| Density (calculated)              | 1.364 Mg/m <sup>3</sup>  |                   |
| Absorption coefficient            | 0.519 mm <sup>-1</sup>   |                   |
| F(000)                            | 1744   |                   |
| Crystal size                      | 0.32 x 0.23 x 0.06 mm <sup>3</sup>   |                   |
| Theta range for data collection   | 2.26 to 25.38°.  |                   |
| Index ranges                      | -17 ≤ h ≤ 17, -19 ≤ k ≤ 21, -14 ≤ l ≤ 20   |                   |
| Reflections collected             | 26788  |                   |
| Independent reflections           | 7527 [R(int) = 0.0656]   |                   |
| Completeness to theta = 25.38°    | 99.4 %   |                   |
| Absorption correction             | None   |                   |
| Max. and min. transmission        | 0.9695 and 0.8515  |                   |
| Refinement method                 | Full-matrix least-squares on F <sup>2</sup>                                      |                   |
| Data / restraints / parameters    | 7527 / 2 / 529   |                   |
| Goodness-of-fit on F <sup>2</sup> | 1.024  |                   |
| Final R indices [I > 2σ(I)]       | R1 = 0.0683, wR2 = 0.1884  |                   |
| R indices (all data)              | R1 = 0.1178, wR2 = 0.2228  |                   |
| Largest diff. peak and hole       | 0.730 and -0.520 e.Å <sup>-3</sup>   |                   |

---

---

Table A.4: Crystal data and structure refinement for (3.14)

|                                   |  |                  |
|-----------------------------------|--|------------------|
| Empirical formula                 | C <sub>58</sub> H <sub>40</sub> FeN <sub>10</sub> S <sub>4</sub> |                  |
| Formula weight                    | 1061.09  |                  |
| Temperature                       | 173(2) K   |                  |
| Wavelength                        | 0.71073 Å  |                  |
| Crystal system                    | Monoclinic   |                  |
| Space group                       | C2/c   |                  |
| Unit cell dimensions              | a = 17.343(4) Å  | α = 90°.         |
|                                   | b = 17.136(4) Å  | β = 108.315(5)°. |
|                                   | c = 17.227(4) Å  | γ = 90°.         |
| Volume                            | 4860(2) Å <sup>3</sup>   |                  |
| Z                                 | 4  |                  |
| Density (calculated)              | 1.450 Mg/m <sup>3</sup>  |                  |
| Absorption coefficient            | 0.535 mm <sup>-1</sup>   |                  |
| F(000)                            | 2192   |                  |
| Crystal size                      | 0.37 x 0.13 x 0.10 mm <sup>3</sup>                               |                  |
| Theta range for data collection   | 1.88 to 26.00°.  |                  |
| Index ranges                      | -16 ≤ h ≤ 21, -16 ≤ k ≤ 21, -21 ≤ l ≤ 20                         |                  |
| Reflections collected             | 26762  |                  |
| Independent reflections           | 4768 [R(int) = 0.0713]   |                  |
| Completeness to theta = 26.00°    | 99.9 %   |                  |
| Absorption correction             | Numerical  |                  |
| Max. and min. transmission        | 0.9509 and 0.8253  |                  |
| Refinement method                 | Full-matrix least-squares on F <sup>2</sup>                      |                  |
| Data / restraints / parameters    | 4768 / 0 / 391   |                  |
| Goodness-of-fit on F <sup>2</sup> | 1.028  |                  |
| Final R indices [I > 2σ(I)]       | R1 = 0.0617, wR2 = 0.1539  |                  |
| R indices (all data)              | R1 = 0.1098, wR2 = 0.1838  |                  |
| Largest diff. peak and hole       | 0.841 and -0.468 e.Å <sup>-3</sup>                               |                  |

---

---

Table A.5: Crystal data and structure refinement for **(3.20)**

|                                       |  |                                |
|---------------------------------------|--|--------------------------------|
| Empirical formula                     | $C_{20}H_{14}N_2S_2$   |                                |
| Formula weight                        | 346.45   |                                |
| Temperature                           | 293(2) K   |                                |
| Wavelength                            | 0.71073 Å  |                                |
| Crystal system                        | Triclinic  |                                |
| Space group                           | P -1   |                                |
| Unit cell dimensions                  | $a = 5.7605(4)$ Å  | $\alpha = 80.7610(10)^\circ$ . |
|                                       | $b = 16.4249(13)$ Å  | $\beta = 85.089(2)^\circ$ .    |
|                                       | $c = 18.2271(14)$ Å  | $\gamma = 83.5010(10)^\circ$ . |
| Volume                                | $1687.3(2)$ Å <sup>3</sup>                                       |                                |
| Z                                     | 4  |                                |
| Density (calculated)                  | $1.364$ Mg/m <sup>3</sup>  |                                |
| Absorption coefficient                | $0.318$ mm <sup>-1</sup>   |                                |
| F(000)                                | 720  |                                |
| Crystal size                          | $0.77 \times 0.25 \times 0.20$ mm <sup>3</sup>                   |                                |
| Theta range for data collection       | $1.13$ to $27.50^\circ$ .  |                                |
| Index ranges                          | $-4 \leq h \leq 7$ , $-20 \leq k \leq 21$ , $-23 \leq l \leq 23$ |                                |
| Reflections collected                 | 21401  |                                |
| Independent reflections               | 7685 [R(int) = 0.0282]   |                                |
| Completeness to theta = $27.50^\circ$ | 0.988 %  |                                |
| Absorption correction                 | None   |                                |
| Max. and min. transmission            | 0.9649 and 0.8745  |                                |
| Refinement method                     | Full-matrix least-squares on F <sup>2</sup>                      |                                |
| Data / restraints / parameters        | 7685 / 0 / 425   |                                |
| Goodness-of-fit on F <sup>2</sup>     | 1.030  |                                |
| Final R indices [I > 2sigma(I)]       | R1 = 0.0714, wR2 = 0.1932  |                                |
| R indices (all data)                  | R1 = 0.1000, wR2 = 0.2277  |                                |
| Largest diff. peak and hole           | $1.537$ and $-0.917$ e.Å <sup>-3</sup>                           |                                |

---

---

Table A.6: Crystal data and structure refinement for **(3.23)**

|                                   |   |                              |
|-----------------------------------|---|------------------------------|
| Empirical formula                 | $C_{50.5}H_{37}ClFeN_6S_2$                  |                              |
| Formula weight                    | 883.28                                      |                              |
| Temperature                       | 150(1) K                                    |                              |
| Wavelength                        | 0.71073 Å                                   |                              |
| Crystal system                    | Monoclinic                                  |                              |
| Space group                       | P 21/n                                      |                              |
| Unit cell dimensions              | $a = 17.3899(11)$ Å                         | $\alpha = 90^\circ$ .        |
|                                   | $b = 9.6294(6)$ Å                           | $\beta = 105.551(3)^\circ$ . |
|                                   | $c = 26.6152(17)$ Å                         | $\gamma = 90^\circ$ .        |
| Volume                            | $4293.7(5)$ Å <sup>3</sup>                  |                              |
| Z                                 | 4   |                              |
| Density (calculated)              | 1.366 Mg/m <sup>3</sup>                     |                              |
| Absorption coefficient            | 0.555 mm <sup>-1</sup>                      |                              |
| F(000)                            | 1828  |                              |
| Crystal size                      | 0.60 x 0.20 x 0.08 mm <sup>3</sup>          |                              |
| Theta range for data collection   | 2.65 to 25.00°.                             |                              |
| Index ranges                      | -20 ≤ h ≤ 20, -11 ≤ k ≤ 11, -28 ≤ l ≤ 31    |                              |
| Reflections collected             | 29494                                       |                              |
| Independent reflections           | 7436 [R(int) = 0.1196]                      |                              |
| Completeness to theta = 25.00°    | 98.2 %                                      |                              |
| Absorption correction             | Semi-empirical from equivalents             |                              |
| Max. and min. transmission        | 1.048 and 0.362                             |                              |
| Refinement method                 | Full-matrix least-squares on F <sup>2</sup> |                              |
| Data / restraints / parameters    | 7436 / 7 / 564                              |                              |
| Goodness-of-fit on F <sup>2</sup> | 1.123                                       |                              |
| Final R indices [I > 2σ(I)]       | R1 = 0.0923, wR2 = 0.2001                   |                              |
| R indices (all data)              | R1 = 0.1846, wR2 = 0.2482                   |                              |
| Largest diff. peak and hole       | 0.381 and -0.527 e.Å <sup>-3</sup>          |                              |

---

---

Table A.7: Crystal data and structure refinement for **(3.24)**

|                                   |  |                               |
|-----------------------------------|--|-------------------------------|
| Empirical formula                 | $\text{C}_{49}\text{H}_{36}\text{FeN}_6\text{S}_6$                 |                               |
| Formula weight                    | 957.05   |                               |
| Temperature                       | 150(2) K   |                               |
| Wavelength                        | 0.71073 Å  |                               |
| Crystal system                    | Triclinic  |                               |
| Space group                       | P -1   |                               |
| Unit cell dimensions              | $a = 10.1613(5)$ Å   | $\alpha = 102.549(3)^\circ$ . |
|                                   | $b = 15.1701(9)$ Å   | $\beta = 91.113(4)^\circ$ .   |
|                                   | $c = 16.5684(10)$ Å  | $\gamma = 106.291(3)^\circ$ . |
| Volume                            | $2384.1(2)$ Å <sup>3</sup>   |                               |
| Z                                 | 2  |                               |
| Density (calculated)              | 1.333 Mg/m <sup>3</sup>  |                               |
| Absorption coefficient            | 0.620 mm <sup>-1</sup>   |                               |
| F(000)                            | 988  |                               |
| Crystal size                      | 0.20 x 0.08 x 0.02 mm <sup>3</sup>                                 |                               |
| Theta range for data collection   | 2.59 to 25.07°.  |                               |
| Index ranges                      | $-12 \leq h \leq 12$ , $-18 \leq k \leq 17$ , $-19 \leq l \leq 19$ |                               |
| Reflections collected             | 8363   |                               |
| Independent reflections           | 8363 [R(int) = 0.102]  |                               |
| Completeness to theta = 25.07°    | 99.0 %   |                               |
| Absorption correction             | Semi-empirical from equivalents                                    |                               |
| Max. and min. transmission        | 0.978 and 0.687  |                               |
| Refinement method                 | Full-matrix least-squares on F <sup>2</sup>                        |                               |
| Data / restraints / parameters    | 8363 / 37 / 570  |                               |
| Goodness-of-fit on F <sup>2</sup> | 0.989  |                               |
| Final R indices [I > 2sigma(I)]   | R1 = 0.0706, wR2 = 0.1639  |                               |
| R indices (all data)              | R1 = 0.1430, wR2 = 0.1906  |                               |
| Largest diff. peak and hole       | 0.517 and -0.439 e.Å <sup>-3</sup>                                 |                               |

---

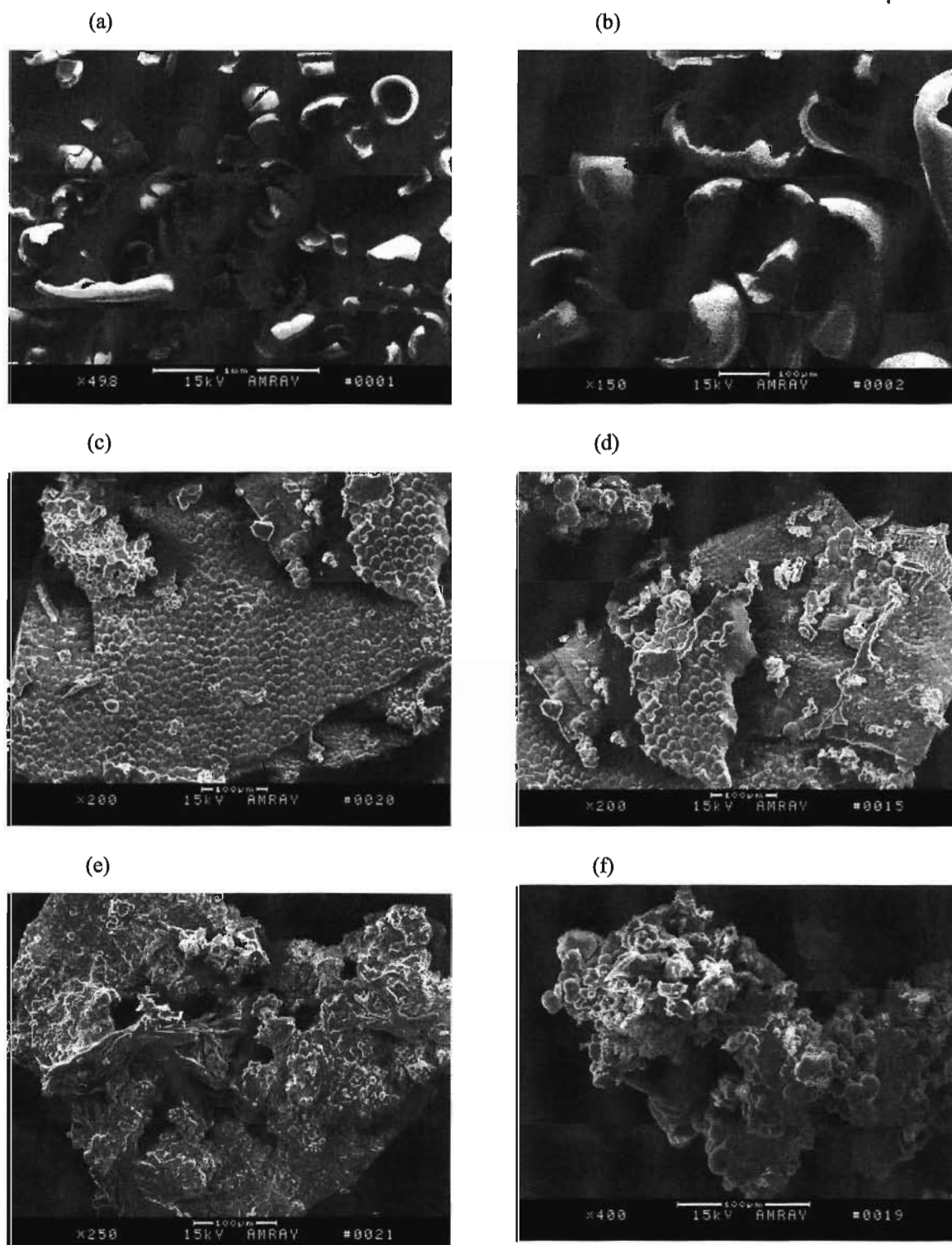
---

Table A.8: Crystal data and structure refinement for **(5.05)**

|                                   |  |                              |
|-----------------------------------|--|------------------------------|
| Empirical formula                 | $C_{26}H_{14}O_4S_2$   |                              |
| Formula weight                    | 454.49   |                              |
| Temperature                       | 295(2) K   |                              |
| Wavelength                        | 0.71073 Å  |                              |
| Crystal system                    | Monoclinic   |                              |
| Space group                       | C2/c   |                              |
| Unit cell dimensions              | $a = 16.404(2)$ Å  | $\alpha = 90^\circ$ .        |
|                                   | $b = 11.7203(16)$ Å  | $\beta = 116.637(3)^\circ$ . |
|                                   | $c = 12.1821(17)$ Å  | $\gamma = 90^\circ$ .        |
| Volume                            | $2093.6(5)$ Å <sup>3</sup>   |                              |
| Z                                 | 4  |                              |
| Density (calculated)              | 1.442 Mg/m <sup>3</sup>  |                              |
| Absorption coefficient            | 0.287 mm <sup>-1</sup>   |                              |
| F(000)                            | 936  |                              |
| Crystal size                      | 0.60 x 0.20 x 0.06 mm <sup>3</sup>                                 |                              |
| Theta range for data collection   | 2.22 to 26.50°.  |                              |
| Index ranges                      | $-20 \leq h \leq 10$ , $-14 \leq k \leq 14$ , $-13 \leq l \leq 15$ |                              |
| Reflections collected             | 12036  |                              |
| Independent reflections           | 2174 [R(int) = 0.0283]   |                              |
| Completeness to theta = 26.50°    | 100.0 %  |                              |
| Absorption correction             | None   |                              |
| Max. and min. transmission        | 0.9830 and 0.8467  |                              |
| Refinement method                 | Full-matrix least-squares on F <sup>2</sup>                        |                              |
| Data / restraints / parameters    | 2174 / 0 / 173   |                              |
| Goodness-of-fit on F <sup>2</sup> | 1.036  |                              |
| Final R indices [I > 2sigma(I)]   | R1 = 0.0396, wR2 = 0.1044  |                              |
| R indices (all data)              | R1 = 0.0568, wR2 = 0.1161  |                              |
| Largest diff. peak and hole       | 0.217 and -0.145 e.Å <sup>-3</sup>                                 |                              |

---

## Appendix B: Polymer images



**Figure A-1:** SEM images of (5.07) [with  $\text{NaB(Ph)}_4$ ] precipitates at (a) 50X (b) 150X (c) 200X (d) 200X (e) 250X (f) 400X magnification



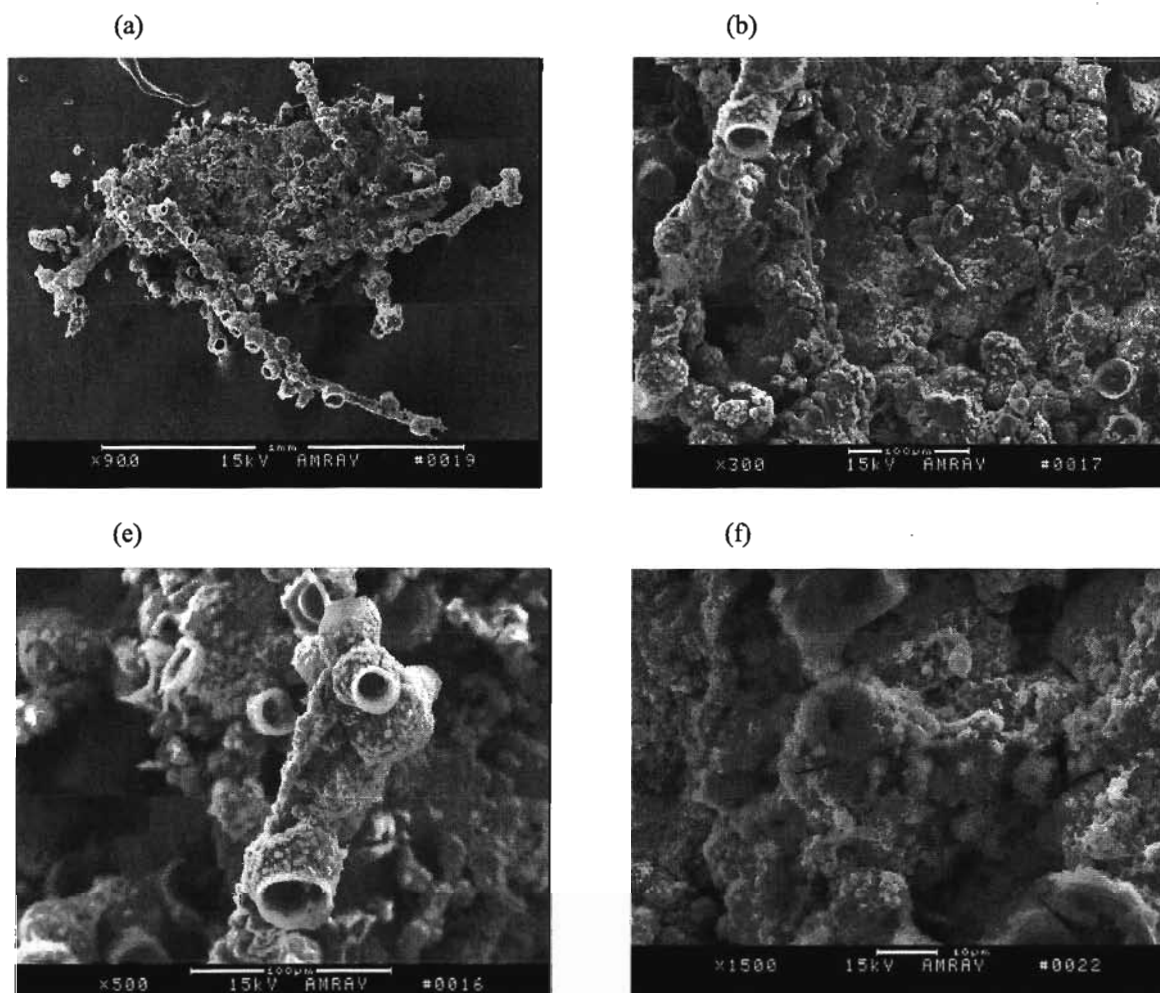


**Figure A-2:** SEM images of (5.10) precipitates at (a) 90X (b) 300X (c) 500X (d) 1500X magnification

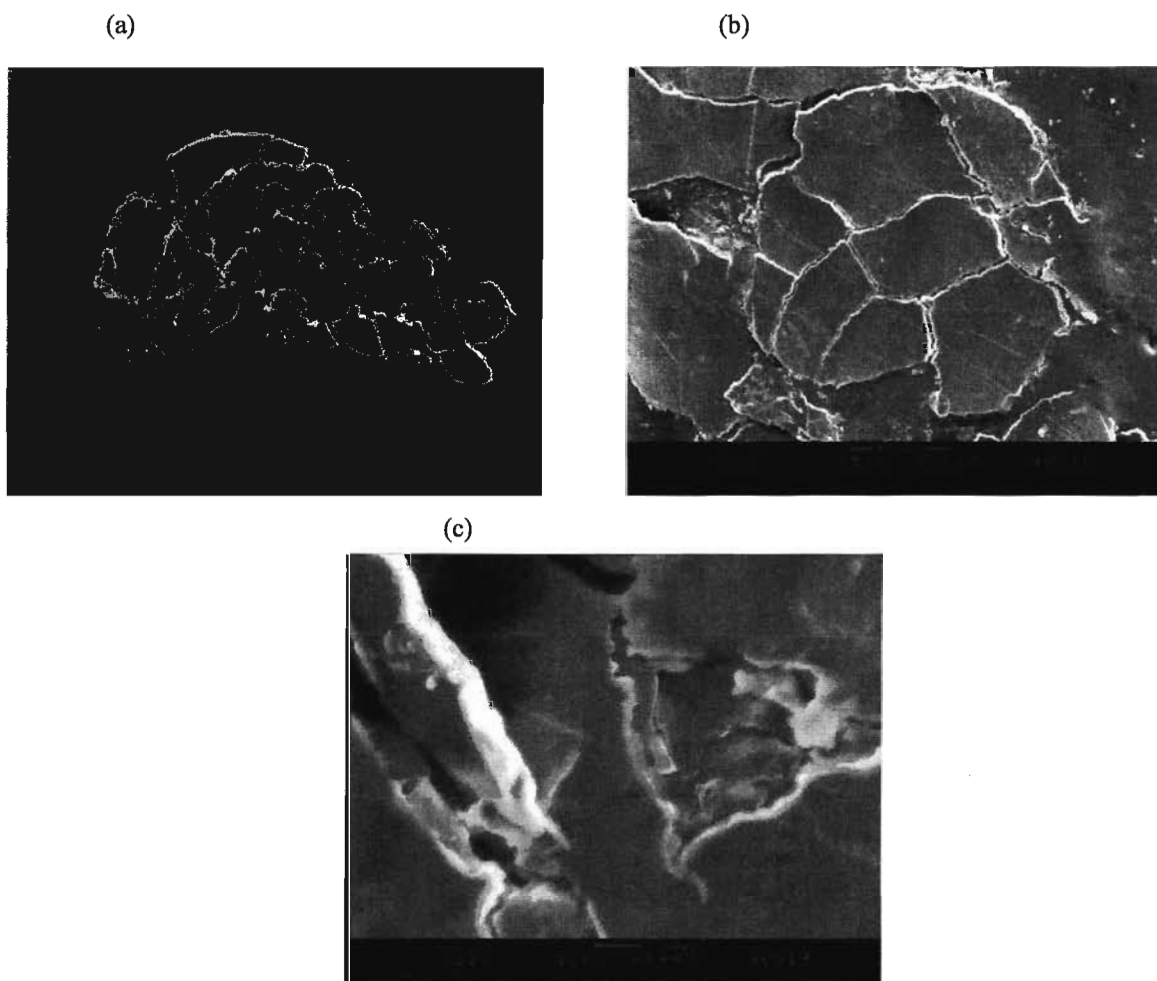


**Figure A-3:** SEM images of (6.12) at (a) 50X (b) 250X (c) 1250X magnification

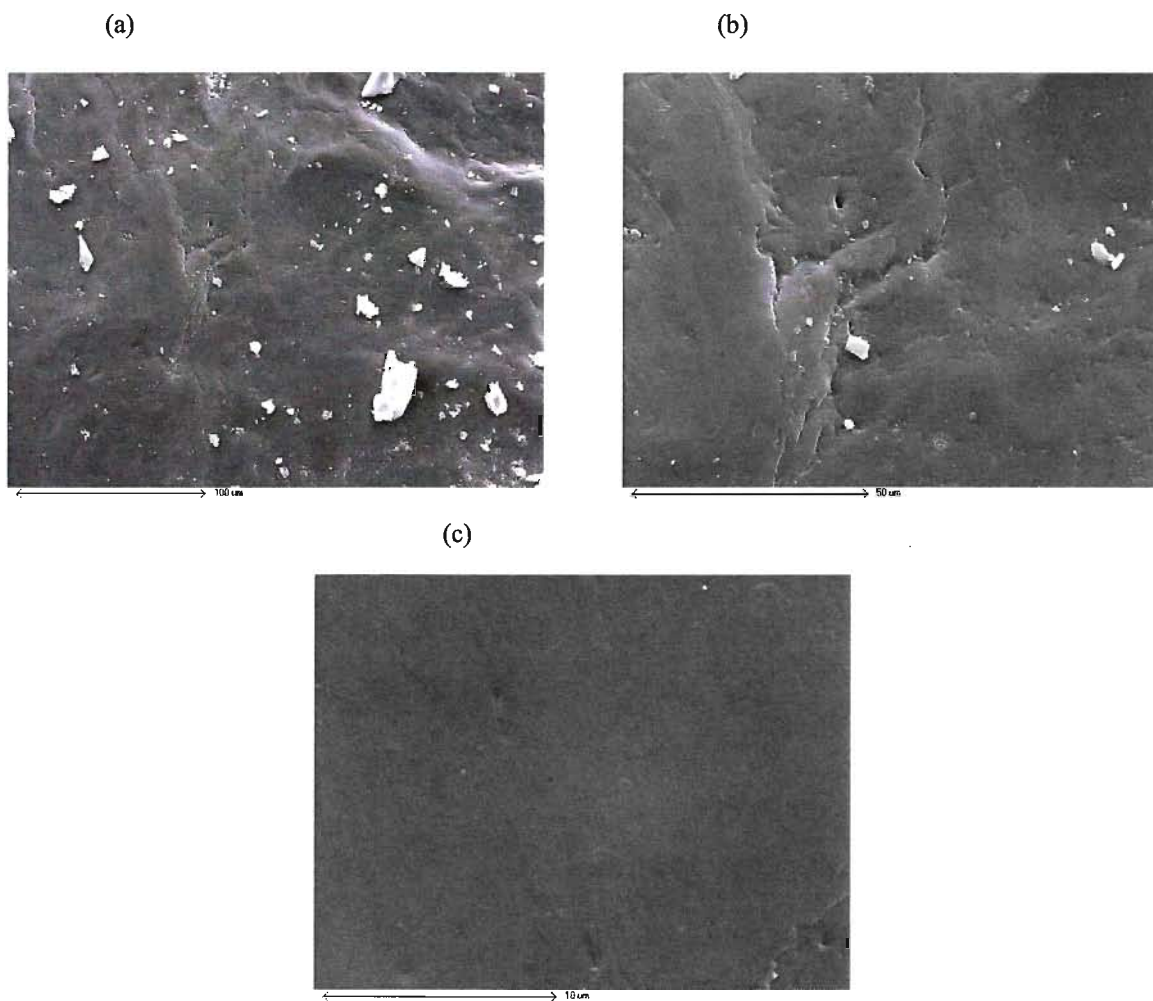


**Figure A-4:** SEM images of (6.15) at (a) 406X (b) 1010X (c) 5000X magnification

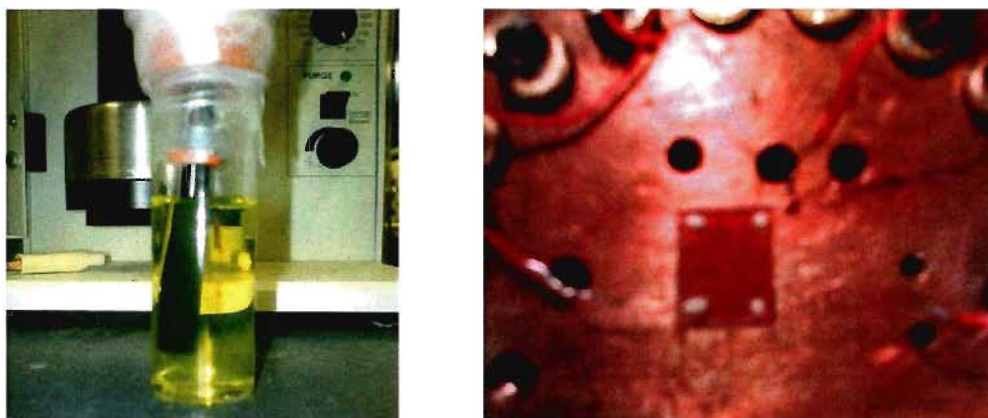


**Figure A-5:** Electropolymerization of (4.06) (left) and (6.15) connected to the variable temperature resistivity apparatus (right)